SAPIENZA
UNIVERSITÀ DI ROMA

Sapienza University of Rome

Physics Departement
Doctoral School in Astronomical, Chemical, Physical, Mathematical and Earth Sciences "Vito Volterra"

Thesis For The Degree Of Doctor Of Philosophy

Galaxy evolution studies with the SPICA telescope

Thesis Advisors
Dott. Luigi Spinoglio
Prof. Enzo Pascale

Correlatore
Dr. Juan Antonio Fernández-Ontiveros

Candidate
Sabrina Mordini

Academic Year MMXVIII-MMXXI (XXXIV cycle)

Poets say science takes away from the beauty of the stars – mere gobs of gas atoms. Nothing is "mere." I too can see the stars on a desert night, and feel them. But do I see less or more? The vastness of the heavens stretches my imagination – stuck on this carousel my little eye can catch one-million-year-old light. A vast pattern – of which I am a part – perhaps my stuff was belched from some forgotten star, as one is belching there. Or see them with the greater eye of Palomar, rushing all apart from some common starting point when they were perhaps all together. What is the pattern, or the meaning, or the why? It does not do harm to the mystery to know a little about it. For far more marvelous is the truth than any artists of the past imagined!

Richard Feynman

Acknowledgements

I would like to thank my supervisor Dr. Luigi Spinoglio for his essential advices, for his enthusiasm for the project, for his support, encouragement and patience;

my co-supervisor Dr. Juan Antonio Fernández Ontiveros for his insightful comments and suggestions, and his assistance at every stage of the research project;

Mr. Liu Scige John for his assistance, and all the conversations that were vital in inspiring me to think outside the box and analyze multiple perspectives.

I would also like to acknowledge all the SPICA team, for their incredible work in this amazing project and for making me a part of this incredible community.

Lastly, I would like to thank my friends and family, for their support and unwavering belief in me.

Sabrina Mordini, Rome, December 2021

Abstract

Lines in the mid- to far-infrared wavelength range, less affected by dust extinction than optical lines, are ideally suited to study the physical processes taking place in the dust-hidden regions in galaxies, where heavily obscured star formation and accretion onto supermassive black-holes at their nuclei take place. These tools are fundamental for the study of local galaxies, but become of paramount importance to probe galaxies at the "Cosmic Noon", at redshift z∼1-3, when the peak of star formation activity has taken place and most of the baryonic mass in galaxies has been assembled.

One of the main goals of this Thesis is to provide reliable calibrations of mid- to far-IR ionic fine structure lines, H_2 molecular lines and PAH (polycyclic aromatic hydrocarbon features), that will be used in the near and mid term to derive crucial information on the physics driving galaxy evolution. Based on these calibrations I identify the best spectroscopic measurements for the star formation rate and the black hole accretion rate in galaxies. This is done by comparing the marginal correlation of the different line luminosities versus the total IR luminosity for three samples of galaxies in the local Universe: star-forming galaxies, active galactic nuclei, and low-metallicity dwarf galaxies. For the most commonly observed fine-structure lines in the far-IR, I compare the calibrations derived from local galaxies to the existing ALMA observations of high redshift galaxies, finding an excellent agreement. These calibrations will be exploited for distant galaxies by present and future ground-based facilities observing in the millimeter and sub-millimeter range, and for galaxies in the nearby Universe through mid-IR spectroscopic observations with the upcoming *James Webb Space Telescope* (*JWST*).

The second goal of this Thesis is to design future spectro-photometric surveys that will be able to address the most challenging problems that limit our current understanding of the galaxy evolution: the co-evolution of star formation and black hole accretion, the build-up of heavy elements and the chemical evolution of galaxies, and the feedback from active galactic nuclei. Using my calibration of the mid- to far-IR lines as a basis, I have simulated deep spectro-photometric surveys covering large cosmological volumes over extended fields (1–15 deg^2) with an imaging spectrometer covering the mid-IR spectral range (17–36μm interval), following the study case of the SPace Infrared telescope for Cosmology and Astrophysics (SPICA). A SPICA-like mission would be able to provide an unobscured three-dimensional view of galaxy evolution back to an age of the universe of less than ∼ 3 Gyrs. This survey strategy would produce a full census of the Star Formation Rate in the Universe, using PAH bands and fine-structure ionic lines, reaching the characteristic knee of the galaxy luminosity function, where the bulk of the population is distributed, at any redshift up to z∼3.5. Deep follow-up pointed spectroscopic observations with grating spectrometers onboard the satellite, from mid- to far-IR spectral range, would also measure the Black Hole Accretion Rate from high-ionisation fine-structure lines down to the knee of their luminosity function. Moreover, other two relevant goals of IR spectroscopic observations from space are the studies of feedback from AGN/starburst galaxies and of the metallicity evolution.

While at the present time the SPICA mission will not be further developed, a similar study on galaxy evolution can be partially addressed by the ALMA telescope in the mm/sub-mm range, and the *James Webb Space Telescope* (*JWST*) in the mid-IR. These facilities, while unable to perform wide-field blind surveys, will allow to study the processes that led to the Cosmic Noon,using the ALMA telescope to observe galaxies at redshift above z∼3, and the late evolution of galaxies after their peak activity, with *JWST* observing local galaxies up to redshift z∼1.

Contents

List of Figures

List of Tables

Chapter 1

Introduction

1.1 The evolution of galaxies

The galaxies that we observe in the local Universe exhibit a wide variety of properties, such as morphology, colors, luminosity, and dynamics. Ideally, an in-depth understanding of how these properties were established would encompass the full sequence of events that led from the formation of the first stars after the end of the cosmic dark ages to the present-day diversity of forms, sizes, masses, colors, luminosities, metallicities, and clustering properties of galaxies. So far, astronomers have focused on the emission properties of the galaxy population as a whole, tracing the evolution of the galaxy luminosity density through cosmic time at various wavelengths, to empirically determine the global history of galaxy evolution overlooking individual galaxy sub-populations. The energetic drive of galaxy evolution can be found in two processes, namely star formation and black hole accretion (BHA), and their interplay, while the results of these processes and their mutual interaction can be found in the chemical evolution of galaxies and, in particular, in their metallicity evolution.

In this Chapter, I present a brief review of the history of galaxy evolution, and the limits that the current theories and observations present on the same theme.

1.1.1 First observational evidences

On 26 April 1920 was held the so-called Great Debate at the Smithsonian Museum of Natural History, between the astronomers Harlow Shapley and Heber Curtis, on the nature of spiral nebulae and the size of the Universe. Shapley was arguing in favor of the Milky Way as the entirety of the universe, suggesting that "spiral nebulae" such as Andromeda were simply part of the Milky Way. Curtis, on the other hand, contended that Andromeda and other such "nebulae" were separate galaxies, or "island universes". In 1924, Edwin Hubble measured the distance to Andromeda, demonstrating that it is located beyond the limits of our own galaxy, and in 1926 he proposed a morphological classification scheme for galaxies, still in use. This 'tuning fork' diagram, shown in Fig. 1.1, shows different types of galaxies, from elliptical galaxies to barred and unbarred spirals. These lasts are then further classified according to the tightness and structure of their arms, which appears to correlate with the fraction of light present in the central area, the bulge. An intermediate morphology between elliptical and spirals is found in the lenticular galaxies, indicated as S0: like spiral galaxies, lenticulars show a disk like structure with an inner nuclear bulge, but do not present spiral arms, and share the smoothness and colors of the elliptical population.

The morphology of the luminous component of galaxies, namely stars, gas and dust, is the most obvious

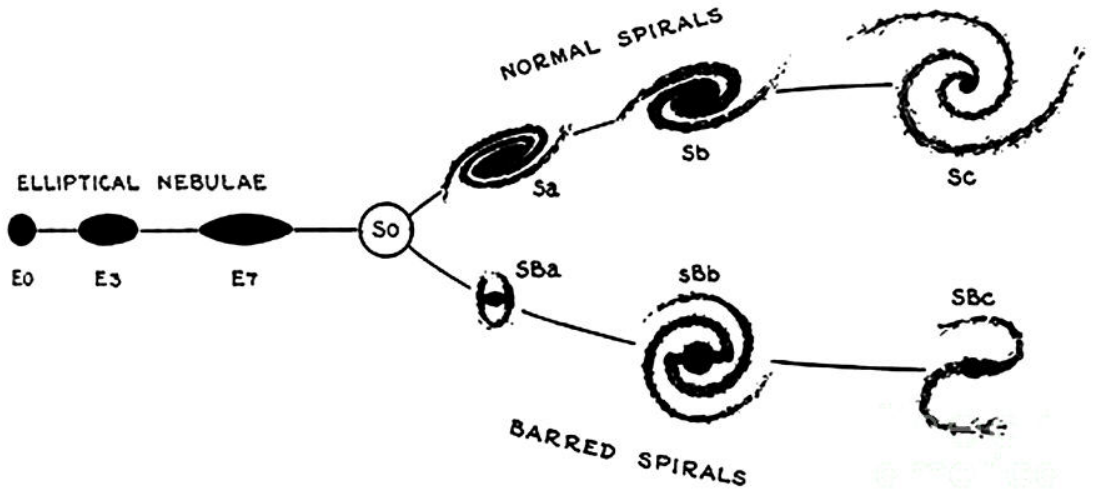

Figure 1.1: The Hubble Sequence in the form of a 'tuning fork' (Hubble 1936). Spheroidal galaxies lie in the stem of the fork and spirals and barred spirals in each prong.

manifestation of the diversity of galaxy properties. Essentially, the Hubble classification scheme is based on the relative proportions of the two major structural parts of the luminous component of galaxies, namely the bulge and the disk. The bulge is generally made of relatively old and evolved stars, which are characterized by red colors, and is shaped like an ellipsoid with various degrees of flattening and oblateness. In general the bulge contains no appreciable amount of dust and gas, and therefore has no activity of star formation. The disk is composed by a mixture of old and young stars and by gas and dust, and it is frequently the site of star formation activity. Its colors are generally bluer than those of the bulge. The most visually striking feature of the disk is the frequent presence of the spiral arms, density waves that generate in the disk and which contain active regions of star formation. Bulge and disk do not only differ for the composition of their stellar populations and interstellar medium, but also for their dynamics.

Initially, it was believed that the Hubble sequence was the manifestation of an evolutionary process such that galaxies originated as elliptical galaxies, which were therefore called the 'early types', and evolved to become spirals and irregulars, which were called the 'late types'. Although it has been shown that such ideas were incorrect, nonetheless the nomenclature has remained, and today it is common to refer to elliptical and lenticular galaxies as 'early type galaxies'.

The integrated colors of galaxies of different type shows a strong trend explained in terms of their current star formation rate (SFR): blue late type galaxies are particularly active in forming stars, while redder early types are more quiescent. However, this trend does not imply that one type evolves into the other, but can suggest a sequence in which the star formation declines from its initial values. Analysing the optical and infrared colors of a sample of local galaxies, Tinsley (1977) argued that spiral galaxies, constantly forming galaxies, would appear the same in the past, while the elliptical galaxies that locally appear red, at redshift $z>0.5$ should appear significantly bluer, because seen during star formation.

While the morphological aspect is one of the more noticeable results of galaxy evolution, other patterns have been observed. For instance, another product of the evolution of galaxies with time was first discovered by Lequeux et al. (1979). Studying the HII regions inside irregular and blue compact galaxies, the authors found that the heavy element content in the gaseous components of galaxies correlates with their mass. More recently, Tremonti et al. (2004) found a tight correlation (± 0.1 dex) between stellar mass and the

gas-phase oxygen abundance, extending over 3 orders of magnitude in stellar mass and a factor of 10 in oxygen abundance, analyzing a sample of ∼53000 star forming galaxies at redshift $z < 0.1$. The presence of a correlation between mass and metallicity shows that galaxies with different masses follow different evolutionary tracks. It also emerges that, for galaxies of mass equal to $10^{10}\mathrm{M}_{\odot}$, the mass metallicity relation saturates, suggesting that these objects have reached the end of their evolution process (Zahid et al. 2014).

Next to star formation and evolution, and the chemical evolution of the gas, another important element to consider among the ingredient of galaxy evolution is the super-massive black holes in the nuclei of galaxies. Magorrian et al. (1998) were the first to observe, on a large sample of present-day galaxies not selected for the easy identification of a present black hole, a correlation between the black hole mass ($\mathrm{M_{BH}}$) and the mass of the bulge stellar component ($\mathrm{M_{bulge}}$). The study not only suggested that almost all galactic bulges contain a black hole that satisfies the $\mathrm{M_{BH}} - \mathrm{M_{bulge}}$ relation, but introduced the idea that, in the past, the stellar and black hole component evolved together. Subsequent studies refined this finding (e.g. Kormendy & Ho 2013), leading to include the effect of the SMBH as one of the main component in the description of galaxy evolution. For instance, Di Matteo et al. (2005) simulated the simultaneous star formation and black hole accretion (BHA) during galaxy-galaxy collision. It emerges that the merge leads to a burst of star formation, but also to a strong gas inflow that feeds the SMBH. The energy released by the BH expels enough gas to quench both star formation and further BH growth, thus explaining the relationship between the black hole mass and the stellar velocity dispersion in the galactic bulge. On the other hand, there seems to be no correlation between the mass outside the bulge and the BH at the center of the galaxy, suggesting little influence from the BH to the larger environment (Heckman & Best 2014).

A tight correlation between $\mathrm{M_{BH}}$ and the velocity dispersion σ was found by Ferrarese & Merritt (2000) and Gebhardt et al. (2000), with a scatter consistent with just the measurement alone. This relation is very important because it constitutes a simple method to measure $\mathrm{M_{BH}}$ from an easy to make measure, and is moreover a strong indication of the link between the BH growth and the bulge formation (Kormendy & Ho 2013). Fig. 1.2 shows the two correlations, $\mathrm{M_{BH}} - \mathrm{M_{K,bulge}}$ and $\mathrm{M_{BH}} - \sigma$, as determined for the same sample of galaxies. Other observations proved that BH masses do not correlate with galaxy disks (Kormendy et al. 2011; Kormendy & Gebhardt 2001), and, although it was originally proposed by Ferrarese (2002) as a correlation, later studies found no correlation also with the dark matter halo of the hosting galaxy (Kormendy & Bender 2011).

1.1.2 The current picture

In the current framework, the understanding of galaxy evolution is linked to a cosmological model of he Universe.

In 1916, Albert Einstein published his paper on the theory of General Relativity, and in 1922 Friedmann, derived from the field equations of General Relativity the fundamental equations for the description of the evolution of the Universe, the Friedmann equations. In 1929, Hubble, with astronomical observations, introduced his law on the Universe expansion, and measured the value of the expansion rate of the Universe, the Hubble constant $\mathrm{H_0}$. Before this, the Universe was considered static, infinitely old, and with an infinite volume.

The Big−Bang model follows from the Friedman equations: the Universe started expanding from an infinitely dense primordial plasma. The time $t = 0$ indicated the moment of the Big Bang, a space-time singularity and an infinite energy density of matter. During the Universe expansion, the temperature and the particle density of the primordial plasma drop down. Consequently, the particle reaction rate decreases

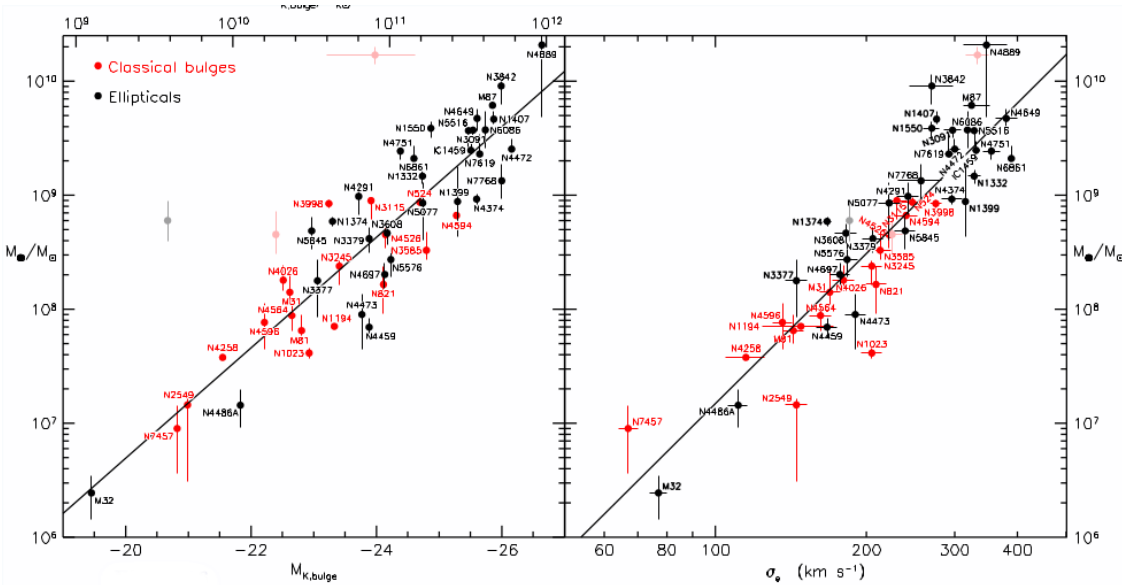

Figure 1.2: Correlation of dynamically measured M_{BH} vs. K-band absolute magnitude of the bulge (on the left) and vs. velocity dispersion σ_e (on the right). Red dots represent classical bulges, while black dots represent elliptical galaxies. The points with a lighter color represent objects that deviates significantly from the theoretical relation. Figure from Kormendy & Ho (2013).

with time and at a certain point some particle species stop interacting with the rest of the plasma. When the temperature of the Universe reached a value below ~0.3eV, electrons and protons combined into neutral hydrogen atoms. This event is called recombination and occurred at the redshift $z_{rec} \approx 1100$. Before recombination, photons were in thermal equilibrium with matter through elastic Thomson scattering off free electrons. After recombination, the lack of free electrons caused the decoupling of photons from matter: the photons started freely propagating in the Universe, giving origin to the so called Cosmic Microwave Background (CMB). The CMB spectrum, predicted by Gamow in 1946 and accidentally detected by Penzias & Wilson (1965), is very close to that of a black body with a temperature of 2.7 K, presenting only very small anisotropies at the level of 10^{-5}. These small fluctuations depend on the values of the cosmological parameters. At the end of the 20th century, several balloon-borne experiments measured the CMB fluctuations on small angular scales, providing a better estimate of several cosmological parameters (e.g., de Bernardis et al. 2000). The measures of the anisotropies from the WMAP satellite, launched in 2001, provided precise estimates of many cosmological parameters at the level of a few percent. In particular, they confirmed the energy budget of the Universe. After WMAP, the CMB anisotropies were studied by a more advanced satellite, Planck, which was launched in 2009.

The Standard Model of cosmology is based on two fundamental concepts: the Standard Model of particle physics, which is used for the matter content, and General Relativity, which describes gravitational interactions. The Einstein equations relate the geometry of the space-time to the matter content, and if the matter content and its distribution are known, it is possible to determine the space-time geometry. In general, it is highly non-trivial to solve the Einstein equations, but analytic solutions can be found only if is assumed the presence of symmetries of the space-time. The Standard Model of cosmology assumes the so-called Cosmological Principle: *The Universe is homogeneous and isotropic*. The assumption relies on the fact that there are no preferred points or preferred directions in the Universe

If the Cosmological Principle is valid, the geometry of the Universe is described by the Friedmann-Robertson-Walker (FRW) metric, which only depends on a constant parameter k and a function of time $a(t)$.

The constant k may be positive, negative, or zero, respectively for the case of closed, open, or flat universe; $a(t)$ is the scale factor and determines the evolution of distances between distant, not bound objects in the Universe. Inserting the FRW metric in the Einstein equation permits to derive the Friedmann equations, which determine how $a(t)$ depends on time for different forms of cosmological matter.

In the Friedmann cosmology, all physically relevant cosmological models started from an initial singularity, where the scale factor was zero. After the singularity, the big-bang, the Universe expansion began, with the expansion rate and final destiny of the Universe depending on its 3 dimensional geometry and the matter content. In the cases of matter dominated or radiation dominated models, the Universe first expands and then recollapses if it is closed (k > 0), or it expands forever if it is open (k < 0) or flat (k = 0). In the presence of vacuum energy the fate of the Universe depends on the specific contribution of its components. Current observations support the so-called Λ cold dark matter model (ΛCDM model), in which the Universe is almost flat and today it is dominated by vacuum (or vacuum-like) energy (almost 70%), while the other 30% is made of non-relativistic matter. The contribution from other components is much smaller and irrelevant for the current expansion regime.

One feature of the model is the partitioning of mass-energy into entities that obey different equations of state. Allen et al. (2004); Fukugita & Peebles (2004) report this partitioning as follows: total density $\Omega = 1$, divided in dark energy density $\Omega_\Lambda = 0.73$ and matter density Ω_M=0.27. The matter density is again divided in dark matter density $\Omega_{dm} = 0.22$ and baryonic density $\Omega_b = 0.05$. These values come from matching the theory to observations of the CMB, from the distance-redshift relation obtained from Type Ia supernova or observations of rich galaxy clusters a different redshifts. In particular, informations about the density of the baryonic matter come from the CMB angular power spectrum (Spergel et al. 2003) or measures of the abundances of light elements compared with big bang nucleosynthesis theory (Coc et al. 2004), while the existence of the dark matter component is derived from the dynamics and clustering of galaxies (e.g. de Blok et al. 2001, Kleyna et al. 2001 and Borriello & Salucci 2001) or gravitational lensing measurements (Mellier 1999 and Sand et al. 2004).

The Standard Model of cosmology is very successfully in explaining a huge amount of observational data, including – as the most remarkable ones – Hubble's law, the primordial abundances of light elements, and the main peaks in the power spectrum of the cosmic microwave background.

The fluctuations in the CMB can explain the present day observations of the large scale structure of the Universe: the anisotropies are linked to primordial fluctuations that also created overdensities in the accumulation of dark matter. The anisotropies grew over time due to gravitational instabilities. Numerical simulations have shown that the structure formation in the dark matter component proceeds via the formation of sheets or giant walls, which in turn form filaments where they intersect. At the intersections of the filaments, there is the formation of dark matter halos, which create a gravitational pull in which fall both dark and baryonic matter. The simulations show that there is a very strong correspondence between the dark matter and gas density fields on large scales. This illustrates that gas flows on large scales is dominated by gravity (Somerville & Davé 2015). For large enough dark matter halos, the gas was able to cool, form stars, and form proto-galaxies. Galaxies within these halos then continue to form stars (in situ) as well as to grow through merging (ex situ), because their dark matter halos merge (Wechsler & Tinker 2018). Fig. 1.3 shows a $100 \times 100 \times 20$ comoving Mpc (cMpc) slice from the Evolution and Assembly of GaLaxies and their Environments (EAGLE, Schaller et al. 2015) simulation, with a zoom-in on a 10 cMpc and a 60 ckpc (comoving kiloparsec), showing the relative dimensions between a galaxy and its dark matter halo.

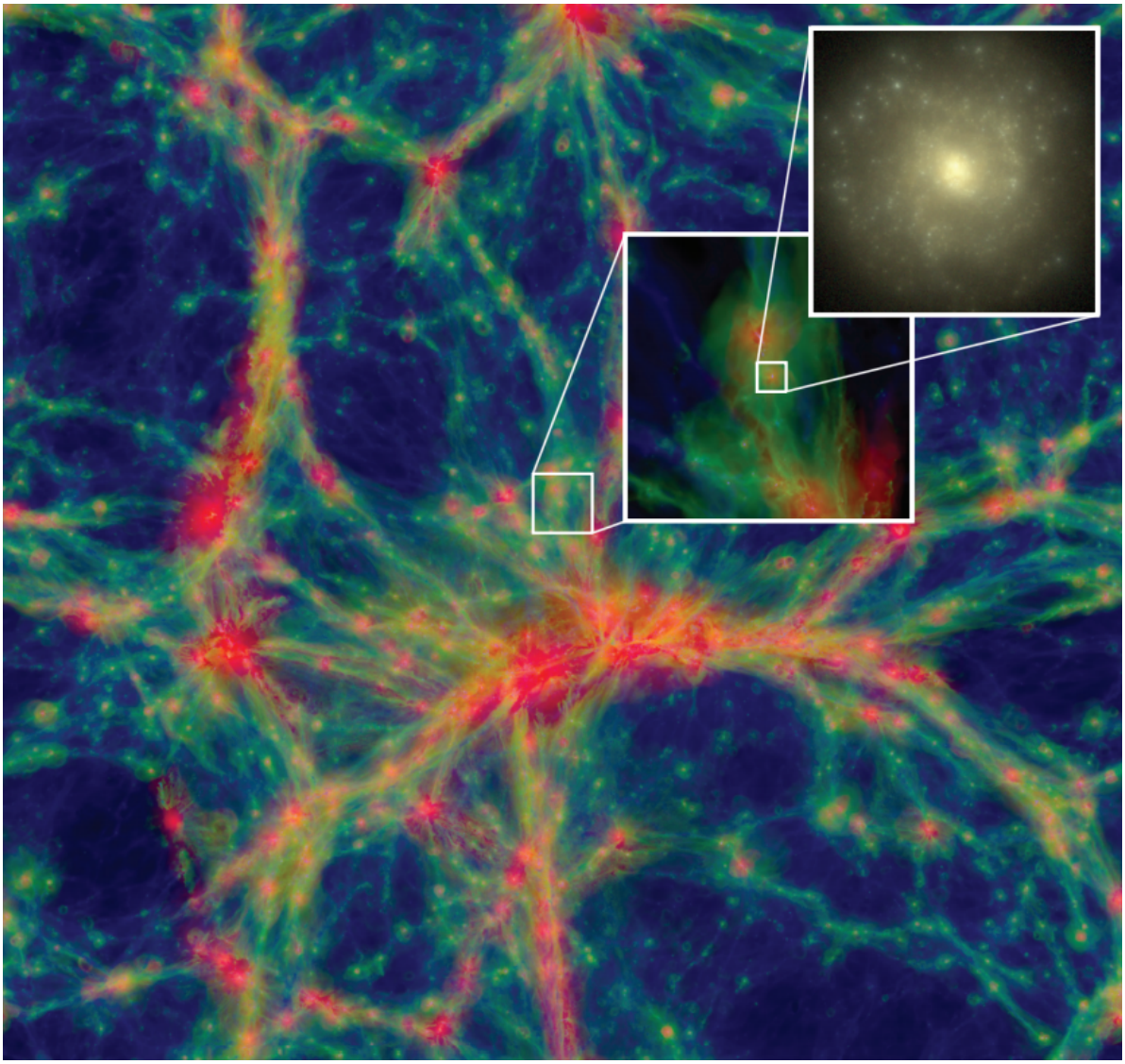

Figure 1.3: A $100 \times 100 \times 20$ comoving Mpc (cMpc) slice through the EAGLE simulation. The intensity represents the gas density, whereas the color indicates the gas temperatures (blue through green through red indicate cooler to hotter). The inset shows a region 10 cMpc and 60 ckpc (comoving kiloparsec) on a side. The zoom into an individual galaxy with stellar mass $3 \times 10^{10} M_{\odot}$ shows the optical band stellar light. Image from Somerville & Davé (2015).

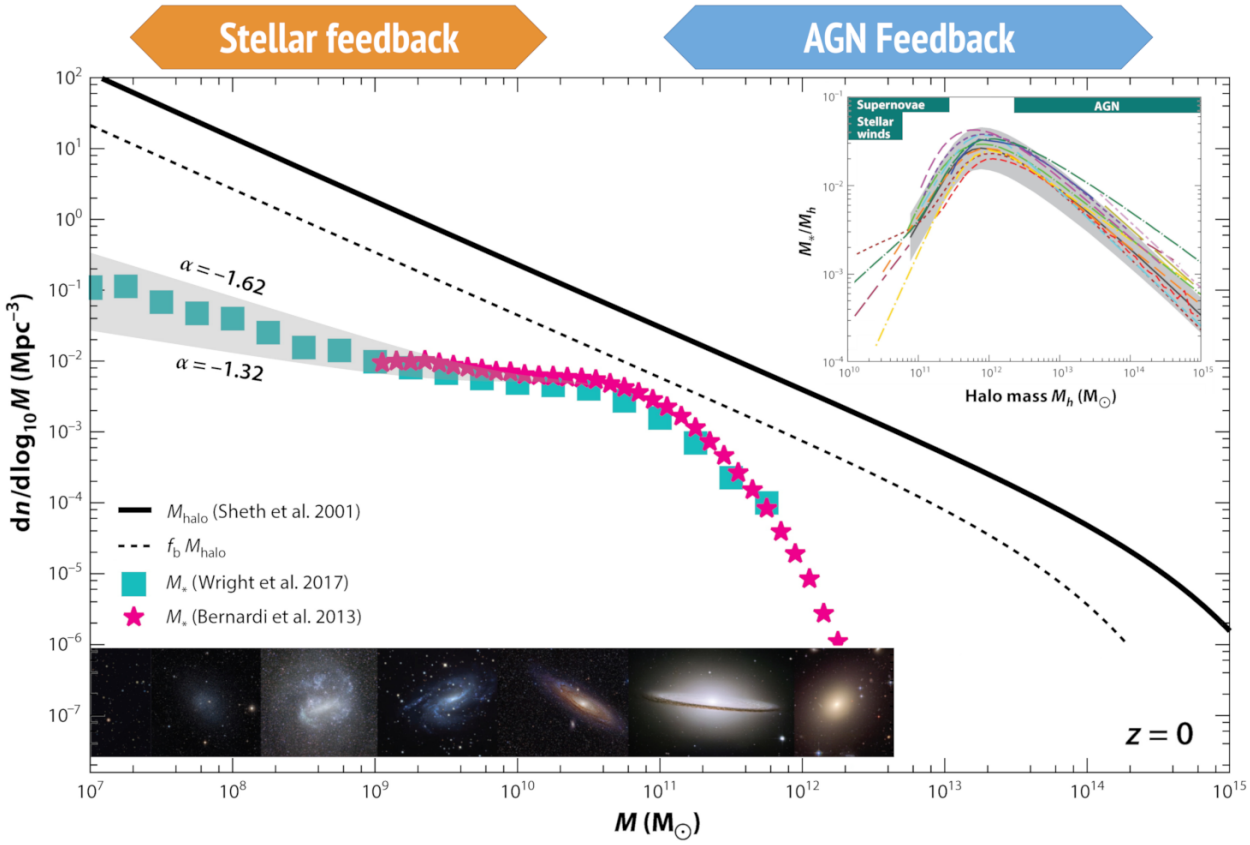

Figure 1.4: The field galaxy baryonic mass function as presented by Bullock & Boylan-Kolchin (2017). The thick black line shows the global dark matter mass function. The dotted line is shifted to the left by the cosmic baryon fraction for each halo. The magenta stars show the stellar mass function of galaxies from Bernardi et al. (2013), while the cyan squares show the stellar mass function from Wright et al. (2017). The shaded bands demonstrate a range of faint-end slopes. At the bottom are shown examples of galaxies at different mass ranges.In the top left corner, the mass function is parametrized by different method, as described by Wechsler & Tinker (2018).

1.1.3 Discrepancies between theory and observations

The Λ−CDM model seems successful in describing the formation and evolution of the large scale structure in the Universe, the state of the early Universe, the predictions of the cosmic microwave background (CMB) or the abundances of light elements. Moreover, it has been tested against some discoveries like the lensing of the CMB (Das et al. 2011; Smith et al. 2007b) or the B-mode polarization (Hanson et al. 2013).

The model, however, presents several difficulties: discrepancies are present between the 2013 Planck parameters (Planck Collaboration et al. 2014) and σ_8 obtained from cluster number counts and weak lensing, the actual value of the Hubble parameter, H_0, and supernovae IA data. The Planck 2015 data are still in tension with Canada-France-Hawaii Telescope (CFHT) lensing survey (Raveri 2016) data, and with the σ_8 growth rate (Macaulay et al. 2013). Another problem is found in the statistical anomalies shown by the large-angle fluctuations in the CMB, contradicting the idea that the Universe should be a realisation of a statistically isotropic and Gaussian random field, which implies a statistical independence in the CMB multipoles. The origin of these anomalies is uncertain: they could be related to unknown systematics, to statistical effects (Bennett et al. 2011), or they could be the indication of a new physics.

Fig. 1.4 shows the relationship between visible matter mass and dark halo mass: at all masses, the baryonic content of galaxies is below the predicted cosmological value. The minimum distance is reached for a dark matter halo mass of $\sim 1\times10^{12}M_\odot$, corresponding to $M_* \sim 3\times10^{10}M_\odot$, while at lower and higher

values the difference is more pronounced.

These discrepancies can be explained with feedback processes, either preventive or ejective. The preventive feedback retards star formation by stopping gas from accreting into the ISM, whereas ejective feedback describes processes that remove the gas from the ISM after it has been accreted. Single processes can act both in a preventive and ejective way. Stellar feedback is used to explain why the stellar and baryon fraction within galactic-sized halos is much smaller than the universal value, reaching a maximum of 20% the predicted value (Behroozi et al. 2010; Moster et al. 2010). This effect is linked to large-scale galactic outflows powered by massive stars and SNe, with star forming galaxies that show mass-loss rates likely of the same order as the SFR or larger (Veilleux et al. 2005), and could explain the discrepancy for the low-mass end of the distribution.

When considering the accretion onto a black hole, on the other hand, is possible to explain the discrepancy observed at the high end of the mass spectrum (Veilleux et al. 2005). There are several physical mechanisms for which a large amounts of energy and momentum produced by AGNs can couple with the gas in and around galaxies, thus regulating the growth of the BH itself or suppressing cooling and star formation on galactic scales. In a simplified view, an AGN can heat gas up, drive winds that eject gas, and ionize or photo-dissociate gas. Radiation may also drive winds via pressure on spectral lines, free electrons, or dust. The winds may originate either in the accretion structure near the BH, or on larger nuclear scales, of the order of a few kpc. Winds arising on small scales may drive galaxy-scale winds by shocking and sweeping up ISM gas, or they may vent out of the galaxy without ejecting much mass.

When performing numerical simulations to reproduce galaxy formation and evolution, the feedback model is introduced, and its parameters are regulated ad-hoc, in order to reproduce the observed relations, such as the Magorrian relation (Magorrian et al. 1998; see Section 1.1) or the bimodality observed in the color distribution of galaxies (Baldry et al. 2004). The model takes into consideration the infall of great amounts of gas in galaxies central regions is responsible for both star formation and BHA, and when the BH reaches a limit mass/luminosity value, the accretion couples with the interstellar medium quenching both star formation and BHA (Hopkins et al. 2006, and references therein). Part of galaxy evolution is regulated by secular processes that involve accretion of metal-poor material from minor mergers or the intergalactic medium, star formation, and the expulsion of metal-rich gas and dust in the interstellar and intergalactic medium, although it is still unclear how the processes that regulate these exchanges interact with each other. In particular, the conditions needed for star formation are governed by the processes controlling the cooling and compression of the ISM, while feedback is responsible for the energy that heats gas and dust. In the local Universe, galaxy-scale feedback is observed in all phases of the interstellar medium, but a study at different epoch is needed to properly understand how galaxy evolve. When introducing the feedback model in galaxy evolution simulations, however, the ad-hoc parameters are needed to compensate the inability of the simulations to reach the scales at which the feedback processes take place. This leads to significant difficulties in constraining the net effect of the feedback processes in the context of galaxy evolution.

1.1.4 The baryon cycle and the dust-obscured build-up of galaxies

The complex interplay between the star formation and BH accretion affect galaxy evolution not only in terms of energy output, but also influencing the so-called baryon cycle (see Fig. 1.5, and Davé et al. 2012) inside the galaxy: gas accretion is a catalyst for both star formation and BHA, and while star formations produce the chemical elements that enrich the interstellar and intergalactic medium, accretion processes can ionize atomic gas and dissociate molecular gas; the interstellar medium is composed of matter in various physical

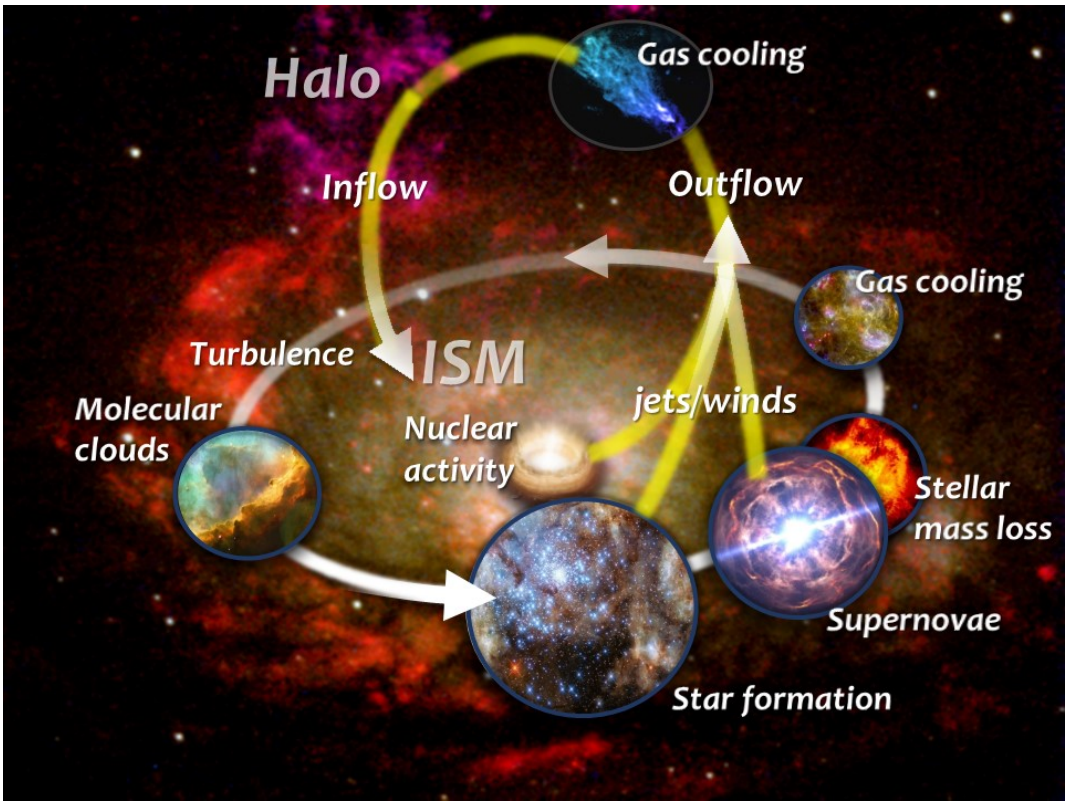

Figure 1.5: Interplay between the different processes that take place inside a galaxy, in the so-called baryon cycle.

states, e.g. ionized, neutral, atomic and molecular gas, or dust, and they are actively interacting with each other and with the surrounding intergalactic medium.

The observational study of the baryon cycle can be done preferentially through IR spectroscopy, in particular because the presence of dust, which prevents observations at shorter wavelengths, does not affect IR observations; moreover, most molecular and atomic cooling lines occur in the IR (e.g. H_2, CO, OH, H_2O, and all ionic fine-structure lines). Heavy elements and dust have a strong influence on the observational properties, even if they contribute in a minimal part to the total mass of a galaxy, and need to be studied for a better understanding of the interplay among all the phenomena that take place in a galaxy. Studying the baryon cycle through cosmic time is a key aspect to understand how galaxies evolve with redshift: we know that galaxies in the $z \sim 1-3$ interval are heavily embedded in dust (Madau & Dickinson 2014), thus it is essential to be able to probe the most obscured regions to better understand what phenomena are taking place. The total content of heavy elements and dust in a galaxy is the result of the interplay among star formation, AGNs and episodes of gas accretion and ejection, although so far the influence that these phenomena play on the ISM over cosmic time is not clear. Tracking the migration of baryons both inside and between galaxies is thus a necessary step to gain a comprehensive understanding of the evolution of galaxies.

It is possible to reconstruct the history of BH accretion and star formation throughout cosmic time, using different tracers. Fig. 1.6 shows the comparison between the star formation rate (SFR) density and the black hole accretion rate (BHAR) density at different redshifts, also comparing different bands of observations. Both phenomena show a peak of activity at redshift z~1-3, with a steep decline toward the present epoch, thus suggesting a possible co-evolution between nuclear activity and star formation; the majority of the growth of SMBHs and of the stellar components in galaxies is thought to have occurred between redshifts 0.5 and 2, and the present-day growth rates of both populations are over an order of magnitude smaller than

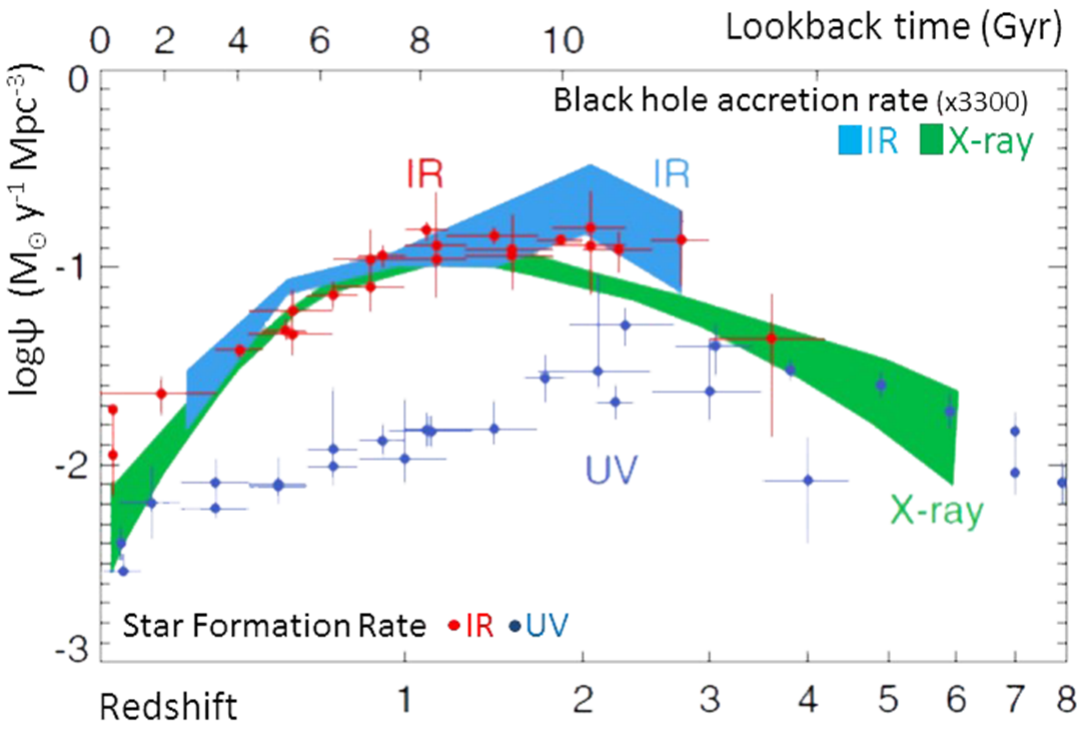

Figure 1.6: Comparison of the star formation rate density across the cosmic time determined from UV (blue dots) and IR observations (red dots) with the black hole accretion rate density measured by X-ray (shaded-green area; Shankar et al. 2009 and Aird et al. 2010) and infrared data (shaded-blue area; Delvecchio et al. 2014). The shading indicates the $\pm 1\sigma$ uncertainty range on the total bolometric luminosity density. The radiative efficiency has been set to $\epsilon = 0.1$. The comoving rates of black hole accretion have been scaled up by a factor of 3300 to facilitate visual comparison to the star-formation history (Madau & Dickinson 2014).

at the peak epoch (Heckman & Best 2014; Madau & Dickinson 2014). Looking at the different bands of observation, however, the IR data have higher values than the ones determined by the UV data for the SFR, and the X-ray data for the BHAR. For the star formation processes, in particular, it has been estimated that the UV can only account for ~10% of the total emitted light because of the heavy dust extinction encountered up to redshift z~3 (Madau & Dickinson 2014). At the same time, X-ray surveys cannot penetrate the more obscured galaxies at the peak of BHA, leading to a bias toward less obscured environments. The difficulty of gaining a complete picture of galaxy evolution using only optical/UV data (for star formation processes) and X-ray data (for BHA processes) summed to the lack of IR data above redshift z~3 leads to an incomplete understanding of galaxy evolution with cosmic time. In particular, when considering the peak of activity of both processes, at redshift $2< z <4$, is important to take into account that most of the energy emitted by stars and accreting BH is absorbed by dust and subsequently re-emitted at longer wavelengths. The presence of a significant number of sources radiating the bulk of their energy in the IR implies that the critical phases of SF and BHA took place in heavily obscured systems, embedded in large amounts of gas and dust. The obscuration of these objects makes their characterization trough optical and UV data critically biased or impossible. This implies that in order to gain a real understanding of the physics of galaxy evolution it is necessary to observe large, unbiased samples of galaxies in the IR, covering a wide range in physical parameters like luminosity, redshift, nuclear activity and so on.

1.2 Star formation and black hole accretion

A variety of physical processes are thought to shape the observed distribution of galaxy properties, ranging from those responsible for galaxy growth (e.g. star formation and galaxy merging) to those that regulate such growth (e.g. energetic feedback from supernovae (SNe) and active galactic nuclei (AGNs), and feeding through accretion onto super massive black holes (SMBHs) in AGNs). The current observational picture is that the two main energetic processes inside a galaxy, star formation and BHA, evolved together throughout cosmic time, and are thus fundamental to understand how galaxies evolve. In this section, I show how star formation and BHA can be measured from surveys carried out in different bands, and the main results of these surveys.

1.2.1 Star formation

Star formation is galaxy evolution in the making, and the SFR gives us a measure of how much mass is been converted into stars in units of $\mathrm{M}_\odot\ \mathrm{yr}^{-1}$; one of the key assumptions to measure the SFR of a galaxy is its *star formation history* (SFH), with most classical estimators based on the assumption of a constant SFR over a period of 100 Myr (Kennicutt 1998). Most star-forming galaxies have an SFR that is well-correlated with their stellar mass, a correlation which is often called 'Main Sequence' (MS) on which the specific SFR (sSFR) depends only weakly on stellar mass, $s\mathrm{SFR} \propto m^{\beta}$ with β ~-0.1, with a scatter of order 0.3 dex, showing that more massive galaxies are less efficient in forming new stars (Lilly et al. 2013). A few percent of galaxies have significantly elevated sSFR, but these contribute only about 10% of the overall star-formation over a range of redshifts $0 < z < 2$ (Rodighiero et al. 2011). The *star formation rate density* (SFRD) is used to analyze the evolution of star formation per unit volume with cosmic time, and it is expressed in units of $\mathrm{M}_\odot\,\mathrm{yr}^{-1}\,\mathrm{Mpc}^{-3}$. One of the very first modern SFRD measurements was done by Lilly et al. (1995) and Madau et al. (1996). There are different ways to measure this quantity, in particular the UV continuum between 1400Å and 1700Å, and the mid- and far-IR light. The UV continuum emission is associated with young, massive stars, that have a short lifetime, making the UV emission quite short in time. Bolometrically, over a 10-Gyr period, at least half of the luminosity produced by a simple stellar population[1] emerges in the first 100 Myr, mainly in the UV, then the luminosity stabilizes when the O-stars population evolves off the main sequence (Madau & Dickinson 2014). The relation between the UV light and the SFR can be expressed as:

$$\mathrm{SFR} = \mathrm{K}_{\mathrm{FUV}} * \mathrm{L}_\nu(\mathrm{FUV}) \tag{1.1}$$

where $\mathrm{L}_\nu(\mathrm{FUV})$ is the specific far UV luminosity (in $\mathrm{erg\,s^{-1}\,Hz^{-1}}$) and $\mathrm{K}_{\mathrm{FUV}}$ is a conversion factor that depends on the history of star formation, metallicity and *initial mass function* (IMF)[2]. The biggest problem with UV measurements is due to dust obscuration, because even modest amounts of dust are able to significantly suppress the UV emission, requiring a correction for UV-only based measures, or a complementary IR measure. Dust re-emits the UV light in the mid- and far-IR bands, which can be used to trace star formation. Even though the older stellar populations can contribute to the IR emission heating dust in the interstellar medium, this becomes relevant only at very low SFR, where the young stellar population emission in the Far-IR range becomes comparable to the mid-IR emission due to new stars (Kennicutt 1998)

[1] A simple stellar population is defined as a group of stars born at the same time with an homogeneous chemical composition.

[2] The IMF is an empirical function that gives the distribution of masses in a stellar population at the epoch of formation. It gives the ratio between hot, bright stars that dominate the light and cool, faint stars that dominate the mass. Consequently, it controls the evolution (both in luminosity and in color) of a stellar population, as stars with different masses evolve at different time scales.

. If we consider a star forming galaxy without an AGN, the SFR can be related to the IR luminosity much like the UV emission (more in section 1.2.1):

$$\mathrm{SFR_{IR}} = \mathrm{K_{IR}} * \mathrm{L_{\nu}(IR)} \tag{1.2}$$

where the IR component of the SFR refers only to the dust-obscured portion of the SFR (Madau & Dickinson 2014).

UV surveys

One of the most used method to measure the cosmic SFRD uses rest-frame ultraviolet continuum measurements, largely because the method is quite sensitive and can be applied over a very broad range of redshifts. Optical photometry can be used to measure rest-frame FUV (1500Å) SFRs at $1.4 < z < 6$, using ground based or HST imaging, while at $z < 1$, space based telescopes are necessary to measure rest-frame UV. Lilly et al. (1996) found that the 2800Å luminosity density declined by approximately one order of magnitude from z=1 to the present time, which they interpreted as a steep decline in the SFRD. Taken together, the *Hubble Deep Field* (HDF) measurements at z>1 (Ferguson 1995) and the *Canada-France Redshift Survey* (CFRS) measurements at z<1 (Crampton 1993) suggested a general 'rise and fall' picture of a UV luminosity density with the peak of star formation between $z \approx 2-3$. Various surveys subsequently extended this finding using other data sets or different analyses. A HST/WFC3-UVIS survey of gravitationally lensed galaxies behind the massive cluster Abell 1689 has been used for Lyman break color selection to unprecedentedly faint FUV luminosities at z≈2 and found no turnover to the LF at the observed magnitude limit of $\mathrm{M_{AB}} \approx -13$ (Alavi et al. 2014). A Keck spectroscopic campaign looking for Lyman break-selected galaxies (LBG)[3], especially at z≈2-3, has been extended over several years (Steidel et al. 2003, 2004). Using UV rest-frame selection for LBG studies means missing the heavily dust-obscured star formation regions at these redshifts.

At higher redshifts, $4 < z < 7$, deep HST observations have dominated surveys for LBGs in recent years. Several fields have been revisited over the years to add deeper optical imaging and near-IR data, with these observations making Lyman break selection at $z \approx 6$ far more robust and extending the method out to $z \approx 8$, with a handful of unconfirmed candidates identified out to $z \approx 12$.

Early analyses of the GOODS data found mild evolution of the UV luminosity density at redshifts $2 < z < 5$ and evidence that there were fewer high-luminosity galaxies at $z \approx 6$ (Giavalisco et al. 2004). Subsequent studies, using deeper data and more rigorous analyses, found that the UVLF evolves significantly at z > 4, with this evolution being primarily luminosity evolution, at least at $4 < z < 7$ (Bouwens et al. 2012). This resulted in the number density of bright LBGs increasing rapidly with time, more quickly than does the integrated luminosity density. Analyses using the *Cosmic Assembly Near-infrared Deep Extragalactic Legacy Survey* (CANDELS; Grogin et al. 2011) and the *Hubble Ultra Deep Field* (HUDF; Beckwith et al. 2006) near-IR imaging suggest an extended evolution out to z=8 and perhaps beyond (Lorenzoni et al. 2013; Schenker et al. 2013), although only a handful of galaxies at $z \approx 7$ have reasonably secure spectroscopic confirmation. Several studies have also extended SFRD analyses to redshifts $9 < z < 12$, using data from the HUDF or from studies of lensing clusters, but have little impact on the global star formation history, since current estimates show how only $\sim 1\%$ of the cosmic star mass density observed today was formed at

[3]Star-forming galaxies at high redshift that are selected using the differing appearance of the galaxy in several imaging filters due to the position of the Lyman limit. The technique has primarily been used to select galaxies at redshifts of $z \simeq 3-4$ using ultraviolet and optical filters. For high redshift galaxies $z > 3$, the Lyman break will appear to be at wavelengths of about 3600 Å, detectable by ground- or space-based telescopes.

redshift $z > 6$ (Madau & Dickinson 2014).

IR surveys

Before the advent of space observatories, infrared astronomy was limited by two problems: Earth's atmosphere absorbs most of the IR radiation, with only a few clear windows, that become almost completely opaque between 10 and 1000μm. Moreover, the atmospheric temperature of ~300 K results in strong emission throughout the IR spectrum, creating a background significantly stronger than that due to zodiacal light from interplanetary dust. This makes earthbound telescopes significantly less sensitive than space-bound ones.

The *InfraRed Astronomical Satellite* (IRAS), launched in 1983, was the first IR space observatory ever launched. It observed ~96% of the sky in four IR bands centered at 12μm, 25μm, 60μm and 100μm, allowing the firs view of the IR universe not limited by Earth's atmosphere. It enabled the first measurements of the local far-IR luminosity function with observations at 60μm, using far-IR luminosities integrated over a broader wavelength range, or extrapolated from IRAS fluxes using fitting formulas. Luminosity functions have also been measured for IRAS samples selected at 12 and 25μm (the former particularly suited for selecting active galaxies, see Rush et al. 1993a; Spinoglio & Malkan 1989).In 1995the Infrared Space Observatory (ISO, Kessler et al. 1996) was launched, operating between 2.5 and 240μm. ISO's detectors, with a thousand times higher sensitivity and a hundred times better angular resolution (at 12μm) respect to IRAS, allowed a much closer look, a much more detailed perception of the infrared emission of galaxies.

Locally, the bright end of the IR luminosity function appears to be dominated by galaxies with warmer dust temperatures, which tend to be starburst galaxies and dusty AGNs, while the faint-end has not been well-sampled locally. In nearby galaxies more than half of the far-IR luminosity seems to arise from dust in the ISM heated from intermediate and older stellar populations (Sodroski et al. 1997), implying that a significant fraction of the total IR luminosity ($\mathrm{L_{IR}}$, the integrated luminosity in the 8-1000μm interval) does not result from current star formation, thus making far-IR a good proxy of SFR in local galaxies only for galaxies in which the contamination from the older population is negligible. At higher redshift, when the specific SFR of typical galaxies was much larger and the net dust extinction to star-forming regions was, on average, larger, we expect the IR luminosity function to more reliably trace the total SFRD. When a galaxy presents both star formation and AGN signatures, the $\mathrm{L_{IR}}$ is measured by fitting a dust emission model to multi-wavelength observations. These multi-wavelength data are usually not available on a general basis, thus the discrimination among the different contributions is made using a spectral energy distribution (SED) template derived from observations of the local Universe, and then applied to extrapolate the $\mathrm{L_{IR}}$ from a single observed flux. This method carries with itself strong uncertainties due to the differences of the dust emission properties of each galaxy.

The deepest surveys with ISO at 15 μm detected a few hundred galaxies, mainly at z ≤ 1, in the HDF and a few other deep survey regions where spectroscopic and photometric redshifts were available. In general, these observations showed that the emission from dusty star formation increased steeply with redshift (Franceschini et al. 2001). Chary & Elbaz (2001) used measurements from ISO and SCUBA, and COBE constraints on the far-IR background to constrain a model for the evolution of the cosmic SFH. Their model exhibited a sharp decline in the SFRD by a factor of 10 or more from $z \approx 0.8$ to the present, with nearly constant star formation at redshifts $0.8 < z < 2$, while at higher redshifts the SFRD was poorly constrained, with upper limits set by the cosmic infrared background and lower limits determined by sub-mm sources. Acceptable solutions ranged from flat evolution to an increase by a factor of ~10 from z =4.5 to 2 (Madau

& Dickinson 2014).

The Spitzer Space Telescope (Werner et al. 2004) greatly enhanced the sensitivity and mapping efficiency for deep IR observations, particularly at 24 μm. Integrating over derived IR luminosity functions, Le Floc'h et al. (2005) suggest that the evolution of the IR luminosity density is significantly steeper than the UV luminosity density; they also found that galaxies with $L_{IR} > 10^{11} L_{\odot}$ produced $70\% \pm 15\%$ of the IR luminosity density at $z \sim 1$, compared with 5-15% at the present time. Several studies extended Spitzer 24μm measurements up to $z \sim 2.5$, finding a flatter evolution of the IR luminosity density, and a brighter characteristic IR luminosity at $z > 1$, implying that ULIRGs emitted close to 50% of the total energy density at $z \sim 2$ (Rodighiero et al. 2010). Depending on the data, methodology, and assumptions adopted, the IR luminosity functions derived for high redshift galaxies differ at both the faint and bright ends. At the faint end, the available data rarely constrain the slope of the luminosity function at high redshift, thus most analyses simply assume a faint-end slope based on the measurements at lower redshifts, making them subject to large and uncertain extrapolations. Depending on the SED templates adopted, there are significant differences in the extrapolations from observed MIR rest-frame measurements to the bolometric IR luminosity and SFR (Madau & Dickinson 2014). Moreover, several studies using longer far-IR, radio and/or sub-mm observations, found that standard SED templates tend to overestimate typical bolometric corrections for galaxies at $z \sim 2$ (Daddi et al. 2007; Papovich et al. 2007), suggesting that true far-IR measurements are needed to accurately determine the SFRDs at high redshifts.

The Herschel Space Observatory significantly improved the far-IR coverage (70-500 μm), and several large programs were dedicated to surveys of the most important multi-wavelength deep fields. Magnelli et al. (2013) found stronger luminosity evolution at $z > 1$ than in the Spitzer data, suggesting a larger contribution of ULIRGs to the total IR luminosity density at $z \sim 2$. Gruppioni et al. (2013) found that the characteristic IR luminosity continued to brighten at $z > 2$, albeit at a slower rate. Neither survey reliably measured the faint-end slope of the IR luminosity function at high redshift, and both fixed it to the values derived in the local Universe. Broadly speaking, both studies find a decrease by a factor of ~6 between $z = 1.1$ and today and, comparatively, a flat evolution at higher redshift with an increasing range of values allowed within the measurement uncertainties.

So far, the available IR data consists mainly of broad band imaging surveys, and are affected by uncertainties due to the model dependence needed to constrain high redshift observations. Fig. 1.7 shows the comparison between the cosmic optical and IR background in the 0.1-1000μm interval. While the IR background is less constrained than the optical background, the two appear to be equivalent, with the brightness of the optical background estimated to $\sim 23 \times 10^{-6}$ W m^2 sr^{-1}, and the brightness of the IR background estimated to $\sim 24 \times 10^{-6}$ W m^2 sr^{-1} (Dole et al. 2006). Moreover, it is estimated that the processes concerning galaxy formation and evolution produce a brightness equivalent to ~5% of the CMB via equal amounts of light from direct starlight (optical background) and from dust-reprocessed starlight (IR background). The cosmic IR background shows the relic emission of the formation and evolution of galaxies, including star formation and accretion onto a BH processes. Locally, the IR emission of galaxies is only a third of the optical emission (Soifer & Neugebauer 1991), so the peak emission at 150μm observed in Fig. 1.7 is linked to a strong evolution of galaxies in the past epochs that is now observed as far-IR emission (Dole et al. 2006).

When a galaxy presents both star formation and AGN signatures, the L_{IR} is measured by fitting a dust emission model to multi-wavelength observations. These multi-wavelength data are usually not available on

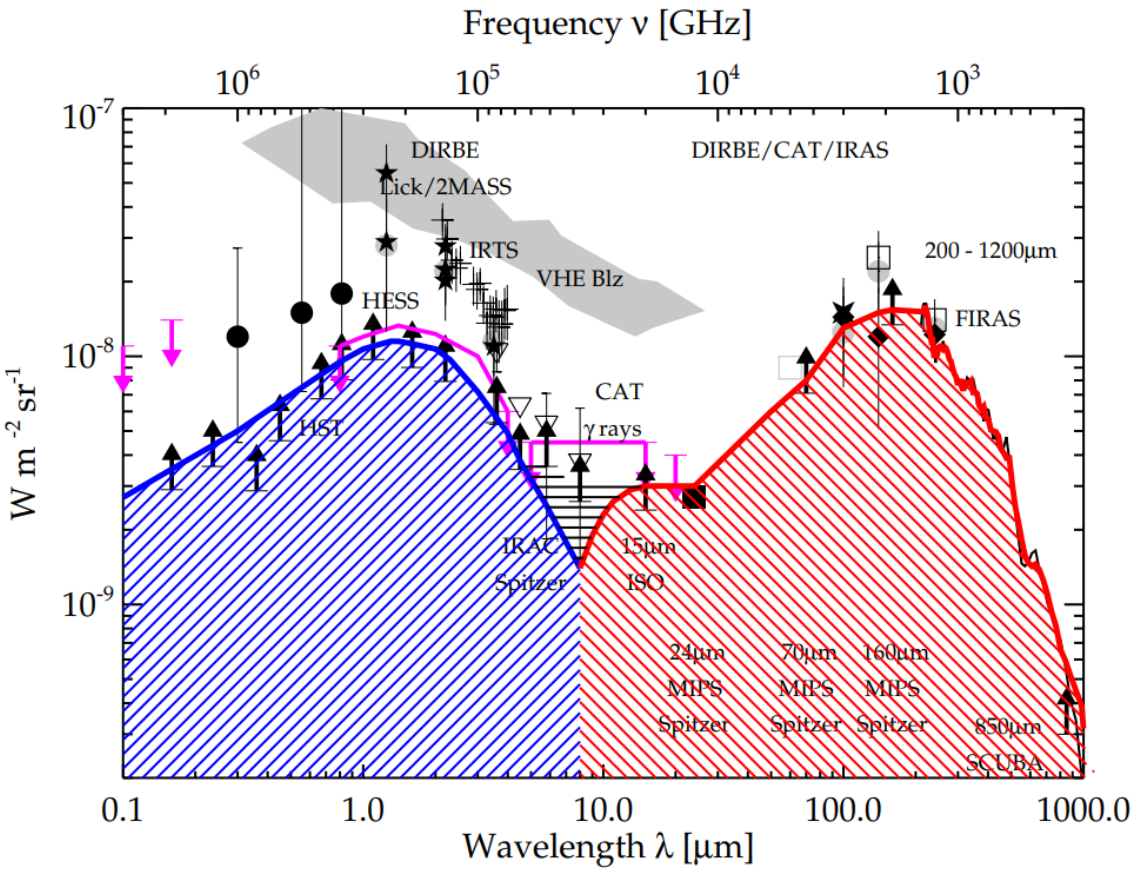

Figure 1.7: Best Cosmic Optical Background (blue shaded) and Cosmic Infrared Background (red-shaded) estimates from measurements of the Extragalactic Background Light (EBL) Spectral Energy Distribution from 0.1 μm to 1 mm. The gray-shaded area represents the region of overlap. Black arrows represent lower limits. Purple arrows and lines represent upper limits. Figure from Dole et al. (2006).

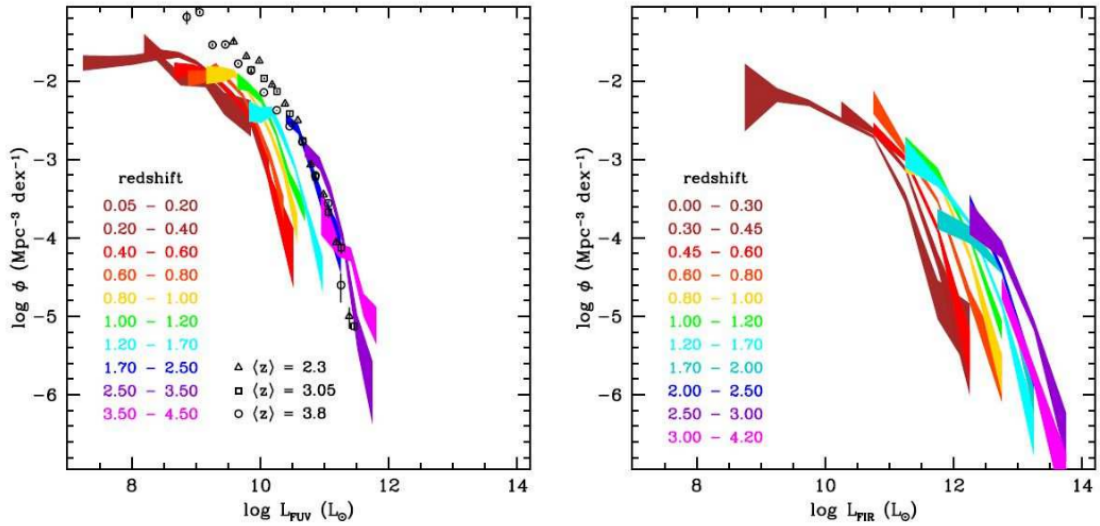

Figure 1.8: On the left, the redshift evolution of the FUV luminosity function at $0 < z < 4$. The colored bands indicate the 68% confidence intervals on the space densities over the observed luminosities (uncorrected for dust attenuation), in different redshift ranges. Data points, coded by shape, show the FUV luminosity functions for LBGs at mean redshifts $\langle z \rangle = 2.3$ and $\langle z \rangle = 3.05$. These luminosity functions use color selection techniques to extend the measurements to fainter luminosities than those measured in the purely spectroscopic samples from Cucciati et al. (2012). The FUV luminosity functions at $2 < z < 3.8$ are observed to be quite similar. On the right panel, the redshift evolution of the far-IR luminosity function at $0 < z < 4$ from Gruppioni et al. (2013). The bands indicate the 68% confidence intervals at each redshift (figure from Madau & Dickinson 2014).

a general basis, thus the discrimination among the different contributions is made using a spectral energy distribution (SED) template derived from observations of the local Universe, and then applied to extrapolate the L_{IR} from a single observed flux. This method carries with itself strong uncertainties due to the differences of the dust emission properties of each galaxy.

Summarizing, the main results from both UV and IR surveys are:

- Compared with the UV luminosity functions, the IR luminosity functions cut off is less steep at high luminosities, and even show power-low slopes.
- The IR luminosity functions extend to much higher luminosities than the UV luminosity functions at the same redshifts, as the most actively star-forming galaxies tend to be strongly obscured by dust (figure 1.8).
- There is strong luminosity evolution, particularly for the IR luminosity functions, but also in the UV, with more modest density evolution.

1.2.2 Black hole accretion

AGNs: an overview

The term AGN indicates a compact region at the center of a galaxy that presents a luminosity so high that cannot be produced by stars alone, and is instead produced by the accretion of matter onto a SMBH at the center of the galaxy. The AGN phenomenon has been thoroughly described by Beckmann & Shrader (2012) and Netzer (2013). Accretion onto massive objects and the associated release of the binding gravitational energy are important sources of radiation. The process is geometry dependent and can proceed in various

ways. Two fundamental quantities that are related to such processes are the Eddington luminosity and the Eddington accretion rate. The Eddington luminosity is defined as the maximum luminosity a body can achieve when the gravitational force is balanced by the radiation pressure:

$$\mathrm{L_{Edd}} = \frac{4\pi c \mathrm{GM} \nu m_p}{\sigma_\mathrm{T}} \simeq 1.5 \times 10^{38} \frac{\mathrm{M}}{\mathrm{M}_\odot} [\mathrm{erg\,s^{-1}}] \tag{1.3}$$

with ν means molecular weight, $\mathrm{N_e}$ electron density and σ_T is the Thomson cross section. This value is calculated for solar metallicities, and for pure hydrogen is $\simeq 1.28 \times 10^{38} (\mathrm{M/M_\odot})\,\mathrm{erg/s}$. $\mathrm{L_{Edd}}$ defines the maximum luminosity allowed for objects that are powered, over a long period of time, by a steady state accretion. The Eddington accretion rate ($\dot{\mathrm{M}}_\mathrm{Edd}$) is the accretion rate required to produce the total luminosity of $\mathrm{L_{Edd}}$:

$$\dot{\mathrm{M}}_\mathrm{Edd} = \frac{\mathrm{L_{Edd}}}{\eta c^2} \tag{1.4}$$

AGNs can be separated in type-I and type-II AGNs. This classification is based on the observed characteristics in the optical/UV spectra: type-I AGNs have broad (FWHM $\sim$ 1000 – 20000 $\mathrm{km\,s^{-1}}$) permitted lines (e.g. hydrogen, recombination, and intercombination lines), together with narrow (FWHM$\leq$ 1000 $\mathrm{km\,s^{-1}}$) forbidden lines (e.g. [CIV]1549Å, [MgII]2798Å, and helium in the UV). On the other hand, in type-II AGNs all lines are narrow (FWHM$\leq$ 1000 $\mathrm{km\,s^{-1}}$). We observe different spectra because in type-I AGNs we see a very dense gas region ($n_\mathrm{H} \sim 10^9\,\mathrm{cm^{-3}}$) very close to the AGN accretion disk, the so-called broad line region (BLR), while in type-II AGNs this region is either absent or obscured, and the emission only comes from the so-called narrow line region (NLR), where gas density is lower ($n_\mathrm{H} \sim 10^{2-4}\,\mathrm{cm^{-3}}$). According to the unified model, the BLR is obscured by a dusty torus and can be seen (sometimes) in polarized or infrared spectra (Antonucci 1993). Figure 1.9 gives a schematic description of the various AGN sub-classifications, also taking into account the radio emission.

The optical signature of Type-II AGN can be also produced by O-type stars associated with star formation activity. In order to gain a better method to separate the two component, Baldwin et al. (1981) systematically analyzed the difference between the relative intensities of the strong forbidden and permitted emission-lines resulting from photo-ionization by AGN and those produced by the much softer continuum of O-type stars. The diagnostic diagrams developed from this analysis, the so-called the BPT diagrams (see figure 1.10), are based on pairs of emission line ratios: the flux ratio [OIII] 5007/Hβ vs. [NII] 6584/Hα, [OI] 6300/Hα, or [SII] 6716,6731/Hα. The same diagnostic diagrams work for type-I AGN provided that only the narrow components of the Balmer lines are considered.

The basic morphology of the BPT diagrams reveals the presence of two populations: a purely star forming one, from the upper left to the lower center on the plots, and an AGN one, next to the star forming population in the center and extending upward and to the right. Since real galaxies contain both AGN and regions of star-formation within the observed area, the extension of the AGN population away from the star-forming locus can be viewed as a mixing line along which the AGN contribution to the total emission-line spectrum increases progressively relative to that from the star-forming regions, as the points move further away from the star-forming domain (Kewley et al. 2006; LaMassa et al. 2012).

X-ray and IR surveys

AGN are powerful X-ray emitters in the 0.1-100 keV interval, with the X-ray flux represents a significant part ($\sim 5 - 40\%$) of the bolometric emission of AGNs. Moreover, the rapid variability observed suggests that the

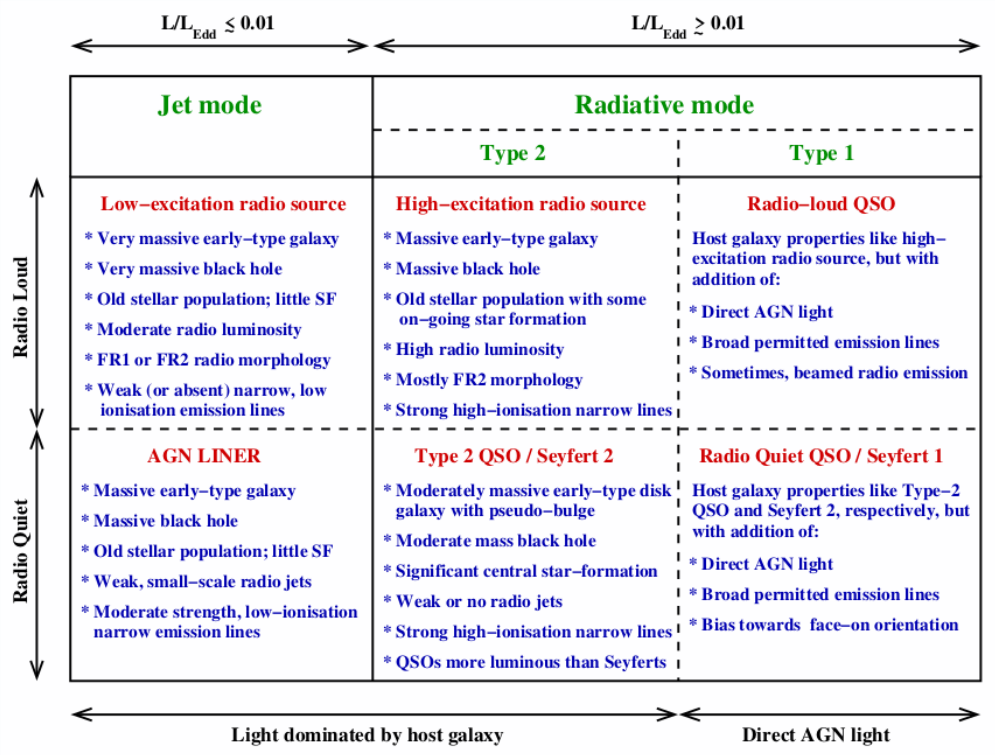

Figure 1.9: Categorization of AGN population, with the description of the typical properties of each AGN class. Figure from Heckman & Best (2014).

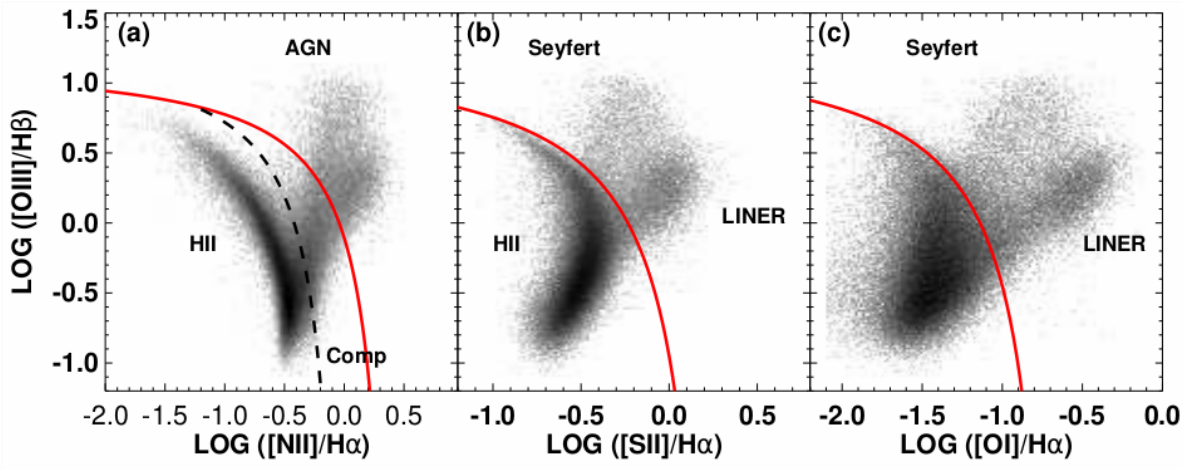

Figure 1.10: A set of BPT diagnostic diagrams for the SDSS main galaxy sample; the red line is the maximal starburst line, while the dashed line in the left panel shows the more stringent dividing line between pure star-forming galaxies and AGN. The separation between star-forming galaxies and AGN is most cleanly done using the left panel while the center and right panels can be used to separate Seyferts from LINERs (Heckman & Best 2014; Kewley et al. 2006).

X-ray emission comes from close to the central black hole, thus offering a chance to study the immediate surroundings of the SMBHs and the process of accretion. The X-ray emission is characterized by two main components: the soft X-rays emission has a steep spectrum, while the hard component shows a spectrum in the form of a power law (Fabian 2006; Fabian et al. 1989). Both components mostly arise from the inner region of AGN, close to the central SMBH. The soft component is probably formed in the accretion disk, which is also a strong source of the soft UV and optical photons, while the hard component is caused by high-energy electrons in hot corona above the disk, where photons from the UV and optical emission are accelerated trough inverse-Compton scatter (Fabian et al. 2000, 1989).

NASA's Chandra X-ray Observatory and ESA's X-ray Multi-Mirror Mission-Newton (XMM-Newton) have carried out a number of deep extragalactic X-ray observing programs, representing the most extensive and sensitive X-ray surveys performed so far, resolving the majority of the 0.1-10 keV background (Brandt & Hasinger 2005).

The *Cosmic X-Ray Background* (CXRB), first discovered in 1962, was initially supposed to be generated by a strong Galactic X-ray source(Sco X-1) with diffuse emission of approximately constant intensity from all directions. The discrete nature of the CXRB became evident with sensitive, high angular resolution imaging with telescopes that, observing previously known AGNs, showed how these objects were powerful X-ray emitters. Deep ROSAT surveys were able to resolve $\sim 75\%$ of the soft CXRB into discrete sources, with optical follow up identifying the bulk of these sources as AGNs (Lehmann et al. 2001), demonstrating how at least the 0.5-2 keV part of the X-ray emission is due to accretion onto a SMBH. The ROSAT surveys found evidence of luminosity dependent density evolution of AGNs (Miyaji et al. 2000). Other surveys were carried out in the 2-3 keV band with the *Advanced Satellite for Cosmology and Astrophysics* (ASCA) which performed medium to deep sky surveys in the 2-10 keV band, resolving $\sim 35\%$ of the CXRB. Studies in the 5-10 keV band were carried out using Beppo-SAX, resolving $\sim 20-30\%$ of the CXRB in this band.

The CXRB provides a constrain on the cosmic evolution of SMBHs, and in particular the emission peak at ~30 keV suggests a significant contribution from heavily obscured AGN whose emission is attenuated at lower energies and show strong signatures of Compton reflection.

The main problem with X-ray AGN detection is represented by the 'Compton-thick' AGN population[4], which constitute $\approx 15-25\%$ of the AGNs in the local Universe (Akylas & Georgantopoulos 2009; Beckmann et al. 2009; Brightman & Nandra 2011; Tueller 2011). Such high absorption effectively blocks the direct line-of-sight via a combination of Compton scattering and photoelectric absorption, even at 10-200 keV. Compton-thick AGNs are thus only visible via indirect reflections of X-rays that are $\approx 50-150$ times weaker. Many Compton-thick AGNs remain undetected even in the deepest X-ray surveys to date, and only a small number have been isolated among the currently detected X-ray sources in deep surveys, but additional ones could be residing among the currently detected sources with limited photon statistics.

Putting all the data together, optical observations suggest that the AGN comoving space density is, at redshift $z \approx 2$ almost 100 times higher than what we see in the local Universe, while there seems to be a strong decline at redshifts $z \gtrsim 2.7$. X-ray data, detecting significantly less luminous AGNs than those found in optical surveys, found that the AGN peak space density moves to smaller redshifts with decreasing luminosity, and that the rate of evolution from the local Universe to the peak redshift is slower for less-luminous AGN. It appears that SMBH generally grow in an "anti-hierarchical" fashion: while the $10^{7.5}-10^{9}\,\mathrm{M}_{\odot}$ SMBH in rare, luminous AGN could grow efficiently at $z \approx 1-3$, the $10^{6}-10^{7.5}\,\mathrm{M}_{\odot}$ SMBH

[4]The distinction between Compton thin and Compton thick matter is given by the column density at which the optical depth for Compton scattering reaches the unity, and is $\mathrm{N_H} \simeq 1.5 \times 10^{24}\ \mathrm{cm}^{-2}$.

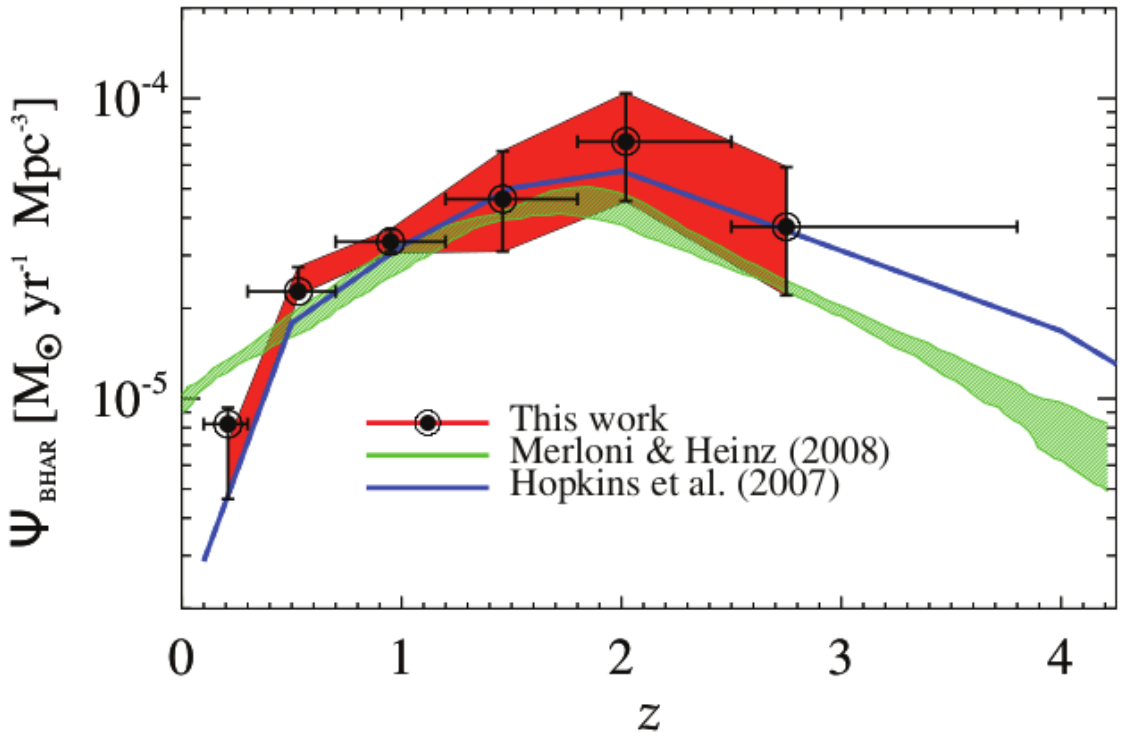

Figure 1.11: BHAR density estimates from the bolometric AGN LF as function of redshift. The black dots represents the estimates by Delvecchio et al. (2014), with the red shaded area showing the ±1σ uncertainty. Estimates from other works are reported from comparison (figure from Delvecchio et al. 2014).

in more-common, less-luminous AGN had to wait longer to grow ($z \lesssim 1.5$; Brandt & Hasinger 2005). In the 0.5-2 keV band the sensitivity and statistics are good enough to detect a clear decline of the luminous AGN space density toward higher redshifts and such a high-redshift decline is also hinted at in some 2-10 keV band analyses (Fiore et al. 2003; Steffen et al. 2003). The missing Compton-thick population, however, can strongly influence these results, thus making IR observations necessary, since IR observations are only mildly affected by obscuration, and can detect warm dust signature for both obscured and unobscured AGNs (Delvecchio et al. 2014), giving us a complementary picture to the X-ray one. For an accreting BH, the main IR emission comes from the torus thermal radiation, heated by the enclosed accreting BH, thus providing an indirect measure of the AGN luminosity (Polletta et al. 2006). Most of the emission in the near to mid IR bands is mainly due to emission by cold, warm, or hot dust grains that are heated by the primary AGN radiation source, while a minor part comes from the radiation that is the direct result of the accretion process itself (Netzer 2013). Most of the thermal far-IR emission is thought to be due to colder dust that is being heated by young stars in large star-forming regions in the host galaxy. Broad and narrow emission lines are seen in the mid to far IR part of the spectrum of many AGNs, and are thought to originate in the broad- and narrow-line regions. The same IR surveys described in section 1.2.1 collected data also on AGNs, and in particular Delvecchio et al. (2014) analyzed Herschel data aiming to trace the BHAR up to redshift $z \sim 3$ from far-IR selected objects. They found that the BHARD seems to increase quickly from redshift $z > 3$ to $z \sim 2$, where it peaks, and then decreases toward the present epoch; this result is consistent with others in the literature from X-ray data (see figure 1.11, and Hopkins et al. 2007; Merloni & Heinz 2008), although it is not guaranteed that the two selection methods trace the same AGN population (Delvecchio et al. 2014), especially considering there is no direct comparison between the obscured AGN component and the X-ray detected population. Akylas et al. (2012), in particular, tried to constrain the Compton thick population

modeling the CXRB, obtaining a possible content of Compton thick objects bin the 10-20% range at the 68% confidence level, keeping into account not just the observed CXRB, but mainly the detected population of Compton thick objects in the local Universe.

1.3 Thesis goals

The studies described in this Chapter portrait a common scenario for both BHA and star formation. Despite the limitations of the different methods employed to determine the SFR and BHAR and their evolution with cosmic time, the general conclusions support a scenario in which the peaks of these phenomena appear between redshift $z \sim 1-3$, followed by a steep decline toward the present epoch, in agreement with the downsizing scenario[5]. In order to better understand this behaviour, however, it is necessary to probe the more obscured populations of accreting and star forming objects, at the peak of their activity, with surveys deep enough and wide enough to gain a comprehensive view on how star formation and BHA evolve through time and in different environmental conditions.

The photometric surveys described in Section 1.2 cannot empirically discriminate between star formation and BHA processes. This distinction is instead based local galaxies templates and subsequently adapted to higher redshifts scenarios, leaving space to significant uncertainties in the interpretation of the resulting data. Spectroscopy, on the other hand, can physically discriminate between the star formation and BHA. The mid- to far-IR range, in particular, is populated by a large number of spectral lines and features that can be linked to the two phenomena, leading to a clear physical view on how BHA and star formation interact inside the same galaxy, but also throughout cosmic time. Being minimally affected by dust obscuration, IR spectroscopy can penetrate the more heavily obscured regions at the peak of galaxy activity, at the cosmic noon, and better disentangle the various phenomena taking place. In this work, I characterize the main mid- to far-IR lines depending on the source metallicity and on the main energy production mechanism, in order to better characterize the extreme physical conditions of high-redshift galaxies. From these lines, I identify the best tracers for the SFR or the BHAR. When possible, I also test these tracers against observations of high redshift galaxies.

To better understand how star formation and BHA co-evolve with cosmic time and influence galaxy evolution, it is not sufficient to study a limited sample of objects at different redshifts, but requires a comprehensive view of the two phenomena throughout time. For this reason, I design a survey strategy with the aim to quantify how many observations are needed in order to constrain the effects of star formation and BHA, and their evolution with redshift. The basis for this study is constituted by blind spectro-photometric surveys carried out with the *Space IR telescope for cosmology and astrophysics* (SPICA, Roelfsema et al. 2018). These blind surveys, covering different areas at different depth of observations, aim to reconstruct a 3D view of the Universe, where each detected object is characterized by its redshift and by the main processes taking place inside it, as revealed by IR tracers, and is put in its environment and compared to the large scale structure measured in its field.

This work is organized as follows: Chapter 2 presents the SPICA mission, a 2.5 meter cryogenically cooled telescope initially proposed as a candidate for the ESA M5 mission call, and its suit of instruments. Although the SPICA mission was cancelled, the scientific and technological work done in preparation can still be used as a reference for future work in the field. Chapter 3 presents the the calibration of mid- to

[5]Higher mass galaxies formed earlier in time than lower mass objects, while the local Universe is dominated by galaxies with low BHAR and SRF.

far- IR lines and features, and their applications as SFR and BHAR tracers in local galaxies. Chapter 4 compares the results obtained in Chapter 3 for SFR tracers to high redshift objects detected with the ALMA telescope. Chapter 5 presents a survey strategy, based on the SPICA telescope project, with the aim to study galaxy evolution between the present time and the cosmic noon, up to redshift z~4, using the line calibrations derived in chapter 3. Chapter 6 proposes a possible application of the work done in this thesis using first-class present and future facilities: ALMA and the James Webb Space Telescope. In Chapter 7, lastly, I present the conclusions that can be derived from this work.

Chapter 2

The SPICA observatory project

2.1 The definition of the science requirements for galaxy evolution

The design of an instrument needs necessarily to start from the definition of the scientific goals that one wants to achieve with that instrument. For the case of using an IR space telescope to spectroscopically study the evolution of galaxies, it is mandatory to define a minimum sensitivity that needs to be reached and therefore the detector performances and the size of the telescope, that follow. For the detection of Black Hole accretion and Star Formation along cosmic times, among the best mid-IR tracers there are the [OIV]26μm line, as a BHAR tracer, and the [NeII]12.8μm line as well as the 11.3μm PAH feature. To detect these features in statistically significant samples of objects in the redshift interval z=1-4, covering well the so-called "cosmic noon", one needs to reach, or to get close to, the so-called "Main Sequence" luminosity, where the bulk of galaxies at any redshift resides.

I have therefore computed the predicted fluxes of the three features chosen as a function of redshift (z=1,4) and luminosity (log $L/L_{\odot}$ = 11, 13.5, depending on redshift). Fig.2.1a shows the table with the computed line fluxes and in Fig.2.1b the line flux (W/m^2) as a function of the galaxy luminosity (in $L_{\odot}$).

	L_IR (log)	o4_25.9 (W/m2)	ne2_12.8 (W/m2)	pah_11.3 (W/m2)
z=1:	11.0	7.356e-20	2.085e-20	7.708e-20
	11.5	2.026e-19	6.519e-20	2.382e-19
	12.0	5.580e-19	2.038e-19	7.361e-19
	12.5	1.537e-18	6.370e-19	2.275e-18
	13.0	4.233e-18	1.991e-18	7.030e-18
	13.5	1.166e-17	6.225e-18	2.172e-17
z=2:	L_IR (log)	o4_25.9 (W/m2)	ne2_12.8 (W/m2)	pah_11.3 (W/m2)
	11.5	3.692e-20	1.188e-20	4.341e-20
	12.0	1.017e-19	3.714e-20	1.341e-19
	12.5	2.801e-19	1.161e-19	4.145e-19
	13.0	7.714e-19	3.629e-19	1.281e-18
	13.5	2.125e-18	1.134e-18	3.959e-18
z=3:	L_IR (log)	o4_25.9 (W/m2)	ne2_12.8 (W/m2)	pah_11.3 (W/m2)
	12.0	3.814e-20	1.393e-20	5.031e-20
	12.5	1.050e-19	4.354e-20	1.555e-19
	13.0	2.893e-19	1.361e-19	4.804e-19
	13.5	7.968e-19	4.255e-19	1.485e-18
z=4:	L_IR (log)	o4_25.9 (W/m2)	ne2_12.8 (W/m2)	pah_11.3 (W/m2)
	12.0	1.922e-20	7.018e-21	2.535e-20
	12.5	5.293e-20	2.194e-20	7.834e-20
	13.0	1.458e-19	6.858e-20	2.421e-19
	13.5	4.015e-19	2.144e-19	7.482e-19

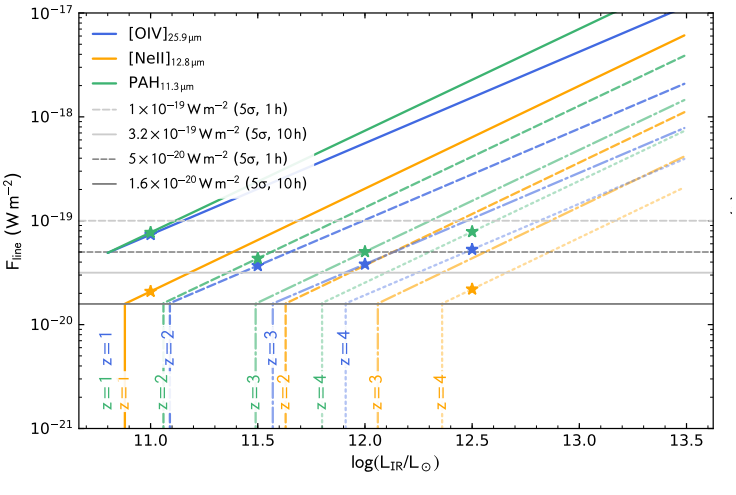

Figure 2.1: (Left panel:a) The predicted line fluxes for the [OIV]26μm line, the [NeII]12.8μm line and the 11.3μm PAH feature as a function of redshift and luminosity. **(Right panel:b)** The line flux of the [OIV]26μm line, the [NeII]12.8μm line and the 11.3μm PAH feature as a function of the galaxy luminosity, as compared to the overall telescope-instrument sensitivity. The star symbols (⋆) denote the Main-Sequence luminosities at each of the four redshifts considered.

From Fig.2.1b it emerges that the required overall sensitivity to detect both the BHAR and SFR tracers at L$\star$ luminosities, needs to be included in the range 2-5 $\times$ 10^{-20} W/m^2 at 3σ in integration times ranging from 1 to 10 hours. This requirement translates into an effective telescope area of 4.8 m^2, i.e. an effective telescope diameter of 2.5m. Moreover, to obtain a sensitivity of the order of 5$\times$ 10^{-20} W/m^2 at 3σ, 1 hour, detectors with total Noise Equivalent Power (NEP) of less than 2$\times$ 10^{-19} W Hz$^{-1/2}$ are required.

In the following of this chapter it will be pointed out that the SPICA concept fully meets the requirements given above, and therefore can reach the goal to map spectroscopically the evolution of galaxies at the cosmic noon and possibly beyond, up to redshift z$\sim$4.

2.2 The SPICA telescope

The SPace Infrared telescope for Cosmology and Astrophysics (SPICA[1]) was first presented by Nakagawa & Spica Working Group (2002, 2004); Onaka & Nakagawa (2005) as a Japanese mission for IR astronomy. Few years later many European scientists, after the successful experience on the ESA led Herschel mission (Pilbratt et al. 2010), joined the project (Swinyard et al. 2009). Later updates have been presented by Nakagawa et al. (2014); Roelfsema et al. (2018); Sibthorpe et al. (2015). While at the beginning of this PhD project, SPICA was one of three candidates for the ESA M5 mission call, and was being developed in collaboration with the Japanese space agency (JAXA), at the time this work is being completed the mission has been cancelled just months before the final mission-selection review (Clements et al. 2020). Nevertheless, the studies for the scientific preparation of the SPICA mission will be used as a reference for the future work in the field of galaxy evolution via IR astronomy.

The main science drivers of the SPICA mission were:

- to understand the role of star formation and black hole accretion and feedback in the evolution of galaxies over cosmic time, especially covering the cosmic noon (z=1-3), when galaxies are deeply dust obscured;
- to unveil the evolution of the chemical composition and of the dust during cosmic time and tack with spectroscopy the baryon cycle in galaxies;
- to observe distant galaxies and discover the first galaxies and black holes;
- to characterize the evolution of water and minerals from primordial protoplanetary discs to planetary systems;
- to understand how the Solar System relates to other planetary systems and how life could evolve elsewhere.

2.3 The mission

The SPICA mission concept uses a 2.5 meter Ritchey-Chrétien telescope, cooled to below 8 K. Table 2.1 summarises the main parameters for the mission, and Fig. 2.2 shows the overall configuration of the spacecraft concept: the service module (SVM), which provides the spacecraft support, is on the bottom, while the payload module (PLM), together with the Science Instrument Assembly (SIA), and the Cryogenic Assembly

[1]https://sci.esa.int/web/cosmic-vision/-/53635-spica, and https://www.ir.isas.jaxa.jp/SPICA/SPICA_HP/index-en.html

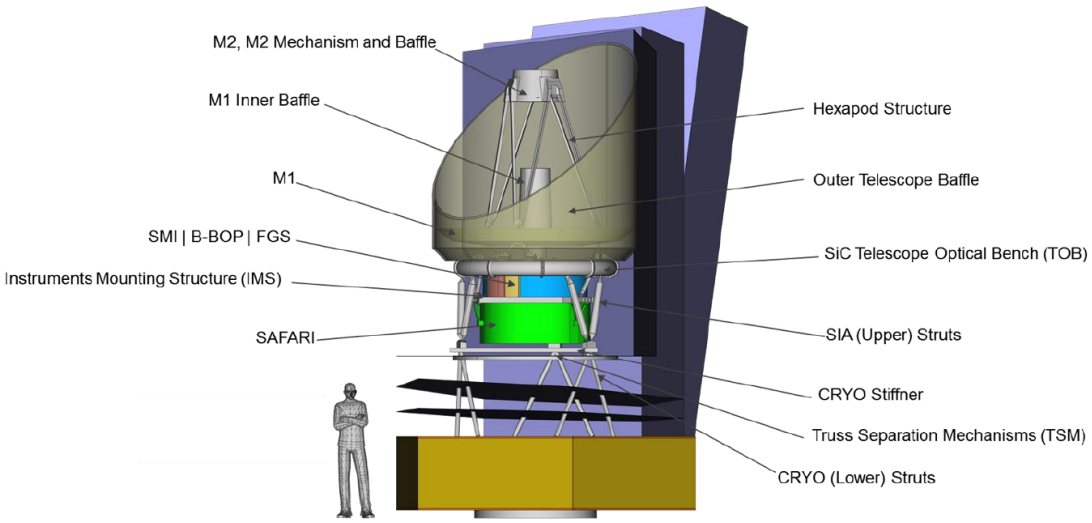

Figure 2.2: The Payload module, composed of the Science Instrument Assembly (SIA) mounted on the CRYOgenic module composed of sunshields, thermal shields and truss with separation mechanisms, offering a low conductive and radiative thermal environment to the SIA.

(CRYO) rest on top. The Science Instrument Assembly (SIA) is constituted by the Infrared Telescope Assembly (ITA) and the Focal Plane Instrument Assembly (FPIA). The ITA includes the Telescope Optical Bench (TOB), the mirrors and their supporting structure, the Secondary Mirror Mechanism (SMM) used for the telescope in-orbit re-focus, and the baffles. The telescope optical bench is interfaced with the CRYO stiffener, and supports also the Focal-Plane Instrument Assembly (FPIA) through dedicated bipods. The FPIA is composed of the Instruments Mounting Structure (IMS) supporting the Focal Plane Instruments (FPI) and the Fine Guidance Sensor (FGS). The main goal of the cryogenic assembly, that combines radiative cooling with V-Groove shields with mechanical cryo-coolers, is to cool the telescope assembly (STA) to below 8 K, and to provide cold temperature stages for the instruments at 4.8 K and 1.8 K.

The progress in detector performances and cryogenic cooling technologies allows an observatory like SPICA, with a large, cold mirror and a suit of instruments that takes full advantage of the sensitivity obtainable with low thermal background, to achieve a gain of over two orders of magnitude in spectroscopic sensitivity as compared to other observatories like *Herschel* (Pilbratt et al. 2010), *Spitzer* (Werner et al. 2004) or SOFIA (Young et al. 2012) (see Fig. 2.3 left), filling the gap between JWST (Gardner et al. 2006) and (Wootten & Thompson 2009). The real leap forward is given by the actively cooled mirror(see Fig. 2.3 right), that allows an unprecedented increase of sensibility.

The mission concept provides extremely sensitive spectroscopic capabilities in the 17-230µm range, with a resolution R between 50 and 11000, as well as imaging and polarimetric capabilities in the 34-350µm range. In particular the *SPICA* Far-infrared Instrument (SAFARI) is a grating spectrograph with low (R $\sim$ 300) and medium (R $\sim$ 3000–11 000) resolution observing modes instantaneously covering the 35–230 µm wavelength range. The *SPICA* Mid-infrared Instrument (SMI) has three operating modes: a large field of view ($10' \times 12'$) low-resolution 17–36 µm imaging spectroscopic (R $\sim$ 50–120) mode and photometric camera at 34 µm (SMI-LR), a medium resolution (R $\sim$ 1300–2300) grating spectrometer covering wavelengths of 18–36 µm (SMI-MR) and a high-resolution echelle module (R $\sim$ 29 000) for the 10–18 µm domain (SMI-HR). Finally, B-BOP, a large field of view ($2'.6 \times 2'.6$), three channel, (70 µm, 200 µm and 350 µm) polarimetric camera complements the science payload.

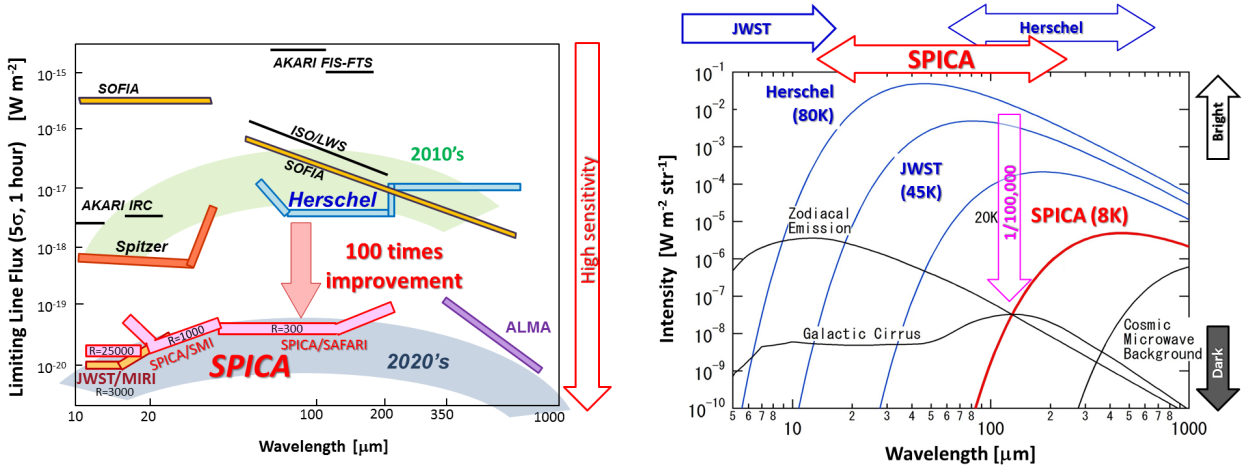

Figure 2.3: Left: Sensitivity of various missions with respect to the covered wavelength interval. The SPICA mission, in pink, shows an improvement of two orders of magnitudes respect to the Herschel mission, and fills the gap between JWST and ALMA in wavelength coverage. The shaded areas show the level of detector sensibility in the 2010's (green) and in the 2020's (gray). Right: limiting intensity for different mirror temperatures for the Herschel (80K), JWST (45K) and SPICA (8K) mission. The actively cooled mirror of SPICA would allow an improvement of five orders of magnitude in detectable intensity with respect to Herschel at the same wavelength.

Table 2.1: Main SPICA mission parameters

Item Specification
Spacecraft system
Height: ~ 5.9 meter
Diameter: ~ 4.5 meter
Mass including consumables: 3.65 tonnes
Launcher: JAXA H3
Attitude control: 3-axis stabilized with startracker, gyro and fine attitude sensors
Absolute Pointing Error ~ 0.5"
Power: ~ 14 m^2 solar array providing 3 kW
Data handling: 24 hour autonomous operation, 100 GB on-board data storage, X-band downlink at ~ 10 Mbps
Cooling system
Passive cooling combined with mechanical coolers
End of life cooling power:
Stirling coolers: > 200 mW at 20K
4K Joule-Thomson coolers: 40 mW at 4.5K
1K Joule-Thomson coolers: 10 mW at 1.7K
Telescope
2.5 meter Ritchey-Crétien
Strehl ratio for telescope/instruments > 0.80 at 20 μm
Cooled below 8 K
Instruments
Mid-infrared spectroscopy 12-36 μm - SMI
Far-infrared spectroscopy - 34-250 μm - SAFARI
Mid-infrared imaging 30-37 μm - SMI
Far-infrared imaging polarimetry 70/200/350 μm - POL

2.4 The Instruments

2.4.1 The SAFARI Instrument

The *SpicA FAR infrared Instrument* (SAFARI) is a four band grating spectrometer with continuous spectroscopic capabilities in the 34-230 μm range. It can operate in the grating low-resolution (LR) mode, with R∼300, or in the high resolution (HR) mode, with R∼2000-11000, using a Martin-Puplett interferometer (Martin & Puplett 1970). The scientific driver for the low resolution mode is the study of the Star Formation and Black Hole accretion tracers, as well as the metallicity tracers over cosmic time, through the measure of the integrated intensities of the emission lines and features over line widths of the order of a few hundred km/s, while the high resolution mode responds to the requirement to study line profiles and measure the velocities, in particular the infall and outflows of matter in AGN and star forming galaxies (see Section 5.6).

A diagram for the SAFARI system is shown in Fig. 2.4. The system is divided in two main components: the Focal Plane Unit (FPU), mounted on the optical bench and the electronics mounted on the CRYO assembly. The signal from the telescope is directed toward either the LR or HR modes. The 34-230μm interval is covered by four different bands, each with its own grating and detector array. The signal is conditioned and split over the four bands using filters and dichroics, and then is sent to the Grating module, in which are located the grating optics and band detectors. The spectrometer specifications and capabilities are listed in Table 2.2.

The low resolution dispersion uses diffraction gratings. In this way, the photon noise, which is proportional to the width of the spectral element, is reduced, maximising the line sensitivity. A generic grating module design is used for all the four bands: the light beam enters trough a slit and hits the grating at a high incidence angle via a collimator and a flat mirror. A mirror then refocus the dispersed signal onto the detector. The high incidence grating allows a more compact optics, but also limits the use to a single polarization.

The high resolution mode uses a Martin-Puplett interferomer, that modulates all wavelengths entering in the SAFARI optical path. The resulting interference between two beams of the interferometer is distributed to the four grating modules, and then onto the detectors after being dispersed. If the interferometer is scanned over the entire optical displacement, the detectors will measure a high resolution interferogram convolved with the grating response function for that particular detector. The final product, after a Fourier transformation, is a small bandwidth, high resolution spectrum for each interferogram. The final high resolution spectrum is obtained combining the spectra from the individual detectors. The optical path difference allows for a resolution from R∼1500 at 230μm up to R∼11000 at 34μm.

The intrinsic design of SAFARI allows for the immediate access to the entire 34-230μm wavelength interval, whether it is used in low or high resolution mode, point source or mapping mode. The basic observational mode, with maximum efficiency, is point source spectroscopy, but mapping modes are also implemented. Using a beam steering mirror is possible to cover a small area ($< 2'$) without the need to re-position the telescope. For larger mapping areas, an on-the-fly mapping mode can be implemented, with the spacecraft slowly 'painting the sky' and the spectrometer continuously recording data.

Table 2.2: SAFARI performance summary.

Band	SW	MW	LW	VLW
λ range	34-56μm	54-89μm	87-143μm	140-230μm
high R	11700-7150	7400-4500	4600-2800	2850-1740
nom. R	300	300	300	300
FWHM	4.5"	7.2"	12"	19"
Point source spectr. 5σ-1hr flux limit (10^{-20} Wm^{-2})				
high R	13	13	13	15
nom. R	7.2	6.6	6.6	8.2
Mapping spectr. 1'×1' 5σ-1hr flux limit (10^{-20} Wm^{-2})				
high R	189	113	73	51
nom. R	84	49	30	23
Mapping phot. $1' \times 1'$ 5σ-1hr flux density limit (μJy)				
	209	192	194	239
5σ conf.	15	200	2000	10000

high R - high resolving power mode; μm
R ~ 11000 at 34 to R ~ 1500 at 230 μm
nom. R - nominal resolving power; R ~ 300
5σ conf. - 5σ confusion limit

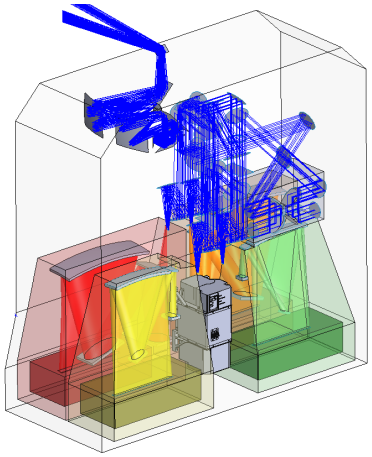

Figure 2.4: The SAFARI Focal Plane Unit (FPU). The beam from the telescope secondary mirror comes from the top left and is sent into the instrument via the pick-off mirror on the top of the instrument box. On the right the Martin-Puplett signal path and its moving mirror stage can be seen. On the bottom are shown three of the four grating modules, and between them the cooler unit (in grey).

2.4.2 The SMI Instrument

The SPICA Mid-IR instrument (SMI) is a spectrometer/camera that covers the 10-37μm interval with both imaging and spectroscopy. The instrument has 4 observational modes: low, medium and high resolution spectroscopy, and a broad band imaging mode. In Fig. 2.5 is shown the optical layout of SMI. The light is introduced into the SMI system by fore-optics optimized to remove curvature and astigmatism aberrations. The SMI low resolution (SMI/LR) mode is a multi slit prism spectrometer with continuous low resolution (R=50-120) coverage in the 17-37μm interval. It is composed of four slits of 10' in length and 3.7" in width. In order to accurately determine the position of the slits in the sky is implemented a broad-band imager centred at 34μm (SMI/CAM) that covers a 10'×12' field of view. SMI/CAM and SMI/LR are operated simultaneously, thus providing both spectra and deep imaging for each field of view. SMI/LR covers the field of view in 90 steps. The light entering SMI/LR-CAM passes through the four slits and a beam is

directed toward the spectrometer, where it is dispersed by a prism, and one beam is reflected by a split-plate and forwarded to the CAM instrument, where a 34 µm band-pass filter defines the band-pass for broad-band photometry.

The SMI mid resolution (SMI/MR) mode covers the 17-37µm interval with a resolution R=1300-2300, while the SMI high resolution (SMI/HR) mode covers the 10-18µm interval with resolution R∼28000. The two instrument share fore-optics. SMI/MR can operate either in step-scan mode, or access a 2'×2' on-sky area using a beam steering mirror. This mode employs a slit of 60" in length and 3.7" in width, after which the light is dispersed using an Echelle grating combined with a cross-disperser. SMI/HR is constituted by a slit 4" long and 1.7" wide. The dispersion is obtained using a grating immersed in a cadmium-zinc-telluride alloy and a cross disperser.

SMI can be used either in staring mode, SMI/LR mapping mode, SMI/LR-CAM survey mode or SMI/MR mapping mode. The staring mode can be used for targeted spectroscopy at the three resolutions, plus for MR and HR the mapping of a small area is possible also in this mode, using the beam-steering mirror. SMI/LR mapping mode ca be used to generate 10'×12' spectral maps, while the SMI/LR-CAM survey mode is used for wide area surveys. The SMI/MR mapping mode is used for spectral mapping of extended sources, and is achieved by combining raster steps scans and movements of the beam steering mirror.

Table 2.3: SMI performance parameters.

Band	HR	MR	LR	CAM	
λ range	10-18	17-37	17-37	34	µm
R	28000	2300-1300	50-120	5	
FoV	4"×1.7"	1'×3.7"	10'×3.7"	10'×12'	
FWHM	2"	2.7"	2.7"	3.5"	
Scale	0.5	0.7	0.7	0.7	"/pix.
Continuum sensitivity 5σ-1hr					
Point	1500	400	50	13	µJy
Diffuse			0.05	0.05	MJy/sr
Line sensitivity 5σ-1hr					
Point	1.5	4	8	10^{-20}W/m^2	
Diffuse	1.5	1		10^{-10}W/m^2/sr	
Limit	∼20000	∼1000	∼20	∼1	Jy

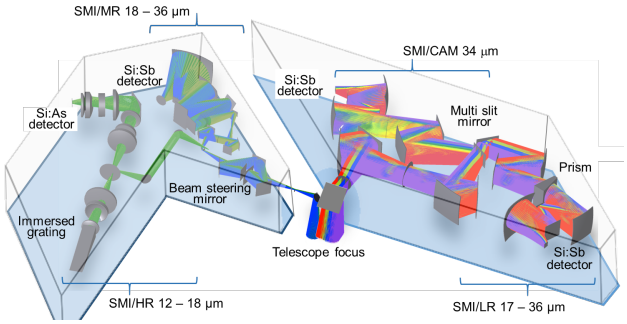

Figure 2.5: SMI optical layout

2.4.3 The B-BOP instrument

The SPICA *B-fields with BOlometers and Polarizers* (B-BOP) instrument was conceived for characterising the statistical properties of the magnetised ISM and probing the role of magnetic fields in the formation

and evolution of the interstellar web of dusty molecular filaments giving birth to most stars in our Galaxy (André et al. 2019). For this reason it was necessary to design an instrument capable of observing the widest possible field of view, and at different wavelengths simultaneously.

B-BOP is an imaging instrument that provides diffraction-limited imaging in total power mode, i.e. measuring the total flux of the sky, and in a polarimetric mode simultaneously, where it records signals that are linked to the linear polarized fraction and linear polarization angle of the incoming flux. It can observe in three bands, centered at 70, 200 and 350μm, in order to observe the filaments on both sides of their thermal continuum peak emission. The fields of view for the three channels are almost identical, and comprised between 3.2"×3.2" to 3.7"×3.7". The instrument characteristics are reported in Table 2.4, while Fig. 2.6 shows its optical layout.

B-BOP has a common entrance optics for the three bands, with field- and aperture stops to suppress stray light, and a pupil image for the half-wave plate, followed by individual brances for the three bands where the light is separated using dichroic filters. The half-wave plate adopts an achromatic design, providing constant phase shift across the entire wavelength range. Moreover, it provides access to the $\pi/4$ and $(3/4)\pi$ orientations, and allows for removal of polarization effects introduced by the instrument. The dynamic range necessary to obtain polarization mapping is achieved using semiconductor bolometers, which consists of two suspended interlaces spirals, each sensitive to a single polarization component.

B-BOP can produce a combined, total power and difference signal for two orthogonal polarization. To operate in imaging mode, any mapping scheme can be used. For polarimetry, the default observation mode is via scan maps, along two approximately orthogonal scan directions. The map will then be repeated with one or more different orientation of the half-wave plate.

Table 2.4: B-BOP performance parameters

Band	70 μm	200 μm	350 μm
λ range	52-88 μm	135-225 μm	280-420 μm
Array size	32×32	16×16	8×8
Pixel size	5"×5"	14"×14"	28"×28"
FWHM	7.6"	21.7"	37.9"
Point source sensitivity 2.5'×2.5' 5σ-1hr			
Unpol.	21 μJy	42 μJy	85 μJy
Q, U	30 μJy	60 μJy	120 μJy
Point source sensitivity 1 deg^2 5σ-10hr			
Unpol.	160 μJy	320 μJy	650 μJy
Q, U	230 μJy	460 μJy	920 μJy
Surface brightness sensitivity 1 deg^2 5σ-10hr			
Unpol.	0.09 MJy/sr	0.045 MJy/sr	0.025 MJy/sr
Q, U	2.5 MJy/sr	1.25 MJy/sr	0.7 MJy/sr

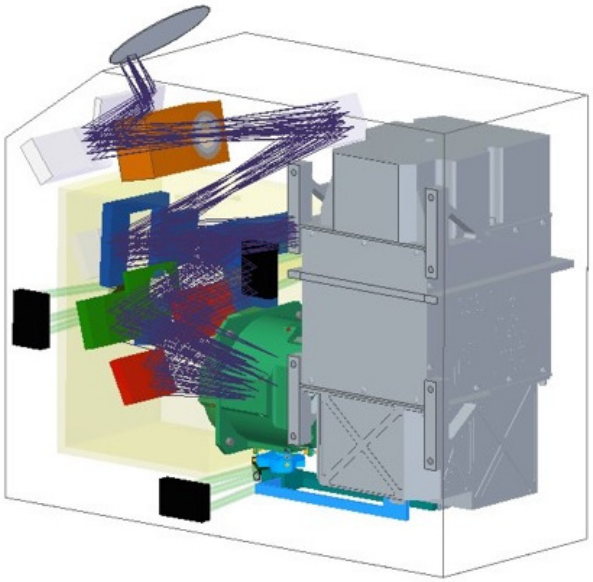

Figure 2.6: B-BOP optical layout

Chapter 3

Calibration of IR lines

3.1 Introduction

The bulk of star formation and black hole accretion processes cannot be accurately evaluated using optical/UV or X-ray observations: the heavily dust-obscured environments at the peak of galaxy activity require the use of tracers that can account for the obscured component of the two phenomena. For this reason, it is necessary to identify SFR and BHAR tracers that can be applied under different conditions, independently of metallicity or dust content. IR emission line spectra can be used to physically separate the different contributions to the total IR light (see Fig.3.1 and Spinoglio & Malkan 1992): the mid- to far-IR spectral range includes a suite of atomic and molecular lines and features, covering a wide range of physical conditions like excitation, density, ionization, radiation field, metallicity or dust composition. In the highly obscured ISM of actively star-forming galaxies and AGN, the IR lines are among the few probes of the physical conditions in the gas and dust surrounding the active regions, whether those are in local or high redshift galaxies. The neutral gas around star-forming regions can be traced using the [OI] lines at 63 and 145 μm, while density or temperature can be studied using different tracers: the gas density can be analyzed using line ratios of the same element in the same ionization states at different wavelength (e.g. [OIII]52/88μm, [NII]122/205μm or [SIII]18.7/33.5 μm), while the strength of the radiation field can be derived from line pairs of the same element in different ionization states (e.g. [NeIII]15.55/[NeII]12.81 or [OIV]25.89/[OIII]88). Fig. 3.2, in particular, shows two diagnostic diagrams where the [OIV]25.89/[OIII]88 ratio is confronted with the [NeIII]15.55/[NeII]12.81 and [SIV]10.51/[SIII]18.71 ratios: a clear distinction emerges between sources characterized by different dominant ionization spectra. The AGN dominated sources are separated from the star formation dominated galaxies, and the star forming galaxies are discriminated according to their metallicity.

Lines in the IR range are almost insensitive to interstellar reddening, thus offering ideal tracers to probe the ISM of dusty galaxies (Nagao et al. 2011; Pereira-Santaella et al. 2017), both at the cosmic noon (z≃1-3), where almost 90% of the emitted light by both star formation and BHA is absorbed and reprocessed in the IR (Madau & Dickinson 2014), but also in nearby galaxies where new stars are forming in dust obscured regions. Moreover, the emissivity of IR lines is only weakly dependent on the gas temperature, since the atomic levels responsible for the transitions are closer to the ground state than in UV or optical lines (See Fig. 3.3, and e.g. Bernard Salas et al. 2001).

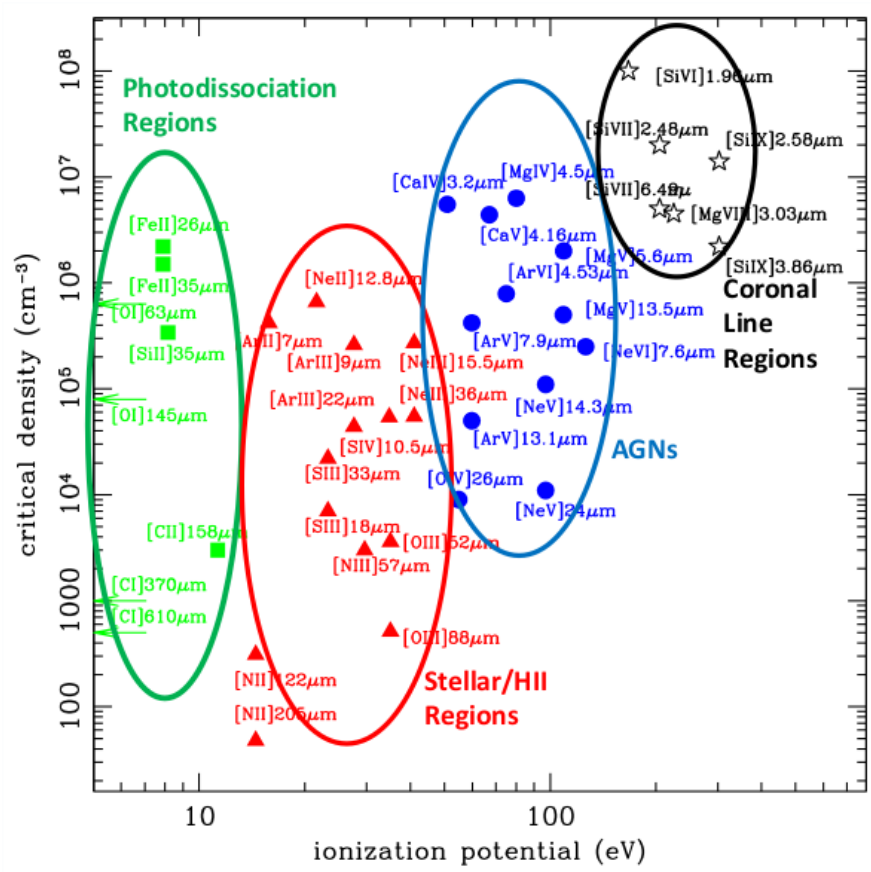

Figure 3.1: Critical densities for collisional de-excitation vs. ionization potential of IR fine structure lines. Figure from Spinoglio & Malkan (1992), revised in Spinoglio et al. (2017).

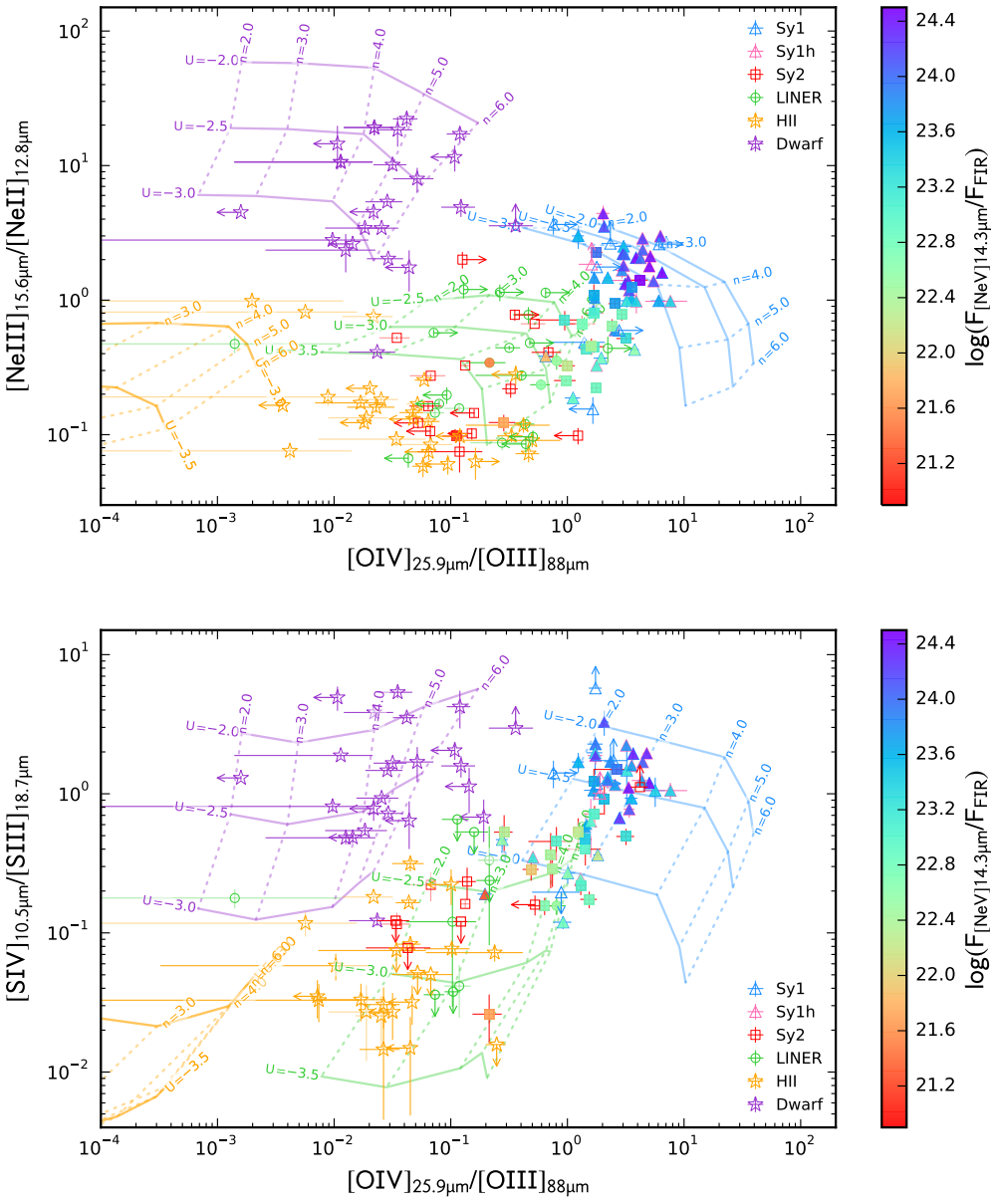

Figure 3.2: Ionization-sensitive line ratios, with symbols corresponding to different spectral types: blue triangles for Seyfert 1 galaxies, pink triangles for Seyfert 1 with hidden broad-line regions, red squares for Seyfert 2 galaxies, green circles for LINERS, yellow stars for starburst galaxies, purple stars for LMG. Open symbols are used for upper and lower limits derived from PACS data, and for ISO/LWS data. Photoionization models of AGN, LINER, starburst galaxies, and LMG are shown as blue, green, yellow, and purple grids, respectively. The logarithmic values of the density ($n_{\rm H}$) and ionization potential (U) of the photoionization models are indicated in the figures. Symbols are color-coded according to their $F_{[NeV]14.3}$/ $F_{\rm FIR}$ flux ratio, when available (see the color bar). **Top:** the [NeIII]15.6/[NeII]12.8 line ratio vs. the [OIV]25.9/[OIII]88 ratio. **Bottom:** the [SIV]10.5/[SIII]18.7 line ratio vs. the [OIV]25.9/[OIII]88 ratio (figure from Fernández-Ontiveros et al. 2016).

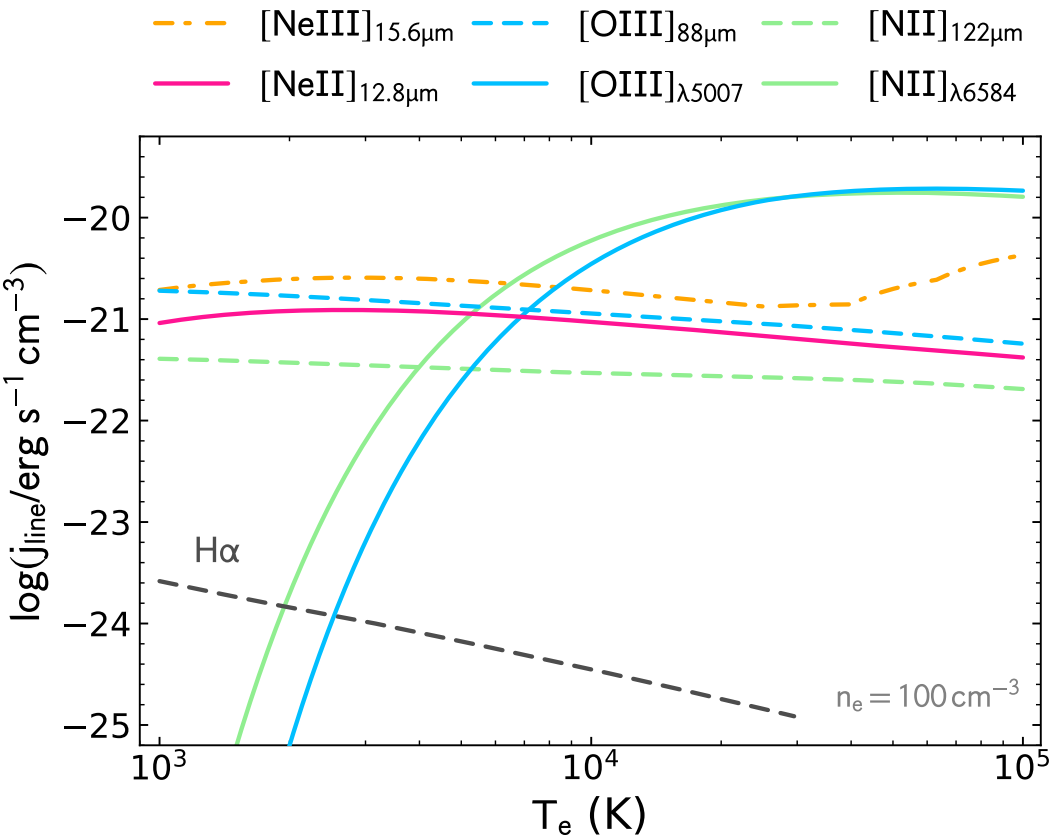

Figure 3.3: The emissivity ($j_{\rm line}$) of the fine-structure lines in the optical range (blue solid line: [OIII] λ5007; green solid: [NII] λ6584) is a strong function of the electron temperature $\rm T_e$ in the 2 000–30 000 K range, in contrast with the IR lines (pink solid: [NeII]12.8 μm; orange dot-dashed: [NeIII]15.6 μm; blue dashed: [OIII]88 μm; green dashed: [NII]122 μm). The emissivities are computed using PyNeb (Luridiana et al. 2015) for a fixed $n_{\rm e}$ = 100 $\rm cm^{-3}$. For comparison, the emissivity of the Hα recombination line is also shown (black dashed line).Adapted from Fernández-Ontiveros et al. (2021)

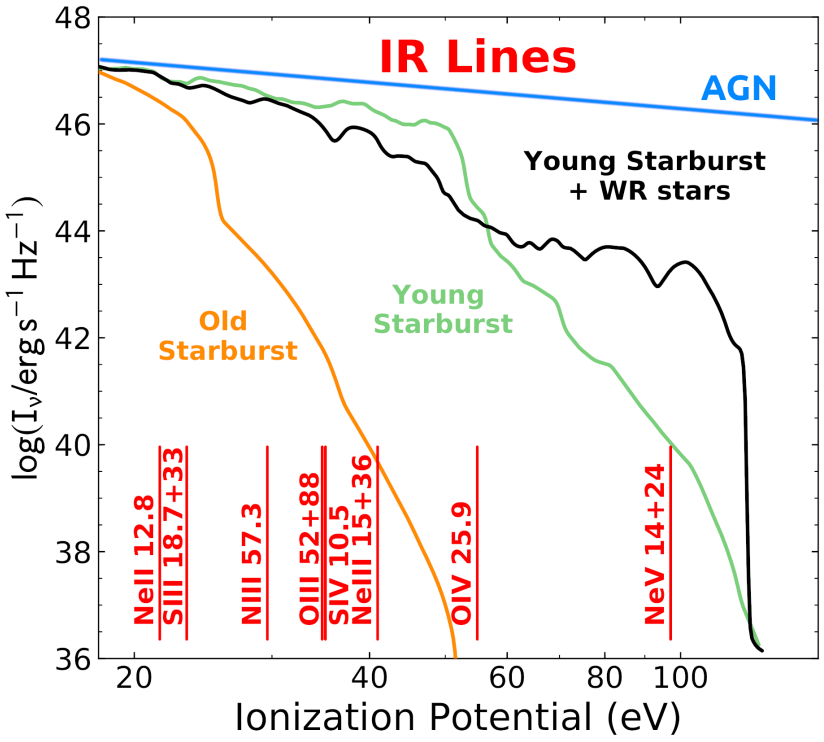

Figure 3.4: Ionization spectrum for different sources: old starburst population (orange solid line), young starburst population (green solid line), young starburst population and Wolf-Rayet stars (black solid line) and AGN (blue solid line). The vertical red lines show the ionization potential of key IR lines. Adapted from Spinoglio et al. (2017)

The IR spectral range is characterized by a suit of lines that can be separated according to their ionization potential, and thus attributed to different excitation mechanisms. Fig.3.4 shows the ionizing spectra of different sources, from AGN to various types of starburst galaxies, as a function of their ionizing potentials; the IR lines that can better trace these spectra are also shown. Comparing the ionization potential of different lines and their critical density, as shown in Fig. 3.1, it is possible to identify specific regions of the diagram where lines can be attributed to specific regions in the ISM: these lines can be then used as proxy to trace these regions and measure their physical parameters. Choosing two lines at similar or equal ionization potential, their ratio is a good tracer of electron density, while choosing two lines at equal critical density, their ratio will measure ionization. For instance, low ionization lines like [NeII]12.81 or [SIII]18.7 can be used to derive the SFR linked to stellar and HII regions, while the AGN accretion rate can be measured using high-ionization lines such as [NeV]14.32 or 24.32, or [OIV]25.89μm.

In this chapter I present, following and expanding the work by Spinoglio et al. (2012), a revised calibration of the mid- to far-IR lines, including fine-structure lines, the brightest H_2 pure rotational lines and the PAH features. The calibrations have been computed for three classes of objects, namely star forming galaxies (SFG), AGN dominated galaxies, and low metallicity galaxies (LMG). The LMG calibration was included to characterize the response of the lines to the conditions of low metallicity (average 1/5 $Z_\odot$, Madden et al. 2013). Low-metallicity AGN are not included because they are rare in the local Universe and only a few examples are found (e.g. Circinus, Oliva et al. 1999). Both the broad and narrow-line regions in AGN, however, show little to no chemical evolution up to $z \sim 7$ (Juarez et al. 2009; Nagao et al. 2006; Onoue et al. 2020), suggesting that the quasar phase appears mostly inside galaxies that are already chemically mature.

The different lines and features are calibrated against the total IR luminosity as a mean to trace the

reprocessed radiation, and the IR range gives a measure of the luminosity of the hidden star formation or AGN activity. Using these calibrations, I then derive different methods to measure the SFR and the BHAR in galaxies using mid- and far-IR fine structure lines (e.g. De Looze et al. 2014; Ho & Keto 2007; Meléndez et al. 2008), H_2 pure rotational lines and PAH features (Shipley et al. 2016).

Anticipating the results of this analysis, it emerges that the [CII]158 μm line can be used as SFR tracer for both LMG and SFG, covering 6 orders of magnitudes in luminosity, independently of the source metallicity. For the first time, the sum of the two far-IR oxygen lines, the [OI]63μm line and the [OIII]88μm line, is proposed as a tracer for the SFR. A combination of low- and intermediate-ionization lines from neon and/or sulfur is also a robust proxy for the SFR, independent of the metallicity. In particular, the [SIV]10.5 μm+[NeII]12.8 μm SFR tracer will be accessible to ELTs facilities from the ground in the near future for galaxies in the local Universe. The brightest PAH features at 6.2 and 11.3 μm are robust SFR tracers in both SFG and AGN, while the weakness of these features prevents their use in LMG. I present for the first time a correlation between the SFR and the H_2 molecular line fluxes at 9.7, 12.3 and 17.0μm. Regarding the measure of the BHAR, the [NeV]14.3μm, [NeV]24.3μm and [OIV]25.9μm lines are all reliable tracers of the BHAR when compared to both the 2-10 keV luminosity or the 12 μm luminosity.

3.2 Analyzed lines and features and galaxy samples

In this analysis I have used three different samples of galaxies, one for normal star forming galaxies (SFG), one for AGN and one for low metallicity star forming galaxies (LMG), with data from objects detected in the local Universe for which IR spectroscopy is available, mainly from *Spitzer*-IRS (Houck et al. 2004) and *Herschel*-PACS (Poglitsch et al. 2010), but also from the *Infrared Space Observatory* (*ISO*) SWS and LWS spectrometers (Clegg et al. 1996; de Graauw et al. 1996). Each sample was constructed with the aim of maximizing its statistical significance, both in terms of number of objects considered in each analysis, and in number of lines and features analyzed. Compared to previous results (e.g. Gruppioni et al. 2013; Spinoglio et al. 2012, 2014) this work takes into consideration the LMG sample, previously not analyzed, but also wider SFG and AGN samples. Moreover, this work aims to expand the previous correlations to a wider range of lines and features, including various PAH features, the H_2 molecular lines, and different far-IR lines, each calibrated for the three different classes of objects.

For each of the three galaxy populations, I derived linear relations in logarithmic space between the line luminosity and the total IR luminosity. From these relations, I then derived the best tracers for SFR and BHAR, using the discussed IR lines and features, and compared them with what has been reported in the literature.

The lines and features considered in this analysis, in order of decreasing ionization/excitation are:

- Four high-ionization fine structure lines, typical of AGN: [NeVI]7.65 μm, [NeV]14.32 μm, [NeV]24.32 μm and [OIV]25.89 μm;
- Ten intermediate ionization fine structure lines, typical of stellar/HII regions: [SIV]10.51 μm, [NeII]12.81 μm, [NeIII]15.55 μm, [SIII]18.71 μm, [SIII]33.48 μm, [OIII]51.81 μm, [NIII]57.32 μm, [OIII]88.36 μm, [NII]121.9 μm and [NII]205 μm;
- Five low-ionization/neutral fine structure lines, typical of PDR: [FeII]25.99 μm, [SiII]34.81 μm, [OI]63.18 μm, [OI]145.5 μm and [CII]157.7 μm;

- Four H_2 pure rotational lines at 9.67, 12.28, 17.03 and 28.22 μm;
- Five PAH features at 6.2, 7.7, 8.6, 11.3 and 17 μm.

The fundamental parameters for the fine-structure lines considered in this analysis are reported in Table 3.1.

In this analysis, I have included the fine-structure lines observed with the *Spitzer*-IRS high resolution (HR) channel in the 10-35μm range, for which good spectra are available in the literature. The only exception is the [NeVI]7.65μm line, an exclusive AGN line, for which I included ISO-SWS observations. Other well known fine-structure lines, such as [ArII]6.98μm, [ArIII]8.99μm and [NeIII]36.0μm, which could indeed have a relevant role for future observations, especially in view of the JWST launch, at present do not have enough high quality spectra in the literature to be included. Moreover, I do not consider upper limits to derive the correlations. This is because, in general, the statistics presented are quantitatively appropriate, thus making the inclusion of upper limits not necessary. In particular, all relations show a Pearson *r* coefficient equal or above ~0.6. Where the statistics are less precise (e.g. the [FeII] 26.0μm or [FeIII]22.9μm), upper limits are not always available for the considered lines. For the PAH features, I have used instead the *Spitzer*-IRS low resolution (LR) spectra in the 5-35μm range.

The various samples of galaxies chosen to compute the correlations are described in the following sections and summarized in Table 3.2, with the instruments used to observe the spectral lines and features, the total number of objects selected and the references for each sample.

Table 3.1: Fine-structure lines in the mid- to far-IR range. The columns correspond to the central wavelength, frequency, ionisation potential, excitation temperature, critical density, spectral and spatial resolution of the data presented in this work. Critical densities and excitation temperatures from: Cormier et al. (2012); Farrah et al. (2013); Goldsmith et al. (2012); Greenhouse et al. (1993); Launay & Roueff (1977); Sturm et al. (2002); Tielens & Hollenbach (1985).

Line	λ (μm)	ν (GHz)	**I.P.** (eV)	**E** (K)	$n_{\rm cr}$ ($\rm cm^{-3}$)	**Spec. Res.** ($\rm km\,s^{-1}$)	**Ang. Res.** (arcsec)
[NeVI] $^2P_{3/2}$–$^2P_{1/2}$	7.65	39188.56	126.21	1888	2.5×10^5	~ 1500	14×20
H_2 (0,0) S(3)	9.66	31034.41	4.48	2504	9×10^{5a}	~ 500	4.7×11.3
[SIV] $^2P_{3/2}$–$^2P_{1/2}$	10.51	28524.50	34.79	1369	5.39×10^4	~ 500	4.7×11.3
H_2 (0,0) S(2)	12.28	24413.07	4.48	1682	2×10^{5a}	~ 500	4.7×11.3
[NeII] $^2P_{1/2}$–$^2P_{3/2}$	12.81	23403.00	21.56	1123	7.00×10^5	~ 500	4.7×11.3
[NeV] $^3P_2$–$^3P_1$	14.32	20935.23	97.12	1892	3×10^4	~ 500	4.7×11.3
[NeIII] $^3P_1$–$^3P_2$	15.56	19266.87	40.96	925	2.68×10^5	~ 500	4.7×11.3
H_2 (0,0) S(1)	17.03	17603.78	4.48	1015	2×10^{4a}	~ 500	4.7×11.3
[SIII] $^3P_2$–$^3P_1$	18.71	16023.11	23.34	769	2.22×10^4	~ 500	4.7×11.3
[NeV] $^3P_1$–$^3P_0$	24.32	12326.99	97.12	596	5.0×10^5	~ 500	11.1×22.3
[OIV] $^2P_{3/2}$–$^2P_{1/2}$	25.89	11579.47	54.94	555	10^4	~ 500	11.1×22.3
[FeII] $a^6D_{7/2}$–$a^6D_{9/2}$	25.98	11539.35	7.9	553	2.2×10^6	~ 500	11.1×22.3
H_2 (0,0) S(1)	28.22	17603.78	4.48	1015	2×10^{4a}	~ 500	4.7×11.3
[SIII] $^3P_1$–$^3P_0$	33.48	8954.37	23.34	430	7.04×10^3	~ 500	11.1×22.3
[SiII] $^2P_{3/2}$–$^2P_{1/2}$	34.81	8612.25	8.15	413	$3.4\times10^{5a};10^3$	~ 500	11.1×22.3
[OIII] $^3P_2$–$^3P_1$	51.81	5787.57	35.12	441	3.6×10^3	~ 105	9.4[c]
[NIII] $^2P_{3/2}$–$^2P_{1/2}$	57.32	5230.43	29.60	251	3.0×10^3	~ 105	9.4
[OI] $^3P_2$–$^3P_1$	63.18	4744.77	–	228	4.7×10^{5a}	~ 86	9.4
[OIII] $^3P_1$–$^3P_0$	88.36	3393.01	35.12	163	510	~ 124	9.4
[NII] $^3P_2$–$^3P_1$	121.90	2459.38	14.53	118	310	~ 290	9.4
[OI] $^3P_1$–$^3P_0$	145.52	2060.07	–	98	9.5×10^{4a}	~ 256	10.3
[CII] $^2P_{3/2}$–$^2P_{1/2}$	157.74	1900.54	11.26	91	$20,[2.2^{a};4.4^{b}]\times10^3$	~ 238	11.2
[NII] $^3P_1$–$^3P_0$	205.3	1460.27	14.53	70	48	~ 297	~ 16.8

[a] Critical density for collisions with hydrogen atoms.

[b] Critical density for collisions with H_2 molecules.

[c] The beam size for *Herschel*/PACS is dominated by the spaxel size ($9\farcs4$) below $\sim 120\,\mu$m.

Table 3.2: Characteristics of the different samples used in this analysis. For each class of objects we report, for the different lines and features, the original sample (*heterogeneous* indicates that the sources do not belong to a specific well-defined sample of galaxies), the facility and instrument that observed the sample of galaxies, the number of objects used in the analysis and the references where the original data can be found.

Type	Lines/features	Sample	Observed by	N. of objects	References
AGN	[NeVI]7.7μm	heterogeneous	ISO-SWS	8	Sturm et al. (2002)
	MIR lines in the 10-35μm range including H_2 rotational lines	12MGS	*Spitzer*-IRS HR	88	Tommasin et al. (2010, 2008)
	PAH features	12MGS	*Spitzer*-IRS LR	103	Wu et al. (2009)
	FIR lines in the 50-205μm range	heterogeneous	*Herschel*-PACS and SPIRE	149	Fernández-Ontiveros et al. (2016)
SFG	MIR lines in the 10-35μm range	GOALS sample	*Spitzer*-IRS HR	153	Inami et al. (2013)
		+ heterogeneous		10	Bernard-Salas et al. (2009)
		+ heterogeneous		28	Goulding & Alexander (2009)
	H_2 rotational lines	GOALS sample	*Spitzer*-IRS HR	153	Stierwalt et al. (2014)
		+ heterogeneous		10	Bernard-Salas et al. (2009)
		+ heterogeneous		28	Goulding & Alexander (2009)
	PAH features	GOALS sample	*Spitzer*-IRS LR	179	Stierwalt et al. (2014)
		+ heterogeneous		12	Brandl et al. (2006)
	FIR lines in the 50-205μm range	GOALS sample	*Herschel*-PACS	153	Díaz-Santos et al. (2017)
		+ heterogeneous	*Herschel*-PACS and SPIRE	20	Fernández-Ontiveros et al. (2016)
		+ heterogeneous	ISO-LWS	23	Negishi et al. (2001)
LMG	MIR lines in the 10-35μm range	DGS	*Spitzer*-IRS HR and LR	40	Cormier et al. (2015)
	FIR lines in the 50-158μm range	DGS	*Herschel*-PACS	40	Cormier et al. (2015)

3.2.1 The AGN sample

The AGN sample has been drawn from the $12\,\mu\mathrm{m}$ selected active galaxies sample (12MGS, Rush et al. 1993b), which is the brightest complete and unbiased sample of Seyfert galaxies in the local Universe. For the mid-IR fine structure lines and the H_2 rotational lines, I have used the sub-sample of the 12MGS observed by *Spitzer* IRS at high spectral resolution (R= 600) which contains 88 AGN (Tommasin et al. 2010, 2008). For the PAH features at 6.2 μm and 11.2 μm I have used the *Spitzer*-IRS data at low spectral resolution (R∼ 60–120; Buchanan et al. 2006; Wu et al. 2009) of the 12MGS (103 objects), because this setting matches better the intrinsic width of these features. It is important to note that Wu et al. measure the PAH features using a spline function to determine the continuum level. In order to make these measurements comparable to those obtained using automated fitting procedures (e.g. PAHFIT, Smith et al. 2007a), I applied a correction factor of 1.7 and 1.9 to increase the fluxes of the $6.2\,\mu\mathrm{m}$ and $11.3\,\mu\mathrm{m}$ PAHs in Wu et al., respectively, following the results found by Smith et al. (2007a). The adoption of the 12MGS as the main AGN catalog allows to derive statistically robust calibrations.

For the [NeVI]7.65 $\mu\mathrm{m}$ line, the 12MGS could not be used, because this line was not detected by *Spitzer* at low resolution and was outside its spectral range at high-resolution. Therefore I used the data from Sturm et al. (2002), where are presented 8 AGN with detections of the [NeVI]7.65 $\mu\mathrm{m}$ line with *ISO*-SWS at medium resolution (R ∼ 1500), and thus not contaminated by the PAH emission at 7.7 $\mu\mathrm{m}$.

For the far-IR spectral range, namely the 50–$205\,\mu\mathrm{m}$, I we used the catalogue of AGN presented by Fernández-Ontiveros et al. (2016), which includes all the Seyfert galaxies and the quasars of the Véron-Cetty & Véron (2010) catalogue which have far-IR spectra observed by *Herschel*-PACS. The sample of the AGN observed in the far-IR lines counts 170 galaxies and contains about 50% of objects from the 12MGS, while the others do not come from a complete sample.

3.2.2 The SFG sample

The SFG sample was constructed using *The Great Observatories All-Sky LIRG Survey* (GOALS sample, Armus et al. 2009), from which I extracted 158 galaxies, with data from Inami et al. (2013), who report the fine structure lines at high resolution in the 10–36 μm interval, and Stierwalt et al. (2014), who include the detections of the H_2 molecular lines and the PAH features at low spectral resolution. For those galaxies in the GOALS sample that have a single IRAS counterpart, but more than one source detected in the emission lines, I have added together the line/feature fluxes of all components, to consistently associate the correct line/feature emission to the total IR luminosity computed from the IRAS fluxes.

To cover also lower luminosity galaxies, as the GOALS sample only includes Luminous IR Galaxies (LIRGs) and Ultra-Luminous IR Galaxies (ULIRGs), I have included 38 galaxies from Bernard-Salas et al. (2009) and Goulding & Alexander (2009), to reach the total sample of 196 galaxies with IR line fluxes in the 5.5–35 μm interval in which an AGN component is not detected. For the Bernard-Salas et al. (2009), Goulding & Alexander (2009) and the GOALS samples we excluded all the composite starburst-AGN objects identified as those with a detection of [NeV] either at 14.3 or 24.3 μm.

It is worth to note that the original samples from Goulding & Alexander (2009) and Bernard-Salas et al. (2009) have spectra covering solely the central region of the galaxies. To estimate the global line intensity, I corrected the published line fluxes of the *Spitzer* spectra by multiplying them by the ratio of the continuum reported in the IRAS Point Source Catalogue to the continuum measured on the *Spitzer* spectra extracted from the CASSIS database (Lebouteiller et al. 2015). In particular, I considered the continuum at 12 μm for the [NeII]12.8 μm and [NeIII]15.6 μm lines, and the continuum at 25 μm for the [OIV]25.9 μm, [FeII]26 μm, [SIII]33.5 μm and [SiII]34.8 μm lines. This correction was not needed for the AGN sample and the GOALS sample because of the greater average redshift of the galaxies in the 12MGS and GOALS samples. In particular, the 12MGS active galaxies sample has a mean redshift of 0.028 (Rush et al. 1993b), while the GOALS sample has a mean redshift of 0.026. The galaxies presented by Bernard-Salas et al. (2009) have instead an average redshift of 0.0074, while the sample by Goulding & Alexander (2009) has an average redshift of 0.0044. For the other lines in the 10–36 μm interval, Goulding & Alexander (2009) do not report a detection, and I used the data presented in Bernard-Salas et al. (2009) for a total of 15 objects. Both Bernard-Salas et al. (2009) and Goulding & Alexander (2009) report data from the high-resolution *Spitzer*-IRS spectra.

Data in the 50–205 μm interval were taken from Díaz-Santos et al. (2017) for the GOALS sample, 20 starburst galaxies from Fernández-Ontiveros et al. (2016), and 23 objects from the ISO-LWS observations of Negishi et al. (2001), resulting in a total sample of 193 objects. Lastly, the PAH features fluxes were measured from the low resolution *Spitzer*-IRS spectra by Brandl et al. (2006), including 12 objects from the sample of Bernard-Salas et al. (2009) and 179 objects from Stierwalt et al. (2014).

3.2.3 The LMG sample

The LMG sample was selected from Cormier et al. (2015), where the 10–36 μm interval was observed by *Spitzer*-IRS in both high and low resolution, and the 50–158 μm interval was observed by *Herschel*-PACS. For the *Spitzer*-IRS data, I only considered the high resolution results, for a total sample of 40 objects.

3.3 Results

For each line or feature in each galaxy sample, I derived the correlation between the logarithms of the total IR luminosity in the 8–1000 µm range and the line luminosity. The total IR luminosity was computed from the IRAS fluxes following Sanders & Mirabel (1996); the equations are expressed in the form:

$$\log \mathrm{L_{Line}} = (a \pm \delta a) \log \mathrm{L_{IR}} + (b \pm \delta b) \tag{3.1}$$

All luminosities are in units of $10^{41}\,\mathrm{erg\,s^{-1}}$. Table 3.3 reports the best fit parameters obtained for each line/feature. In order to derive these correlations, I used the orthogonal distance regression fit (Boggs & Rogers 1990) because the two variables are independent of each other; the ordinary least square minimization, on the other hand, would consider one variable as dependent on the other. The orthogonal distance regression is particularly useful in deriving the inverse relation between two variables from the best-fit coefficients. Table 3.3 also reports the number of objects N used to derive each correlation, and the Pearson correlation coefficient r.

3.3.1 Spectral lines and features luminosity vs. total IR luminosity

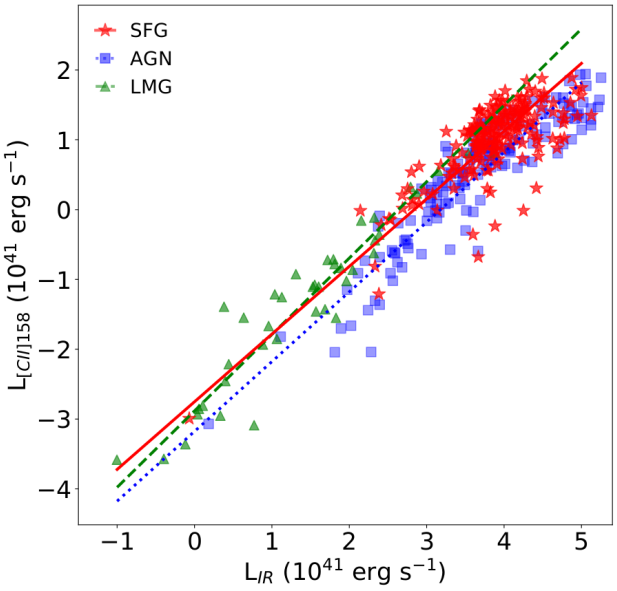

Figure 3.5: The [CII]158 µm line luminosity as a function of the total IR luminosity. Blue squares represent detections in AGN, red stars indicate SFG and green triangles LMG. The solid red line represents the linear relation calculated for SFG, the blue dotted line shows the relation for AGN and the green dashed line the one for LMG.

Among the different correlations that I have derived, and that are summarized in Table 3.3, I present in this section the main results. The figures illustrating all the correlations not described here can be found in Appendix A.

The correlations obtained for the [CII]158µm line for the three classes of objects can be seen in Fig. 3.5. SFG and LMG follow a tight relation over six orders of magnitude in $\mathrm{L_{IR}}$, with a consistent regression slope and offset values within the uncertainties. The same regression can be applied from low luminosity dwarf galaxies to LIRGs and ULIRGs, a result previously obtained by De Looze et al. (2014). The AGN sample, on the other hand, presents a higher IR luminosity for a given [CII]158µm line luminosity when compared

to SFG and LMG. This is likely due to the contribution of the AGN continuum emission to the total IR luminosity. Various authors (e.g. Croxall et al. 2017; Herrera-Camus et al. 2015) have reported an observed deficit in [CII] luminosity, with the increase of the total IR luminosity, in particular for ULIRGs. Different mechanisms have been proposed to explain this deficit (Sutter et al. 2019, 2021, and references therein). In particular, Sutter et al. (2019) have found that the [CII] deficit is particularly evident when the emission arises from ionized gas, while the effect is negligible when the emission comes predominantly from PDR regions.

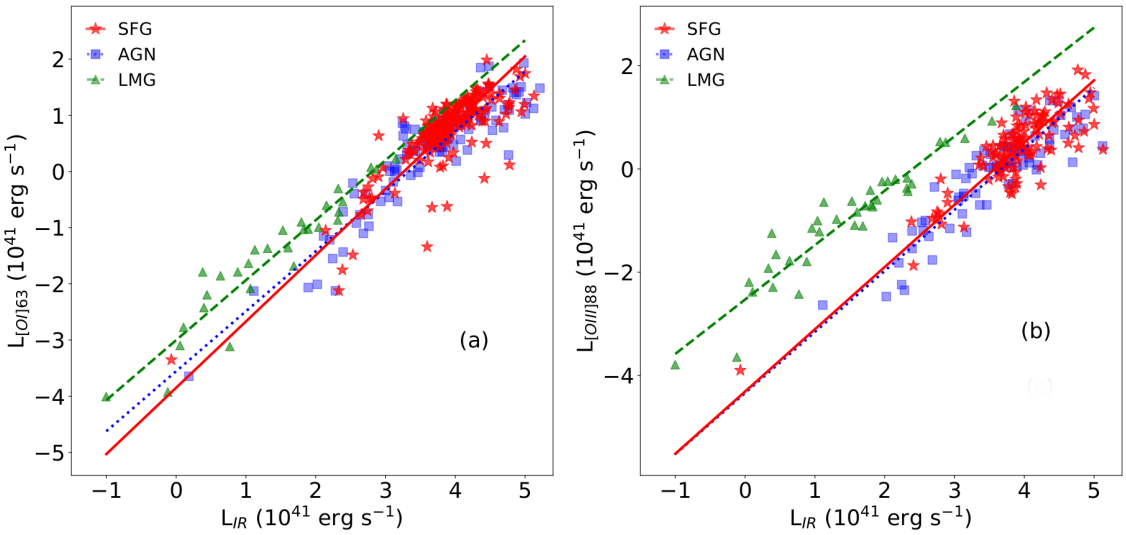

Figure 3.6: (a: left) The [OI]63 µm line luminosity as a function of the total IR luminosity. **(b: right)** The [OIII]88 µm line luminosity as a function of the total IR luminosity. The same legend as in Fig. 3.5 was used.

Fig. 3.6a and b show respectively the correlation obtained for the [OI]63µm and the [OIII]88µm lines. For the [OI]63µm line, the LMG have higher line emission, while SFG and AGN behave similarly. A possible explanation could rely on the lower N/O ratio observed in LMG, enhancing the oxygen abundance. For the [OIII]88µm line, instead, the AGN and SFG samples have a comparable correlation, while the LMG sample shows a [OIII] line about one order of magnitude brighter at a given IR luminosity. This result could be due to the differences in the ionizing spectra and conditions in the ISM of LMG with respect to the SFG and AGN. In LMG, an increased number of photons can ionize gas at a greater distance from the star forming regions, facilitating cooling through ionized gas emission. The lower dust-to-gas ratio in LMG, moreover, is also expected to cause a decrease of the IR luminosities in these galaxies.

Fig. 3.7a and b show the [NeII]12.8µm and [NeIII]15.6µm line correlation respectively. For the [NeII] line there is a slight difference between SFGs and the other samples, but the differences are not statistically relevant, being consistent within 3σ of each other. The [NeIII] line shows a similar behaviour to the [OIII]88µm line, with the AGN and SFG samples presenting similar correlations, and the LMG sample showing a [NeIII] line about one order of magnitude brighter at a given IR luminosity.

The correlations for the PAH feature at 6.2 and 11.3 µm (in Fig. 3.8a and b respectively) show that both features are present in both AGN and SFG, and well correlate with the total IR luminosity. In this analysis, I have not considered the PAH detections in LMG. These detections are available only in a few cases, and are not enough to obtain a statistically significant result. As shown by different authors (Calzetti et al. 2007; Engelbracht et al. 2005; Madden 2000; Smith et al. 2007a; Wu et al. 2006), in LMG there is evidence for a deficit of PAH emission and the available measurements present features significantly weaker than SFG.

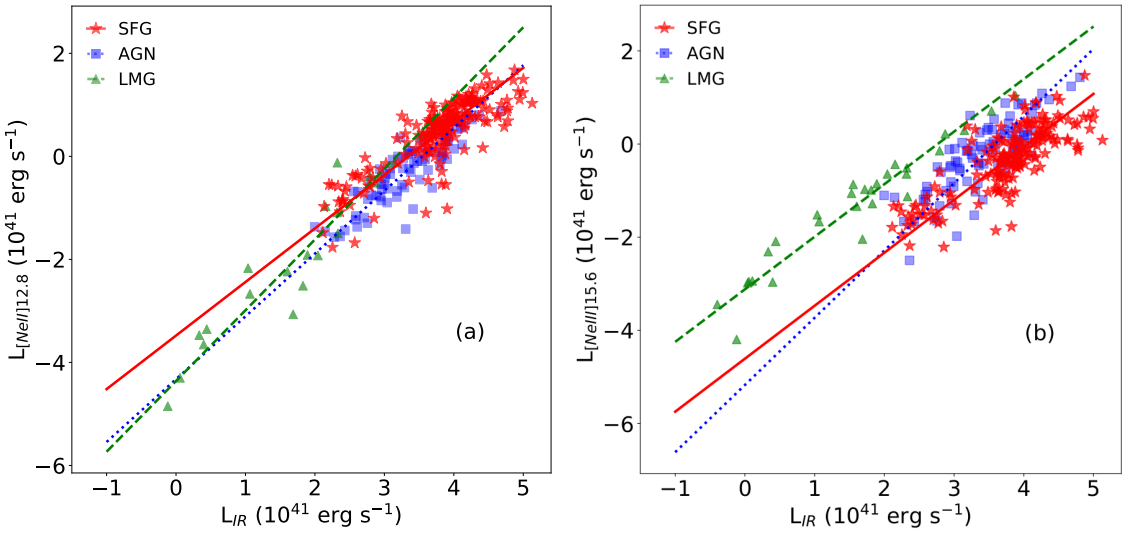

Figure 3.7: (a: left) The [NeII]12.8 µm line luminosity as a function of the total IR luminosity. **(b: right)** The [NeIII]15.6 µm line luminosity as a function of the total IR luminosity. The same legend as in Fig. 3.5 was used.

Moreover, the higher ionizing continuum present in LMG contribute to destroy these features (Cormier et al. 2015; Engelbracht et al. 2008). For AGN and SFG, the slope of the correlation of the PAH feature at 11.3µm to the total IR luminosity is comparable within the errors, with the difference linked to a higher L_{IR} for equal PAH emission in AGN.

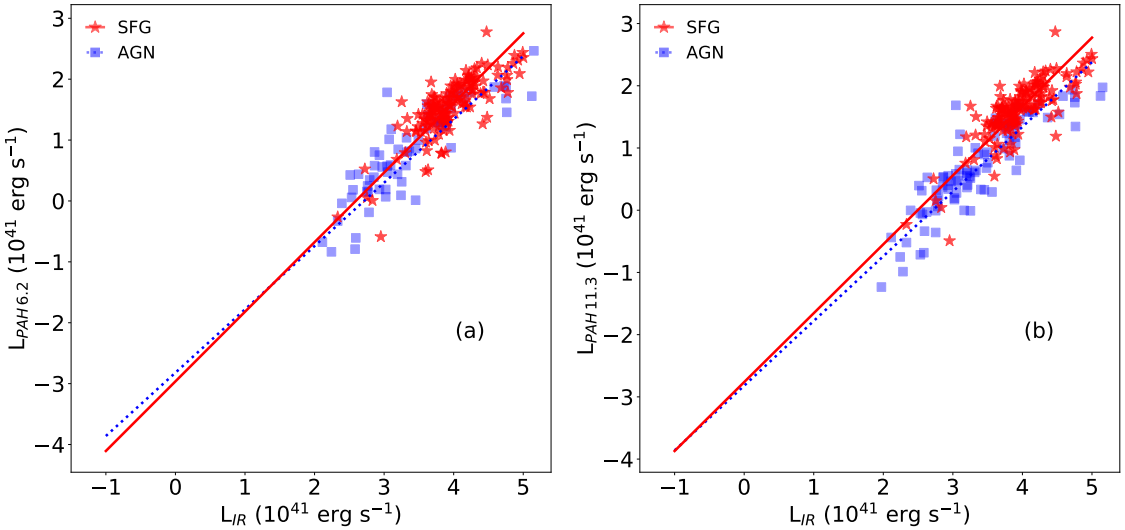

Figure 3.8: (a: left) The luminosity of the PAH feature at 6.2 µm as a function of the total IR luminosity. **(b: right)** The luminosity of the PAH feature at 11.3 µm as a function of the total IR luminosity. The same legend as in Fig. 3.5 was used.

In the [OIV]25.9µm line correlations (Fig. 3.9), the AGN emission is one order of magnitude brighter than in SFG (see also Tommasin et al. 2010). LMG show a shallower relation with IR luminosity, with a decreasing slope at higher luminosities. This could be linked to the high ionization potential of the [OIV]25.9µm line: the few ionizing photons beyond 54.4 eV (the threshold for the double ionization of helium) produced by LMG might not scale linearly with the overall luminosity. The data, however, do not allow us to draw a firm conclusion due to the relatively poor statistics of LMG, for which only 16 detections of the [OIV] line are available. In order to obtain a reliable correlation for the AGN sample, I have limited

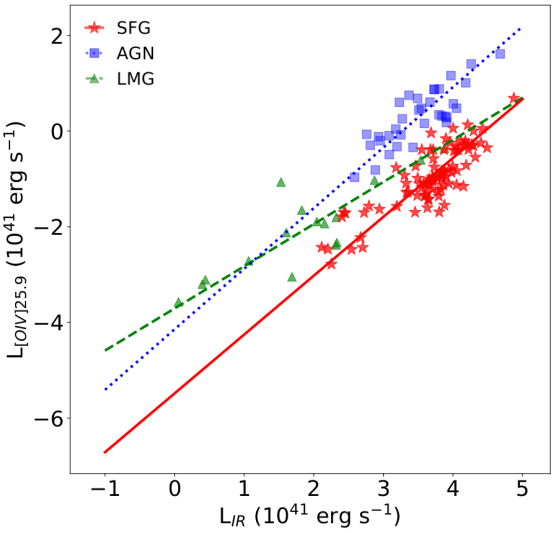

Figure 3.9: The [OIV]25.9 µm line luminosity as a function of the total IR luminosity. The same legend as in Fig. 3.5 was used.

the AGN sample used to determine this correlation. I have considered only those objects for which an AGN component at the 19µm continuum greater than 85%, as defined in Tommasin et al. (2010). I applied this limit in order to minimize a possible contamination in the line due to emission from strong starburst activity (see, e.g. Lutz et al. 1998). The same sample is later used when deriving a correlation between the [OIV] line and the BHAR (Sec. 3.5).

While the correlations for the AGN sample have been calculated considering a local sample of galaxies with total IR luminosity in the range of $L_{IR} \simeq 10^{40} - 10^{46}$ erg s^{-1}, it is possible that in brighter galaxies these correlations might not hold true.

It is important to note that a negative correlation between the equivalent width and the continuum luminosity of optical/UV broad emission lines has been observed in bright AGNs (the so-called Baldwin effect; see e.g. Baldwin 1977). A common explanation for the Baldwin effect refers to the spectral shape of the ionizing continuum which appears softer in high luminosity sources than in AGN with lower luminosities. This leads to a lower number of ionizing photons in the broad line regions, and consequently to smaller equivalent widths. More recent observations have shown that the same effect is present also in optical forbidden lines, like [OIII]5007Åor [NeV]3425Å(see e.g. Stern & Laor 2012; Zhang et al. 2013). In the mid-IR range, the Baldwin effect was observed in 8 near-by Seyfert galaxies for the [SIV]10.5 and [NeII]12.8µm lines (Hönig et al. 2008). This suggest that the correlations derived in this work, covering the $L_{IR} \simeq 10^{40} - 10^{46}$ erg s^{-1} luminosity range, might not hold true for brighter objects where the Baldwin effect might be more pronounced.

Table 3.3: Updated calibration between the total IR luminosity (L_{IR}) and the line luminosity obtained for fine-structure lines and PAH bands in the mid- to far- IR range. For each class of objects, are reported the slope (a) and intercept (b) of the linear correlation with relative errors, the number of data from which the linear correlation was calculated (N) and the best-fit coefficients of determination (r).

Line/feature	**AGN**				**SFG**				**LMG**			
	$a \pm \delta a$	$b \pm \delta b$	N	r	$a \pm \delta a$	$b \pm \delta b$	N	r	$a \pm \delta a$	$b \pm \delta b$	N	r
PAH 6.2	1.04±0.07	-2.73±0.24	65	0.87	1.15±0.06	-2.99±0.24	150	0.81	–	–	–	–
[NeVI]7.65	1.22±0.24	-4.12±0.82	8	0.89	–	–	–	–	–	–	–	–
PAH 7.7	–	–	–	–	1.29±0.07	-2.98±0.27	150	0.81	–	–	–	–
PAH 8.6	–	–	–	–	1.43±0.23	-4.25±0.67	16	0.84	–	–	–	–
$H_2$9.67	1.20±0.28	-4.97±1.17	9	0.82	1.39±0.06	-5.43±0.26	137	0.87	–	–	–	–
[SIV]10.51	1.37±0.11	-5.19±0.38	75	0.80	1.58±0.24	-7.00±0.94	51	0.59	1.03±0.08	-3.08±0.16	29	0.91
PAH 11.3	1.04±0.06	-2.82±0.20	90	0.88	1.11±0.06	-2.79±0.23	150	0.81	–	–	–	–
$H_2$12.28	1.25 ± 0.10	-5.41 ± 0.37	31	0.91	1.18 ± 0.05	-4.79± 0.19	114	0.91	–	–	–	–
[NeII]12.81	1.19±0.07	-4.23±0.26	86	0.85	1.04±0.43	-3.48±0.17	186	0.84	1.37±0.10	-4.36±0.20	21	0.95
[NeV]14.32	1.32±0.11	-5.01±0.39	74	0.78	–	–	–	–	–	–	–	–
[NeIII]15.56	1.44 ±0.10	-5.16±0.36	88	0.80	1.13±0.06	-4.60±0.21	182	0.80	1.13±0.06	-3.11±0.12	28	0.96
PAH 17	–	–	–	–	1.14±0.06	-3.08±0.23	131	0.84	–	–	–	–
$H_2$17.03	1.14±0.06	-4.64±0.19	76	0.91	1.22±0.05	-4.58±0.20	135	0.89	–	–	–	–
[SIII]18.71	1.22±0.09	-4.62±0.30	70	0.83	1.26±0.11	-4.79±0.42	140	0.60	1.14±0.06	-3.42±0.12	25	0.96
[FeIII]22.93	–	–	–	–	1.33±0.13	-5.79±0.44	14	0.64	–	–	–	–
[NeV]24.32	1.27±0.11	-4.73±0.37	65	0.80	–	–	–	–	–	–	–	–
[OIV]25.89	1.27±0.14	-4.13±0.48	34	0.82	1.15±0.05	-5.00±0.20	144	0.86	0.88±0.13	-3.71±0.27	16	0.86
[FeII]25.98	–	–	–	–	0.80±0.18	-3.99±0.51	35	0.44	–	–	–	–
$H_2$28.22	1.04±0.14	-4.44 ± 0.45	25	0.81	1.65±0.24	-6.51±0.82	11	0.91	–	–	–	–
[SIII]33.48	1.10±0.07	-3.85±0.23	75	0.87	1.13±0.05	-3.94±0.20	170	0.83	1.11±0.08	-3.24±0.17	20	0.96
[SiII]34.81	1.21±0.08	-3.99±0.28	73	0.84	1.15±0.04	-3.72 ±0.15	167	0.91	1.05±0.08	-3.14±0.18	17	0.95
[OIII]51.81	0.92±0.13	-3.10±0.54	19	0.85	–	–	–	–	–	–	–	–
[NIII]57.32	0.98±0.06	-3.96±0.24	31	0.94	-	-	-	-	-	-	-	-
[OI]63.18	1.07±0.04	-3.56±0.17	106	0.91	1.18±0.05	-3.86±0.21	183	0.83	1.07±0.06	-3.00±0.11	31	0.96
[OIII]88.36	1.18±0.06	-4.34±0.22	81	0.91	1.20±0.06	-4.27±0.25	117	0.85	1.05±0.06	-2.53±0.10	37	0.95
[NII]121.9	1.08±0.06	-4.43±0.22	77	0.89	0.90±0.06	-3.39±0.22	75	0.86	0.96±0.09	-4.17±0.23	8	0.97
[OI]145.5	1.06±0.07	-4.53± 0.26	64	0.88	1.03±0.05	-4.14±0.16	13	0.99	1.05±0.07	-4.14± 0.18	12	0.97
[CII]157.7	1.00±0.04	-3.18± 0.14	149	0.90	0.97±0.05	-2.76±0.20	183	0.78	1.09±0.06	-2.88±0.10	40	0.95
[NII]205	0.88±0.05	-3.88± 0.18	60	0.92	1.02±0.07	-4.36±0.23	13	0.97	–	–	–	–

3.4 Star formation rate tracers

In this section I present different SFR tracers, each based on different components of the ISM. The ISM is composed of atomic hydrogen for ∼40% of the total volume, molecular hydrogen (H_2) for ∼1% of the volume, ionized hydrogen (HII regions) for ∼10% of the volume, and hot gas for ∼50% of the volume. Of these component, the molecular and ionized hydrogen clouds can be detected via IR emission lines. In particular, HII regions form around accreting protostars after they exceed the ∼10$M_\odot$ mass limit (Keto 2002, 2007). These regions are then ionized by UV radiation from the new star, which is absorbed and re-emitted in the IR. The strength of the UV radiation allows the emission of fine structure lines characterized by intermediate ionization potential, such as [SIV]10.5, [NeII]12.8, [NeIII]15.6, [SIII]18.7 or [OIII]88μm lines. These lines give an information on stars that have already formed. Moving farther from the star, photodissociation regions (PDR), are characterized by neutral gas excited by the remaining UV photons. These regions, however, occur in any region of interstellar gas where the gas has enough low density and temperature to remain neutral, but the column density cannot prevent the penetration from far-UV photons, which are absorbed and re-emitted in low ionization/neutral fine structure lines such as [OI]63 or [CII]158μm. Cooling lines, while not necessarily linked to star formation processes, are a good indicator of star formation activity: a gas cloud, in order to collapse and start the process of star formation, needs to cool down. Cooling lines such as [CII] or [OI], emitted from collapsing gas clouds, thus give an indication of the energy radiated away, which allows collapsing. It is important to note, however, that cooling lines present a deficit in ULIRGs. This is due to the extreme compact environment in these objects, where the strong far-IR emission is limited by self-absorption thus causing a deficit in line luminosity. For this reason I do not include the ULIRG sample when deriving the correlations presented in this Section. These galaxies, however, are shown in the figures as a reference.

Star forming regions are also characterized by the production of Polycyclic Aromatic Hydrocarbons (PAH) features (Lutz et al. 2008; Shipley et al. 2016). The proposed mechanism for the emission of the PAH bands is a one-photon mechanism that leads to the heating of the PAH molecules and ions by UV, visible, and/or NIR photons (Salama 2008). On the other hand, molecular hydrogen forms on the surface of dust grains, acting as a major coolant of the ISM, playing a relevant role in the processes that regulate star formation and the subsequent galaxy evolution. Of the different mechanisms that can excite this molecule (see Section 3.4.5), UV fluorescence (Black & van Dishoeck 1987) is the one linked mainly to star formation.

Analyzing the different emission lines produced by the various regions that constitute the ISM, it is possible to trace the obscured component of star formation, i.e. the absorbed UV radiation then re-emitted in the IR. Combining different tracers, moreover, allows to trace different regions of the ISM, gaining a more comprehensive view on the phenomenon.

In order to calibrate these proposed tracers, I use two different methods. For SFG, the SFR is measured directly from the total IR luminosity following Kennicutt (1998):

$$\mathrm{SFR} = k_{\mathrm{IR}} * \mathrm{L_{IR}} \tag{3.2}$$

where $k_{\mathrm{IR}} = 4.5 \times 10^{-44} \mathrm{M_\odot yr^{-1} erg^{-1} s}$. The same conversion is also tentatively applied to AGN, (see Sec. 3.4.4), where the sample is however limited to sources with $\mathrm{L_{IR}} \leq 10^{45} \mathrm{erg\,s^{-1}}$. This limit aims to minimize the AGN effect on the $\mathrm{L_{IR}}$ and to avoid overestimating the SFR because of AGN activity. I selected the $\mathrm{L_{IR}}$ threshold value from Fig. 3.8: above $\mathrm{L_{IR}} = 10^{45} \mathrm{erg\,s^{-1}}$ there is a pronounced difference between the PAH to total luminosity relation in AGN or SFG. Since the PAH features are not produced by AGN activity,

but are only linked to star formation activity, I assume that the difference in slope between the two relations is due to an excess of IR luminosity due to the AGN itself, that appears evident only for high luminosity objects.

For LMG, following Rémy-Ruyer et al. (2015), I adopt the SFR derived from H_α and corrected by the total IR luminosity. The total IR luminosity alone does not accurately represent the total SFR in LMG due to the lower dust-to-gas ratio in their ISM. Including the optical component to calculate the SFR is thus necessary to properly account for the emission not reprocessed by dust. An alternative method of measuring the SFR in LMG, that leads to comparable results, is to use the FUV luminosity corrected for the total IR luminosity as tracer. While the SFR for LMG could also be determined using the FUV luminosity, this method could be used only on ~78% of the sample. The optical luminosity, on the other hand, allowed to cover ~90% of the sample (Rémy-Ruyer et al. 2015).

The resulting correlations are presented in the following Sections, and summarized in Table 3.4.

3.4.1 Low ionization and PDR SFR tracer

The [CII]158 μm line can be used as a tracer of the SFR, as proposed by different authors (see, e.g., De Looze et al. 2014). Here I compare the line intensity of SFG and LMG to the SFR. Applying the orthogonal distance regression fit, I find a strong correlation between the two quantities:

$$\log\left(\frac{\mathrm{SFR}}{\mathrm{M_\odot\,yr^{-1}}}\right) = (0.89 \pm 0.02)\left(\log\frac{\mathrm{L_{[CII]}}}{10^{41}\,\mathrm{erg\,s^{-1}}}\right) + (0.62 \pm 0.02) \tag{3.3}$$

Fig. 3.10a shows the correlation obtained for 227 galaxies, of which 37 are LMG and 190 are SFG. The relation is nearly linear, with a Pearson correlation coefficient of $r = 0.92$. This relation covers more than five orders of magnitude in SFR, indicating that the [CII]158μm emission line is an overall good tracer of SFR for local star forming galaxies, independently of their metallicity. The AGN sample was excluded from this correlation since the SFR was derived from the total IR luminosity, and as can be seen in Fig.3.5, the AGN sample presents an excess IR continuum emission not due to star formation processes.

In local SFG, the bulk of the [CII] emission arises from neutral gas (Croxall et al. 2017), with only a minor part arising from ionized gas. In LMG, however, PDR regions are less frequent, and the [CII] emission arises mainly from ionized regions (see e.g. Madden et al. 1997). The two components, however, compensate each other, thus rendering this line an ideal tracer for star formation activity in galaxies with different ISM conditions.

Fig. 3.10b shows the comparison of the correlation I obtained with the results of De Looze et al. (2014) and Sargsyan et al. (2012). While for this analysis and in the work of Sargsyan et al. the SFR was determined following Kennicutt (1998), De Looze et al. trace the SFR using the GALEX FUV emission (Cortese et al. 2012) and the *Spitzer*-MIPS 24 μm emission (Rieke et al. 2004). The results by De Looze et al. (2014) and Sargsyan et al. (2012) are comparable within the errors. When compared to the correlation presented here, I find a good agreement with the results obtained by De Looze et al. (2014) for their total sample at luminosities of $\mathrm{L_{[CII]}} > 10^{41}$ erg s^{-1}, while there is a difference of ~0.3 dex for lower luminosities.

In De Looze et al. the dwarf sample, when considered alone, shows a flatter slope than the total sample, equal to 0.80 ± 0.5 (see Fig. 3.10b, the blue diamond line). The authors link the flatter slope to an underestimation of the SFR based on the far-UV emission. I observe a similar flattening of the slope when considering the LMG sample alone, equal to 0.69 ± 0.05, consistent with the result by De Looze et al. within 3σ.

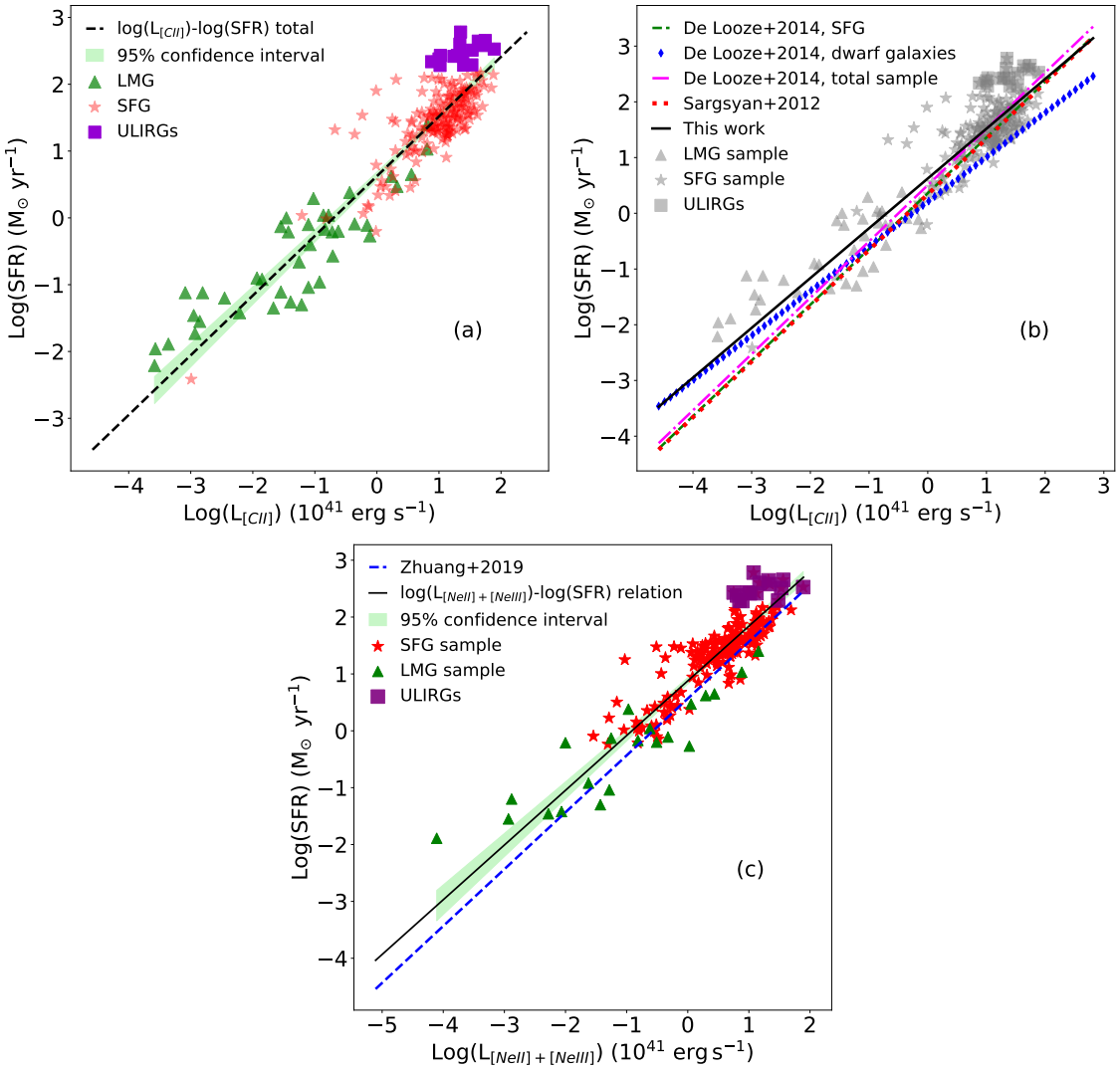

Figure 3.10: (a: top left) Correlation between the [CII]158 µm line luminosity and the SFR derived from the total L_{IR}. Red stars represent SFG, green triangles the LMG. Purple squares show the ULIRG population of SFG, and the shaded green area indicates the 95% confidence interval. **(b: top right)** Comparison of the log$L_{[CII]}$-log(SFR) relation obtained in this work (black solid line) with the results obtained by De Looze et al. (2014): the green dashed line represents a sample of HII/star forming galaxies, the blue diamond line shows the results for the low metallicity dwarf sample, and the pink dash-dotted line considers the whole sample. The red dotted line shows the results obtained by Sargsyan et al. (2012). **(c: bottom)** Correlation between the [NeII]12.8 µm and [NeIII]15.6 µm summed emission lines luminosity, in units of 10^{41} erg s^{-1} and the SFR derived from the total IR luminosity (black dashed line) for SFG (red star) and from the H_α luminosity (corrected for the IR luminosity) for LMG (green triangles). The shaded green area indicates the 95% confidence interval. The blue dashed line shows the results obtained by Zhuang et al. (2019) for the same relation.

De Looze et al. (2014) find that the ULIRG population presents a scatter of almost one order of magnitude in the [CII]-SFR relation, when compared to the total sample. I find the same result in my correlation, with the ULIRG population (composed of 16 objects) lying between 0.2 and 1.0 dex above the correlation derived for the total sample. Given the small number of sources, however, I do not derive a specific [CII]-SFR correlation for the ULIRG sample.

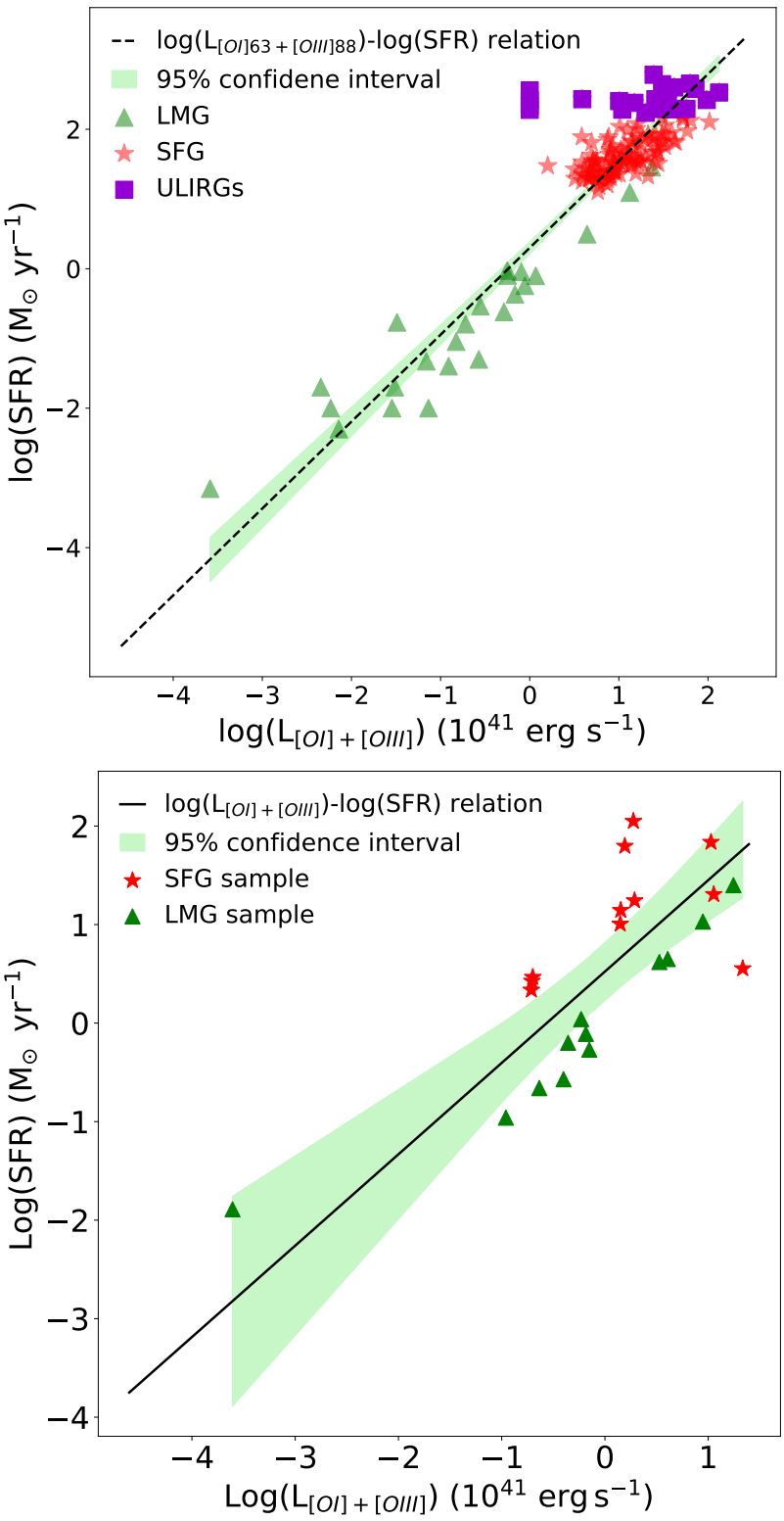

Figure 3.11: Correlation between the [OI]63µm and [OIII]88µ summed emission line luminosities (**top**) and between the [OI]145µm and [OIII]88µ summed emission line luminosities (**bottom**), in units of $10^{41}\,\mathrm{erg\,s^{-1}}$, and the SFR derived from the total IR luminosity (black dashed line) for a composite sample of SFG (red stars) and from the H_α luminosity (corrected for the IR luminosity) for LMG (green triangles). Purple squares indicate the sample of ULIRGs included in the SFG sample.

3.4.2 High ionization and PDR SFR tracer

Besides C^+, also O and O^{2+} are two important coolants of the ISM. The [OI]63,145μm lines trace the warm and/or dense PDRs, while the [OIII]88μm emission line originates from diffuse, highly ionized regions near young, hot stars.

The [OIII] line can be an important SFR tracer in LMG (De Looze et al. 2014), where PDRs are weak or absent in the ISM and the ionization field is stronger. In order to trace the SFR in SFG, however, a tracer that can account for PDRs needs to be included. For this reason, combining these two lines can provide an accurate estimate of the SFR, both in SMG and LMG, probing both neutral and ionized medium.

The top panel in Fig. 3.11 shows the correlation, between the SFR and the summed luminosities of the [OI]63μm and [OIII]88μm lines, as obtained for a sample of 151 objects, 24 LMG and 124 SFG, of which 22 ULIRGs. The correlation, with a Pearson correlation coefficient of $r = 0.94$, can be expressed by:

$$\log\left(\frac{\mathrm{SFR}}{\mathrm{M_\odot\,yr^{-1}}}\right) = (1.25 \pm 0.04)\log\left(\frac{\mathrm{L_{[OI]+[OIII]}}}{10^{41}\,\mathrm{erg\,s^{-1}}}\right) + (0.30 \pm 0.04) \tag{3.4}$$

The bottom panel shows instead the correlation between the SFR and the summed luminosities of the [OIII]88μm and [OI]145μm lines, as obtained using 11 SFG and 12 LMG. The correlation has a Pearson correlation coefficient of $r = 0.77$ and can be expressed by:

$$\log\left(\frac{\mathrm{SFR}}{\mathrm{M_\odot\,yr^{-1}}}\right) = (0.93 \pm 0.14)\log\left(\frac{\mathrm{L_{[OI]+[OIII]}}}{10^{41}\,\mathrm{erg\,s^{-1}}}\right) + (0.52 \pm 0.14) \tag{3.5}$$

The relatively small number of objects used to derive this correlation is due to the few detections of the [OI]145μm line in local galaxies, which broadens the confidence interval of the relation, reported in Fig. 3.11 as a shaded area. This relation, however, will be useful for measuring the SFR in high redshift objects, for which the [OI]145μm line can be more easily measured by the ALMA telescope compared to the [OI]63μm line (see Ch.6 Sec.6.3.2).

3.4.3 Mid- to high ionization tracers

A promising SFR tracer, proposed by Ho & Keto (2007); Zhuang et al. (2019), is the sum of the [NeII]12.8 μm and the [NeIII]15.6 μm emission line fluxes. By adding the two lines, this tracer is fairly independent from the effects related to the hardness of the radiation field, which are stronger at lower metallicities affecting single line diagnostics. For instance, while the [NeII]12.8 μm line intensity scales consistently in LMG and SFG, the [NeIII]15.6 μm line becomes remarkably brighter in LMG (Fig. 3.7). Although some dependency on density is still expected, the high critical density of the sulphur ($> 7 \times 10^3\,\mathrm{cm^{-3}}$; see Table 3.1) and the neon lines ($> 5 \times 10^4\,\mathrm{cm^{-3}}$) used in this Section guarantees a minor effect on these tracers for the vast majority of the galaxy population.

Fig. 3.10c shows the correlation found between the summed luminosities of the [NeII] and [NeIII] emission lines and the SFR: this relation was obtained using 203 local star forming galaxies, of which 182 SFG and 21 LMG, and is expressed as

$$\log\left(\frac{\mathrm{SFR}}{\mathrm{M_\odot\,yr^{-1}}}\right) = (0.96 \pm 0.03)\log\left(\frac{\mathrm{L_{[NeII]+[NeIII]}}}{10^{41}\,\mathrm{erg\,s^{-1}}}\right) + (0.88 \pm 0.03) \tag{3.6}$$

where $\log(\mathrm{L_{[NeII]+[NeIII]}})$ is the luminosity corresponding to the sum of the fluxes of the [NeII]12.8 μm and the [NeIII]15.6 μm lines. This relation has a Pearson correlation coefficient of r=0.91.

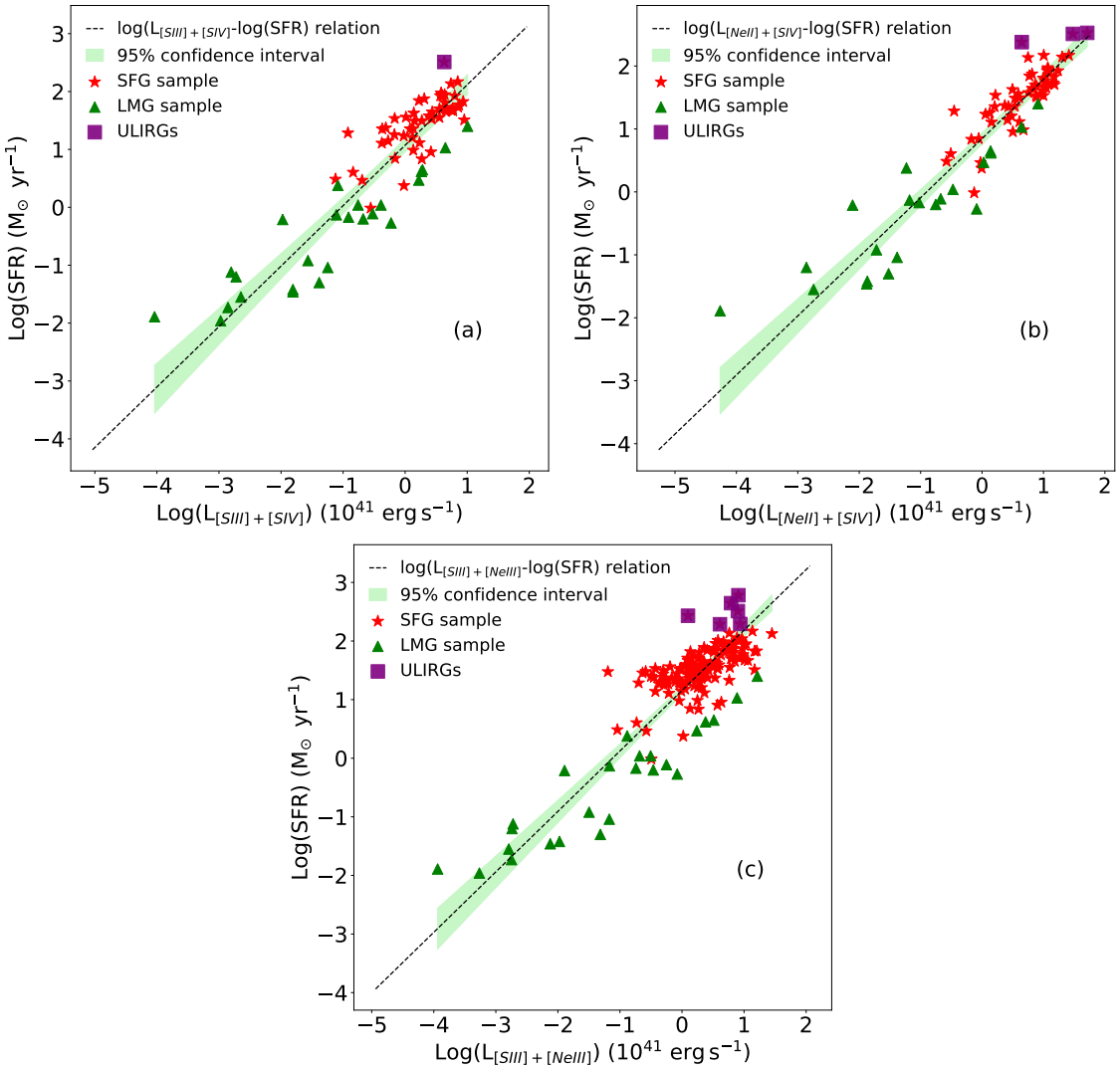

Figure 3.12: (a: top left) Correlation between the [SIV]10.5 µm and [SIII]18.7 µm summed emission lines luminosity, expressed in units of 10^{41} erg s^{-1} and the SFR derived from the total IR luminosity (black dashed line) for a composite catalogue of SFG (red star) and from the H_α luminosity (corrected for the IR luminosity) for LMG (green triangles). The shaded green area in the three plots indicates the 95% confidence interval. **(b: top right)** Correlation between the [NeII]12.8 µm and [SIV]10.5 µm summed luminosities and the SFR derived from the total IR luminosity (black dashed line) for SFG (red star) and from the H_α luminosity (corrected for the IR luminosity) for LMG (green triangles). **(c: bottom)** Correlation between the [NeIII]15.6 µm and [SIII]18.7 µm summed emission lines and the SFR derived from the total IR luminosity (black dashed line) for SFG (red star) and from the H_α luminosity (corrected for the IR luminosity) for LMG (green triangles).

In the same figure is reported the theoretical relation obtained by Zhuang et al. (2019), derived following the assumption that the neon lines trace all the ionizing photons in a star forming region. The relation derived here is based on observational data, and shows a lower slope, and thus a larger offset, thus suggesting lower efficiency in reprocessing the ionizing photons by the neon transitions.

Analogously to the case of the two neon lines, I also take into consideration the sum of two sulfur lines, i.e. [SIII]18.7 µm and [SIV]10.5 µm, as a tracer of the SFR. Fig. 3.12a shows the correlation of the luminosity derived by summing [SIII]18.7 µm and [SIV]10.5 µm with the SFR derived from the total IR

luminosity for the SFG, and from the H_α line corrected using the total IR luminosity for the LMG:

$$\log\left(\frac{\mathrm{SFR}}{\mathrm{M_\odot\,yr^{-1}}}\right) = (1.04 \pm 0.05)\log\left(\frac{\mathrm{L_{[SIII]+[SIV]}}}{10^{41}\,\mathrm{erg\,s^{-1}}}\right) + (1.07 \pm 0.06) \tag{3.7}$$

For this relation 52 SFG and 25 LMG were used, obtaining a relation with a Pearson r coefficient of r=0.90.

As shown in Table 3.1, Ne^+ has a ionization potential (IP) of 21.56 eV, while Ne^{2+} has a IP of $40.96\,\mathrm{eV}$ and a potential of the next stage at $63.45\,\mathrm{eV}$, thus covering the $\sim$ 20 – 60 eV interval in energy. This is roughly the same ionization interval covered by the [NeII]+[SIV], with [SIV] having a IP of 34.79 eV and the next stage IP at 47.22 eV, or by [NeIII]+[SIII], with [SIII]18.7 μm that has a IP of 23.34 eV. Analyzing the former pair, I find a linear correlation between $\mathrm{L_{[NeII]+[SIV]}}$ and SFR, as shown in Fig. 3.12b. This correlation can be expressed as:

$$\log\left(\frac{\mathrm{SFR}}{\mathrm{M_\odot\,yr^{-1}}}\right) = (0.94 \pm 0.04)\log\left(\frac{\mathrm{L_{[NeII]+[SIV]}}}{10^{41}\,\mathrm{erg\,s^{-1}}}\right) + (0.85 \pm 0.05) \tag{3.8}$$

This relation has been calculated using 77 galaxies, of which 56 SFG and 21 LMG, and has a Pearson correlation coefficient $r = 0.93$. The small number of SFG used for determining this relation is due to the lack of [SIV] measurements available in literature, due to the intrinsic line faintness in star forming galaxies (see Table 3.3) and the position of the line in the silicate absorption band in the 9-11 μm range.

The relation between SFR and the [NeIII]+[SIII] lines emission sum is shown in Fig. 3.12c and can be expressed as:

$$\log\left(\frac{\mathrm{SFR}}{\mathrm{M_\odot\,yr^{-1}}}\right) = (1.03 \pm 0.04)\log\left(\frac{\mathrm{L_{[NeIII]+[SIII]}}}{10^{41}\,\mathrm{erg\,s^{-1}}}\right) + (1.16 \pm 0.04) \tag{3.9}$$

This relation has been calculated using 165 galaxies, of which 140 SFG and 25 LMG, and has a Pearson correlation coefficient $r = 0.86$.

3.4.4 PAH features as SFR tracers

In the mid-IR range, the emission features due to the PAH molecules arise from PDR around HII regions embedding young stars (e.g., Draine & Li 2007), and can be used as SFR tracers. We analyze the PAH features at 6.2 and 11.3 μm, considering the same sample of 155 SFG and the sample of 103 AGN galaxies described in section 3.2 for the PAH analysis.

The use of the PAH as a measure of the SFR was originally proposed by Wu et al. (2005), who used the *Spitzer*-IRAC camera (Fazio et al. 2004) 8 μm band, whose flux density is dominated by the strongest PAH feature, i.e that at 7.7 μm. They derive a calibration of the 8 μm SFR using the radio VLA emission at 1.4GHz and the Hα luminosity from the SFR-radio luminosity relation given by Yun et al. (2001) and the SFR-Hα luminosity from Kennicutt (1998), respectively.

More recently, the relatively bright PAH features at 6.2, 7.7 and 11.3 μm have been used to derive a total PAH luminosity and has been correlated to the extinction corrected Hα luminosity of a sample of 227 galaxies (Shipley et al. 2016). For star-forming galaxies (105 galaxies), the total PAH luminosity correlates linearly with the extinction-corrected Hα luminosity.

The correlation of the single PAH features and the SFR are shown in Fig. 3.13: panel (a) shows the relation calculated for the 6.2μm feature using 142 SFG and 56 AGN, while panel (b) shows the relation for the 11.3μm feature, for which were used 142 SFG and 77 AGN. When computing these correlations,

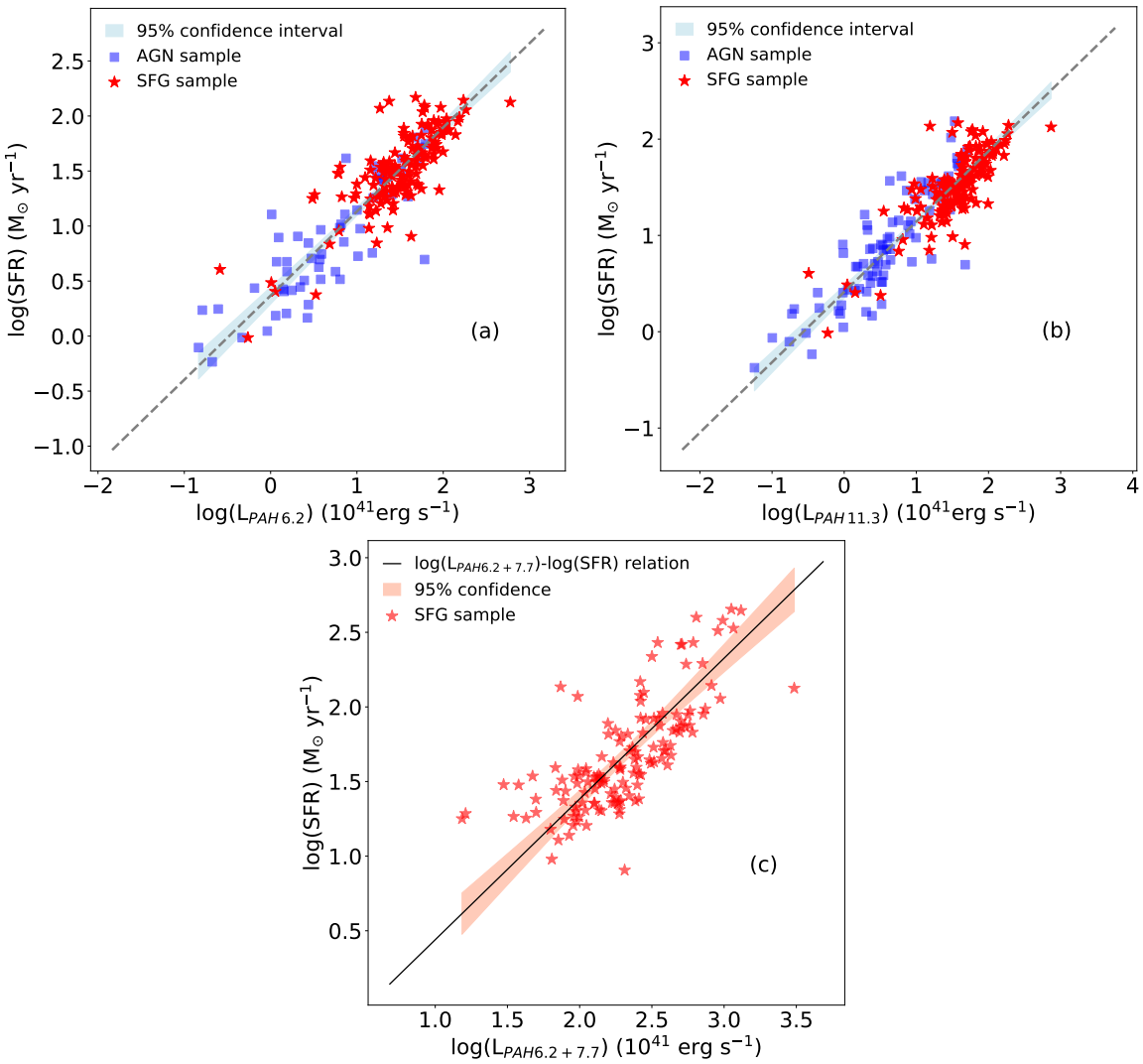

Figure 3.13: (a: top left) Correlation between the PAH emission feature at 6.2 µm, expressed in units of 10^{41} erg s^{-1} and the SFR derived from the total IR luminosity (black line) for a composite catalogue of SFG (red star) and AGN dominated galaxies (blue square). The shaded area in the three plots indicates the 95% confidence interval. **(b: top right)** Correlation between the PAH emission feature at 11.3 µm, expressed in units of 10^{41} erg s^{-1} and the SFR derived from the total IR luminosity (black line) for a composite catalogue of SFG (red star) and AGN dominated galaxies(blue square). **(c: bottom)** Correlation between the summed PAH emission features at 6.2 and 7.7µm, expressed in units of 10^{41} erg s^{-1} and the SFR derived from the total IR luminosity (black line), for a catalogue of 139 SFG (red stars). I exclude ULIRGs from both AGN and SFG samples due to the known PAH deficit in these sources, plus AGN with luminosities above 10^{45} erg s^{-1} that could dominate the IR continuum used to estimate the SFR.

I excluded all ULIRGs from the original sample of AGN and SFG, following the approach by Pope et al. (2013) to avoid saturation effects in the PAH-to-continuum luminosities. Moreover, when considering the AGN sample, we discarded all sources with a total IR luminosity greater than $L_{IR} = 10^{45}\,erg\,s^{-1}$, where the total IR luminosity, and therefore the derived SFR, could be severely contaminated by the AGN.

For the 6.2μm PAH feature, the derived relation is described by:

$$\log\left(\frac{SFR}{M_\odot\,yr^{-1}}\right) = (0.76 \pm 0.03)\log\left(\frac{L_{PAH6.2}}{10^{41}\,erg\,s^{-1}}\right) + (0.37 \pm 0.04) \tag{3.10}$$

This correlation has a Pearson correlation coefficient of $r = 0.87$. The correlation for the 11.3μm feature has instead a Pearson correlation coefficient of $r = 0.89$ and is expressed by:

$$\log\left(\frac{SFR}{M_\odot\,yr^{-1}}\right) = (0.73 \pm 0.02)\log\left(\frac{L_{PAH11.3}}{10^{41}\,erg\,s^{-1}}\right) + (0.41 \pm 0.03) \tag{3.11}$$

The single PAH features, while giving an accurate measurements of the SFR, can be significantly affected by the conditions of the ISM. A combination of two or more features, on the other hand, being produced from different conditions of the ISM, can be considered a more reliable tracer. For this reason, I propose here a SFR tracer derived from the combination of the 6.2 and 7.7μm PAH features. This correlation, shown in Fig. 3.13(c), is derived using 139 SFG, and has a Pearson correlation coefficient of $r = 0.73$. The correlation is expressed by:

$$\log\left(\frac{SFR}{M_\odot\,yr^{-1}}\right) = (0.94 \pm 0.06)\log\left(\frac{L_{PAH6.2+7.7}}{10^{41}\,erg\,s^{-1}}\right) + (-0.50 \pm 0.15) \tag{3.12}$$

In both cases, the correlation has a shallow slope, significantly lower than unity. This is a consequence of including the AGN sample. Considering only the SFG sample, the slopes increase, becoming equal to 0.87 for the PAH feature at 6.2μm, and 0.90 for the PAH feature at 11.3μm. On the other hand, while all ULIRGs were excluded in determining these correlations, including these objects does not lead to a significant change in slope, that instead remains comparable within the errors. In particular, including the entire AGN and SFG samples for the PAH feature at 6.2μm results in a slope of 0.81±0.03, while for the PAH feature at 11.3μm the slope would be of 0.78±0.03.

In Fig. 3.14 is presented a comparison with the results proposed by Shipley et al. (2016), which determine the SFR using the H_α and 24 μm luminosities. In order to apply the same method to our sample, I exclude all AGN, for which the H_α and 24 μm luminosities are contaminated by the AGN emission. This leaves a sample composed of 100 SFG, for which the 6.2, 7.7, 11.3 PAH features, the 24 μm and the H_α data are available in the literature. Using my sample, the estimation of the SFR appears to be 0.25 dex higher than the one derived by Shipley et al. (2016) and almost linear in slope. The equation that describes this relation is expressed as:

$$\log\left(\frac{SFR}{M_\odot\,yr^{-1}}\right) = (1.08 \pm 0.10)\log\left(\frac{L_{\Sigma PAH}}{10^{41}\,erg\,s^{-1}}\right) + (-1.28 \pm 0.23) \tag{3.13}$$

and the relation has a Pearson correlation coefficient of $r = 0.66$.

While the slopes of this relation and the relation found by Shipley et al. are comparable within the errors, the difference in offset can be attributed to the significant difference in the sample characteristics. In particular, the disagreement arises when I extrapolate the results obtained by Shipley et al. for local galaxies. The sample used by Shipley et al. is in fact composed of galaxies with redshift in the $z \sim 0.2-0.6$ range, while

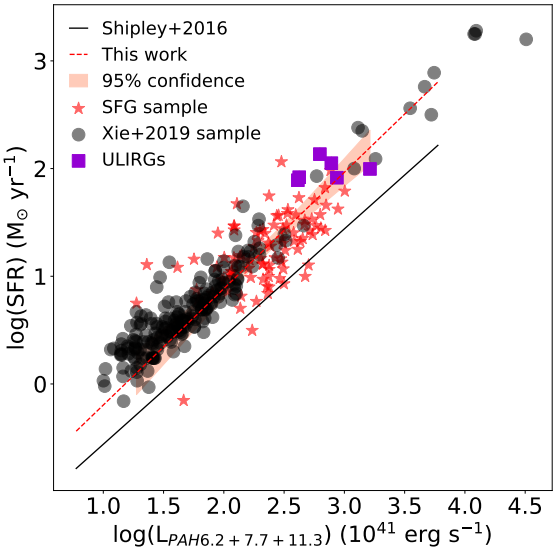

Figure 3.14: Comparison between the relation between PAH total luminosity (summed 6.2, 7.7 and 11.3µm features) and SFR derived by Shipley et al. (2016) (black solid line) and using our sample (red dashed line). Red stars indicate SFG, purple squares indicate the ULIRG sub-sample included in the GOALS sample, and grey circles represent a sample of local galaxies used in Xie & Ho (2019).

my sample has a mean redshift of $z \sim 0.027$. Moreover, while my sample is primarily composed of LIRGs and ULIRGs, the sample used by these authors is mainly constituted of galaxies in the $L_{IR} \sim 10^9 - 10^{12} L_\odot$ interval. I additionally compared the relation derived in this work to a sample of local SFG described by Xie & Ho (2019), for which the SFR derived from Hα and corrected by the flux at 24µm was available in the literature. This sample is composed of local galaxies and, while the bulk of these galaxies present a lower total PAH luminosity, it follows the same relation derived from the GOALS sample. This suggests that the difference observed between my result and the result by Shipley et al. is indeed due to an intrinsic difference of the sample used, mainly linked to a higher redshift and higher mass range of the Shipley et al. sample.

3.4.5 H_2 rovibrational transitions as SFR tracers

Molecular hydrogen is the most abundant molecule in the Universe and can be found in various environments. It can be excited by different mechanisms, like UV fluorescence (Black & van Dishoeck 1987), shocks (Hollenbach & McKee 1989) or X-ray illumination (Maloney 1997), thus probing various astrophysical environments. H_2 forms on the surface of dust grains, affecting the ISM chemistry, and acts as a coolant. It is particularly important in all processes that regulate star formation and galaxy evolution, where the principal mechanism of these lines is associated with the UV radiation from massive stars.

Comparing theoretical models to observations, Rigopoulou et al. (2002) found evidence that an important fraction of the H_2 pure rotational transitions in the mid-IR in SFG can originate in PDRs. In this section I test the use of different H_2 molecular lines as SFR tracers. Fig. 3.15a shows the correlation between the H_2 (S(3)) molecular line at 9.67 µm and the SFR determined from the total L_{IR} for the SFG in the GOALS sample. The correlation can be expressed as:

$$\log\left(\frac{\mathrm{SFR}}{\mathrm{M_\odot\,yr^{-1}}}\right) = (0.71 \pm 0.03)\log\left(\frac{\mathrm{L_{S(3)}}}{10^{41}\,\mathrm{erg\,s^{-1}}}\right) + (1.57 \pm 0.02) \tag{3.14}$$

This equation was determined using 168 SFG, with a Pearson r coefficient of r=0.87. Fig. 3.15b shows

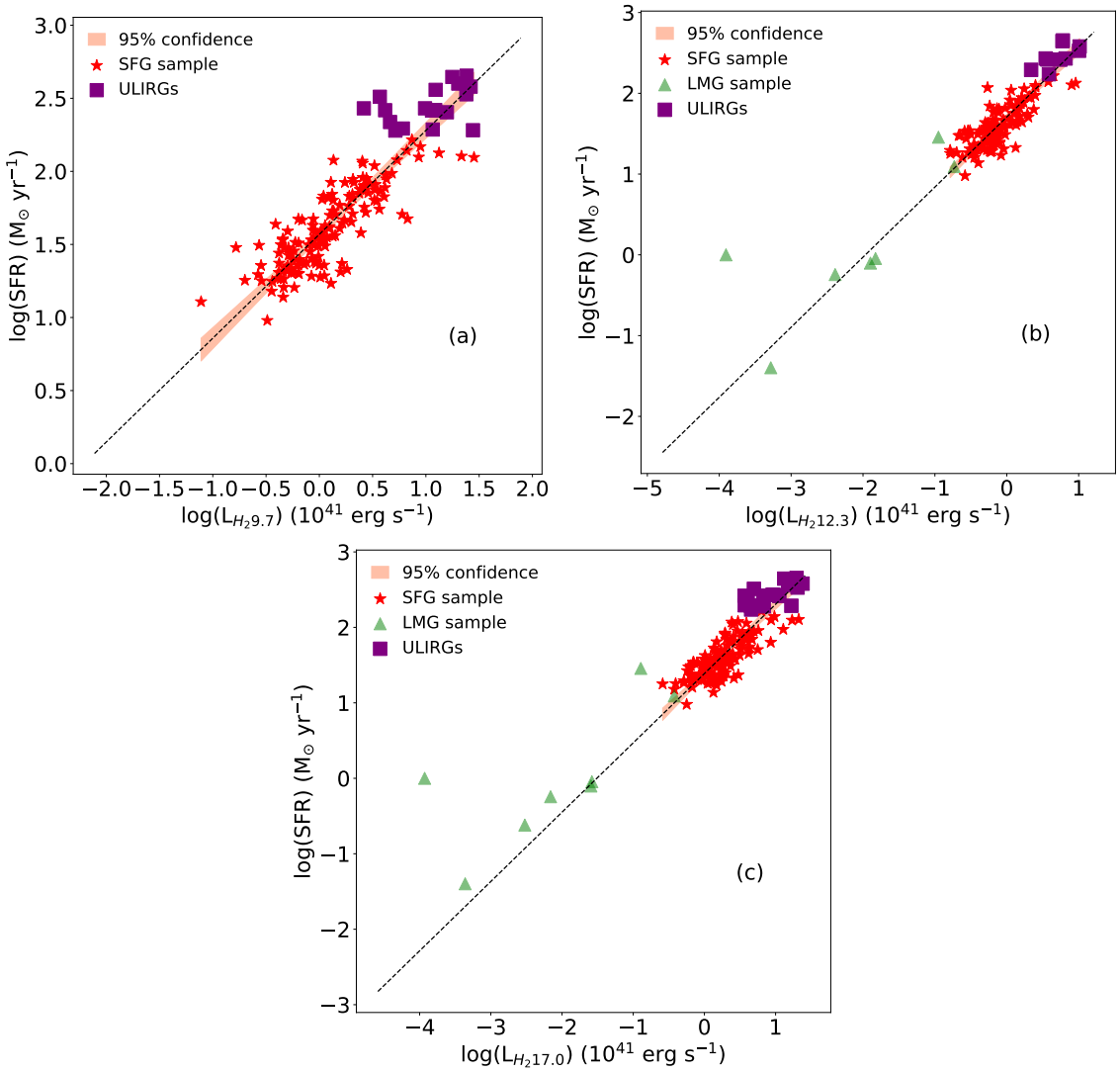

Figure 3.15: (a: top left) Correlation between the H_2 molecular line at 9.67 µm, expressed in units of 10^{41} erg s^{-1} and the SFR derived from the total IR luminosity (black line) for a catalogue of SFG (red star). **(b: top right)** Correlation between the H_2 molecular line at 12.28 µm, expressed in units of 10^{41} erg s^{-1} and the SFR derived from the total IR luminosity (black line) for a catalogue of SFG (red star). The green triangle show LMG detection, not used to derive the correlation. **(c: bottom)** Correlation between the H_2 molecular line at 17.03 µm, expressed in units of 10^{41} erg s^{-1} and the SFR derived from the total IR luminosity (black line) for a catalogue of SFG (red star). In all three figures, the shaded ares shows the 95% confidence interval of the relations. and the purple squares indicate the ULIRG sub-sample in the GOALS catalogue.

the correlation between the H_2 (S(2)) line at 12.28 µm and the SFR, determined with a sample of 126 SFG, with a Pearson coefficient of r=0.86 and expressed by:

$$\log\left(\frac{\mathrm{SFR}}{\mathrm{M_\odot\,yr^{-1}}}\right) = (0.87 \pm 0.04)\log\left(\frac{\mathrm{L_{S(2)}}}{10^{41}\,\mathrm{erg\,s^{-1}}}\right) + (1.71 \pm 0.02) \tag{3.15}$$

Finally, Fig. 3.15c shows the correlation between the H_2 (S(1)) line at 17.03 µm and the SFR, derived from a sample of 154 SFG, with r=0.85 and expressed by:

$$\log\left(\frac{\mathrm{SFR}}{\mathrm{M_\odot\,yr^{-1}}}\right) = (0.92 \pm 0.04)\log\left(\frac{\mathrm{L_{S(1)}}}{10^{41}\,\mathrm{erg\,s^{-1}}}\right) + (1.39 \pm 0.02) \tag{3.16}$$

In Fig. 3.15b and c are also reported, in green, seven detections in LMG of S(2) and S(1), respectively. The LMG sample was not included in the correlation due to the small number of sources, limiting the use of those detections to a comparison of the results. While a good correlation is lacking for the S(1) line, for the S(2) line there is a good agreement between the LMG population and the SFG one. This can be of particular interest in those LMG in which the CO emission is considerably lower than what it would correspond to the estimated SFR, implying the presence of CO-dark molecular gas that is not traced by the CO emission in LMG (Togi & Smith 2016).

The sub-linear slopes obtained for the S(2) and S(3) lines might be linked to the different gas excitation temperature associated with each line. In particular, by moving to higher excitation lines, and thus to shorter wavelengths, the H_2 transitions are originated by an increasingly warmer gas in a thinner layer of the molecular gas clouds. Tracing the warmest material might cause the flattening of the slope, since colder star-forming clouds are not detected by the higher transitions. Additionally, S(2) and S(3) lines could have a larger contribution from other excitation mechanisms, as suggested by the different excitation temperatures measured for these transitions in the Boltzmann diagrams for nearby galaxies (e.g. Tommasin et al. 2010).

The AGN sample was not included in this Section due to the different excitation mechanisms that can contribute to the H_2 rotational lines in these sources, such as shocks or X-ray illumination. For the same reason H_2 lines are also not used as BHAR tracers in Section 3.5, since they respond to the excitation temperature rather than the hardness of the ionizing continuum. This makes quite difficult to establish a clear connection between the line intensities and the SFR or the accreted mass onto the black hole when both contributions are present.

Table 3.4: Correlation between different lines and features and the SFR. For each line/feature is presented the slope of the relation (a) and the intercept (b) and their respective errors, the number of sources used to derive the relation (N), and the Pearson coefficient associated to the relation (r).

Line/feature	a± δa	b± δb	N	r
[CII]158	0.89±0.02	0.62±0.02	227	0.92
[OI]63+[OIII]88	1.25±0.04	0.30±0.04	151	0.94
[NeII]12.8+[NeIII]15.6	0.96±0.03	0.88±0.03	203	0.91
[SIII]18.7+[SIV]10.5	1.04±0.05	1.07±0.06	77	0.90
[NeII]12.8+[SIV]10.5	0.94±0.04	0.85±0.05	77	0.93
[NeIII]15.6+[SIII]18.7	1.03±0.04	1.16±0.04	165	0.86
PAH 6.2	0.76±0.03	0.37±0.04	198	0.87
PAH 11.3	0.73±0.02	0.41±0.03	219	0.89
PAH 6.2+7.7+11.3	1.08±0.10	-1.28±0.23	100	0.66
$H_2$9.67	0.71±0.03	1.57±0.02	168	0.87
$H_2$12.3	0.87±0.04	1.71±0.02	126	0.86
$H_2$17.03	0.92±0.04	1.39±0.02	154	0.85

3.5 BHAR tracers

The lines of [OIV]25.9 µm and the [NeV]14.3,24.3 µm can be used to trace AGN activity, because of their high ionization potential. From the AGN catalogue derived from the 12 µm galaxies sample, I compiled from the literature the 2-10 keV X-rays fluxes corrected for absorption. It is important to note that, while

intense stellar activity can result in X-ray emission, this emission is not comparable with that of an AGN. Limiting the AGN sample to objects with an AGN component at 19µm of at leas 85% ensures that there is no contamination from stellar X-ray emission. I then selected all objects with an hydrogen column density of $N_H \leq 5{\times}10^{23}\,cm^{-2}$, in order to exclude the Compton-thick objects for which the 2-10 keV X-rays are substantially absorbed. Considering this sub-sample, I tested whether the [OIV]25.9µm and [NeV]14.3 and 24.3µm lines can be used as proxies to measure BHAR. The results are presented in the following Sections, and summarized in Table 3.5.

3.5.1 High excitation lines as BHAR tracers: [OIV]$_{25.9\mu m}$

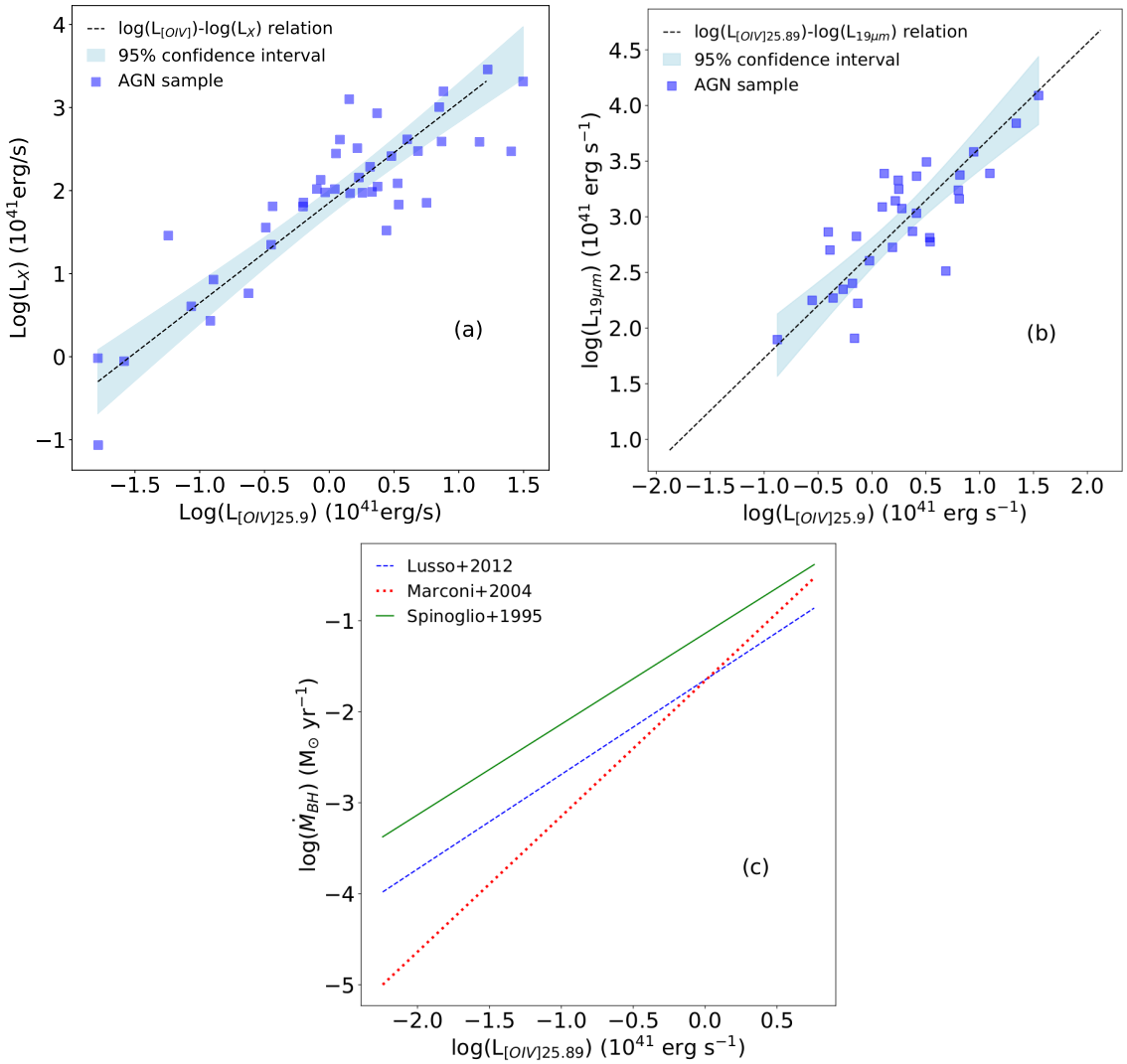

Figure 3.16: (a: top left) Linear correlation between the [OIV]25.9 µm and the 2-10 keV X-ray luminosity. **(b: top right)** Linear correlation between the [OIV]25.9 µm line luminosity and the 19 µm luminosity. All luminosities are expressed in units of 10^{41} erg s^{-1}. **(c: bottom)** Comparison of the three different relations between [OIV]25.9 µm line luminosity and the BHAR: the blue dashed line reports the relation obtained from the Lusso et al. bolometric correction, the red dotted line the relation from the Marconi et al. bolometric correction, and the green solid line the results from the Spinoglio et al. correction.

For the [OIV] line at 25.9µm, the sub-sample of AGN consists of 42 objects. The correlation of this line

luminosity with the 2-10 keV X-ray luminosity, shown in Fig. 3.16a can be expressed as

$$\log\left(\frac{\mathrm{L_X}}{10^{41}\,\mathrm{erg\,s^{-1}}}\right) = (1.21 \pm 0.10)\log\left(\frac{\mathrm{L_{[OIV]25.9}}}{10^{41}\,\mathrm{erg\,s^{-1}}}\right) + (1.85 \pm 0.07) \tag{3.17}$$

with a Pearson correlation coefficient of r=0.87. In order to obtain a measure of the BHAR, it is necessary to convert the luminosity in the 2-10 keV band to the bolometric luminosity of the object, and from there to the BHAR ($\mathrm{L_{AGN}} = \eta\dot{\mathrm{M}}_{\mathrm{BH}}c^2$). Different studies have been carried out to determine the best bolometric correction to apply when considering the 2-10 keV luminosity, with those by Marconi et al. (2004) and Lusso et al. (2012) being the most used in the literature. The resulting bolometric luminosities obtained applying these corrections are different, giving us a range of possible values. Both corrections have been applied to the data, and then from the resulting bolometric luminosities I calculated two linear relations linking the [OIV]25.9 µm line luminosity to the BHAR. Assuming a radiative efficiency of η=0.1, applying the bolometric correction by Lusso et al. leads to the correlation expressed by:

$$\log\left(\frac{\dot{\mathrm{M}}_{\mathrm{BH}}}{\mathrm{M_\odot\,yr^{-1}}}\right) = (1.04 \pm 0.09)\log\left(\frac{\mathrm{L_{[OIV]25.9}}}{10^{41}\,\mathrm{erg\,s^{-1}}}\right) + (-1.65 \pm 0.07) \tag{3.18}$$

with a Pearson correlation coefficient of $r = 0.86$. Applying the bolometric correction by Marconi et al. the correlation between the [OIV]25.9µm line and the BHAR is instead expressed as:

$$\log\left(\frac{\dot{\mathrm{M}}_{\mathrm{BH}}}{\mathrm{M_\odot\,yr^{-1}}}\right) = (1.49 \pm 0.12)\log\left(\frac{\mathrm{L_{[OIV]25.9}}}{10^{41}\,\mathrm{erg\,s^{-1}}}\right) + (-1.66 \pm 0.09) \tag{3.19}$$

This correlation has a Pearson correlation coefficient of $r = 0.87$.

Following the work by Tommasin et al. (2010), I have also analyzed the correlation between the [OIV]25.9 µm line with the luminosity at 19 µm. The luminosity at 19µm ($\mathrm{L_{19\mu m}}$) was used for two main reasons. On one hand, accurate *Spitzer*-IRS observations are available for the 19µm flux density, using two different slit apertures, for the considered sample of galaxies. On the other hand, the 19µm photometry data are the only available accurate photometric data closest to the emission at 12µm. The 12µm emission is, in turn, the best proxy for the bolometric flux of an active galaxy (Spinoglio et al. 1995). In particular, Tommasin et al. (2010) found that the 19µm luminosity correlates with the [NeV]14.3µm line luminosity.

The $\mathrm{L_{19\mu m}}$ has been used by Tommasin et al. to compute the percentage of AGN and starburst components in 51 sources of their sample. Following these results, I selected all sources that present an AGN component at 19 µm equal or above 85%, and for this sub-sample of 35 objects I determined the correlation between the [OIV]25.9 µm line luminosity and the 19µm continuum luminosity. This correlation is shown in Fig. 3.16b, and is expressed as:

$$\log\left(\frac{\mathrm{L_{19\mu m}}}{10^{41}\,\mathrm{erg\,s^{-1}}}\right) = (0.77 \pm 0.10)\log\left(\frac{\mathrm{L_{[OIV]25.9}}}{10^{41}\,\mathrm{erg\,s^{-1}}}\right) + (2.72 \pm 0.06) \tag{3.20}$$

This correlation was calculated using 32 AGN and has a Pearson correlation coefficient of $r = 0.81$. It was then used to determine the bolometric luminosity of the sources, and then the accretion rate. In order to calculate the bolometric luminosity, I used the relation, calculated by Spinoglio et al. (1995), that links the bolometric luminosity to the 12 µm luminosity. The 12 µm luminosity for the sample was determined using data from Deo et al. (2009): the authors report continuum measurements at 5.5 µm, 14.7 µm and 20 µm taken from *Spitzer* low-resolution spectroscopic observations. Where possible, I interpolated the continuum slope

and the 12 µm continuum flux using the 5.5 µm and 14.7 µm measurements, otherwise (but only in three cases) using the extrapolation from the 14.7 µm and 20 µm fluxes. I then matched the Deo et al. sample with the Tommasin et al. sample, calculated the bolometric luminosity starting from the monochromatic 12 µm luminosity for those sources with a 85% AGN component. Similarly to what has been done for the 2-10 keV luminosity, I determined the BHAR starting from the bolometric luminosity derived from the 12 µm luminosity. The sub-sample of AGN is composed of 26 objects, and yields a relation shown in Fig. 3.16c and expressed as:

$$\log\left(\frac{\dot{M}_{BH}}{M_{\odot}\,yr^{-1}}\right) = (0.67 \pm 0.15)\log\left(\frac{L_{[OIV]25.9}}{10^{41}\,erg\,s^{-1}}\right) + (-1.14 \pm 0.07) \tag{3.21}$$

with a Pearson correlation coefficient of $r = 0.68$. The reduced number of objects is due to the lack of data for the determination of the continuum at 12 µm.

3.5.2 High excitation lines as BHAR tracers: [NeV]$_{14.3,24.3\mu m}$

The same process applied to the [OIV] line can be also applied to the [NeV]14.3 and [NeV]24.3µm lines. For the [NeV]24.3µm line the sub-sample of AGN galaxies with a hydrogen column density of $N_H \leq 5{\times}10^{23}\,cm^{-2}$ is composed of 34 objects. This is due to the fainter luminosity of the [NeV] line, which is harder to detect than the [OIV] line. The correlation between the [NeV]24.3 line with the 2-10 keV X-ray luminosity, shown in Fig. 3.17a, is described by the equation:

$$\log\left(\frac{L_X}{10^{41}\,erg\,s^{-1}}\right) = (0.95 \pm 0.11)\log\left(\frac{L_{[NeV]24.3}}{10^{41}\,erg\,s^{-1}}\right) + (2.40 \pm 0.08) \tag{3.22}$$

with a Pearson coefficient of r=0.84. Applying the bolometric correction by Lusso et al. (2012), the linear correlation between the line luminosity and the BHAR can be described as:

$$\log\left(\frac{\dot{M}_{BH}}{M_{\odot}\,yr^{-1}}\right) = (1.06 \pm 0.12)\log\left(\frac{L_{[NeV]24.3}}{10^{41}\,erg\,s^{-1}}\right) + (-1.11 \pm 0.09) \tag{3.23}$$

with a Pearson correlation coefficient of $r = 0.83$. The bolometric correction by Marconi et al. (2004) leads instead to a correlation with a Pearson correlation coefficient of $r = 0.84$ and described by the equation:

$$\log\left(\frac{\dot{M}_{BH}}{M_{\odot}\,yr^{-1}}\right) = (1.47 \pm 0.15)\log\left(\frac{L_{[NeV]24.3}}{10^{41}\,erg\,s^{-1}}\right) + (-0.89 \pm 0.11) \tag{3.24}$$

When considering the 19µm continuum luminosity, the correlation with the [NeV]24.3µm line was determined using 30 objects, has a Pearson correlation coefficient of $r = 0.85$, and is described by the equation:

$$\log\left(\frac{L_{19\mu m}}{10^{41}\,erg\,s^{-1}}\right) = (0.81 \pm 0.10)\log\left(\frac{L_{[NeV]24.3}}{10^{41}\,erg\,s^{-1}}\right) + (3.12 \pm 0.06) \tag{3.25}$$

When deriving the 12µm continuum luminosity, the lack of data needed to extrapolate the $L_{12\mu m}$ reduced the sample to 24 objects. The correlation between the [NeV] line luminosity and the BHAR derived from the 12µm luminosity has a Pearson correlation coefficient of $r = 0.71$ and is described by the equation:

$$\log\left(\frac{\dot{M}_{BH}}{M_{\odot}\,yr^{-1}}\right) = (0.77 \pm 0.16)\log\left(\frac{L_{[NeV]24.3}}{10^{41}\,erg\,s^{-1}}\right) + (-0.77 \pm 0.10) \tag{3.26}$$

Finally, for the [NeV]14.3µm line, starting from the total sample of Tommasin et al. (2010, 2008),

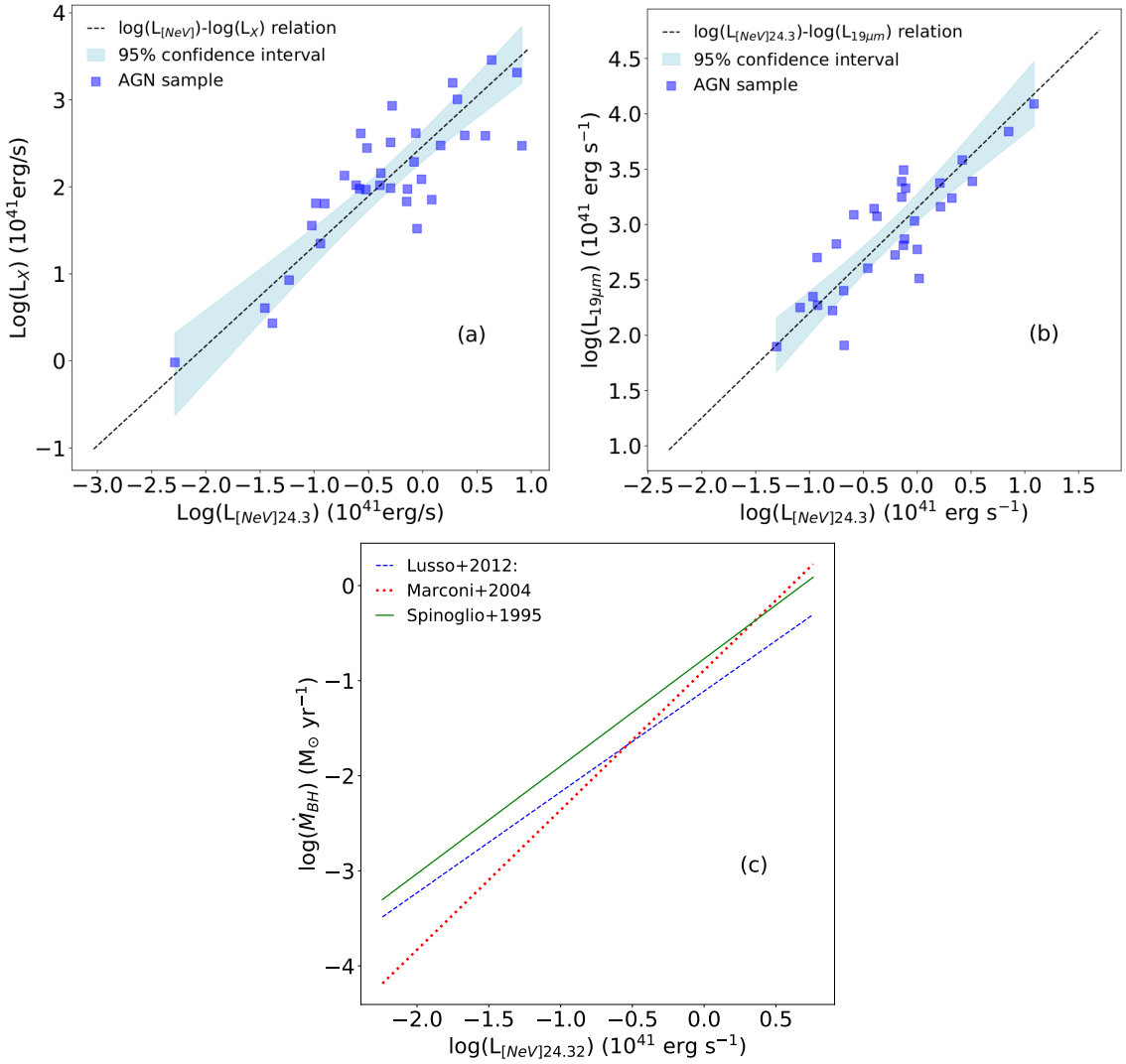

Figure 3.17: (a: top left) Linear correlation between the [NeV]24.3 µm line luminosity and the 2-10 keV X-ray luminosity. **(b: top right)** Linear correlation between the [NeV]24.3 µm line luminosity and the 19 µm luminosity, expressed in units of 10^{41} erg s^{-1}. **(c: bottom)** Comparison of the three different relations between [NeV]24.3 µm line luminosity and the BHAR: the blue dashed line reports the relation obtained from the Lusso et al. bolometric correction, the red dotted line the relation from the Marconi et al. bolometric correction, and the green solid line the results from the Spinoglio et al. correction.

excluding Compton-thick objects leavs a sample of 38 objects. The correlation between the [NeV]14.3 µm line luminosity and the 2-10 keV X-ray luminosity is shown in Fig 3.18a and is expressed by the equation:

$$\log\left(\frac{\mathrm{L_X}}{10^{41}\,\mathrm{erg\,s^{-1}}}\right) = (1.11 \pm 0.13)\log\left(\frac{\mathrm{L_{[NeV]14.3}}}{10^{41}\,\mathrm{erg\,s^{-1}}}\right) + (2.58 \pm 0.10) \tag{3.27}$$

with a Pearson correlation coefficient of r =0.79. From this result, I then apply the bolometric corrections by Marconi et al. (2004) and Lusso et al. (2012) to the 2-10 keV X-ray luminosity, in order to obtain the bolometric luminosity of the AGN. From the bolometric luminosities I then calculate the linear correlation linking the [NeV]14.3 µm line luminosity to the BHAR, with $\mathrm{L_{AGN}} = \eta\dot{\mathrm{M}}_{\mathrm{BH}}c^2$. Assuming a radiative efficiency of $\eta = 0.1$, I report in equation 3.28 the linear correlation applying the bolometric correction from Lusso et al. (2012), and in equation 3.29 the one applying the Marconi et al. (2004) bolometric correction,

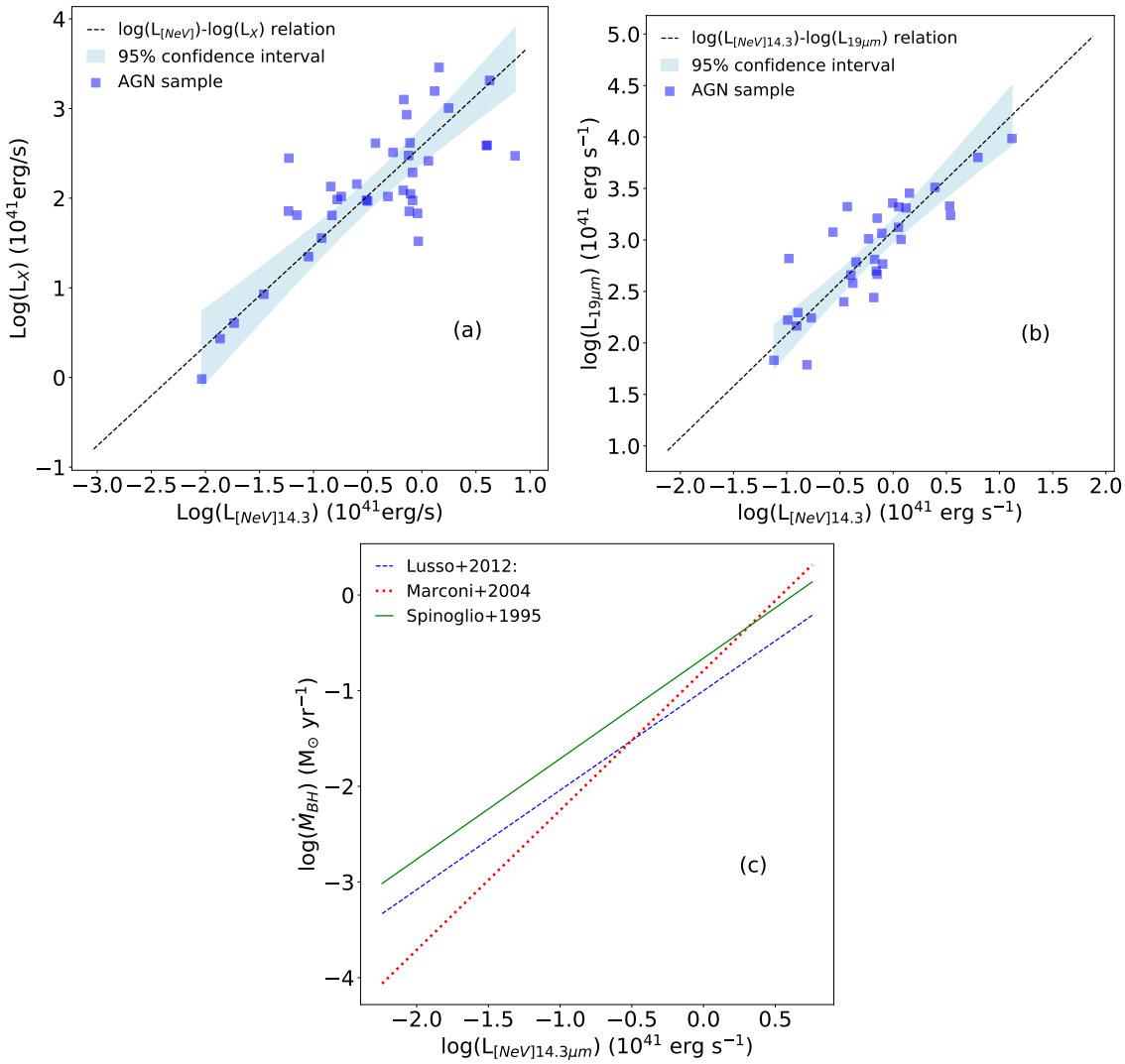

Figure 3.18: (a: top left) Linear correlation between the [NeV]14.3 µm and the 2-10 keV X-ray luminosity. Blue squares show the AGN sample, and the shaded area shows the 95% confidence interval for the relation.**(b: top right)** Linear correlation between the [NeV]14.3 µm line luminosity and the 19 µm luminosity. **(c: bottom)** Comparison between the [NeV]14.3 µm line luminosity and the BHAR derived from the bolometric correction by Spinoglio et al. (green solid line), Marconi et al. (red dotted line) and Lusso et al. (blue dashed line).

and the relative Pearson correlation coefficients r:

$$\log\left(\frac{\dot{M}_{BH}}{M_{\odot}\,yr^{-1}}\right) = (1.04 \pm 0.13)\log\left(\frac{L_{[NeV]14.3}}{10^{41}\,erg\,s^{-1}}\right) + (-1.0 \pm 0.10),\ r = 0.76 \tag{3.28}$$

$$\log\left(\frac{\dot{M}_{BH}}{M_{\odot}\,yr^{-1}}\right) = (1.49 \pm 0.13)\log\left(\frac{L_{[NeV]14.3}}{10^{41}\,erg\,s^{-1}}\right) + (-0.73 \pm 0.17),\ r = 0.78 \tag{3.29}$$

I have then analyzed the correlation between the [NeV]14.3 µm line with the luminosity at 19 µm following the work by Tommasin et al. (2010). I selected only those sources with an AGN component at 19 µm equal or above 85%, obtaining a sub-sample of 32 objects. The correlation between the [NeV]14.3 µm line luminosity and the 19 µm luminosity is shown in Fig. 3.18b, and is expressed by:

$$\log\left(\frac{L_{19}}{10^{41}\,erg\,s^{-1}}\right) = (1.01 \pm 0.10)\log\left(\frac{L_{[NeV]14.3}}{10^{41}\,erg\,s^{-1}}\right) + (3.09 \pm 0.06) \tag{3.30}$$

with a Pearson correlation coefficient of $r = 0.85$. I then calculate the bolometric luminosity from the monochromatic 12 µm luminosity extracted from Deo et al. (2009) using the relation by Spinoglio et al. (1995). From the bolometric luminosity I determine the BHAR and its relation to the [NeV]14.3 µm line luminosity, obtaining:

$$\log\left(\frac{\dot{M}_{BH}}{M_{\odot}\,yr^{-1}}\right) = (1.05 \pm 0.19)\log\left(\frac{L_{[NeV]14.3}}{10^{41}\,erg\,s^{-1}}\right) + (-0.66 \pm 0.11) \tag{3.31}$$

for a sample of 26 objects, with a Pearson correlation coefficient of $r = 0.68$. The small number of objects used to derive this relation is due to the lack of data for the determination of the continuum at 12 µm.

As a general trend, all three lines correlate linearly with the 2-10 keV X-ray luminosity, thus providing a good proxy to measure the AGN activity, as shown in Fig. 3.16a, 3.17a and 3.18a.

Measuring the BHAR requires important approximations in terms of bolometric correction, which can yield significantly different results. Between the three proposed bolometric corrections, the correlations obtained when applying the Marconi correction are steeper than those obtained from the Lusso and Spinoglio correction. In particular, Fig. 3.16c, 3.17c and 3.18c show the comparison of the different bolometric corrections: the results derived from the corrections of Spinoglio et al. (1995) and Lusso et al. (2012) show a similar, flatter slope, indicating, within the errors, the expected linear relation between the line tracers and the BHAR. It is important to note that the Marconi et al. and Lusso et al. bolometric corrections are based on a third-degree polynomial transformation of the X-ray luminosity. This necessarily leads to deviations from the slopes obtained in Eq. 3.17, 3.22 and 3.27.

Table 3.5: Coefficients of the correlations between line luminosity and BHAR. For each line are reported the results for the three different correction used to obtain the BHAR, and for each calibration are indicated the slope (a) and intercept (b) of the correlation with the relative errors, the number of objects used to derive the correlation (N) and the best-fit coefficient of determination (r).

Line	Marconi correction				Lusso correction				Spinoglio correction			
	a± δa	b± δb	N	r	a± δa	b± δb	N	r	a± δa	b± δb	N	r
[NeV]14.3	1.49±0.13	-0.73±0.17	38	0.78	1.04±0.13	-1.0±0.10	38	0.76	1.05±0.19	-0.66±0.11	32	0.68
[NeV]24.3	1.47±0.15	-0.89±0.11	34	0.84	1.06±0.12	-1.11±0.09	34	0.83	0.77±0.16	-0.77±0.10	24	0.71
[OIV]25.9	1.49±0.12	-1.66±0.09	42	0.87	1.04±0.09	-1.65±0.07	42	0.86	0.67±0.15	-1.14±0.07	26	0.68

3.5.3 Mid-ionization lines as BHAR tracers: [NeIII]$_{15.6\mu m}$, [SIV]$_{10.5\mu m}$

While high ionization lines are preferential tracers for AGN activity, mid-ionization lines, are partially affected by AGN activity, and could in theory be used as tracers for the BHAR. For this reason, I have tested two mid-ionization lines, namely the [SIV] 10.5µm line, and the [NeIII]15.6µm line, to evaluate their use as tracers for the X-ray luminosity in the 2-10 keV interval. Starting from the sample of Tommasin et al. (2010, 2008), I again exclude all Compton-thick objects and obtain a sub-sample of 44 objects for the [NeIII] line, and of 39 objects for the [SIV] line. Fig. 3.19a shows the correlation between the [NeIII] line luminosity and the 2-10 keV X-ray luminosity, expressed as:

$$\log\left(\frac{\mathrm{L_X}}{10^{41}\,\mathrm{erg\,s^{-1}}}\right) = (2.20 \pm 0.10) + (1.33 \pm 0.13)\log\left(\frac{\mathrm{L_{[NeIII]15.6}}}{10^{41}\,\mathrm{erg\,s^{-1}}}\right) \tag{3.32}$$

The correlation of the [SIV]10.5 µm line with the 2-10 keV X-ray luminosity, shown in Fig. 3.19b, can be expressed as:

$$\log\left(\frac{\mathrm{L_X}}{10^{41}\,\mathrm{erg\,s^{-1}}}\right) = (2.51 \pm 0.09) + (0.98 \pm 0.10)\log\left(\frac{\mathrm{L_{[SIV]10.5}}}{10^{41}\,\mathrm{erg\,s^{-1}}}\right) \tag{3.33}$$

For both correlations, I found a low Pearson correlation coefficient, equal to $r = 0.63$, lower than the values found for [OIV] ($r = 0.87$) and the [NeV] lines ($r = 0.79$ and $r = 0.84$, for the 14.3µm and 24.3µm lines, respectively). This suggests that, while mid-ionization lines can correlate with the X-ray luminosity, they may suffer from contributions due to star formation activity, and thus are far less reliable as BHAR proxies. In particular, LMG, even more than SFG, might have a significant contamination of the [SIV] and [NeIII] lines from the stellar population, as shown by the LMG in our sample (See Figs. 3.7 for the [NeIII]15.6µm line and Fig. 2c) for the [SIV]10.5µm line, in contrast with the [OIV] and [NeV] lines.

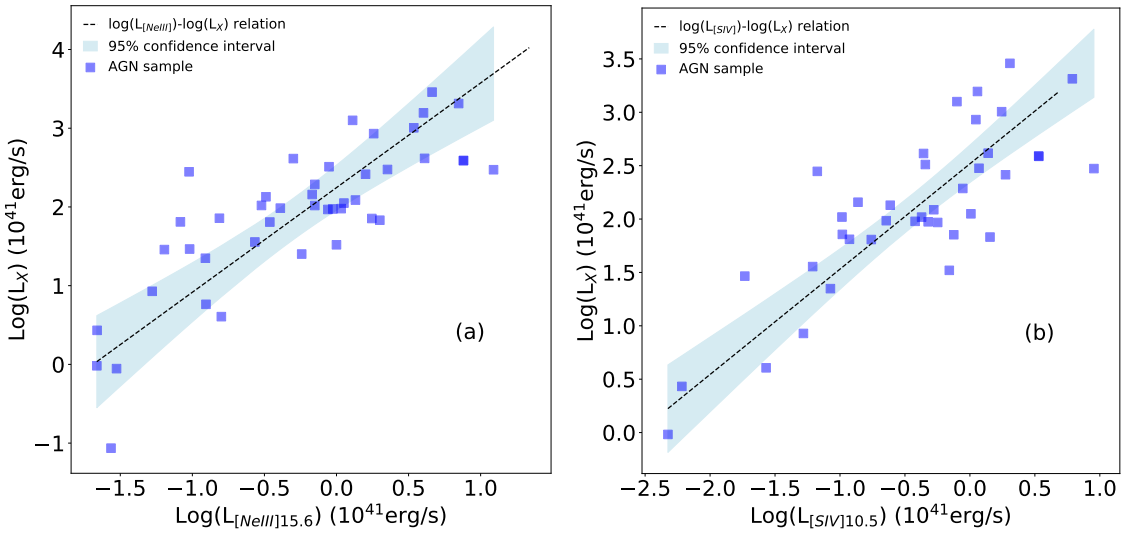

Figure 3.19: (a: left) Linear correlation between the [NeIII]15.6 µm and the 2-10 keV X-ray luminosity. Blue squares show the AGN sample, and the shaded area shows the 95% confidence interval for the relation. **(b: right)** Linear correlation between the [SIV]10.5 µm and the 2-10 keV X-ray luminosity

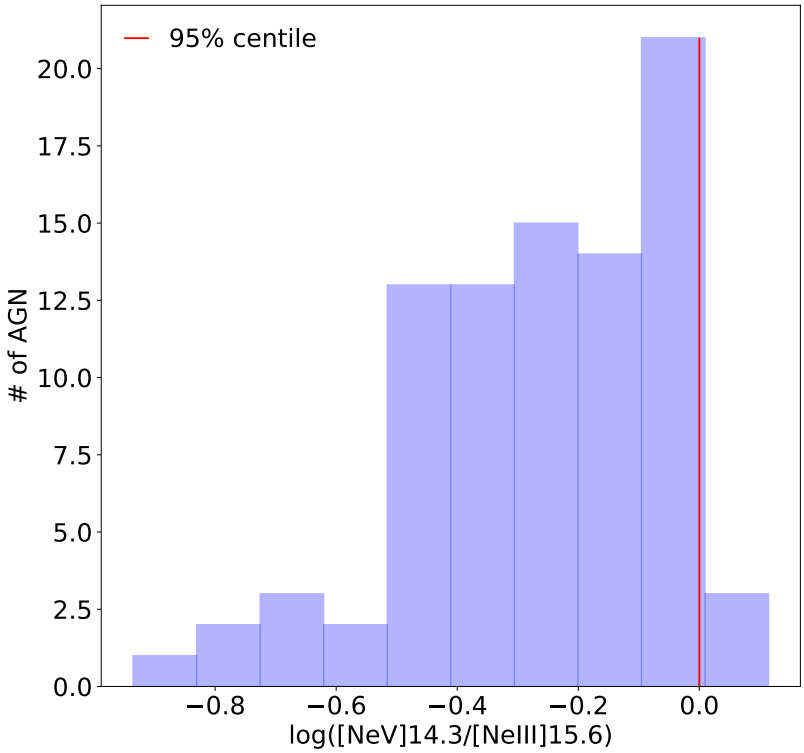

Figure 3.20: Histogram of the logarithm of the [NeV]14.3 to [NeIII]15.6μm line for the Tommasin et al. (2010) AGN sample. The vertical red line shows the 95% percentile of the distribution.

3.6 Discussion

3.6.1 Application to composite objects

The coexistence of AGN and star formation in galaxies is well known (see, e.g. Pérez-Torres et al. 2021, for a review) and therefore it should be expected that many galaxies are characterized by both components at work together. In general, when considering composite objects, with both a SF and an AGN component detectable, the results presented in Section 3.4 and Section 3.5 can still be applied.

It is possible, in a composite object, to estimate what phenomenon is predominant as the main energy contributor to a galaxy. The presence of a high ionization line, produced by AGN activity, and of a mid-ionization line of the same species, that can be produced by both AGN and star formation activity, would allow to determine the fraction of one component over the other. Fig.3.20 shows the [NeV]14.3 to [NeIII]15.6 ratio in the Tommasin et al. (2010) AGN sample. The 95% percentile of the distribution is located at log([NeV]/[NeIII])~-0.04. An higher ratio implies that the AGN component completely dominates the galaxy, while lower ratios indicate an increasingly predominant star formation component.

I have used the GOALS sample to determine whether the results on the SFR tracers can be applied to composite objects (Section 3.4). The GOALS sample is composed of SFG, but for part of the sample an AGN component is also present, if not always detected. When determining the calibrations presented in Section 3.4, I have excluded all sources for which a [NeV] emission line is detected, in order to exclude all possible effects due to AGN activity, either on the line luminosity, or on the total IR luminosity. In this Section, instead, I consider all objects present in the sample, independently of classification. In Fig. 3.21 I plot the ratio of the SFR obtained using the [NeII]+[NeIII] tracer to the SFR obtained using the 11.3μm PAH feature, as a function of the Equivalent Width (EW) of the PAH feature at 6.2μm, as determined by Stierwalt

et al. (2014). The mean ratio for the entire population is -0.049, with the median value equal to -0.023 and 50% of the sample included in the [-0.18, 0.06] interval. While there is some dispersion around zero, for the majority of the sample I obtain a similar SFR whether the [NeII]+[NeIII] tracer or the PAH tracer was used. This suggests that for mixed objects these two tracers are equivalent, and independent of the presence of an AGN. Significant differences are observable for the extreme objects in the sample: the sources with the larger AGN content are located in the top left corner, for which the SFR obtained using the [NeII]+[NeIII] tracer is significantly higher than the SFR obtained using the PAH. This is plausibly due to an increase of the [NeIII] emission related to the presence of the AGN.

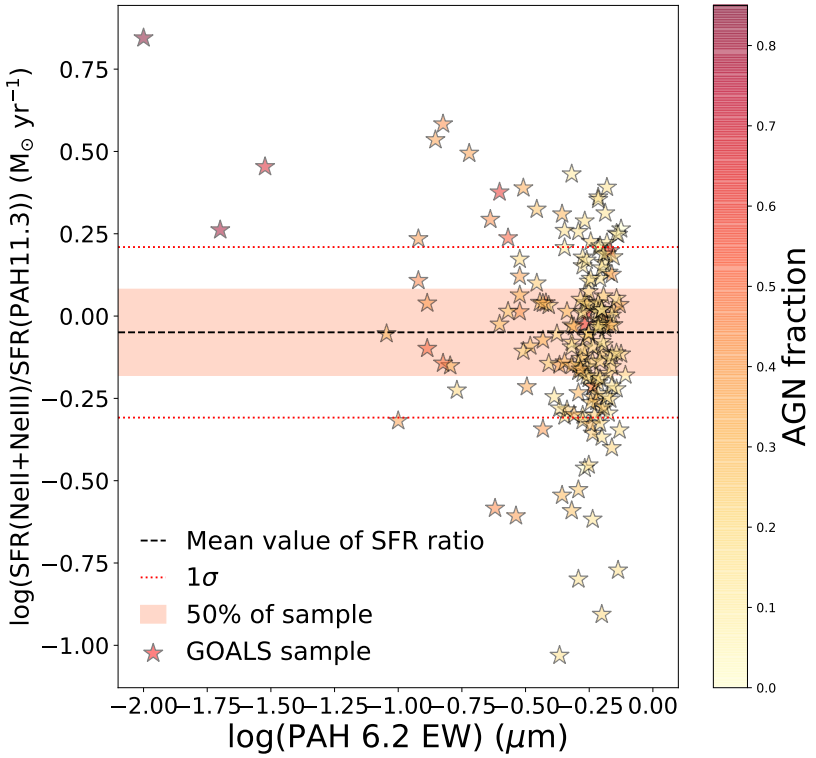

Figure 3.21: Comparison of the ratio between the SFR obtained using the [NeII]+[NeIII] tracer and the SFR obtained using the PAH feature at 11.3μm, against the EW of the PAH feature at 6.2μm for the GOALS sample. The color gradient indicates the percentage of the AGN component in each object as determined by mid-IR tracers (Díaz-Santos et al. 2017). The black dashed line shows the mean value of the SFR ratio for the population, with the shaded area indicating where the 50% of the entire sample is located. The red dotted lines represent the 1σ interval around the mean value.

3.6.2 Comparison among the various tracers

Summarizing the results presented in Section 3.4, among the various SFR tracers presented, for galaxies dominated by SF processes the best tracers are the [CII]158μm line (slope $\alpha = 0.89 \pm 0.02$ and correlation coefficient $r = 0.92$) or the combination of the [OI] and [OIII] lines (slope $\alpha = 1.25 \pm 0.04$ and $r = 0.94$) for high-redshift galaxies observed from the ground with sub-millimeter telescopes. For galaxies observed from space or airborne facilities (but also from the new generation of the very large optical ground based telescopes in the 8-13μm atmospheric window, for local galaxies), the best SFR tracers are the combination of the [NeII] and [NeIII] lines (slope $\alpha = 0.96 \pm 0.03$ and $r = 0.91$) or the combination of the other mid-IR fine-structure lines. For galaxies containing an AGN, the PAH features can reliably be used and the PAH 11.3μm feature is probably the best SFR tracer (slope $\alpha = 0.75 \pm 0.04$ and $r = 0.79$). As an alternative, the

[NeII] and [NeIII] lines can still be used also in AGN, with the correction to the total neon flux that can be computed using one of the [NeV] lines, as suggested by Zhuang et al. (2019).

When measuring the BHAR, following the results presented in Section 3.5, the [NeV] lines at 14.3 and 24.3μm are exclusive probes of AGN activity, because their emission is a direct signature of the hard ionizing spectrum due to the accretion process. However, these lines are fainter than the [OIV]25.9μm line, which can be detected more easily in faint objects. When using the [OIV] line as a BHAR tracer, it is important to keep into account the possible contamination due to SF processes, because its emission can be attributed also, to some extent, to starburst activity (Lutz et al. 1998).

3.6.3 Metallicity and SFR tracers

In Section 3.4.1 the [CII]-SFR relation was revised for a wide galaxy sample, from LMG to extreme ULIRGs. In Section 3.4.3 I derive a measure of the SFR through the neon and sulfur mid-IR lines and propose new SFR tracers using different combinations of these lines. In this section I discuss the possible effects that metallicity, and the associated changes in the ISM of these galaxies, may have on these tracers.

First of all, for the sample of dwarf galaxies, the adopted SFR values are derived from the observed H_α luminosity and corrected from the total IR luminosity (Rémy-Ruyer et al. 2015). This is motivated by the underestimation of the SFR by the IR luminosity at very low metallicities ($12 + \log(\mathrm{O/H}) \lesssim 8.5$; Lee et al. 2013), due to the lower metal abundance in these galaxies compared to SFG. In principle, the lower dust to gas ratio of LMG should also have an impact on the observed intensities of the fine-structure lines. This is, however, balanced by the higher cooling rates in these transitions, as discussed by De Looze et al. (2014).

Fig. 3.10a shows that the [CII]$158\,\mu\mathrm{m}$ emission in LMG follows the trend found in SFG with no need to perform any additional correction for metallicity in these galaxies. Similarly, the different combinations of [NeII]$12.8\,\mu\mathrm{m}$, [NeIII]$15.6\,\mu\mathrm{m}$, [SIII]$18.7\,\mu\mathrm{m}$, and [SIV]$10.5\,\mu\mathrm{m}$, shown in Figs. 3.10 and 3.12, follow the correlation of solar-like metallicity galaxies. The higher cooling rates in LMG are particularly evident when the neon and sulfur transitions are considered. While the [NeII]$12.8\,\mu\mathrm{m}$ emission in LMG scales with $\mathrm{L_{IR}}$ similarly as for SFG (Fig. 3.7a), the [NeIII]$15.6\,\mu\mathrm{m}$ line becomes comparatively much brighter for a given IR luminosity, more than one order of magnitude above the correlation found for SFG, as can also be seen by the value of the constant *b* in the best fit equation for the [NeIII]15.6 μm line in Table 3.1. When considering the sulfur lines, this effect is even more pronounced (see Fig. 4b for the [SIII]18.7μm line correlation, Fig. 6a for the [SIII]33.4μm line correlation and Table 3.1). This means that mid- to high-ionization species such as Ne^{2+} or S^{3+} trace a contribution to the star-formation that is not revealed by either the Ne^{+} and S^{2+} low-ionization gas or the IR emission. Thus, the combination of low and high-ionization lines allows us to trace the total star formation in both low- and solar-metallicity galaxies (Ho & Keto 2007; Zhuang et al. 2019).

In the case of the [CII]158 μm line, the Fig. 3.10a suggests that this transition still remains a dominant coolant of the ISM at low metallicities. Given its low ionization potential (11.3 eV, see Table 3.1), this line can originate from both neutral and ionized gas, and one could expect a decreasing contribution from the neutral component as the ionization field becomes harder at low metallicities. However, Cormier et al. (2019) demonstrated that the PDR contribution to the global [CII]$158\,\mu\mathrm{m}$ emission is still dominant for the same LMG sample used in this work. This is also in line with the results of Croxall et al. (2017), suggesting that the [CII]$158\,\mu\mathrm{m}$ emission linked to ionized gas is of the order of $\sim 10\%$ in LMG, and up to maximum $< 40\%$ where a high-U is required. Moreover, analytical models developed in these studies show a decrease of [CII] emission from ionized gas with decreasing metallicity with $\sim 55-75\%$ of the [CII] emission arising

from PDRs in LMG, reaching almost 100% when the metallicity decreases below 1/4 $Z_{\odot}$. Additionally, the thickness of the [CII] layer increases for molecular clouds exposed to the harder radiation fields typical of LMG. This is shown by the detection of higher [CII]/CO(1-0) ratios in local LMG when compared to SFG with solar or super-solar metallicity (e.g. Hunter et al. 2001; Madden 2000; Madden et al. 1997), and it is supported by PDR models (Bolatto et al. 1999; Röllig et al. 2006).

While a detailed study of the ionized gas and PDR structure is out of the scope of this thesis, the results discussed above suggest that both [CII]158 μm and the different combinations of neon and sulphur lines are robust star formation tracers, virtually independent of dust extinction, that can be applied to a wide diversity of environments with different physical conditions and metallicities. Specifically, the variations expected from the changes in the chemical abundances are mostly balanced by the increase in the cooling rates of these transitions.

3.6.4 Comparison with previous line calibrations

In this Section, I compare the results of the line calibrations obtained in this work with those of Spinoglio et al. (2012, 2014) and Gruppioni et al. (2016). It is important to note that in this work the correlations were derived using the orthogonal distance regression method, instead of the least-squares minimization method, which was used by the other authors, because I consider the total IR luminosity and the line luminosity as two independent variables.

The AGN sample used in this work and in Spinoglio et al. is the same for the lines in the 10-35 μm interval, and the differences in the correlation are only due to the different methods of analysis. In this work, in order to obtain a correlation between the total L_{IR} and the [OIV]25.9 μm line luminosity that better represents the AGN population, I did not use the entire sample of AGNs by Tommasin et al. (2010, 2008), but a sub-sample of objects with an AGN component in the 19 μm luminosity of at least 85% (see Section 3.3.1).

For the SFG sample, while in Spinoglio et al. the sample of galaxies described by Bernard-Salas et al. (2009) was used, in this work the same sample was expanded by including the LIRGs and ULIRGs sample of GOALS, as described in Section 3.2. Nonetheless, I obtain comparable results, except in the cases of the PAH feature at 11.3 μm and of the H_2 line at 17.03 μm, for which my results show line luminosities an order of magnitude higher. This is due to the presence, in the GOALS sample, of LIRGs and ULIRGs, which shift the relation toward a steeper slope.

The results for the fine structure lines in the 50-160μm spectral interval obtained by Spinoglio et al. are derived using an heterogeneous sample of both AGN and SFG. In this work, I maintain instead the division in three classes of galaxies. When comparing the results, I consider the calibrations obtained by Spinoglio et al. and compare them to the results for AGN and SFG obtained for this work. For the analysis in this section, I apply to my samples the ordinary least square method, which was also used in Spinoglio et al. to derive their correlations. Fig 3.22 shows the comparison for the [OIII]52μm, [NIII]57μm and [OI]63μm lines, Fig 3.23 shows the comparison for the [OIII]88μm, [NII]122μm and [OI]145μm lines, and Fig. 3.24 shows the comparison for the [CII]158μm line.

When compared to our AGN sample, the results are consistent within the errors, except for the [NII]57μm and [OIII]88μm lines, where the slopes are comparable within 2σ of each other. If compared to the SFG results, I obtain results comparable within the errors except for [OIII]88μm and [NII]122μm lines, for which the slopes are comparable within 2σ of each other.

For the comparison with Gruppioni et al., I take advantage of the published catalogue and apply the orthogonal distance regression to the sample presented by the authors. Gruppioni et al. presented a sample

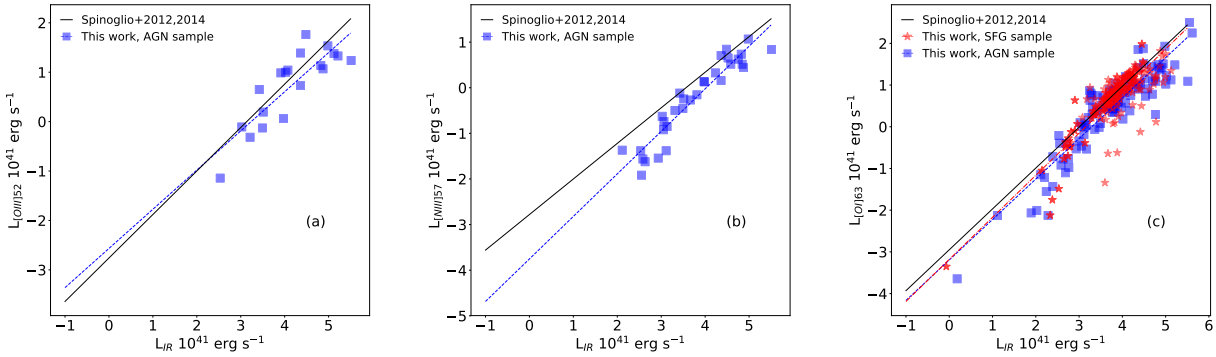

Figure 3.22: (a: left) The [OIII]52µm line luminosity versus the total IR luminosity. **(b: center)** The [NIII]57µm line luminosity versus the total IR luminosity. **(c: right)** The [OI]63µm line luminosity versus the total IR luminosity. In the figures, Blue squares represent AGN while red stars show the SFG sample. The dashed blue line represents the linear he dot-dashed red line the relation for SFG, and the black solid line the relation shows the relation obtained by Spinoglio et al. (2012, 2014).

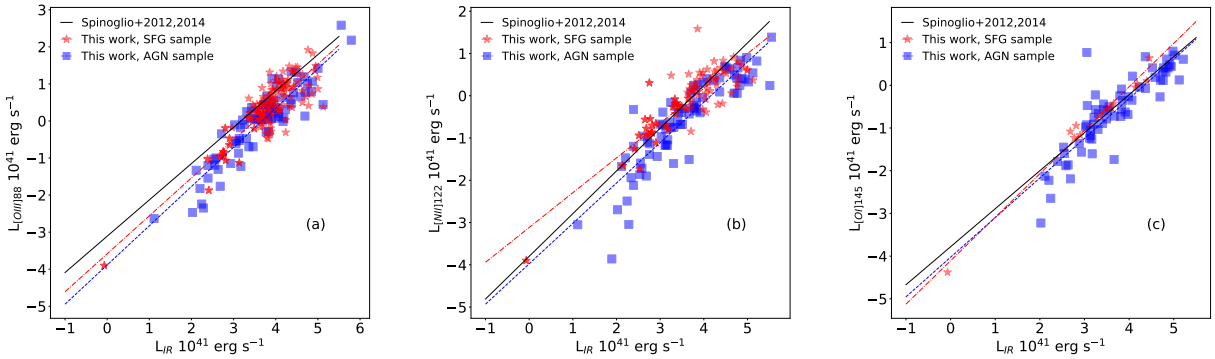

Figure 3.23: (a: left) The [OIII]88µm line luminosity versus the total IR luminosity. **(b: center)** The [NII]122µm line luminosity versus the total IR luminosity. **(c: right)** The [OI]145µm line luminosity versus the total IR luminosity. The same legend as in Fig. 3.22 was used.

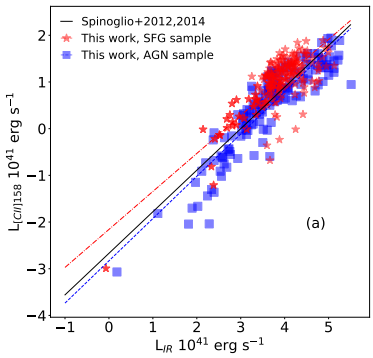

Figure 3.24: (a:) The [CII]158µm line luminosity versus the total IR luminosity. The same legend as in Fig. 3.22 was used.

of 76 AGN, divided in two sub-samples depending on the fraction of 5-40µm luminosity produced by the active nucleus [$f_{\rm AGN}(5-40\mu m)$]. In particular, there are 30 objects with $f_{\rm AGN}(5-40\mu m) \leq 0.4$ and 43 objects with $f_{\rm AGN}(5-40\mu m) > 0.4$.

Figs. 3.25-3.28 show the comparison for the relations calculated for the $f_{\rm AGN}$(5-40 µm)> 0.4 sub-sample, and Figs. 3.29-3.32 show the comparison for the relations calculated for the $f_{\rm AGN}$(5-40 µm)≤ 0.4 sub-sample.

As a general trend, my sample of AGN and the sample by Gruppioni et al. occupy the same region in the $L_{\rm IR}$-L_{line} space. While the data to calculate the correlations were available in the literature, Gruppioni et al. only present the correlations for [NeV]14.3, 24.3µm, [NeIII]15.6µm and [OIV]25.9µm for the $f_{\rm AGN}$(5-40 µm)> 0.4 sub-sample. For these relations, my results show steeper slopes, but consistent within 3σ of each other.

For the $f_{\rm AGN}$(5-40 µm)≤ 0.4 sub-sample, there is a better agreement between the relations, which are comparable within the errors. A significant difference in slope is present for the [NeV]24.3µm line, for which the relations are comparable within 3σ, and for the [SIV]10.5µm line, comparable within 2σ.

When comparing the results obtained using the Gruppioni et al. sample with the results obtained using the SFG sample, I find comparable results only for the PAH features for the $f_{\rm AGN}$(5-40 µm)> 0.4, and for all lines in the $f_{\rm AGN}$(5-40 µm)≤ 0.4 sub-sample, excluding the [SIV]10.5µm and [OIV]25.9µm lines.

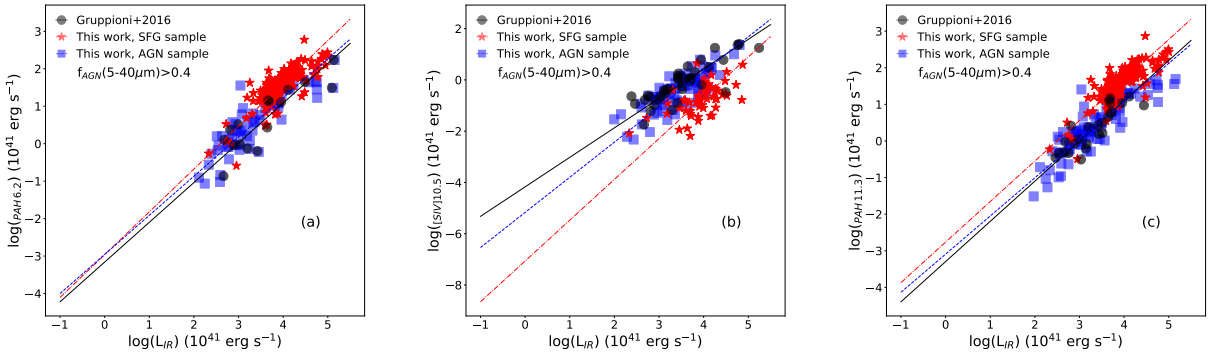

Figure 3.25: (a: left) The PAH 6.2µm luminosity versus the total IR luminosity. Blue squares represent AGN, red stars SFG and black circles are the sample by Gruppioni et al. (2016). The dashed blue line represents the linear relation for AGN, the dot-dashed red line the relation for SFG, and the black solid line the relation for the Gruppioni et al. sample. **(b: center)** The [SIV]10.5µm luminosity versus the total IR luminosity. **(c: right)** The PAH 11.3µm luminosity versus the total IR luminosity. In all three figures, the Gruppioni et al. sample was limited to AGN fractions > 0.4 in the 5-40µm spectral interval (see **Sect.**3.6.4).

I do not compare our results with those obtained by Bonato et al. (2019), since the methods of analysis are widely different. In particular, while in this work the line luminosities are calibrated leaving the slope of the correlations as a free parameter, in Bonato et al. the slope of the relation was fixed to unity, thus giving raise to substantial differences in the results.

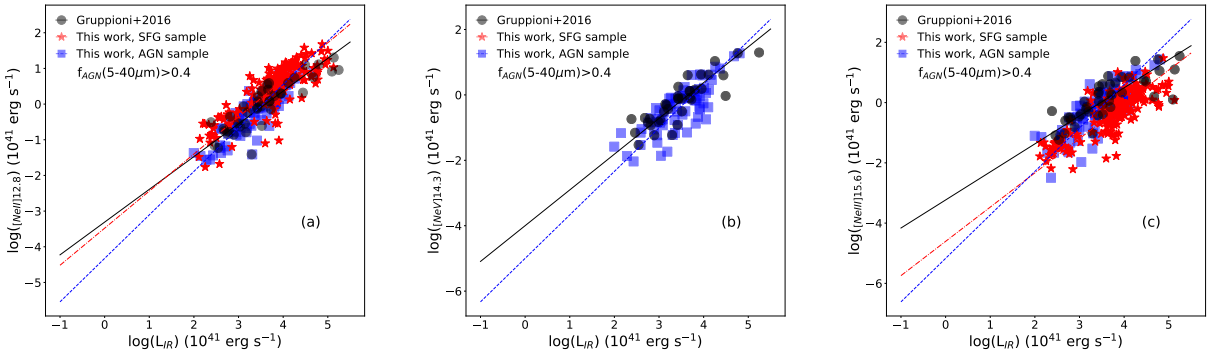

Figure 3.26: (a: left) The [NeII]12.8µm line luminosity versus the total IR luminosity. **(b: center)** The [NeV]14.3µm line versus the total IR luminosity. **(c: right)** The [NeIII]15.6µm line luminosity versus the total IR luminosity. In all three figures, the Gruppioni et al. sample was limited to AGN fractions > 0.4 in the 5-40µm spectral interval (see **Sect.**3.6.4). The same legend as in Fig. 3.25 was used.

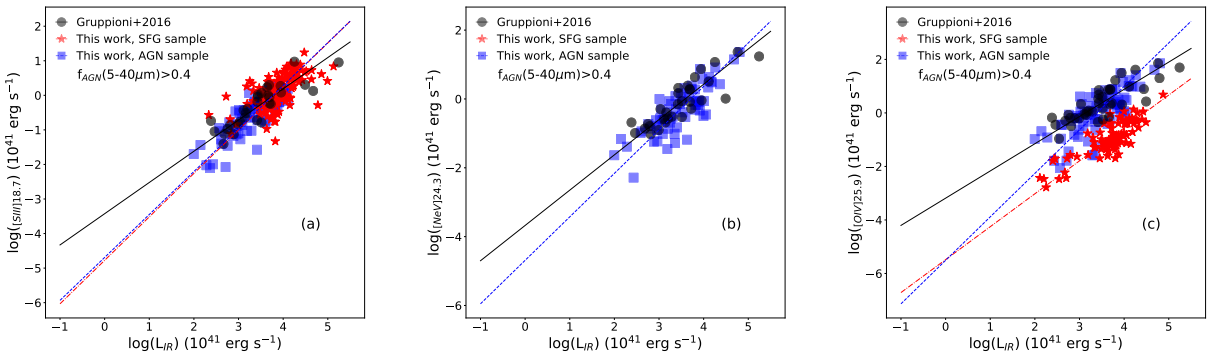

Figure 3.27: (a: left) The [SIII]18.7µm line luminosity versus the total IR luminosity. **(b: center)** The [NeV]24.3µm line luminosity versus the total IR luminosity. **(c: right)** The [OIV]55.9µm line luminosity versus the total IR luminosity. In all three figures, the Gruppioni et al. sample was limited to AGN fractions > 0.4 in the 5-40µm spectral interval (see **Sect.**3.6.4. The same legend as in Fig. 3.25 was used.

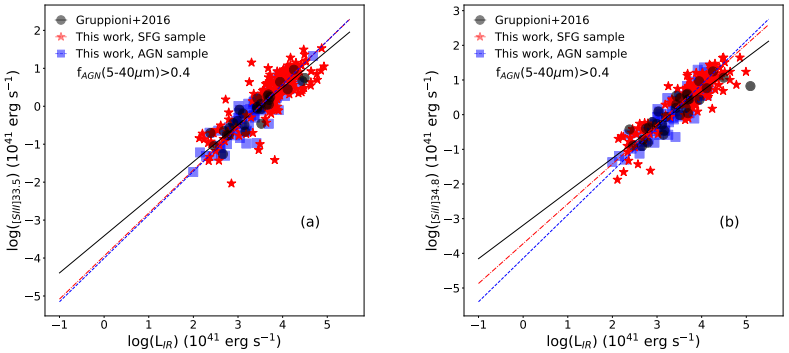

Figure 3.28: (a: left) The [SIII]33.5µm line luminosity versus the total IR luminosity. **(b: right)** The [SiII]34.9µm line luminosity versus the total IR luminosity. In both figures, the Gruppioni et al. sample was limited to AGN fractions > 0.4 in the 5-40µm spectral interval (see **Sect.**3.6.4). The same legend as in Fig. 3.25 was used.

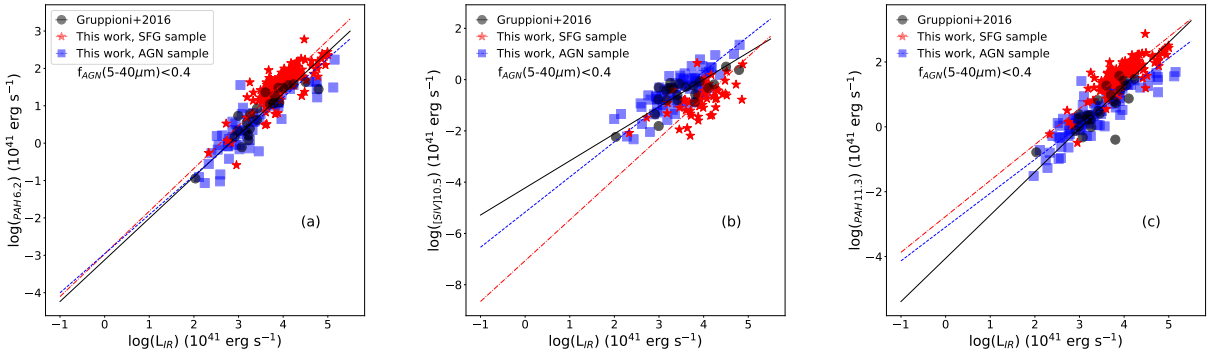

Figure 3.29: (a: left) The luminosity of the PAH feature at 6.2µm versus the total IR luminosity. **(b: center)** The [SIV]10.5µm line luminosity as a function of the total IR luminosity. **(c: right)** The PAH 11.3µm luminosity versus the total IR luminosity. In all figures, the Gruppioni et al. sample was limited to AGN fractions < 0.4 in the 5-40µm spectral interval (see **Sect.**3.6.4). The same legend as in Fig. 3.25 was used.

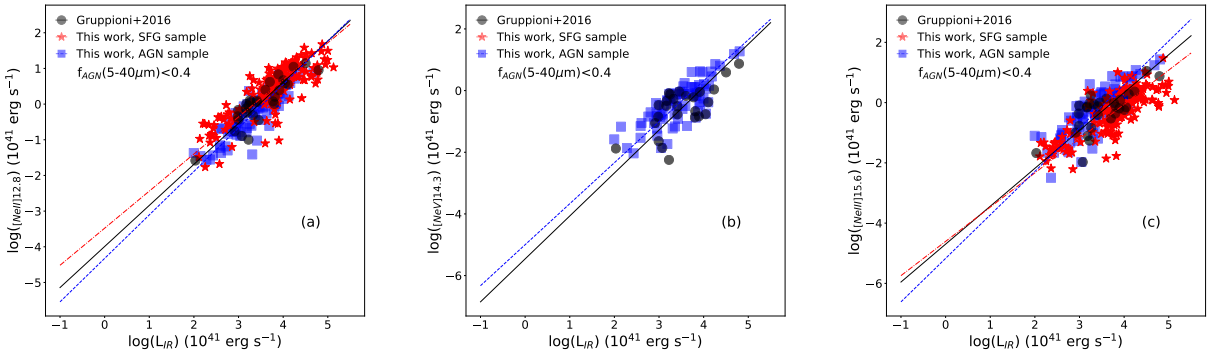

Figure 3.30: (a: left) The [NeII]12.8µm line luminosity versus the total IR luminosity. **(b: center)** The [NeV]14.3µm line luminosity versus the total IR luminosity. **(c: right)** The [NeIII]15.6µm line luminosity versus the total IR luminosity. In all three figures, the Gruppioni et al. sample was limited to AGN fractions < 0.4 in the 5-40µm spectral interval (see **Sect.**3.6.4). The same legend as in Fig. 3.25 was used.

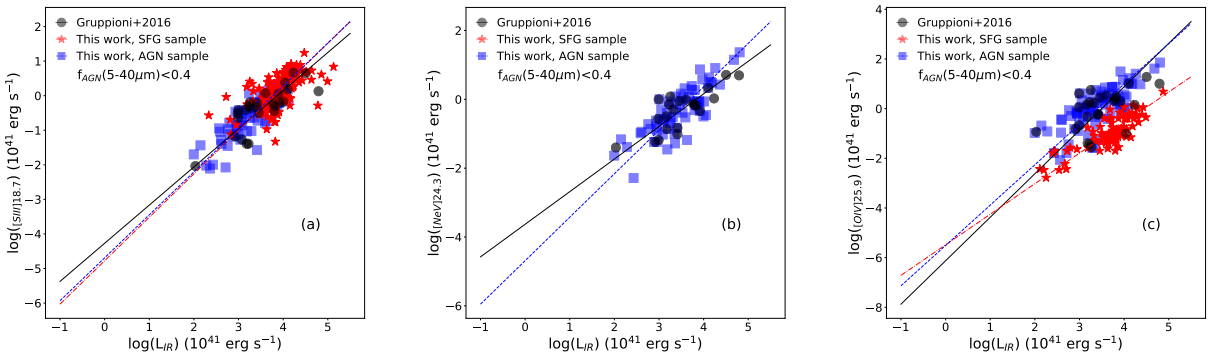

Figure 3.31: (a: left) The [SIII]18.7µm line luminosity versus the total IR luminosity. **(b: center)** The [NeV]24.3µm line luminosity versus the total IR luminosity. **(c: right)** The [OIV]55.9µm line luminosity versus the total IR luminosity. In all three figures, the Gruppioni et al. sample was limited to AGN fractions < 0.4 in the 5-40µm spectral interval (see **Sect.**3.6.4). The same legend as in Fig. 3.25 was used.

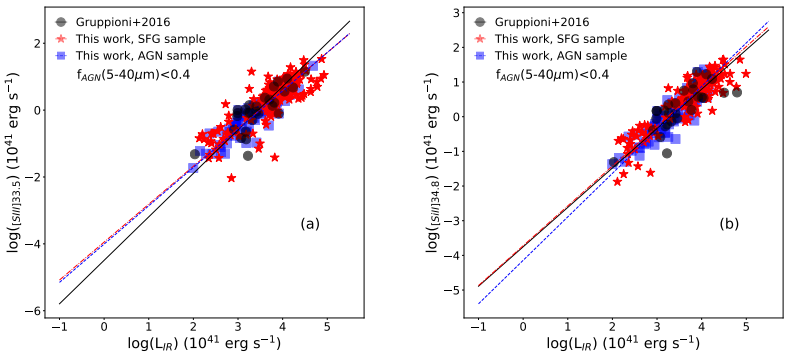

Figure 3.32: (a: left) The [SIII]33.5µm line luminosity versus the total IR luminosity. **(b: right)** The [SiII]34.9µm line luminosity versus the total IR luminosity. In both figures, the Gruppioni et al. sample was limited to AGN fractions < 0.4 in the 5-40µm spectral interval (see **Sect.**3.6.4). The same legend as in Fig. 3.25 was used.

Chapter 4

Comparison with high-redshift results

4.1 Introduction

The calibrations presented in Chapter 3 are obtained using data from local galaxies. Lines in the 50-205µm interval, however, can be observed by the Atacama Large Millimeter Array at redshifts $z > 1$. In this Section I make an assessment of the application of the calibrations calculated for local galaxies for high redshift sources.

It emerges that, for the most part of the tested calibrations, there is good agreement between local calibrations and high redshift detections. As a general trend, while the AGN calibrations hold true for high-redshift quasars, starburst galaxies present an environment similar to local SFG. The [OIII]88µm line, however, shows a correlation for high redshift sources closer to that of local LMG, suggesting that the ISM in high redshift galaxies is characterized by stronger radiation fields when compared to low redshift galaxies with similar total IR luminosities.

4.2 High-redshift results comparison

In this section, I compare the correlations described in Chapter 3 with ALMA detections at redshift z>1. In particular, I consider detections of the [OIII]88 µm, [NII]122 µm, [CII]158 µm and [NII]205 µm lines at $z \geq 3$. Sources identified as QSOs are compared to local AGN results, while sources for which a classification is not given in the literature, or are classified as starburst galaxies, are compared to local SFG.

Fig. 4.1a shows the comparison between local and high redshift detections of the [CII]158 µm line for QSOs, and in particular 27 detections at z∼6 reported in Venemans et al. (2020), plus the detections by Walter et al. (2018) for one source at z∼6.08 and by Hashimoto et al. (2018) for two sources at z∼7.1, for a total of 30 sources. Fig. 4.1b displays the comparison of local and high redshift SFG: 84 detections from the ALPINE catalogue (Faisst et al. 2020) plus other 9 detections (De Breuck et al. 2019; Harikane et al. 2019; Hashimoto 2019; Inoue et al. 2016; Rybak et al. 2019; Vishwas et al. 2018; Walter et al. 2018) for a total of 93 objects with redshift in the $4.2 \lesssim z \lesssim 7.2$ range. While some outliers are present, the bulk of the detections in both cases lies within the prediction interval, shown in the figures at the 95% level, suggesting that the relations derived for local galaxies hold for high redshift sources.

I compare in Fig. 4.1c the $L_{[CII]}$-SFR relation extrapolated for local galaxies (see Section 3.4.1) with ALPINE detections of the [CII]158 µm emission line in starburst galaxies. High redshift objects follow the same $L_{[CII]}$-SFR relation as local SFG and LMG, thus suggesting little or no evolution in the $L_{[CII]}$-SFR

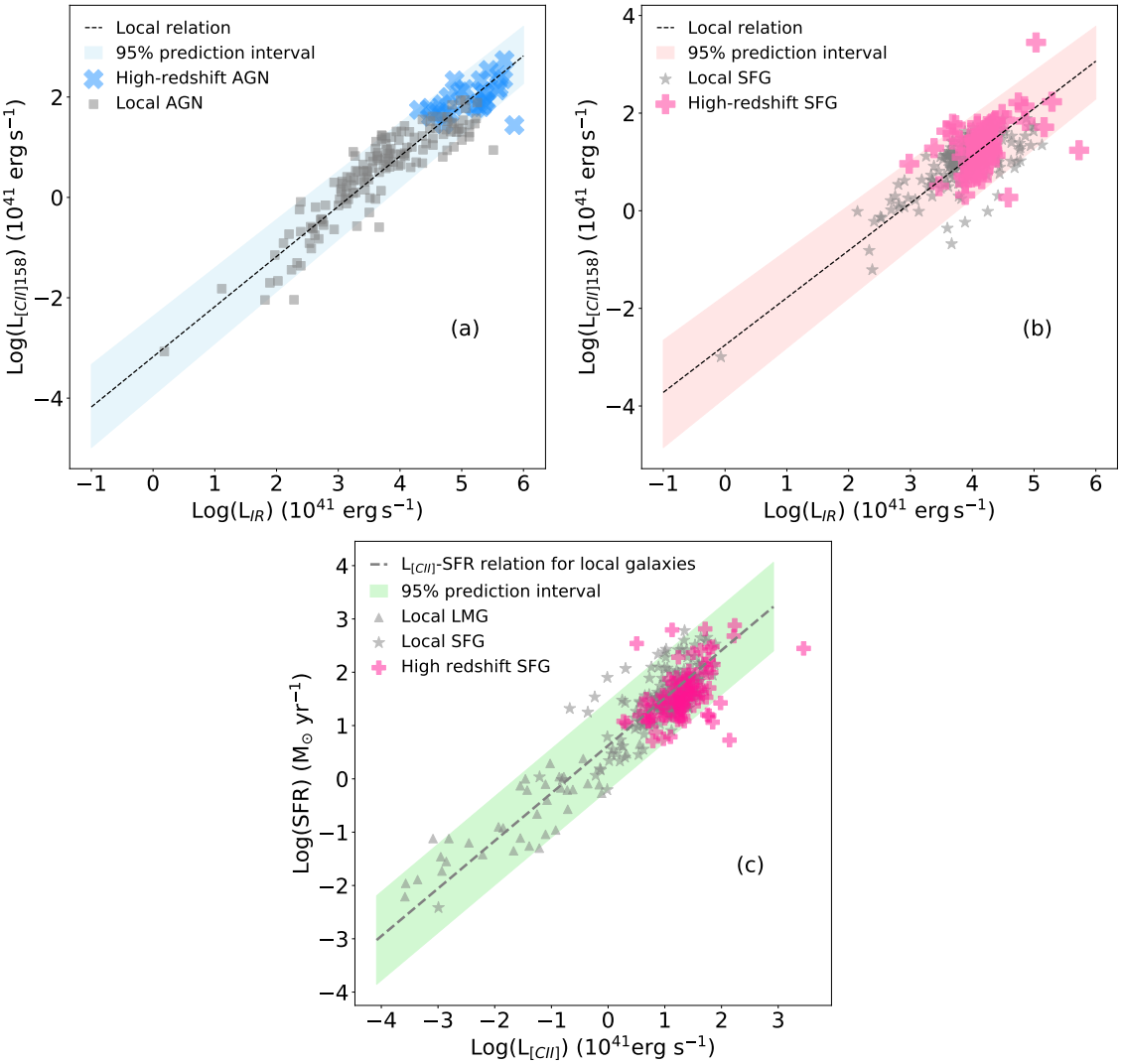

Figure 4.1: (a: top left) Comparison between the L_{IR}-$L_{[CII]158}$ relation (black dashes line) for local AGN dominated galaxies (gray squares) and high redshift detections for QSOs (blue symbols). The shaded area shows the 95% prediction interval. **(b: top right)** Same for high redshift starburst galaxies (pink symbols). **(c: bottom)** Comparison of the local log($L_{[CII]}$)-log(SFR) relation (black dashes line) and $L_{[CII]}$-SFR values of high redshift sources (pink symbols). Grey dots represent local star forming galaxies. The shaded area shows the 95% prediction interval for the local relation.

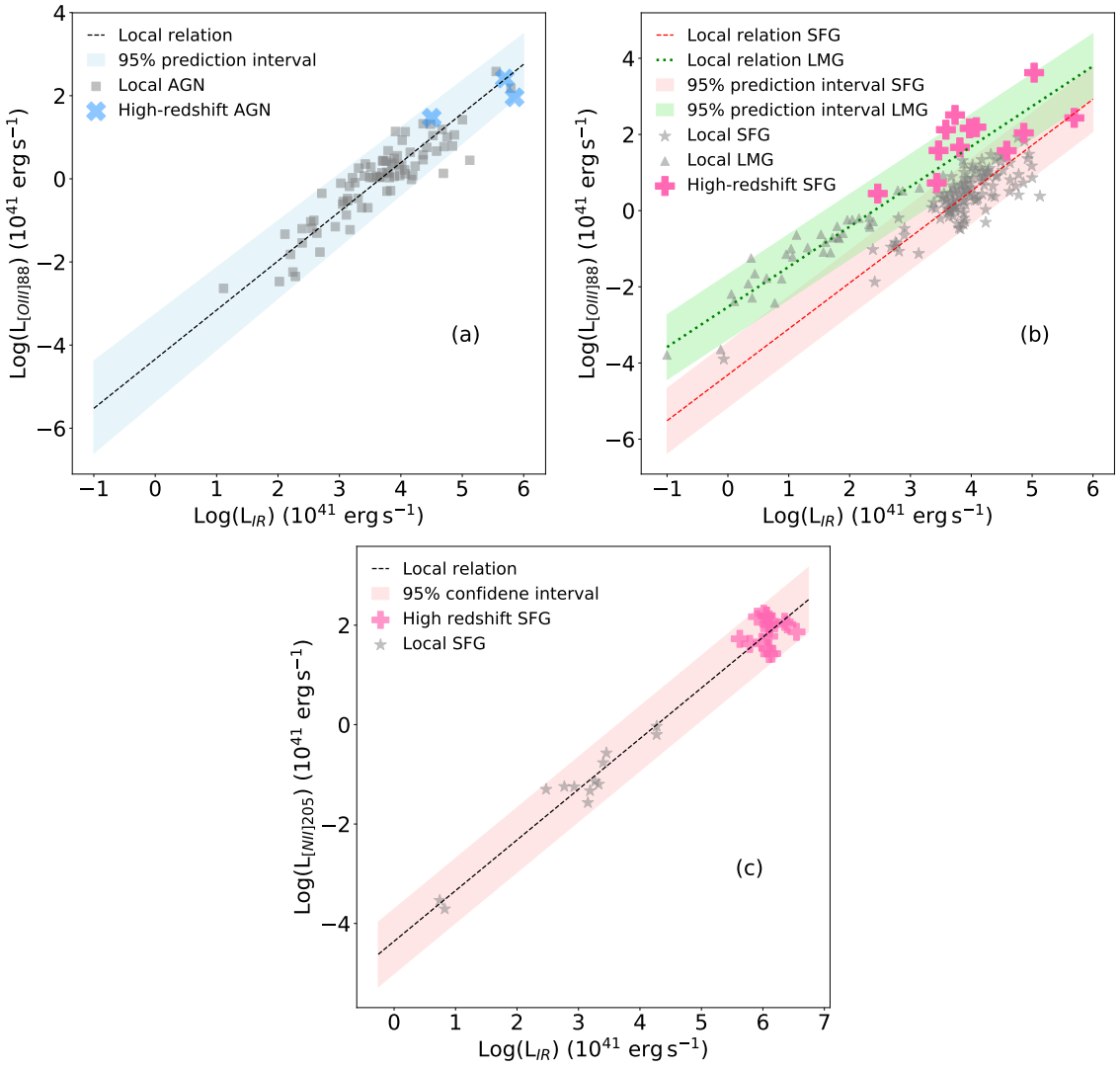

Figure 4.2: (a: top left) Comparison between the L_{IR}-$L_{[OIII]88}$ relation (black dashes line) for local AGN dominated galaxies (gray squares) and high redshift detections for QSOs (blue symbols). **(b: top right)** Comparison between the L_{IR}-$L_{[OIII]88}$ relation (red dashes line) for local SFG (gray stars) and high redshift detections for starburst galaxies (pink symbols). The red shaded area shows the 95% prediction interval of this relation. For comparison, the green dashed line shows the L_{IR}-$L_{[OIII]88}$ relation for local LMG, with gray squares indicating local LMG and the green shaded area giving the 95% prediction interval for this relation. **(c: bottom)** Comparison of the local L_{IR}-$L_{[NII]205}$ relation (black dashes line) for high redshift detections of SFG (pink symbols). Grey stars represent local star forming galaxies. The shaded area in all the figures shows the 95% prediction interval for the local relation.

relation. In particular, no deficit of [CII] emission is seen for the highest SFR values of $\sim 100\,\mathrm{M_\odot\,yr^{-1}}$, suggesting that starbursts at high-z might not behave like local ULIRGs such as those shown in Fig. 3.10 (purple squares). An analogous result was found by Schaerer et al. (2020), who analyzed a large sample of galaxies at high redshift (z~ 4-6) observed by ALMA. Leung et al. (2020) explored the possibility of tracing the SFR at the Epoch of Recombination with [CII]158 µm using simulated data. Although they find a good correlation, when compared to observed data, the simulated sample shows an average [CII] luminosity lower than the one obtained from ALMA pointed observations. A similar result was obtained for simulations of high redshift systems (Ferrara et al. 2019) showing the presence of under-luminous [CII] emission.

Fig. 4.2a shows the comparison between the local L_{IR}-$L_{[OIII]88}$ relation for AGN and high redshift detections in QSOs (Hashimoto et al. 2018; Walter et al. 2018), while panel (b) shows the relation between local and high redshift SFG (De Breuck et al. 2019; Harikane et al. 2019; Hashimoto 2019; Inoue et al. 2016; Tamura et al. 2019; Vishwas et al. 2018; Walter et al. 2018). While the high-redshift detections of [OIII]88 µm in QSOs are comparable with the relation derived from local AGN dominated galaxies, in SFG the majority of high redshift detections appears to be one to two orders of magnitude brighter at comparable L_{IR}. These detections are better represented by the L_{IR}-$L_{[OIII]88}$ relation derived for local LMG (see Fig. 4.2b). This suggests that the [OIII]88 µm line is produced in an environment with a higher ionizing spectrum, similar to the ISM of local LMG (see Section 3.3.1).

Finally, the high redshift detections in panel (c) show the local L_{IR}-$L_{[NII]205}$ relation for SFG and 17 high-redshift detections of [NII]205 µm (Cunningham et al. 2020) with the local correlation that well represents also the high redshift detections. We report in Fig. 4.3b the comparison between the local L_{IR}-$L_{[NII]122}$ relation and high redshift SFG: in this case only one object (De Breuck et al. 2019) has been detected, while three (Harikane et al. 2019) objects have upper limits. Thus, only one object is located almost an order of magnitude higher than the local relation for SFG, and therefore there is no statistical evidence for a difference in the production mechanism of [NII] in high redshift objects, especially considering the results for the [NII]205 µm line.

Fig.4.2a shows five detection of the [OI]63µm line (Coppin et al. 2012; Rybak et al. 2019; Wagg et al. 2020) compared to the L_{IR}-$L_{[OI]63}$ relation for local SFG. Panel c shows the comparison between the L_{IR}-$L_{[OI]145}$ relation for local SFG and a detection of [OI]145µm (De Breuck et al. 2019).

As a general trend, I find that, except for the [OIII]88µm line, all correlation calibrated for local galaxies hold true, within the prediction interval, also for high redshift detection, and in particular the [CII]158µm line can be used as a SFR tracer even for high redshift starburst sources. The [OIII]88µm line, on the other hand, shows a correlation for high redshift sources closer to local LMG than to SFG, while for AGN sources there seems to be no difference between local galaxies and high redshift QSOs.

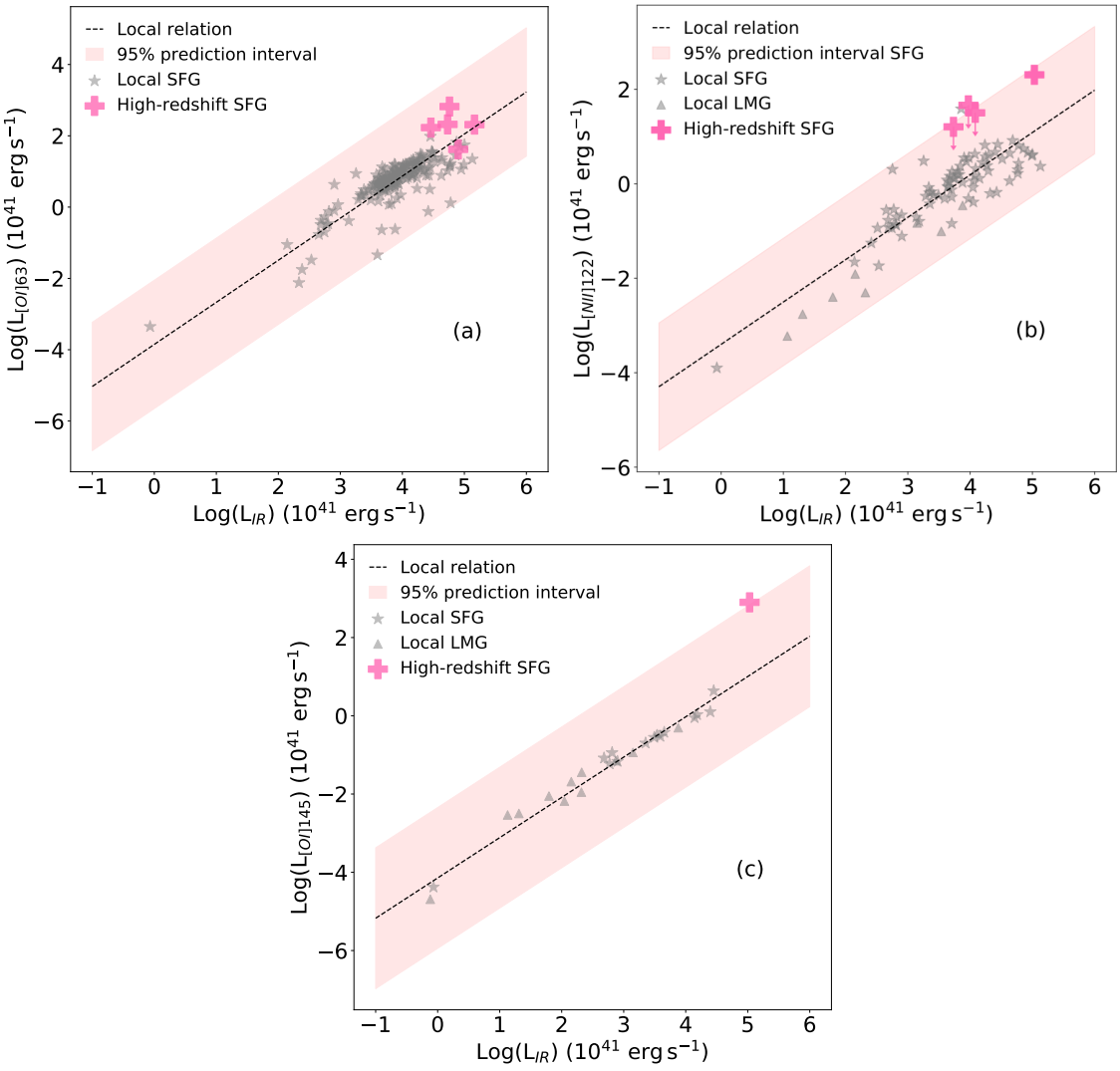

Figure 4.3: **(a:top left)** Comparison between the local L_{IR}-$L_{[OI]63}$ relation for local SFG (black dashed line) and high redshift detections of [OI]63μm line. The shaded area shows the 95% prediction interval for the local relation. The pink + signs indicate the detections for the [OI] line (Coppin et al. 2012; Rybak et al. 2019; Wagg et al. 2020). **(b:top right)** Comparison between the local L_{IR}-$L_{[NII]122}$ relation for local SFG (black dashed line) and high redshift detections of [NII]122μm line. The shaded area shows the 95% prediction interval for the local relation. The pink + sign indicates a detection for the [NII]122 μm line (De Breuck et al. 2019), while symbols with arrows indicate upper limits for high redshift sources (Harikane et al. 2019).**(c:bottom)** Comparison between the local L_{IR}-$L_{[OI]145}$ relation for local SFG (black dashed line) and high redshift detections of [OI]145 μm line (pink symbol (De Breuck et al. 2019). The shaded area shows the 95% prediction interval for the local relation. Grey stars show local SFG, while grey triangles show local LMG.

Chapter 5

A plan for spectroscopic surveys with SPICA

5.1 Introduction

As previously described in Chapter 1, the photometric surveys carried out in the X-ray, UV, optical and IR bands in the last twenty years have shown a common trend in the evolution of star formation and black hole accretion, with a peak between redshifts $z \sim 1$ and $z \sim 3$, (the so-called 'Cosmic Noon') after which both processes follow a steep decline toward the present epoch (Heckman & Best 2014; Madau & Dickinson 2014, and references therein).

Rest-frame optical and UV observations cannot access the obscured regions at the peak epoch of star formation and black hole accretion activity: UV and optical light is absorbed by dust grains and re-emitted in the IR, with almost 90% of the light from young stars emerging in the IR (Madau & Dickinson 2014). This makes UV and optical observation highly unreliable when heavily obscured environments, like those at the cosmic noon, are concerned. Moreover, the determination of the black hole accretion from X-ray observations is affected by uncertainties due to the need to apply a large bolometric correction (factors of 10-100) to the measured flux and hard-X-ray surveys, probing the hot gas around accreting black holes, have limited sensitivities to the Compton-thick population of AGN.

IR photometric surveys with Spitzer and Herschel have been used to measure number counts and galaxy luminosity functions using statistical methods applied to the bulk of galaxy populations as a function of redshift (e.g. Gruppioni et al. 2013; Wang et al. 2019). These surveys have also attempted to measure SFR and BHAR. Photometric surveys, however, suffer from assumptions made about the intrinsic spectra, as most of the measured light is reprocessed emission from dust heated by the central power source and does not contain any information about the original source of emission, making it difficult to discriminate between star formation and black hole accretion.

For these reasons, wide spectroscopic surveys in the mid and far-IR range can be the key to obtain new, dust-unbiased information on galaxy evolution. The IR spectral range contains a great variety of lines and features that can be used as diagnostic tools in a dust-obscured environment, which allows to physically separate processes linked to star formation and stellar evolution to those linked to AGN activity. Wide enough surveys, moreover, are necessary to probe the large scale structure of the Universe, and thus analyze how galaxies evolve in different environments and bypass the bias that can be introduced when observing the large scale structure in small, limited surveys. Mapping a wide enough area with spectro-photometric surveys would allow to gain not only spatial informations on a substantial number of objects, but also physical information such as redshift, SFR, or metallicity.

In this chapter, I present the observational program of IR spectroscopic surveys developed for the preparation of the SPICA mission, highlighting the limits of redshift and luminosity that a SPICA-like telescope could reach with its different spectrometers.

What emerges is that, using first an SMI-like instrument to carry out blind spectro-photometric surveys, and then a SAFARI-like instrument for follow up spectroscopic observations, a SPICA-type mission could analyze star formation and BHA up to redshift z~4, disentangling the two phenomena in the same galaxy population, and also gaining unprecedented knowledge in terms of metal content and episodes of outflows and infall over cosmic time.

5.2 The blind surveys with SMI/LR

When planning future cosmological surveys, the main goal is to obtain a complete characterization of the physical processes that drive galaxy evolution throughout cosmic time, covering all the relevant aspects, like the effect of the environment, and measure the energy signatures of both star formation and black hole accretion, the feedback processes from outflows, and the production and evolution of heavy elements and dust as a function of cosmic time. In particular, the observational program is divided in three steps. The first step requires a blind spectro-photometric survey over a large cosmological volume. These blind surveys have a double objective: first, starting from the low resolution spectroscopic surveys it would be possible to detect lines and features from which to derive the redshifts and SFR for tens of thousands of sources, even at the cosmic noon. Combined with ancillary data from multi-wavelength surveys planned with other facilities, the sources detected in the blind surveys would be characterized also in terms of stellar and dust masses, and bolometric luminosities. The second goal of the blind survey is to define a representative sample of galaxies detected in the blind unbiased surveys to perform further spectroscopic pointed observations in the full IR domain (17-230μm) which will be used to optimally study galaxy evolution. The last step consists therefore in pointed observations of a statistically significant sample of galaxies, in order to completely characterized the physical processes at the base of galaxy evolution.

The SPICA suite of instruments, described in Chapter 2, was designed with the objective of carrying out the proposed survey up to redshift z~4, in order to gain an in-depth knowledge of the processes driving galaxy evolution from the cosmic noon up to the present epoch. For this reason, the SMI instrument is characterized by a low resolution spectrometer covering the 17-36μm range, and a broad band photometer at 34μm that can be operated simultaneously. This would allow to carry out the blind spectro-photometric surveys described in the first step of the observational program. The SAFARI instrument, on the other hand, was developed with the intent of reaching the sensitivity needed to observe key mid-IR lines such as [OIV]25.9μm, [NeV]14.3,24.3μm or [NeII]12.8μm in the dust obscured regions of star formation and accretion at the cosmic noon for galaxies at the 'Main Sequence' luminosity.

For the simulation of the SMI/LR blind surveys, I considered two different approaches: on one hand, I used the IR photometric catalogue of the Herschel Legacy extragalactic Program (HELP, Vaccari 2016) as input data. With this simulation I want to determine whether SPICA spectroscopy with SMI/LR can reach the photometric limit of Herschel's deepest fields, and therefore the simulation results are limited by the Herschel sensitivity. The second approach is instead based on the predictions of galaxy counts derived from the observed IR luminosity functions. With this approach, I want to test the limit of the instrument, and its capability to produce a true unbiased catalogue of IR sources.

In both cases, I considered three different blind surveys:

Deep survey: this survey covers an area of 15 deg^2 reaching a spectroscopic limit of $\sim 1.2\,10^{-19}$W m^{-2} at 34μm (at 5σ), corresponding to 13μJy in the continuum (at 5σ), and is complemented with B-BOP observations at 70 μm at a flux limit of $\sim$ 100μJy (at 5σ). This survey covers a wide area of sky, but is relatively shallow; it has the objective of detecting very bright but rare sources, probing the bright end of the luminosity function;

Ultra-deep survey: this survey covers a 1 deg^2 area reaching the spectroscopic limit of 2.810^{-20}W m^{-2}, which corresponds to 3μJy in the continuum (at 5σ), and is complemented with a B-BOP photometric survey at 70 μm at a flux limit of $\sim$ 60μJy (at 5σ). This survey wants to probe the main population of galaxies, reaching the knee of the luminosity function;

Hyper-deep survey: this survey is carried out over one field of view of SMI/LR (10'×12'=0.033 deg^2) down to the spectroscopic flux limit of $\sim 4.610^{-21}$W m^{-2} at 34μm, corresponding to 0.5 μJy in the continuum at 5σ. This survey reaches the confusion limit for a 2.5 m telescope at 34μm. This survey tests the limits of the instrument, looking for sources in the faint end of the luminosity function, but also for sources beyond the cosmic noon.

According to predictions from the Planck proto-cluster Luminosity Function evolutionary model (Negrello et al. 2017), the 1 deg^2 ultra-deep survey should be able to detect from hundreds to thousands of proto-clusters. The deep survey, however, is necessary to fully address the effects of clustering and environment on galaxy evolution: the spectroscopic depth reached for the 15 deg^2 survey should allow to determine the redshift using the PAH features: Kaneda et al. (2017) simulating a SFG and AGN sources at redshift z~2-4, demonstrate that the source redshift can be measured with an accuracy of $\gtrsim 98\%$ for 84% of the SFG sample, and for 68% of the AGN sample.

5.2.1 Spectral lines and features

In order to determine the observability of a galaxy, I computed the line emission luminosity function starting from the IR continuum luminosity function. Using then the SMI spectrometer sensitivity (Kaneda et al. 2017), I determined in each case, whether a certain line or feature is detectable in each object. The line calibrations used to derive the line emission luminosity functions are presented in detail in Chapter 3. This work follows the same approach presented in Spinoglio et al. (2012) and Gruppioni et al. (2016), but using new calibrations for IR lines, updated galaxy luminosity functions and updated characteristics for the SPICA instruments.

The detection predictions are based on lines and features in the rest frame 6-35μm spectral range. This interval is best suited to study galaxy at the cosmic noon, at redshift $z = 1-3$, and is also ideal to discriminate the different ionizing continuum between AGN and SF galaxies.

For these simulations, I considered the following lines, in order of wavelength: [NeVI] 7.67μm, [SIV]10.51μm, [NeII]12.81μm, [NeV]14.32μm [NeIII]15.56μm, [SIII]18.71μm, [NeV]24.32μm, [OIV]25.89 μm, [SIII]33.38μm and [SiII] 34.81μm. In addition, I included the PAH (Puget & Leger 1989) features at 6.2, 7.7, 8.6, 11.3 and 17μm.

5.2.2 Predictions from Herschel photometric fields

In this simulation, I took advantage of the Herschel Extragalactic Legacy Program (HELP, Vaccari 2016) as input parameter, to determine how many galaxies, detected with the Herschel photometric surveys, would be

detected with the SPICA SMI/LR spectroscopic surveys at each redshift and luminosity. For this simulation I do not introduce the actual observational limit of the instrument, but I only consider the sources presented in the HELP catalogue, and whether they can be spectroscopically detected by SMI/LR.

The selected data was previously analyzed with the Code Investigating GALaxy Emission (CIGALE, Ciesla et al. 2015), Available on the HELP service[1]. The selected data have estimated IR luminosities, stellar masses and SFR. The complete sample is formed by ~15000 sources selected in the COSMOS field (Scoville et al. 2007), covering a 2 deg^2 area. All sources in the sample have fluxes from Spitzer-MIPS (Rieke et al. 2004) at 24μm, from Herschel-PACS (Poglitsch et al. 2010) at 100μm and 160μm, and from Herschel-SPIRE (Griffin et al. 2010) at 250μm.

Starting from the total IR luminosity, I determined the expected line luminosity for each object using the line calibrations I calculated (see Chapter 3). Then, converting the luminosities into fluxes, I compared these to the SMI limiting flux depending on the depth of the survey considered. The use of the HELP catalogue allows to determine how many galaxies, already detected by Herschel photometric surveys, could be detected spectroscopically by a SPICA-like observatory. However, this method presents an important limitation: the estimates suffer from the same completeness limit of the Herschel surveys, in particular they are biased against both low luminosity objects, not detected by Herschel, and high luminosity galaxies, which could have been missed due to the limited field coverage by the survey. The results for this estimates are presented in Section 5.3.1.

5.2.3 Predictions from luminosity functions

When using the luminosity functions to simulate an SMI blind survey, I used the luminosity functions, derived from the Herschel far-IR surveys, presented by Wang et al. (2019). In these luminosity functions, the galaxy population is presented in its entirety, and is not divided into sub-groups depending on a SED classification. Starting from the luminosity functions, I derive the total number of galaxies per Mpc^3 present in a 10'×12' field of view of the SMI/LR instrument, as a function of redshift, and in each luminosity interval. Starting from the IR luminosity and redshift, I then derive the expected flux of the considered tracers starting from the line calibrations for AGN, SFG and LMG. Finally, considering the threshold flux for surveys at different depths, I estimate the fraction of the total galaxy population that this type if survey would be able to classify in the three classes of galaxies I considered. The results for this estimates are presented in Section 5.3.2. It is important to note that, while these simulations are a good indicator of what a SPICA-like space IR telescope can observe, the luminosity functions used to derive these results are based on Herschel observations. The limited sensitivity of Herschel with respect to a SPICA-like telescope (see Fig. 2.3a) implies that the low-end of the luminosity function has not been probed with enough detail to obtain a reliable estimate of the expected number of sources, and the results of the simulations carried out in this work are to be considered only a lower limit.

5.3 Results of the simulations for blind surveys

The predictions for galaxy detections are determined using a single luminosity distribution function for IR galaxies, without making *a priori* assumptions on the distribution of single populations, like AGN and SFG. This means that I derive the fraction of detected sources through the tracers calibrated for each different

[1]Available at: `https://herschel-vos.phys.sussex.ac.uk/`, Shirley (2020)

Table 5.1: SMI Spectrophotometric surveys parameters

Parameters	Deep	Ultra-deep	Hyper-deep
Survey area (deg^2)	15	1	0.033 (10'× 12')
Number of SMI fields (10'×12')	450	30	1
Limiting cont. flux at 34μm (5 σ, R = 2.5) (μJy)	13	3.0	0.5
SMI Time per field (hr.)	1.07	20.2	260.6
Total SMI integration time (hr.)	475.5	605.0	260.6

galaxy population. In other words, I assume that the whole population may consist of SFG, LMG or AGN or even composite objects and the fractions of each galaxy population will be determined *a posteriori* by examining the detected lines and features. This method allows us to determine first the lower limit of detections for the different galaxy types, without any model assumption that could introduce a bias, and then to establish the galaxy fractions through the spectroscopic results.

Many results in the following sections are compared to the 'knee' of the luminosity function, indicated as L*. The definition of the L* has been derived by Schechter (1976) and this value indicates the luminosity where the majority of galaxies can be found. For these spectroscopic surveys, reaching the knee of the luminosity function means that the survey includes, up to redshift z∼2.5, about 50% or more of the total IR light of galaxies; at higher redshifts, this value is slightly lower: at z∼3, L* includes ∼48% of the IR light, while at z∼4 the value is about 46%. Reaching a luminosity that is 1 dex above L* means losing 55-60% of the light and, conversely, going 1 dex below L* includes 60-70% of the total luminosity. For the comparison of the results, I used the luminosity function corresponding to a galaxy mass of $10^{10.7}$ M$_\odot$ at the so-called 'galaxy Main-Sequence' (M.-S., Scoville et al. 2017).

Table 5.1 reports the characteristics of the three surveys simulated in the following two sections.

5.3.1 Simulations based on the Herschel photometric fields detections

Fig. 5.1 shows the results for the simulated hyper-deep survey of the deepest Herschel photometric fields (HELP). This survey considers a 120 arcmin^2 (0.033 deg^2) field of view. In particular, Fig. 5.1(a) shows the detection of SFG using PAH emission features. The SMI/LR sensitivity of this survey is about two and a half orders of magnitude below the knee of the luminosity function. For the LMG, shown in Fig. 5.1(b), the detection limit is about 1.5 order of magnitude below L*, but only reaching galaxies up to redshift z∼2.2, because of the lack of short wavelength tracers, to cover higher redshift in the SMI spectral interval (17-37μm). In Fig. 5.1(c) are presented the results for the AGN population, with SMI/LR reaching luminosities about 1 dex below L*, up to redshift z∼3.5.

Fig. 5.2 shows the results for the simulated 1 deg^2 survey. Fig. 5.2(a) presents the detection of the PAH features in SFG, while Fig. 5.2(b) and (c) show the detection, using fine structure lines, of LMG and AGN galaxies, respectively. In SFG, the PAH features cover the entire redshift range at almost 1 dex below the knee of the luminosity function, with the 7.7μm feature reaching 1.5 dex below L*. This indicates that the bulk of the SFG, already detected by the Herschel photometric surveys, can be easily detected spectroscopically by an SMI-like instrument.

When considering the AGN, instead, the lack of tracers as bright as the PAH features leads to a much higher luminosity limit, with the lowest detections just at L* for redshift z> 0.5. The [NeVI] 7.7μm line can

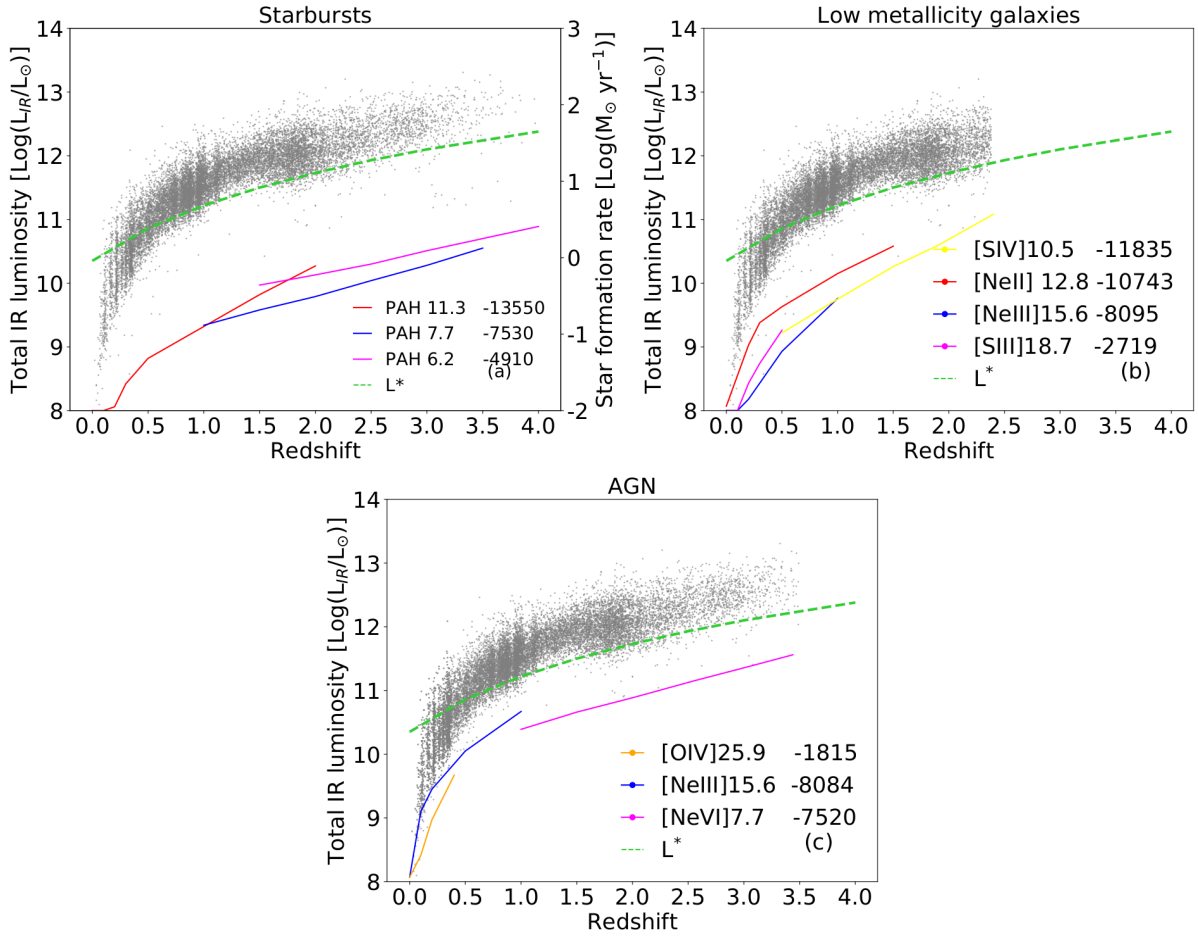

Figure 5.1: Redshift-luminosity diagrams simulating the SMI 120 arcmin^2 hyper-deep survey using the HELP database. In all three panels, the grey dots represent the whole galaxy population as detected photometrically by Herschel, while each continuum coloured line represent the detection limit of SMI at the given line or feature, as indicated by the legend, which also gives the total number of detections in that particular line or feature. The green broken line shows the knee of the luminosity function, as a function of redshift for a $10^{10.7}$ $M_\odot$ galaxy in the Main-Sequence (M.-S., Scoville et al. 2007).**(a: top left):** SFG detectable with SMI in the PAH features. On the right-hand y-axis the SFR corresponding to the total L_{IR} is also given, adopting the conversion factor from Kennicutt & Evans (2012). **(b: top right):** SF galaxies, adopting the line calibration of low-metallicity galaxies ($\sim 1/5\,Z_\odot$) detectable with SMI in intermediate ionization fine-structure lines. **(c: bottom):** AGN detectable with SMI in high-ionization fine-structure lines.

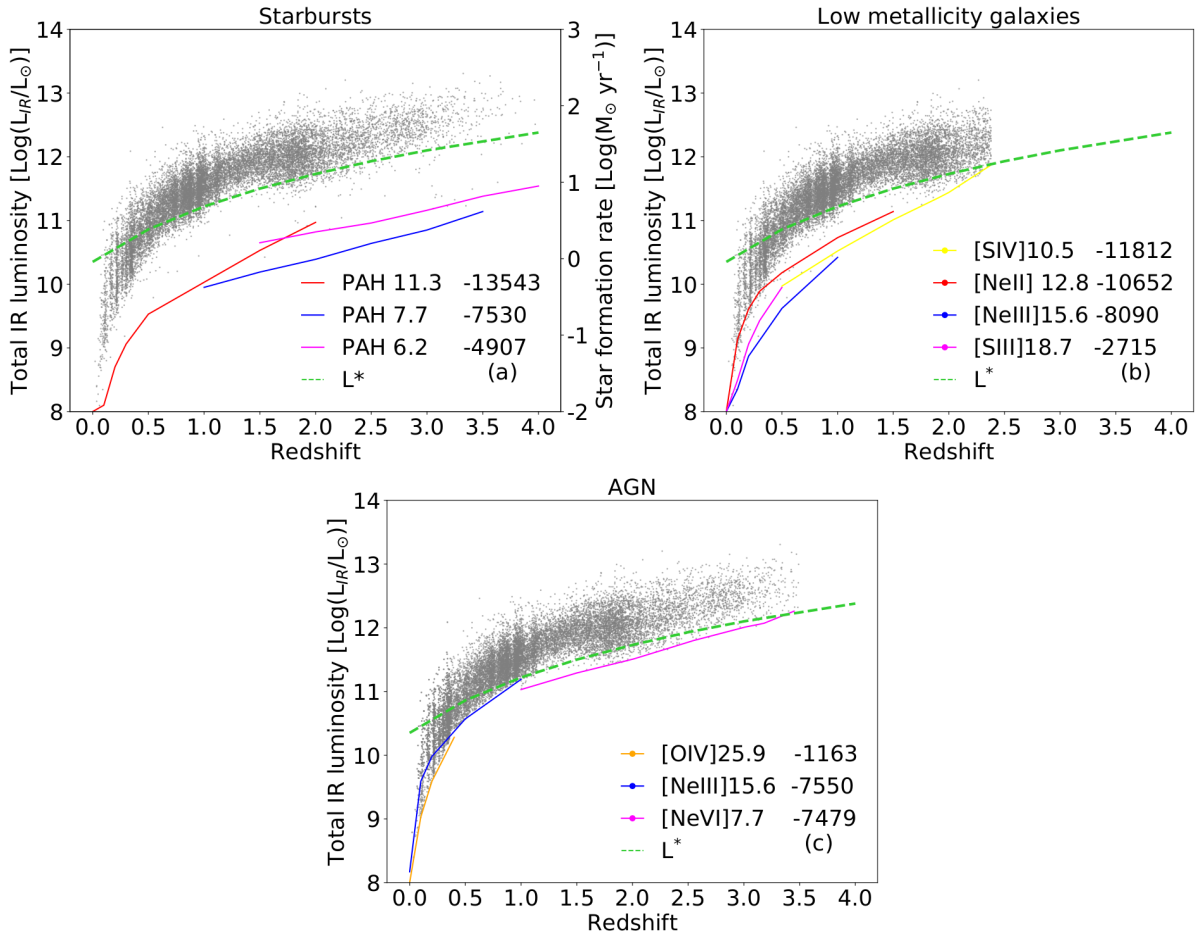

Figure 5.2: Redshift-luminosity diagrams simulating the SMI 1 deg^2 ultra-deep survey using the HELP database. I refer to Fig. 5.1 for the lines coding and legends in each frame. **(a: top left):** SF galaxies detectable with SMI in the PAH features. On the right-hand y-axis the SFR corresponding to the total L_{IR} is also given, adopting the conversion factor from Kennicutt & Evans (2012). **(b: top right):** SF galaxies, adopting the line calibration of low-metallicity galaxies ($\sim 1/5\,Z_\odot$), detectable with SMI in intermediate ionization fine-structure lines. **(c: bottom):** AGN detectable with SMI in high-ionization fine-structure lines.

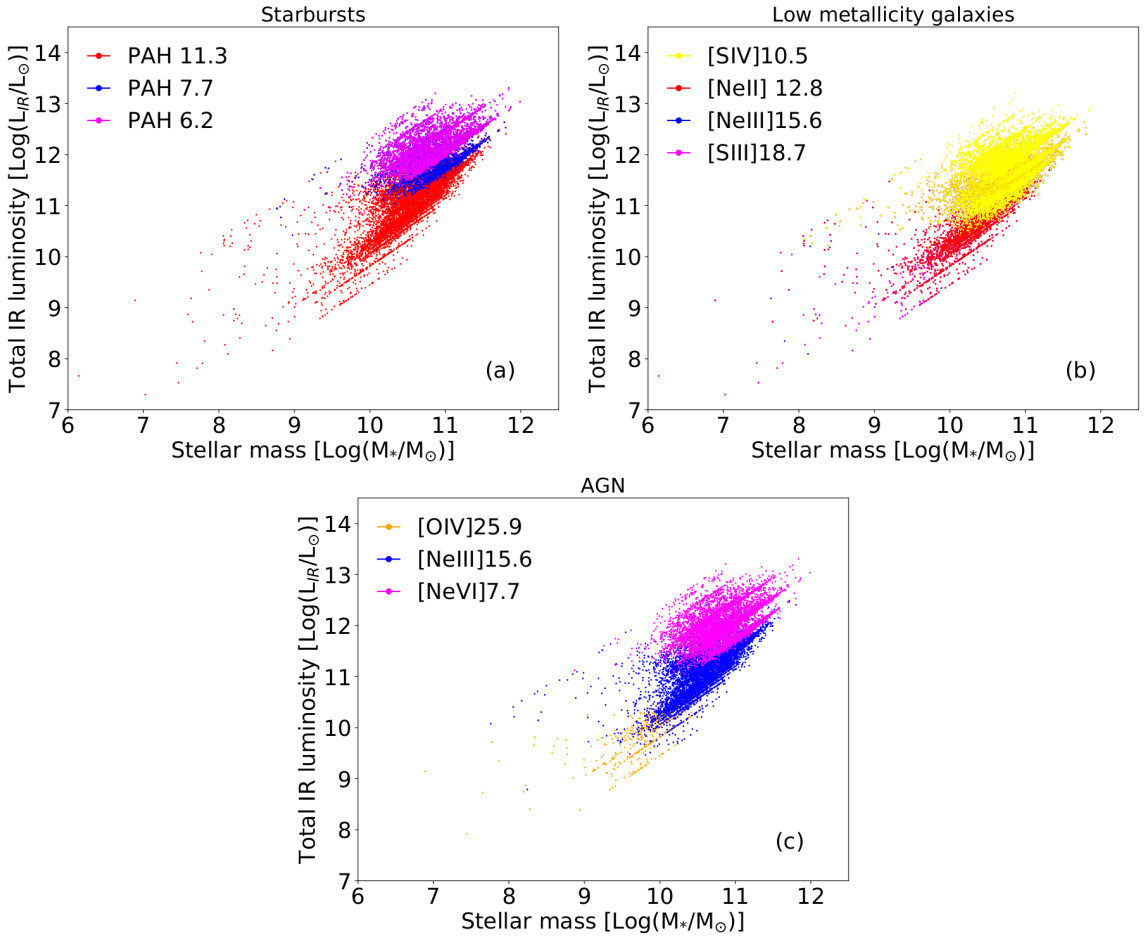

Figure 5.3: Stellar Mass – Luminosity diagrams of galaxies detectable in the SMI 1 deg^2 ultra-deep survey from the HELP database. **(a: top left)** Star Forming galaxies. **(b: top right)** Low Metallicity Galaxies. **(c: bottom)** AGN.

cover the z= $1-3$ redshift interval, while for the local Universe the [OIV]25.9µm line is a good alternative. In the z= $0.1-1$ redshift interval, the best tracer is the [NeIII]15.6µm line. It is important to notice that, while the [NeVI]7.7µm line, in the presence of a strong starburst component, can be hard to detect due to PAH emission in the same spectral range, especially considering the low resolution of the SMI/LR instrument, it can be a relatively bright line in strong AGN, like NGC1068, the prototypical Seyfert 2 galaxy, for which the PAH features are not detected (Lutz et al. 2000).

For LMG, the simulated detections are limited to redshift z~2.4, for the lack of suitable tracers that would cover the entire redshift range. However, the selected tracers can reach the knee of the luminosity function up to redshift z~ 1.5, while in the z= $1.5-2.2$ interval a survey of this type can cover sources that are about an order of magnitude above L*.

An advantage of using the data from the Herschel HELP database, is the possibility to analyze the stellar mass interval of the galaxies that can be detected with these surveys. I show these results in Fig. 5.3(a) for SFG, (b) for LMG and (c) for AGN. The PAH features appear to be a good tracer for the mass-luminosity interval covered by the HELP database, while the fine structure lines used as tracers for LMG cover a narrower interval. The AGN tracers, due to the reduced detection rate, only cover the highest end interval of the mass-luminosity diagram.

Fig. 5.4 shows the results for the simulation of the 15 deg^2 on the Herschel photometric fields. Panel (a) shows the results for the SFG, panel (b) for the LMG and panel (c) for the AGN. The deep survey can

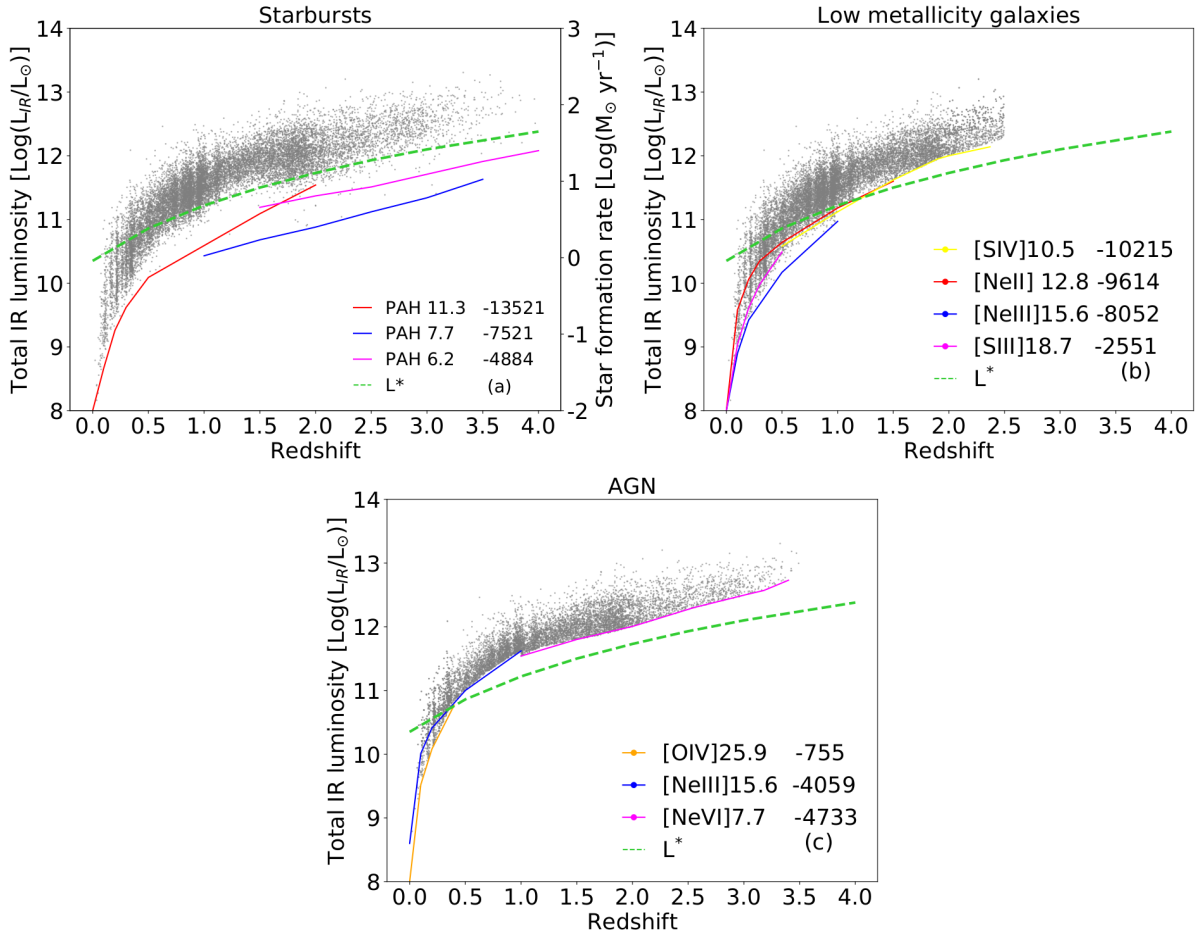

Figure 5.4: Redshift-luminosity diagrams simulating the SMI 15 deg^2 deep survey using the HELP database. I refer to Fig. 5.1 for the lines coding and legends in each frame. **(a: top left):** SF galaxies detectable with SMI in the PAH features. On the right-hand y-axis the SFR corresponding to the total L_{IR} is also given, adopting the conversion factor from Kennicutt & Evans (2012). **(b: top right):** SF galaxies, adopting the line calibration of low-metallicity galaxies ($\sim 1/5\,Z_\odot$), detectable with SMI in intermediate ionization fine-structure lines. **(c: bottom):** AGN detectable with SMI in high-ionization fine-structure lines.

reach SFG galaxies 0.5 to 1 dex below the knee of the luminosity function using the PAH features as tracers, covering the whole redshift interval up to redshift z~3.5. For the AGN tracers, the SMI deep survey will permit to detect sources below the knee of the luminosity function only up to z~ 0.5, while up to z~2.5 the detection limit is 0.5-0.8 dex above L*. For the $z = 2.5 - 3.5$ redshift interval, the detection limit lies ~1 dex above L*. For the LMG, the situation is intermediate between the results for SGF and AGN: the detection limit is below the knee of the luminosity function up to redshift $z \sim 1$, above L* of about 0.3 dex in the z=1-1.5 redshift interval, and 1 dex above L* in the $z = 1.5 - 2.2$ redshift interval.

What can be deduced from this simulation is that a hyper-deep survey, covering only 120 arcmin^2 with an SMI-like instrument, could detect all sources detected by Herschel in its deepest photometric fields, and even reach up to two orders of magnitude below the knee of the luminosity function at any redshift, covering up to z~4, using PAH features as tracers. For LMG, this survey could detect sources one order of magnitude below L* up to redshift z~2, using fine structure lines as tracers. For the AGN population, this survey could cover the redshift interval up to z~3.5 going ~0.8 dex below L*.

An ultra-deep survey covering 1 deg^2 would still detect PAH features in the whole population of galaxies observed by Herschel, allowing a complete census of the SFR density from spectral features. When

considering fine structure lines, however, it would be possible to reach sources below the knee of the luminosity function only up to z∼0.5 if considering AGN tracers. This implies the need of follow up mid- to far-IR spectroscopic observation to provide a complete census of BHAR density as a function of redshift. For LMG, this kind of survey would reach luminosities below L^* up to z∼1, while at higher redshifts the detection limit would be 0.2 dex above the knee of the luminosity function up to z∼1.5, and 1 dex for larger redshifts.

Finally, a 15 deg^2 deep survey will allow to detect galaxies below L^* up to z∼1 when using PAH features as tracers, or fine structure lines for LMG. For AGN, the knee of the luminosity function could instead be reached only up to redshift z∼0.5.

5.3.2 Simulations based on the luminosity functions

While the previous section was based on real photometric data from Herschel deep photometric fields, in this section I focus on the simulations based on the far-IR luminosity function derived by Wang et al. (2019). As for the previous case of HELP, the number of possible detections is computed using PAH features for SFG, intermediate ionization fine structure lines for LMG and high ionization fine structure lines for AGN.

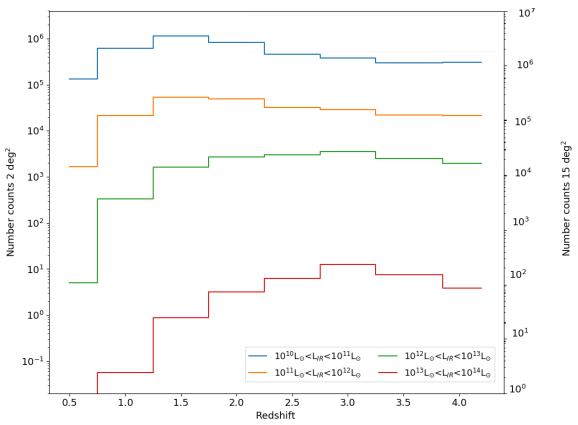

Figure 5.5: Expected galaxy number counts in the two fields of the SMI spectroscopic surveys, as derived from the Wang et al. (2019) luminosity functions. On the left y-axis are shown the counts as a function of redshift for different luminosities for the ultra-deep survey of 1 deg^2. On the right y-axis the same, for the deep survey of 15 deg^2.

Fig. 5.5 shows the number of galaxies present in a 1 deg^2 and 15 deg^2 area predicted by the luminosity functions, at different redshift and for different luminosity intervals. The number of galaxies that the three different surveys could be able to detect are instead reported in Tables 5.4, 5.3 and 5.2 for the hyper-deep survey (120 $arcmin^2$), ultra-deep survey (1 deg^2) and deep survey (15 deg^2), respectively. In these tables, for each redshift-luminosity interval the expected number of sources is reported as derived from the luminosity functions. Below this number is then reported the fraction of expected detection using AGN tracers (first column), LMG tracers (second column) or SFG tracers (third column). The same results are then presented in Figures 5.6, 5.7 and 5.8 In all figures, panel (a) shows the detection limits for PAH features applied to SFG, panel (b) shows the results for LMG and panel (c) shows the results for AGN, and next to each line or feature used as tracer is reported the number of objects that that tracer should detect in the entire survey.

As a general trend, the PAH features appear to be the best tracers to detect galaxies at fainter luminosities, reaching up to 2 dex below the knee of the luminosity function in the hyper deep survey, up to 1 dex below L^* in the ultra-deep survey and 0.5 dex below L^* in the deep survey for the entire redshift interval, reaching z∼4. For the LMG tracers, in the hyper deep survey, the entire interval up to redshift z∼2.4 is covered one

order of magnitude or more below the knee of the luminosity function. In the ultra-deep survey, the redshift interval is covered up to L*, while in the deep survey sources fainter than L* can be detected only up to redshift z∼1.2, while at z∼2.4 the tracers can reach 1 dex above the knee of the luminosity function. For the AGN tracers, the lack of strong tracers allows, in the hyper-deep survey, to cover 1 dex below L* up to redshift z∼3.5. In the ultra-deep survey, the [NeVI] line could be able to detect sources 0.2 dex below the knee of the luminosity function, while in the deep survey sources with luminosities below the knee of the luminosity function would be detected only up to redshift z∼0.5, while for the rest of the redshift interval the detection limit would be 0.5 dex above L*. When considered together, the three surveys would allow to detect a conspicuous amount of galaxies, even below the knee of the luminosity function, thus providing a thorough data set for follow up surveys with the pointed spectroscopic mode. While the detection of SFG below L* can be achieved at all redshift even with the deep survey, for AGN this will be possible only with the ultra- and hyper-deep surveys. However, the predicted number of sources detected should allow for an in-depth analysis of both star formation and black hole accretion through cosmic time, and in Section 5.4 I provide an estimate of the number of sources required to carry out these analysis.

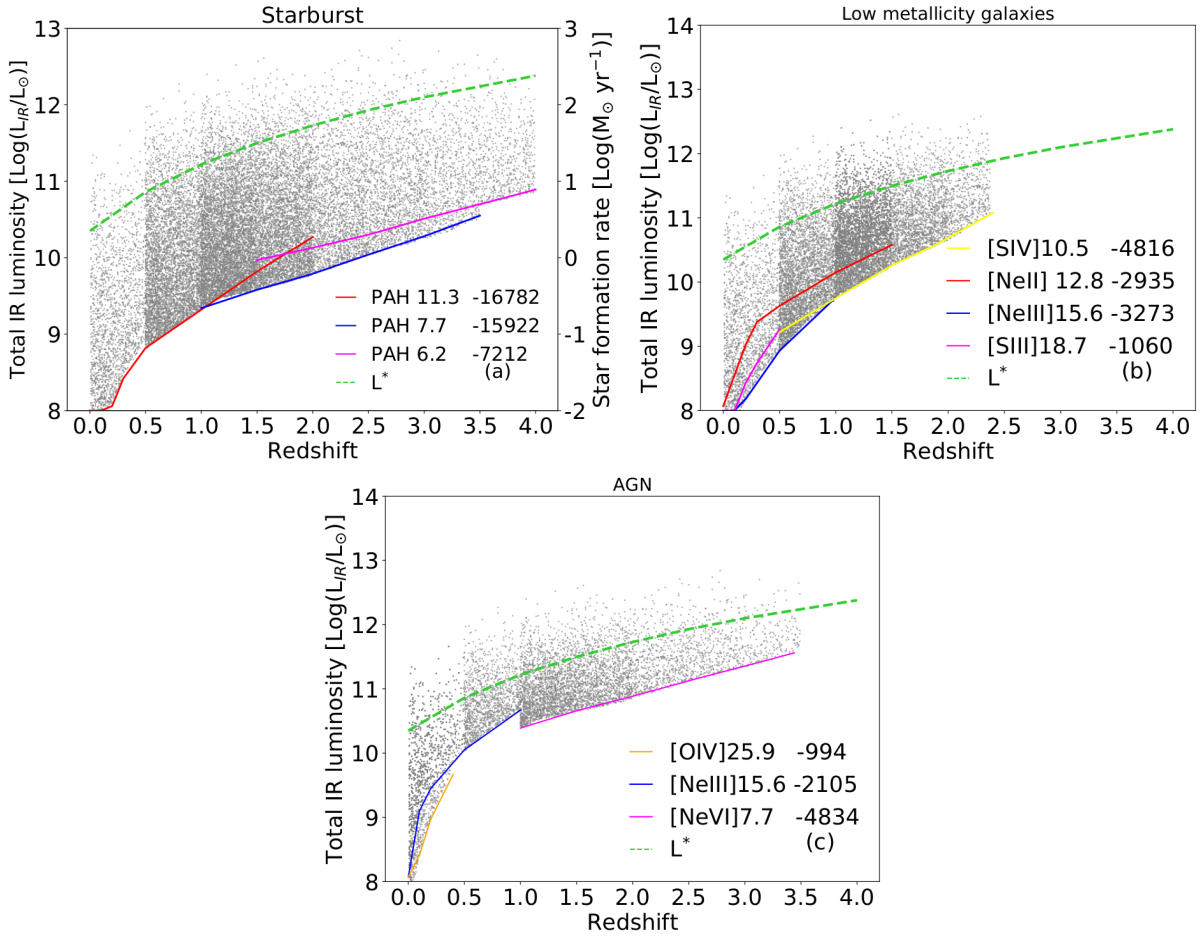

Figure 5.6: Redshift-luminosity diagrams simulating the SMI hyper-deep survey using the predictions from the far-IR Luminosity Functions (Wang et al. 2019). I refer to Fig. 5.1 for the lines coding and legends in each frame. **(a: top left):** SMI simulations of SF galaxies. On the right-hand y-axis the SFR corresponding to the total L_{IR} is also given, adopting the conversion factor from Kennicutt & Evans (2012). **(b: top right):** SMI simulations for SF galaxies assuming the low metallicity calibration. **(c: bottom):** SMI simulations of AGN.

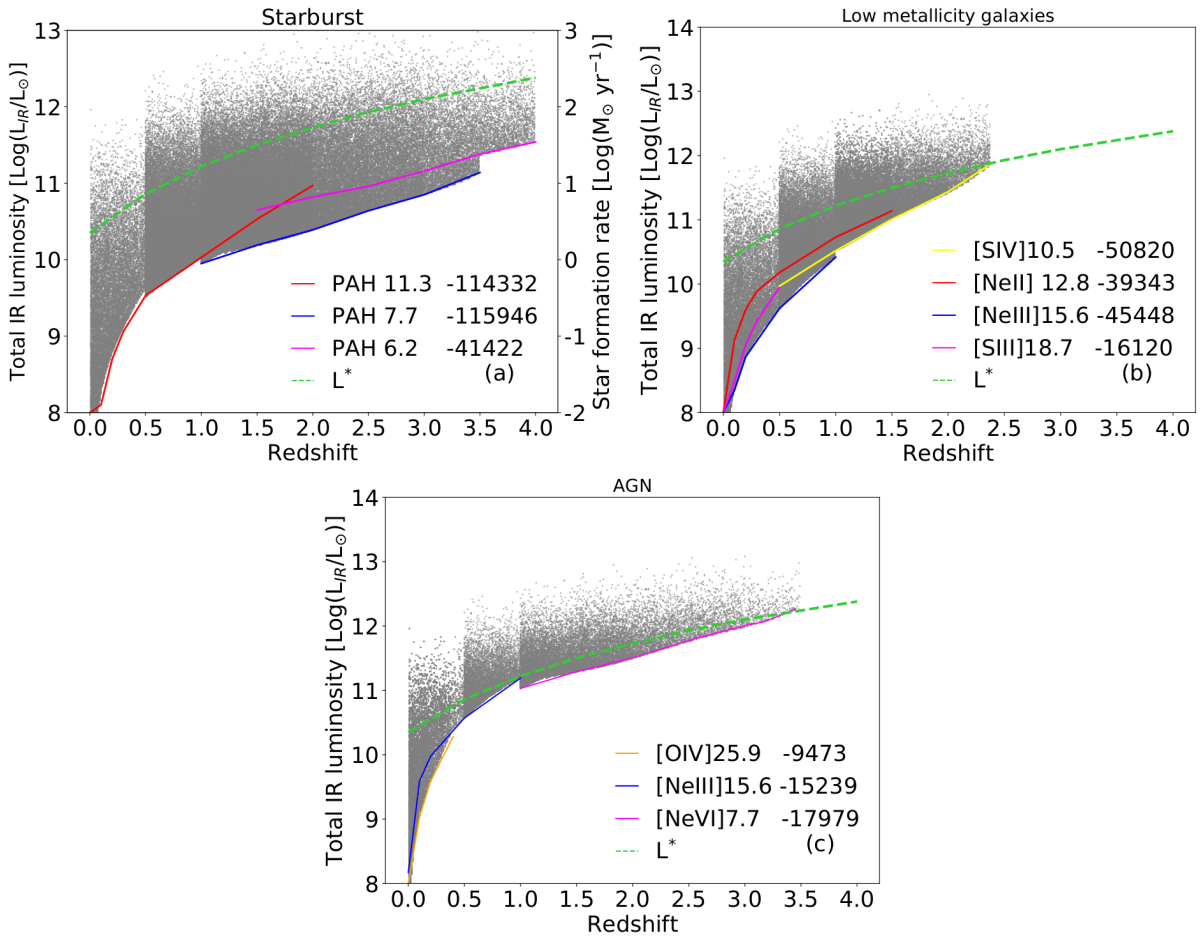

Figure 5.7: Redshift-luminosity diagrams simulating the SMI ultra-deep survey using the predictions from the far-IR Luminosity Functions (Wang et al. 2019). I refer to Fig. 5.1 for the lines coding and legends in each frame. **(a: top left):** SMI simulations of SF galaxies. On the right-hand y-axis the SFR corresponding to the total L_{IR} is also given, adopting the conversion factor from Kennicutt & Evans (2012). **(b: top right):** SMI simulations for SF galaxies assuming the low metallicity calibration. **(c: bottom):** SMI simulations of AGN.

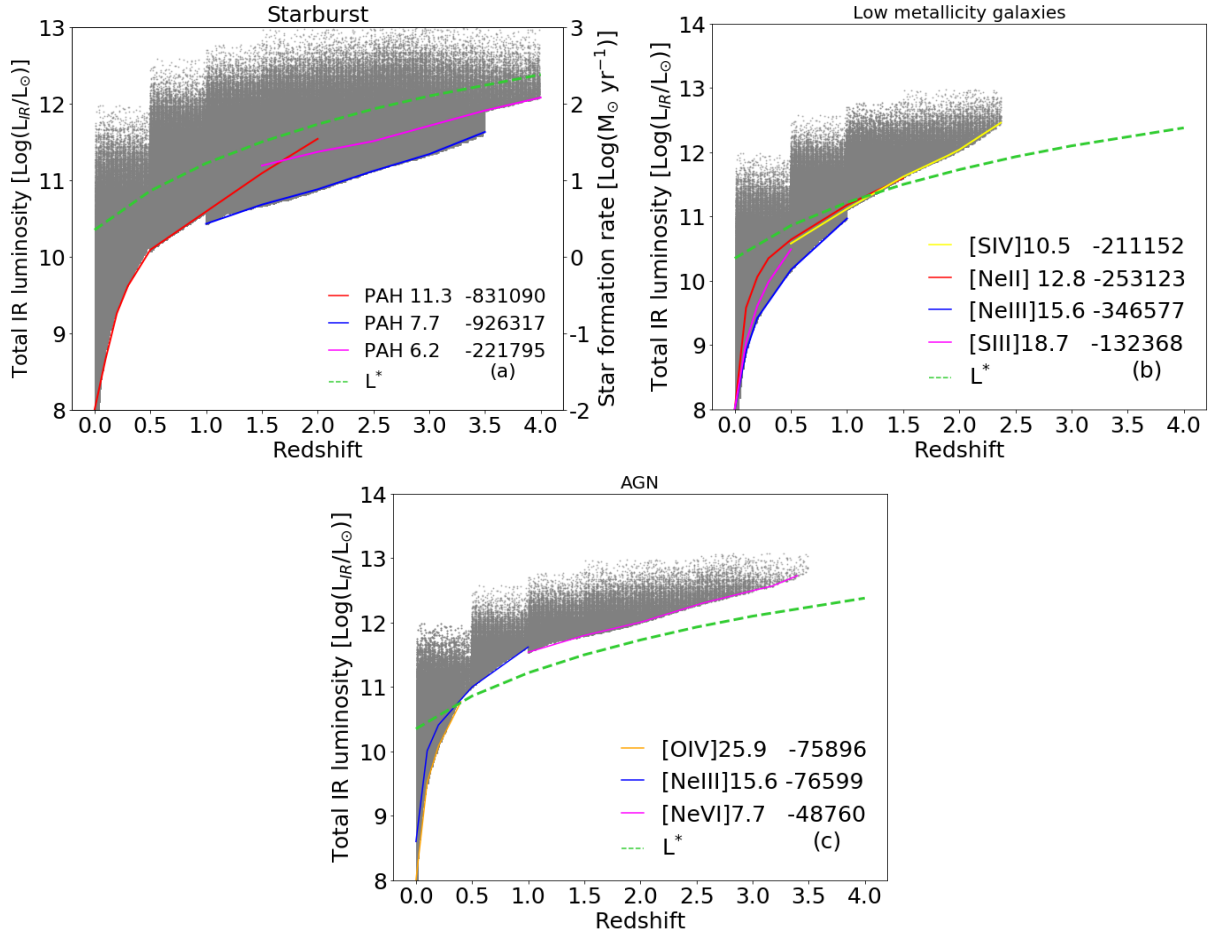

Figure 5.8: Redshift-luminosity diagrams simulating the SMI deep survey using the predictions from the far-IR Luminosity Functions (Wang et al. 2019). I refer to Fig. 5.1 for the lines coding and legends in each frame. **(a: top left):** SMI simulations of SF galaxies. On the right-hand y-axis the SFR corresponding to the total L_{IR} is also given, adopting the conversion factor from Kennicutt & Evans (2012). **(b: top right):** SMI simulations for SF galaxies assuming the low metallicity calibration. **(c: bottom):** SMI simulations of AGN.

Table 5.2: Total number of objects present in a 15 deg^2 area according to the luminosity functions by Wang et al. (2019) in each redshift-luminosity bin (first line in bold-face). For each bin are also reported (in the second line) the fractions of detections of AGN through fine-structure lines (left), of star forming galaxies through PAH features (center) and of low metallicity galaxies through fine-structure lines.

$\mathrm{Log}(L_{IR}/L_{\odot})$	0-0.5	0.5-1.0	1.0-1.5	1.5-2.0	2.0-2.5	2.5-3.0	3.0-3.5	3.5-4.0
13.0-13.5	-	-	-	-	-	-	-	-
12.5-13.0	-	-	**3**	**12**	**23**	**45**	**27**	**14**
			1 1 1	1 1 1	1 1 0.4	1 1 -	1 1 -	0.1 0.2 -
12.0-12.5	-	**29**	**245**	**600**	**901**	**1353**	**873**	**573**
		1 1 1	1 1 1	1 1 1	1 1 -	0.3 1 -	- 1 -	- 1 -
11.5-12.0	**18**	**1200**	**5752**	**9504**	**10279**	**11951**	**8325**	**6692**
	1 1 1	1 1 1	1 1 1	0.6 1 0.3	0.1 1 -	- 1 -	- 1 -	- 0.6 -
11.0-11.5	**576**	**14817**	**45940**	**52468**	**40424**	**38830**	**28955**	
	1 1 1	1 1 1	0.1 1 0.4	- 1 -	- 1 -	- 1 -	- 0.3 -	
10.5-11.0	**5599**	**65369**	**147861**	**129229**	**78949**			
	1 1 1	- 1 1	- 1 -	- 1 -	- 0.6 -			
10.0-10.5	**20937**	**140656**	**273947**	**206049**				
	1 1 1	- 1 0.2	- 0.8 -	- 0.2 -				
9.5-10	**42288**	**213956**						
	0.2 1 1	- 0.2 -						
9-9.5	**63713**							
	- 0.8 0.8							

Table 5.3: Total number of objects present in a 1 deg^2 area according to the luminosity functions by Wang et al. (2019) in each redshift-luminosity bin (first line in bold-face). For each bin are also reported (in the second line) the fractions of detections of AGN through fine-structure lines (left), of star forming galaxies through PAH features (center) and of low metallicity galaxies through fine-structure lines.

$\mathrm{Log}(L_{IR}/L_{\odot})$	0-0.5			0.5-1.0			1.0-1.5			1.5-2.0			2.0-2.5			2.5-3.0			3.0-3.5			3.5-4.0		
13.0-13.5		-			-			-			**1**			**2**			**3**			**2**			**1**		
										1	1	1	1	1	1	1	1	-	1	1	-	1	1	-
12.5-13.0		-			**2**			**16**			**40**			**60**			**90**			**58**			**38**		
				1	1	1	1	1	1	1	1	1	1	1	1	1	1	-	1	1	-	0.2	1	-
12.0-12.5		**1**			**80**			**383**			**634**			**685**			**797**			**555**			**446**		
	1	1	1	1	1	1	1	1	1	1	1	1	1	1	-	0.7	1	-	0.1	1	-	-	1	-
11.5-12.0		**38**			**988**			**3063**			**3498**			**2695**			**2589**			**1930**			**1787**		
	1	1	1	1	1	1	1	1	1	1	1	0.4	0.3	1		-	1	-	-	1	-	-	1	-
11.0-11.5		**373**			**4358**			**9991**			**8615**			**5263**			**4598**			**3560**					
	1	1	1	1	1	1	0.5	1	0.7	-	1	-	-	1	-	-	1	-	-	0.5	-			
10.5-11.0		**1396**			**9377**			**18263**			**13737**			**7689**			**6544**								
	1	1	1	0.2	1	1	-	0.8	-	-	1	-	-	0.8	-	-	0.2	-						
10.0-10.5		**2189**			**14264**			**26300**			**19079**														
	1	1	1	-	1	0.6	-	1	-	-	0.4	-												
9.5-10		**4248**			**19628**																				
	0.4	1	1	-	0.4	-																		
9-9.5		**5843**																							
	-	0.8	1																					

Table 5.4: Total number of objects present in a 120 arcmin^2 area according to the luminosity functions by Wang et al. (2019) in each redshift-luminosity bin (first line in bold-face). For each bin are also reported (in the second line) the fractions of detections of AGN through fine-structure lines (left), of star forming galaxies through PAH features (center) and of low metallicity galaxies through fine-structure lines.

$\text{Log}(L_{IR}/L_{\odot})$	0-0.5			0.5-1.0			1.0-1.5			1.5-2.0			2.0-2.5			2.5-3.0			3.0-3.5			3.5-4.0		
13.0-13.5		-			-			-			-			-			-			-			-	
12.5-13.0		-			-			**1**			**1**			**2**			**3**			**2**			**1**	
							1	1	1	1	1	1	1	1	1	1	1	-	1	1	-	1	1	-
12.0-12.5		-			**3**			**13**			**21**			**23**			**27**			**19**			**15**	
				1	1	1	1	1	1	1	1	1	1	1	1	1	1	-	1	1	-	1	1	-
11.5-12.0		**1**			**33**			**102**			**117**			**90**			**86**			**64**			**60**	
	1	1	1	1	1	1	1	1	1	1	1	1	1	1	1	1	1	-	0.5	1	-	-	0.7	-
11.0-11.5		**12**			**145**			**333**			**287**			**175**			**153**			**119**				
	1	1	1	1	1	1	1	1	1	1	1	1	0.8	1	0.2	0.2	1	-	-	0.3	-			
10.5-11.0		**47**			**313**			**609**			**458**			**256**			**218**							
	1	1	1	1	1	1	1	1	1	0.4	1	0.4	-	1	-	-	1	-						
10.0-10.5		**94**			**475**			**877**			**636**			**350**			**296**							
	1	1	1	0.8	1	1	-	1	0.6	-	1	-	-	1	-	-	0.6	-						
9.5-10		**142**			**654**			**1194**			**861**			**472**										
	1	1	1	-	1	1	-	1	-	-	0.8	-	-	0.2	-									
9-9.5		**195**			**654**			**1612**																
	0.8	1	1	-	0.8	-	-	0.4	-															
8.5-9		**263**																						
	-	1	1																					

5.4 Selection criteria for a sub-sample of galaxies for spectroscopic follow up

The blind spectro-photometric surveys described in Section 5.2 would provide a catalogue of previously undetected galaxies. In particular, with a SPICA like mission it would be possible to carry out deep spectro-photometric surveys at mid-IR wavelengths that will go deeper in photometric limit respect to what was previously obtained with Spitzer and Herschel. Moreover, with respect to optical and UV surveys, a SPICA like mission could detect those galaxies at the cosmic noon, where the bulk of SF and BHA is deeply embedded in dust obscured environments.

The large number of sources expected to be detected with blind surveys like the ones described in the previous Section makes it necessary to establish some criteria to define the number of sources on which to perform follow up spectroscopy. These criteria need to keep into account not only the space of the most relevant physical parameters required to satisfy the science goals of the missions, but also the number of sources necessary to obtain statistically significant results.

5.4.1 Selection criteria from physical parameters

The scientific goal for which these surveys are planned is that of physically characterize the evolution of galaxies via IR spectroscopy, thus measuring redshift, SFR, BHAR, metallicity and other properties of gas and dust. These quantities can then be used to constrain numerical simulations on galaxy evolution, as mentioned in Section 1.1.3 of the Introduction. While I refer to Section 5.6 for the scientific exploitation of the survey results, here I want to highlight the need to provide an atlas of galaxy spectra as a function of redshift, covering all the necessary physical parameters over which to study galaxy evolution.

The main parameters to consider, and that can be determined using a SPICA like observatory, are SFR and BHAR. Stellar mass is another important parameter, but the determination of this parameter relies on rest-frame near-IR observations, where is possible to observe the older stellar population. This task will need the observations, for instance, of Euclid (Laureijs et al. 2011), the Nancy Grace Roman Space Telescope (Green et al. 2012), or the Large Synoptic Survey Telescope (LSST, Ivezić et al. 2019). This adds a second requirement to the blind surveys: the chosen cosmological fields in which to carry out blind surveys needs to be selected depending also on the availability of ancillary data from present and future mission and ground-based facilities, so as to have the highest possible amount of information available.

In order to reach the scientific goals considered for a SPICA-like mission, the accuracy needed to determine the stellar mass should be below the typical intrinsic scatter of the scaling relation considered. For example, when considering galaxies around the M.-S., there is a dispersion of ~0.3 dex (Schreiber et al. 2015). Considering galaxies at high redshift, the uncertainty is primarily due to the assumed IMF, star formation history or the adopted mass-to-light ratio, while the accuracy of the near-IR photometry assumes a secondary role. All together these factors result in a dispersion of ~40% on the determination of the stellar mass value (see Reddy et al. 2012)

SFR Fig. 5.9 shows the SFR of galaxies in the M.-S. Here the values of luminosities as a function of redshift come from Scoville et al. (2007), assuming a galaxy stellar mass of $M_*=10^{10.7}M_\odot$ and a dispersion of 0.35 dex around the M.-S. (the shaded area in the figure, Schreiber et al. 2015). The relation between the L_{IR} and the SFR is taken from Kennicutt & Evans (2012). While this relation holds for local galaxies, it has not been tested for objects at higher redshifts. Other relations, however, are not available at the moment,

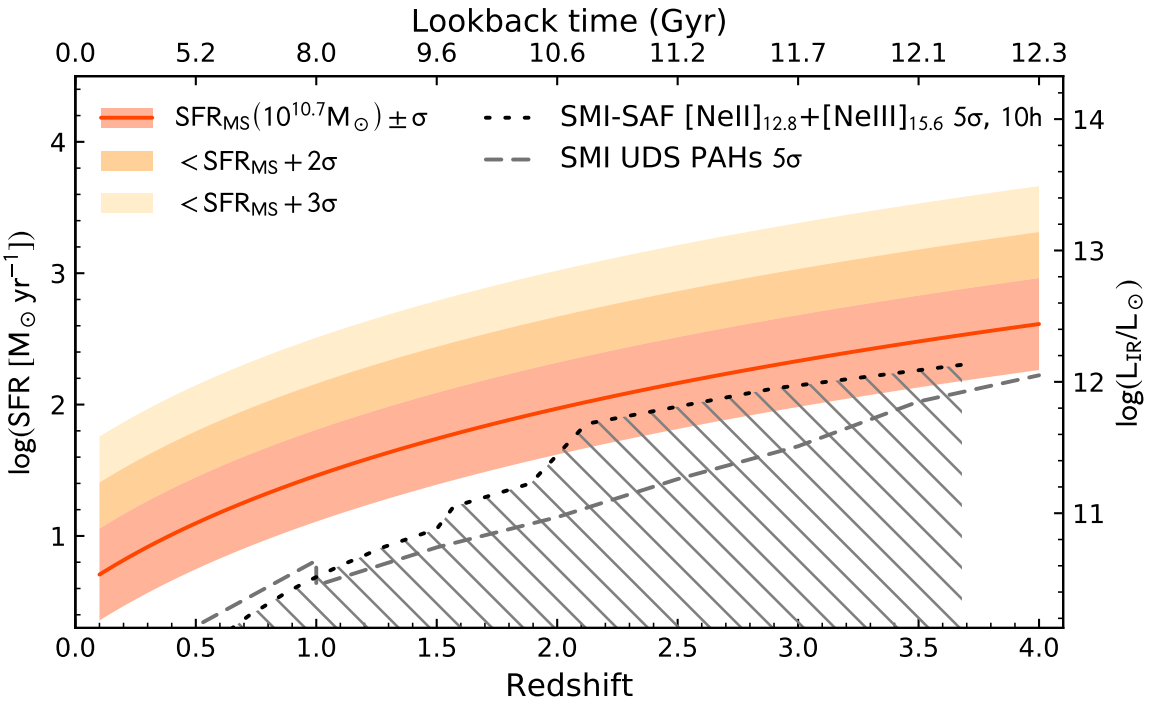

Figure 5.9: Star Formation Rate (SFR in $\mathrm{M_\odot\,yr^{-1}}$) as a function of redshift for a $10^{10.7}\,\mathrm{M_\odot}$ galaxy in the Main-Sequence (M.-S., red solid line; Scoville et al. 2017). The red shaded area shows the $0.35\,\mathrm{dex}$ intrinsic scatter around the M.-S. (Schreiber et al. 2015), while the dark and light orange shaded areas indicate the location of galaxies whose SFR is +2σ and +3σ above the M.-S., respectively. To derive the detectability of galaxies, two extreme scenarios are considered: solar-like metallicities where PAH emission is expected to be dominant in the mid-IR spectrum, and low metallicity galaxies where the brightest features should be the mid-ionization fine-structure lines. The dashed grey line corresponds to the 5σ sensitivity limit in the SFR derived from the PAH emission of star-forming galaxies detected in the SMI ultra-deep survey. Similarly, the black dotted line indicates the SMI and SAFARI 5σ sensitivities for a 10 hr. follow-up observation to derive the SFR from the main tracers at low metallicities, i.e. [NeII]12.8μm and [NeIII]15.6μm. The black dotted line shows the 5σ limit to measure the BHAR in AGN through the [OIV]25.9μm luminosity with SAFARI. The hatched area indicate the location of galaxies that require observations larger than 10 hr.

and the results form Kennicutt & Evans (2012) are used as a lower limit to the estimate of the SFR from the total IR luminosity. In the figure is also reported the 5σ sensitivity limit for the ultradeep SMI survey for PAH detection, while the black dotted line shows the 5σ sensitivity for a 10h limit follow-up with SAFARI or SMI/MR for the detection of the [NeII]12.8 and [NeIII]15.6 μm lines. As was described in Chapter 3 Section 5.9, these lines and features can be used to derive the SFR.

BHAR Fig. 5.10 shows the instantaneous BHAR, proportional to the AGN luminosity, as a function of redshift for an AGN in a M.-S. star forming galaxy with a stellar mass of M_*=$10^{10.7}$M$_\odot$. The SFR to BHAR calibration was taken from Diamond-Stanic & Rieke (2012), for a sample of nearby Seyfert galaxies. In the figure, the green shaded area shows the dispersion of the SFR-BHAR relation, equal to ~0.9 dex. This estimate can be applied only to the portion of galaxies in the M.-S. that are also undergoing a BH accretion phase at each epoch. For this reason, the BHAR has not been averaged over the entire duty cycle of the active nucleus. The BHAR can be measured using the [OIV]25.9 μm line, detectable with SAFARI pointed observations.

The space of the parameters needed to define a sample of galaxies for follow-up observations can be determined using figures 5.9 and 5.10. The sample of galaxies will need to cover:

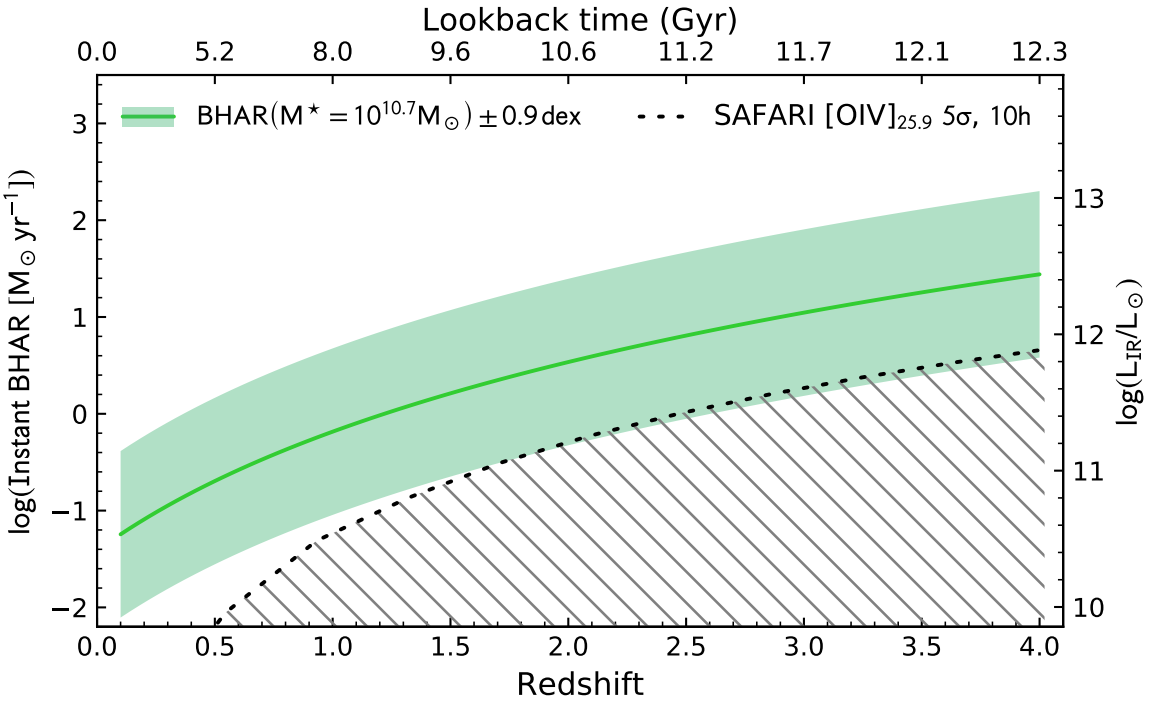

Figure 5.10: The green solid line indicates the instantaneous BH accretion rate (BHAR) as a function of redshift expected for a M-.S. galaxy with a mass of $10^{10.7}\,\mathrm{M}_{\odot}$ during its active BH accretion phase at each epoch. *SPICA* would measure the BHAR in these galaxies through the [OIV]$25.9\,\mu\mathrm{m}$ emission. The SFR-BHAR relation adopted was derived by Diamond-Stanic & Rieke (2012) for a sample of Seyfert galaxies in the nearby Universe. The associated dispersion of this relation is shown as a green shaded area. The hatched area indicate the location of galaxies that require observations larger than $10\,\mathrm{hr}$.

- a redshift range between z=0 and z=4;
- a range in SFR with log(SFR/$M_\odot yr^{-1}$) between 0.5 and 3, depending on redshift;
- a range in instantaneous BHAR with log(BHAR/$M_\odot yr^{-1}$) between -2 and 2, depending on redshift.

The conditions on the SFR and the BHAR translate into a requirement of L_{IR} between $\sim 10^{10}$ and 10^{13} $L_\odot$. Moreover, it is fundamental to consider a large sky distribution, taking into account over- and sub-densities with respect to the theoretical average distribution of galaxies, to appropriately consider the effects of environment in the evolution of galaxies.

5.4.2 Sample size

To establish the number of sources needed to accurately determine the physical parameters of galaxy evolution, a first estimate can come from the redshift intervals. Between redshift z=0 and z=4, considering bins of $\Delta z = 0.5$, results in eight bins. When considering the SFR, which can be translated to L_{IR} in SF galaxies, the minimum number of bins can be set to three. One of these bins would trace the evolution of the M.-S. with redshift for the majority of the galaxy population, thus reaching the knee of the mass function at $\sim 10^{10.7} M_\odot$. The bin width can be set as the intrinsic scatter of galaxies around the M.-S., ~0.35 dex. The other two bins should consider an offset from the M.-S. of +2σ and +3σ, in order to better trace the impact due to feedback processes and chemical enrichment, which are expected to greatly affect galaxies above the M.-S.

Bundy et al. (2015) suggest that, in the definition of a representative sample of galaxies, in order to obtain a precision of 0.1 dex per decade on the determination of the main parameters, it is necessary to have a detected difference between bins of $\sqrt{n/2}$, where n is the number of galaxies in each bin. This means that to have a precision of 4 to 5σ it is necessary to have between n =35 and n =50 galaxies per bin, which considering 3 luminosity bins and 8 redshift bins translates into a sub-sample of galaxies for follow up that includes between 800 and 1200. While this level of precision requires a larger number of objects per bin, a meaningful solution could still be obtained by adopting a lower precision of 3σ, decreasing the number of objects per bin to 20.

5.5 Pointed observations with SAFARI and SMI/MR

In this section, I estimate the limits, in term of total L_{IR} and redshift, that can be reached with pointed observations of the sub-sample defined in Section 5.4, using the SAFARI and SMI/MR template instruments.

In the following simulations, the SAFARI sensitivity was taken from Roelfsema et al. (2018), and for each line or feature I imposed the maximum observation time of 10 hr. Given the high sensitivity of the SMI/MR instrument, in all cases, the limit below the knee of the luminosity function was reached with observations shorter than 1 hr. In the following discussion I focus on the limits of observations carried out with a SAFARI like instrument.

Fig. 5.11 shows the redshift-luminosity diagrams for the high ionization lines of [OIV]25.9μm and [NeV]24.3 μm, ideal to trace AGN activity. Using a SAFARI-like instrument would allow to reach luminosities at the knee of the luminosity function L^* at redshifts $z > 0.5$ with a ~ 1hr observation for the [OIV]25.9 μm line, and with a ~ 5 hr observation for the [NeV]24.3μm line.

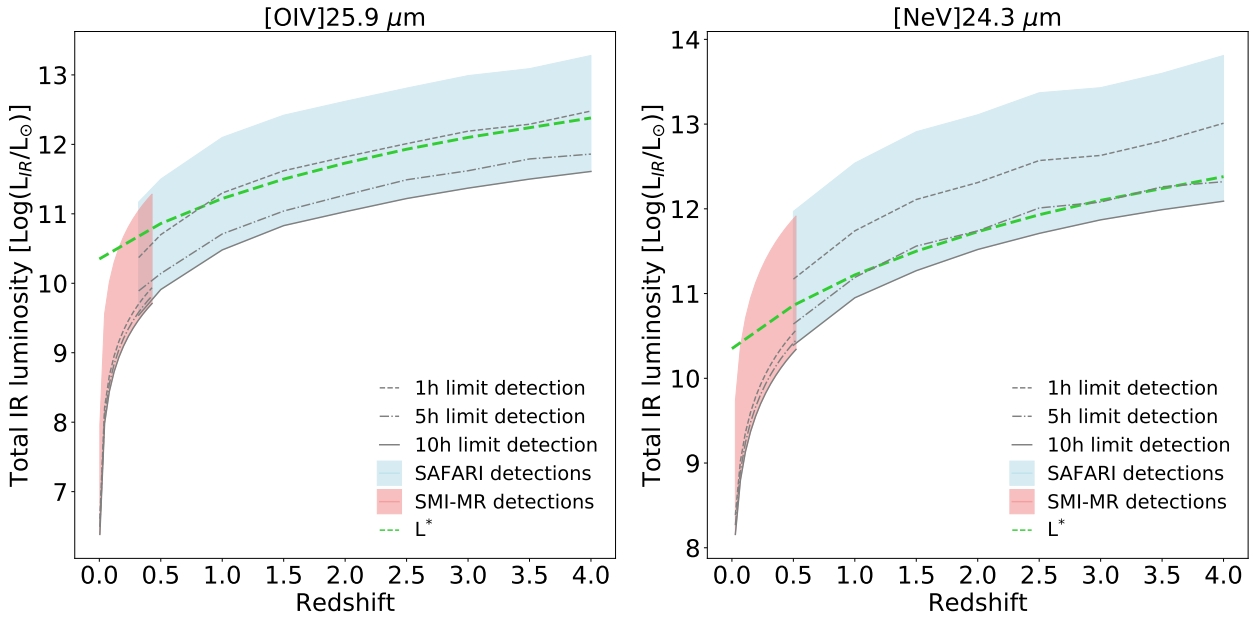

Figure 5.11: Redshift-luminosity diagrams simulating the AGN detections with SAFARI and SMI MR mode. **(a: left):** Detectability of the [OIV]25.9μm line. The red shaded area represents the detectability with SMI-MR, while the blue area indicated the detectability with SAFARI; grey horizontal lines represent lower limits for different observational times, namely less than 1 hour for the dot-dashed lines, 5 hours for the dashed lines, and 10 hours for the solid lines. The horizontal green line indicates the knee of the luminosity function. **(b: right):** Detectability of the [NeV]24.3μm line.

Fig. 5.12 shows the redshift-luminosity diagram for the [NeII]12.8μm and [NeIII]15.6 μm lines for the detection of SFG, while Fig. 5.13 show the same diagrams for the 11.3μm and 17μm PAH features. The [NeII]12.8μm line could be observed in galaxies with luminosities fainter than L^* with a ∼ 5 hr observation, while the [NeIII]15.6μm line, fainter in SFG, cannot be detected below the knee of the luminosity function even with a 10 hr observation, with a limiting luminosity 0.2 dex above L^*. The PAH features, on the other hand, could be detected in galaxies with luminosities below L^* with observations of ∼ 1 hr, reaching between ∼ 0.5 and ∼ 1 dex below the knee of the luminosity function with a pointed observation of 10 hr.

Fig. 5.14 show the redshift-luminosity diagrams for the [SIV]10.5μm and [NeIII]15.6μm lines as detected in LMG. The [SIV]10.5μm line could be observed with a SAFARI-like instrument at L^* with a ∼ 5 hr observation, going to 0.5 dex below the knee of the luminosity function for a ∼ 10 hr observation. In LMG galaxies the [NeIII]15.6μm line is stronger than in SFG, and can be observed below the knee of the luminosity function with a ∼ 1 hr observation, reaching sources one order of magnitude fainter than L^* with a ∼ 10 hr observation.

What emerges from these simulations is that a SPICA like instrument would be able to discriminate, spectroscopically, the star forming and AGN component of a composite galaxy. The deconvolution of the contribution of the two components to the total luminosity of a galaxy would then be done through various techniques, including the use of the EW of the lines and features and of particular line ratios (see, e.g. Diamond-Stanic & Rieke 2012; Tommasin et al. 2010) or through photoionization modeling (see, e.g. Pereira-Santaella et al. 2010; Spinoglio & Malkan 1992; Spinoglio et al. 2005; Zhuang et al. 2019). With the two component disentangled, it would be possible to measure SF and BHA luminosity function in the same population of galaxies. With the pointed observations of the above defined sample of galaxies, a SPICA-type observatory would be able to determine, in addition to SFRs and instantaneous BHARs, also

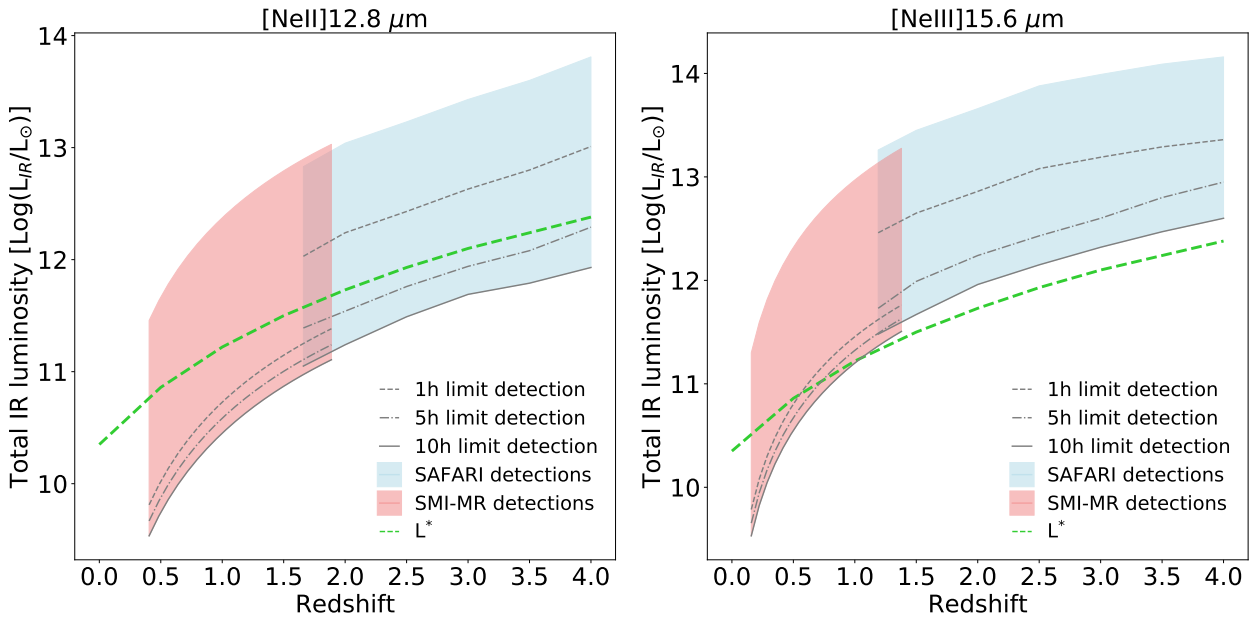

Figure 5.12: Redshift-luminosity diagrams simulating the SFG detections with SAFARI and SMI MR mode. (**a: left**) Detectability of the [NeII]12.8μm line. The same color code is applied as in Fig. 5.11. (**b: right**) Detectability of the [NeIII]15.6μm line.

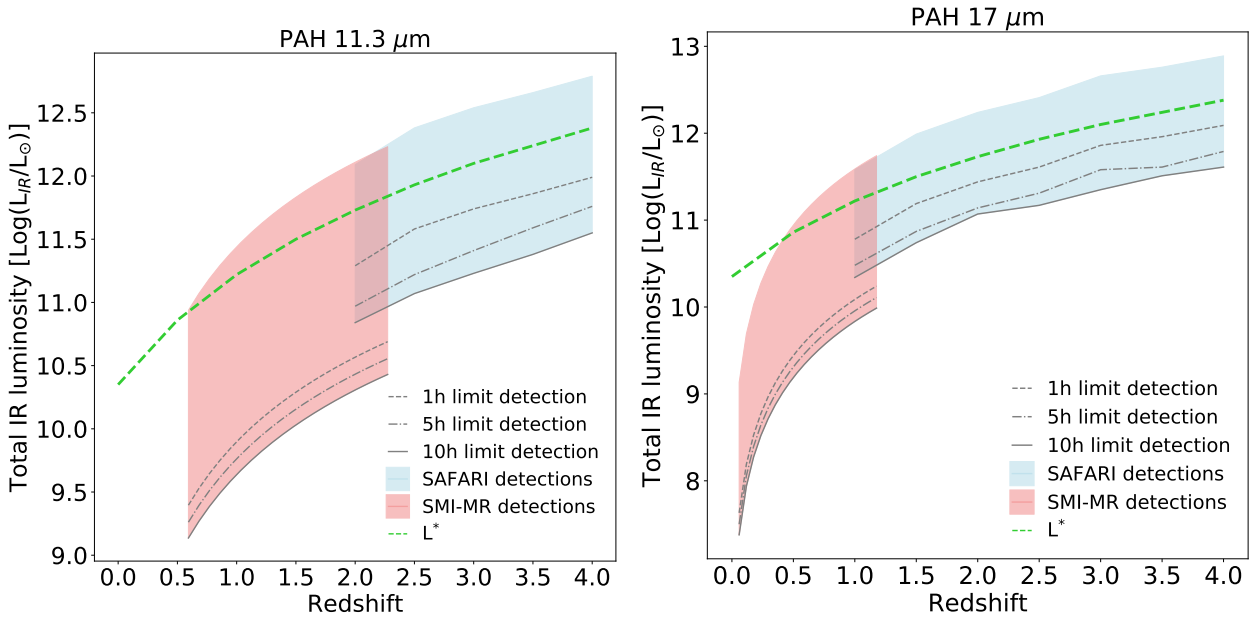

Figure 5.13: Redshift-luminosity diagrams simulating the SFG detections with SAFARI and SMI MR mode. (**a: left**) Detectability of the PAH 11.3μm feature. The same color code is applied as in Fig. 5.11. (**b: right**) Detectability of the PAH 17μm features.

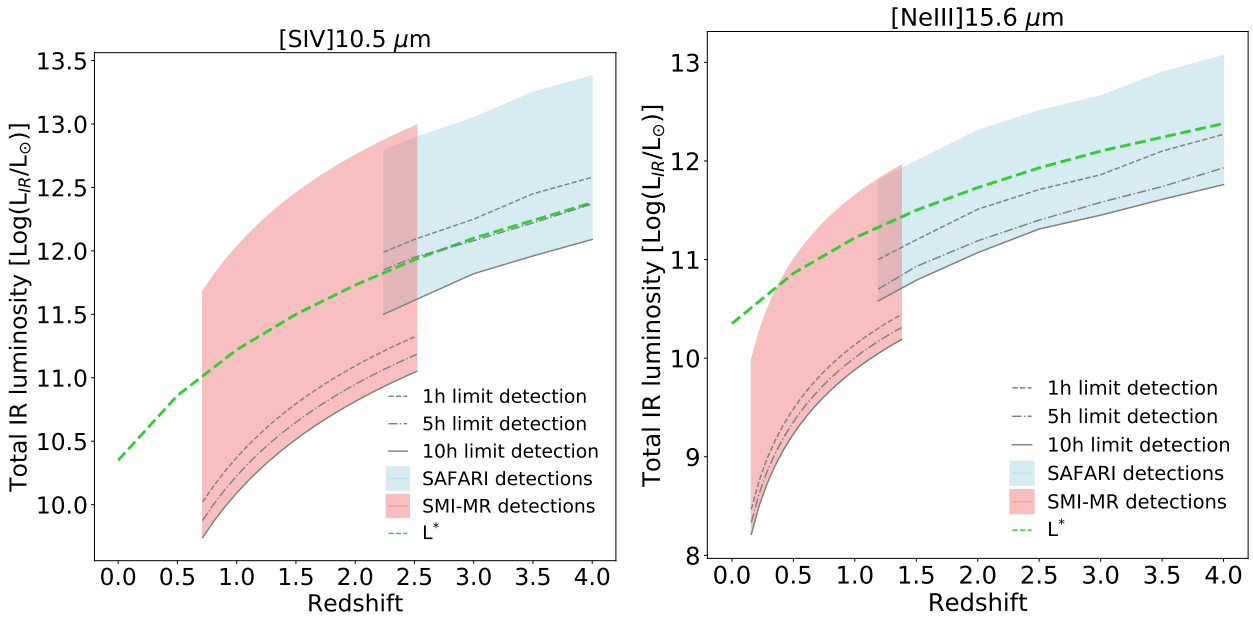

Figure 5.14: Redshift-luminosity diagrams simulating the LMG detections with SAFARI and SMI MR mode. (**a: left**) Detectability of the [SIV]10.5μm line. The same color code is applied as in Fig. 5.11. (**b: right**) Detectability of the [NeIII]15.6μm line.

the metal abundances and outflow/infall occurrence over cosmic time, as I show in the next sections.

5.6 Science output from surveys

The main goal of the cosmological surveys described in this chapter is to provide a characterization of the physical processes driving the growth and evolution of galaxies across cosmic time, and especially at the cosmic noon, covering all the relevant aspects: the environment, the feedback from massive outflows, the production of heavy elements and dust. Using an SMI-like instrument, with the described mapping capabilities, would provide a complete 3D view of the star formation process observing wide and deep cosmological volumes up to redshift z~4, from voids to cluster cores in over 90% of the cosmic time. Following the blind surveys, a relatively large (of order of a thousand) sample of sources would be selected to perform follow-up pointed IR spectroscopic observations, with higher spectral resolution grating spectrometers, such as SMI and SAFARI for the cases of the SPICA project, in order to answer the most challenging questions in the field of galaxy evolution. While the SAFARI instrument was not designed to perform multiple pointed observations at once, future instruments could be developed with spectrometers characterized by a combination features that allows for multiple object simultaneous detections at greater spectral resolution, thus significantly reducing the observational times.

Data from a SPICA like instrument would be used to constrain the results of numerical simulations on galaxy evolution. In particular, pointed observations with a SAFARI like instrument would help to determine the shape of the M_* to SFR function, or analogously of the M_{BH} to BHAR function, taking into considerations samples of galaxies in different environments and at different redshifts. The measured functions could then be used to bind the numerical simulations on the processes regulating the evolution of galaxies, such as the parameters regulating the various phenomena in the baryon cycle.

This Section explores how some of the principal questions regarding galaxy evolution could be answered with observations from a SPICA like instrument, and its synergies with other facilities.

5.6.1 Evolution of SF and BH accretion

The estimates of SFR and BHAR densities across cosmic time show that the two phenomena evolve in a parallel way, with a sharp decline toward the present epoch, with a factor ∼30 decrement in the energy output of the two phenomena from the output measured at the peak at the cosmic noon (see Section 1.2 and Madau & Dickinson 2014). While UV observations are extremely limited due to dust obscuration, and need to be corrected with large unknown extinction factors, and X-ray observations of the AGN population cannot account for the Compton-thick population contribution, mid- to far-IR spectroscopic cosmological surveys would allow to probe the heavily opaque medium of M.-S. galaxies at the cosmic noon ($z = 1 - 3$), to provide a full census of the SFR (using low ionization lines and PAH features) and BHAR (using high ionization lines) up to redshift z∼4 (see Section 5.2). Observations with a SPICA like telescope could help in determining what processes le to the peak of the two phenomena during the cosmic noon: to measure the SF and BHA components in the same large and representative sample of galaxies, covering a wide range in cosmic time, would allow to better comprehend the connection of SF and BHA as a function of stellar mass and environment, but also the relative role of the two phenomena in the galaxy growth and assembly processes. Moreover, while the blind surveys could explain the global properties observed, pointed observations would lead to a better understanding of how individual galaxies behave depending on stellar mass or environment.

Chapter 3 shows how one can derive both the SFR (Section 3.4) and the BHAR (Section 3.5) of galaxies as a function of cosmic time with rest-frame IR spectroscopy. These observations will rely on physical information on the sources (i.e. the gas and dust excitation, related to the ionizing spectra of the ultimate power sources) and not on model dependent assumptions and galaxy template SEDs. Ancillary data from other facilities are however needed to better constrain the results of the observations (e.g. stellar mass from missions like Euclid, Laureijs et al. 2011).

Moreover, from the blind surveys it would be possible to obtain a complete census of the shape and strength of the 9.7µm silicate feature, which could help determine what are the dust properties in AGN and starburst host galaxies, and how obscured these galaxies are. Dust emission and absorption in the line of sight can be measured from the profile of the silicate features and can be combined with additional diagnostics to discriminate between type 1 and type 2 AGN and correlated with X-ray obscuration. In addition, the central wavelength, width, and relative strength of the silicate features carry information on the dust chemical composition and grain properties (Fernández-Ontiveros et al. 2017; Xie et al. 2017). The 9.7µm silicate feature can, however, be difficult to observe in objects with strong PAH emission, since it can be obscured by the adjacent 7.7µm and 11.3µm PAH features. Moreover, the correlation among the silicate absorption in AGN and the hydrogen column density N_H as measured from X-rays, even if often ascribable to host galaxy obscuration and not necessarily to a compact torus surrounding the AGN (Goulding et al. 2012), might demonstrate the usefulness of silicates to detect and recognise heavily obscured AGN.

Deeply buried accreting BHs could be a substantial part of the AGN population, with their large obscuration making them virtually invisible to current X-ray surveys. Future X-ray missions such as *Athena* (Nandra et al. 2013) are particularly focused on detecting these elusive objects. The SPICA-like cosmological surveys would be able to detect the dust reprocessed radiation from Compton-Thick (CT) nuclei, with the largest obscuring columns ($N_H \gtrsim 10^{24.5}$ cm^{-2}) and moderate luminosities (Barchesi et al, 2021; submitted to PASA). In a faint/moderate luminosity regime ($L_X \sim 10^{42.3}$ erg s^{-1}), a SPICA-like observatory would be able to detect a significant fraction of obscured AGNs up to redshift z∼2 with the detection of the silicate feature at 9.7µm. In the high-luminosity regime ($L_X \sim 10^{44}$ erg s^{-1}), both Athena and a SPICA-like observatory

would detect CT AGN. This type of synergy is crucial to reconstruct the accretion history over cosmic time up to redshift z∼4. Mid- to far-IR spectroscopic follow-up of these deeply buried nuclei would then measure the BHAR through the high-ionization fine-structure lines of [OIV] and [NeV].

5.6.2 Evolution of the metallicity

The signature of galaxy evolution can be found in the evolutionary build up of the heavy elements. The metallicity evolution in galaxies is determined by the interplay among the different processes that constitute the baryon cycle (see Section 1.1.4, and Davé et al. 2012). A few of the main questions on the evolution of metallicity in galaxies concern which processes account for the chemical evolution of galaxies, how heavy elements and dust are produced, or how the different physical processes constituting the baryon cycle can be accounted for quantitatively. A complete picture of the role played by the different mechanisms should also explain how the global content of metals and dust in galaxies evolves with cosmic time, and how galaxies were assembled. The baryon cycle determines the relation among fundamental properties of galaxies such as the gas metallicity, the stellar mass, and the SFR.

In order to accurately describe the chemical evolution in galaxies, to quantify the abundances of the different species in the ISM, and to peer into the dust obscured phase of galaxy evolution, it is necessary to use the appropriate tracers, independent of dust extinction, radiation field and gas density. The use of mid- to far-IR tracers offers two main advantages: the IR lines are almost free from dust extinction, and they have a small dependency on the electron temperature (Section 3.1).

One of the main IR diagnostic tools to measure a galaxy metallicity is based on the [OIII]52,88μm to [NIII]57μm line ratio: the N/O ratio is linked to the star-formation history of the galaxy, and the subsequent global metallicity (Pilyugin et al. 2014; Vincenzo et al. 2016). Both elements present similar ionization potentials, and are almost independent of ionization parameter and hardness of the radiation field, and can thus be used as a proxy for the global N/O abundance ratio (Pérez-Montero & Contini 2009). This tracer can be applied to both SFG and AGN, with almost no dependence on temperature, extinction and density, allowing to measure galaxy metallicity up to redshift z∼1.6 using a SAFARI-like instrument (see top of Fig.5.15, and Fernández-Ontiveros et al. 2017; Pereira-Santaella et al. 2017).

A SPICA/SAFARI like instrument performing pointed observation toward an AGN-like object for a maximum of 10hrs, would be able to observe the [OIII]52μm line up to redshift z∼3.4, covering galaxies at the knee of the luminosity function only up to redshift z∼2; the [OIII]88μm line could instead be observed up to redshift z∼1.6, to luminosities ∼0.2dex above L^*. The [NIII]57μm line could instead be observed up to redshift z∼3, but could be observed in objects at the knee of the luminosity function only up to redshift z∼0.5.

Another indirect abundance diagnostic is based on the line ratio between ([NeII]12.8μm+[NeIII]15.6μm) and ([SIII]18.7μm+[SIV]10.5μm). This diagnostic is based on the calibration of line ratios sensitive to the metallicity. The [NeII] and [NeIII] lines on one hand, and the [SIV] and [SIII] lines on the other are the most important stages of ionization for neon and sulfur in both AGN and SFG. The sulfur total luminosity ([SIII]18.7μm+[SIV]10.5μm), remains almost constant with increasing metallicity, possibly due to the depletion of sulfur onto dust grains (Dors et al. 2016; Vidal et al. 2017), while the neon total luminosity ([NeII]12.8μm+[NeIII]15.6μm) increases with the neon abundance, which is not depleted onto dust grains. Fig. 5.15(bottom panel) shows a calibration of this ratio obtained from Spitzer/IRS spectra, compared to the metallicities obtained from indirect optical tracers for a sample of unobscured local SFG and LMG (Moustakas et al. 2010; Pilyugin et al. 2014). The shaded area shows photoionization models obtained with

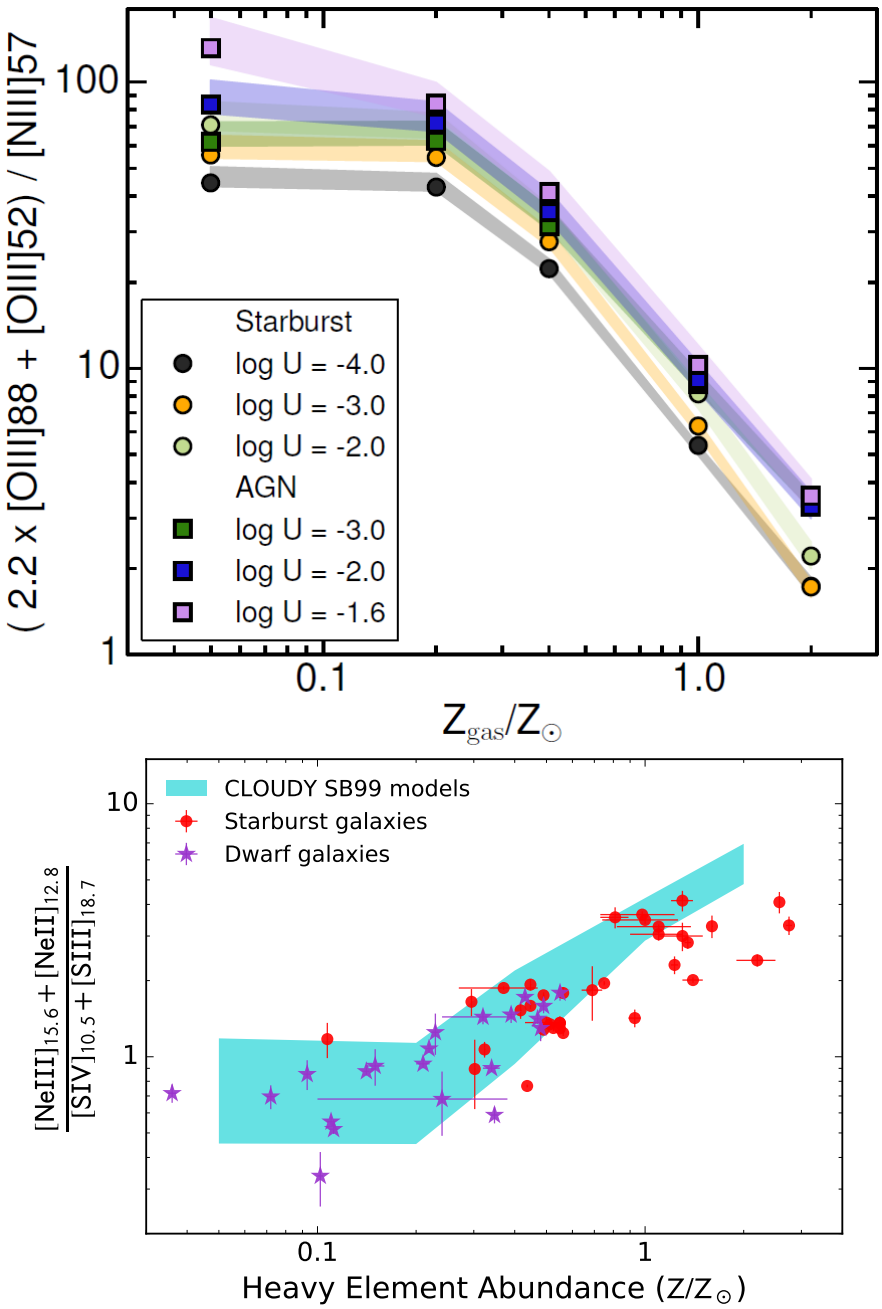

Figure 5.15: Top: AGN and starburst models for the metallicity sensitive (2.2[OIII]88μm+[OIII]52μm)/[NIII]57μm line ratio as a function of gas-phase metallicity. For each metallicity bin, those models with the same ionisation parameter but different densities are grouped and their median ratio is indicated by a circle (square) for the starburst (AGN) models. The shaded area represents the scatter due to the gas density dependence of this ratio for a given ionisation parameter. Figure from Pereira-Santaella et al. (2017). **Bottom:** the ([NeII]12.8μm+[NeIII]15.6μm) to ([SIII]18.7μm+[SIV]10.5μm) line ratio from *Spitzer*/IRS observations of starburst galaxies in the Local Universe vs. indirect gas-phase metallicity determined from strong optical lines (Moustakas et al. 2010; Pilyugin et al. 2014). The CLOUDY simulations including sulphur stagnation above Z>1/5 Z⊙ are in agreement with the observed increase of the line ratio with inscreasing metallicity for Z≳0.2 Z⊙ (Fernández-Ontiveros et al. 2017, 2016)

Cloudy simulations (Ferland et al. 2017) for a SFG galaxy, assuming constant sulphur abundance above Z=0.2 Z⊙. The neon abundance, on the other end, is set to increase linearly with the total metallicity (Fernández-Ontiveros et al. 2016). Model and observations agree, and suggest that the neon abundances derived with this method will be independent of ionization correction factors.

A SPICA-like instrument would be able to detect these lines in galaxies with luminosity ≃L* up to redshift z∼3-4. Using, for instance, pointed observations of a SAFARI like instrument toward LMG, it would be possible to observe the [NeII]12.8μm in galaxies with luminosities at the knee of the luminosity function up to redshift z∼4 in ∼5hr integration time, while the [NeIII]15.6μm line could be observed up to redshift z∼3.5 in less than 1hr integration time, and up to 5hr integration time for objects at redshift z∼4. The [SIII]18.7μm line could be observed in the z∼0.8-4 redshift interval in a 5hrs observation up to luminosities of the order of L*, while the [SIV]10.5μm line could instead be observed in the z∼2.2-4 redshift interval up to the knee of the luminosity function with an observation of 10hrs.

Another important diagnostic tool can be found in the [NeIII]15.6/[NeII]12.8 (or [SIV]10.5/[SIII]18.7) versus [OIV]25.9/[OIII]88 ratio (see Fig. 3.2 in Section 3.1, and Fernández-Ontiveros et al. 2016). In both cases, the ratio in the vertical axis, either [NeIII]15.6/[NeII]12.8 or [SIV]10.5/[SIII]18.7 ratio, is sensitive to the ionization, mostly driven by the metallicity in the stellar population, thus discriminating between star formation and BHA processes, with the LMG population that is significantly separated from both SFG and AGN. On the horizontal axis, on the other end, the [OIV]25.9/[OIII]88 ratio is a tracer able to discriminate between non-thermal excitation in AGN and thermal ionization produced by any kind of star formation activity. The combination of these line ratios allows to separate the different populations, providing an extinction-free diagnostic.

5.6.3 Feedback in the context of galaxy evolution

Feedback is invoked by current galaxy evolution simulations to explain the properties of massive galaxies in the local Universe, like the stellar mass-funciton, the quenching of star formation and the migration of galaxies from the blue to the red and dead sequence (Davé et al. 2012; Silk & Mamon 2012).

The most extreme cases of extragalactic feedback are observed in luminous and ultra-luminous infrared galaxies ((U)LIRGs), where both atomic/ionic and molecular winds have been observed, being molecular winds particularly important to understand the feedback process, since stars are formed from molecular gas and the central regions of obscured galaxies are rich in molecular gas (González-Alfonso et al. 2014).

Herschel/PACS (Pilbratt et al. 2010; Poglitsch et al. 2010), observed molecular outflows traced by hydroxyl (OH) in ULIRGs and were found to be ubiquitous in local ULIRGs (Fischer et al. 2010; González-Alfonso et al. 2017b; Spoon et al. 2013; Sturm et al. 2011; Veilleux et al. 2013). Figure 5.16 shows the P Cygni profiles of the OH 119μm doublet, indicating the presence of outflows in ULIRGs (González-Alfonso et al. 2017a).

At high redshift, however, direct evidence of outflows and the impact of feedback are less constrained, although they have been reported in ionic line observations (e.g. Harrison et al. 2014; Nesvadba et al. 2016), indicating that AGN feedback in the warm ionized phase could be common at high z, while so far there have been only a few possible detections of molecular outflows (González-Alfonso et al. 2017b). Massive outflows are expected in bright galaxies above the M.-S., where strong feedback should regulate their growth by quenching the SF, driving these galaxies back to the M.-S. (e.g. Tacchella et al. 2016). An important issue when analyzing feedback is the relative role of AGN driven winds versus starburst/SNe driven winds. Untangling the two phenomena is crucial and can be done by considering the energy balance that can be

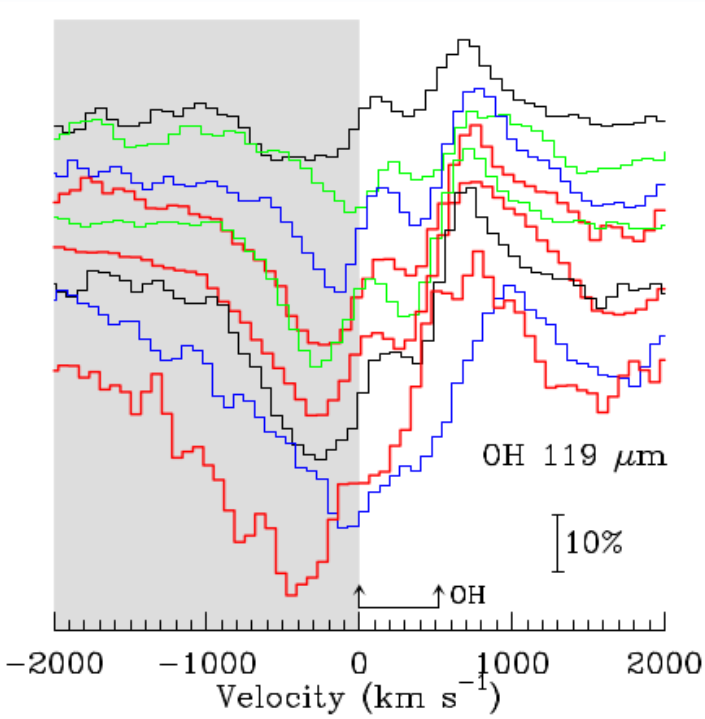

Figure 5.16: The OH doublet at 119μm in 9 local ULIRGs observed with Herschel/PACS, selected as examples of ULIRGs with P-Cygni profiles to illustrate the molecular gas outflow (figure from González-Alfonso et al. 2017a).

constrained by the measure of the outflow kinetic energy, the AGN bolometric luminosity and the SFR (see, e.g. Cicone et al. 2014; Fiore et al. 2017).

Moreover, an in-depth analysis of the feedback phenomenon could help explain the observed trend in AGN and star formation activity, in particular in determining if there is a trend between feedback processes and AGN and star formation activities, or what is the link between AGN feedback on small scales and the molecular outflows observed on larger spatial scales, and how these affect the chemical composition of the ISM, or whether the AGN feedback is sufficient to explain star formation quenching.

A SPICA-type observatory would be able to detect massive molecular gas outflows through P-Cygni profiles in the OH119 μm and OH79 μm doublets, as well as strong absorption profiles in the OH doublets at 65 μm and 84 μm, up to $z \sim 2$, while at lower redshift (z<1) also H_2O and $OH_,$ lines would be detected at high spectral resolution (González-Alfonso et al. 2017b). The ionized phase of AGN outflows would be traced, with the high-resolution spectrometers onboard a SPICA-like observatory, by highly ionized emission lines such as [OIV] 25.9μm (Pereira-Santaella et al. 2010) and [Ne V] 14.3 and 24.3μm (Spoon & Holt 2009), or through [OIII] 52 and 88μm in nearby galaxies. While this phase represents a minor fraction of the total outflowing mass, its velocity is typically much higher ($\lesssim \times 5$) when compared to the molecular phase, and can be driven farther away from the galaxy. Thus, the spatially resolved kinematic analysis of highly ionized gas in local, $z < 0.1$, galaxies with SPICA would allow the determination of the amount of gas that can effectively escape the galactic potential well, contributing to the definitive quenching of the host. For $z < 0.3$, nuclear outflows would be detected in the [OIV] 25.9μm line with the sensitivity required to detect the OH doublets, which would be combined with the simultaneous observations of the [OIII] lines to probe the ionization parameter of the outflowing ionized gas, the relationship with the ultra-fast outflows in X-rays and the molecular phase, including the stratification of the winds (e.g., Tombesi et al. 2015), and

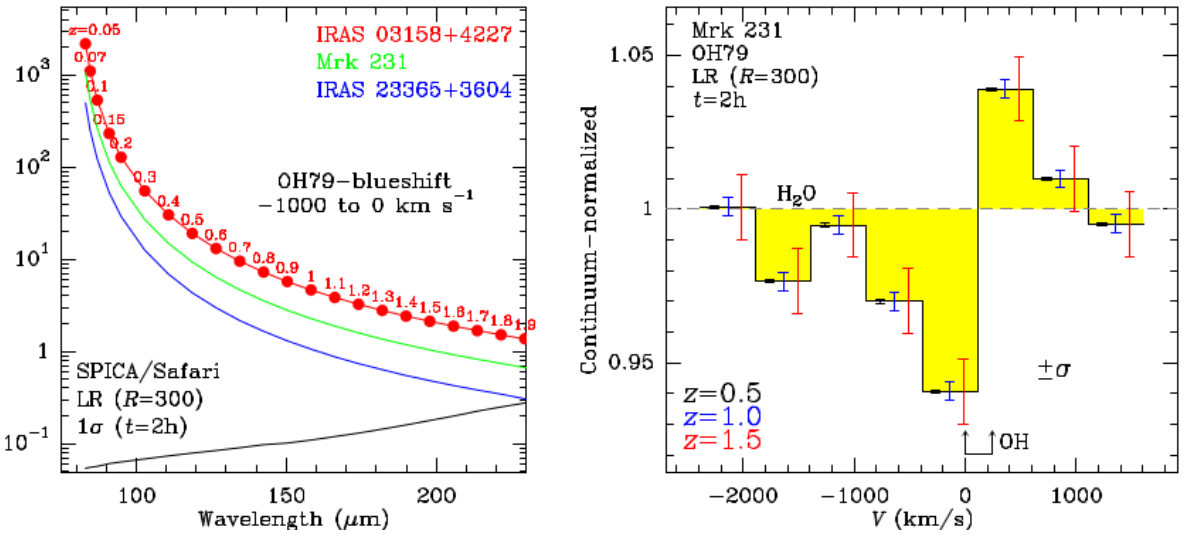

Figure 5.17: Left: Predicted integrated absorbing flux of the OH79 doublet in three local ULIRGs (IRAS 03158+4227, Mrk 231, and IRAS 23365+3604, all showing P-Cygni profiles in OH79) at blueshifted velocities (from -1000 km s^{-1} to 0 km s^{-1}) as a function of redshift (red numbers) and observed wavelength (abscissa). The black curve shows the sensitivity (1σ) expected for SPICA/SAFARI LR (R = 300) with 2 hours of observing time, indicating that molecular outflows would be easily detected in ULIRGs up to $z = 1.3 - 1.9$. Right: The continuum-normalized OH79 spectrum of Mrk 231 as observed with Herschel/PACS smoothed to the resolution of SPICA/SAFARI LR, with 2 spectral points per resolution element. The three errorbars in each spectral channel indicate the $\pm\sigma$ uncertainty for SAFARI with 2 hours of observing time at the selected redshifts of z =0.5, 1.0, and 1.5. The absorption at V < -1300 km s^{-1} is due to H_2O $4_{23} - 3_{12}$. Note that not only the blueshifted absorption wing would be detected, but also the redshifted emission feature (i.e. P-Cygni), unambiguously revealing outflowing gas (figure from González-Alfonso et al. 2017a).

their AGN/SB origin.

In particular, considering observations with the low resolution channel (R~300), a SAFARI like instrument could detect the OH 79μm doublet up to redshift z~1.9 in strong emitters, or up to redshift z~1.3 for more moderate emitters, with a 2hr observation (see Fig. 5.17). Simulations of the low resolution observing mode of a SAFARI like instrument predict, in fact, a clear P-Cygni line shape for the OH79 doublet in outflowing sources, thus unambiguously revealing massive molecular outflows (González-Alfonso et al. 2017b).

On the other hand, the ground-state OH 119μm doublet could be observed with a SPICA/SAFARI like instrument up to redshift z~0.94. Fig. 5.18 shows the simulations for the observation of the OH119 doublet at high (R~600) resolution, showing how the P-Cygni profile should be visible with a 4hr observation. The observation of the various OH doublets would allow to estimate the different energy contributions associated with the outflows (González-Alfonso et al. 2017c), potentially constraining the outflow luminosity function in several redshift bins up to redshift z~1. In addition, it would also be possible to derive statistics on the outflow velocity (Stone et al. 2016; Sturm et al. 2011; Veilleux et al. 2013), the mass outflow rates, momentum and energy fluxes (González-Alfonso et al. 2017c) as a function of the SF or AGN luminosities.

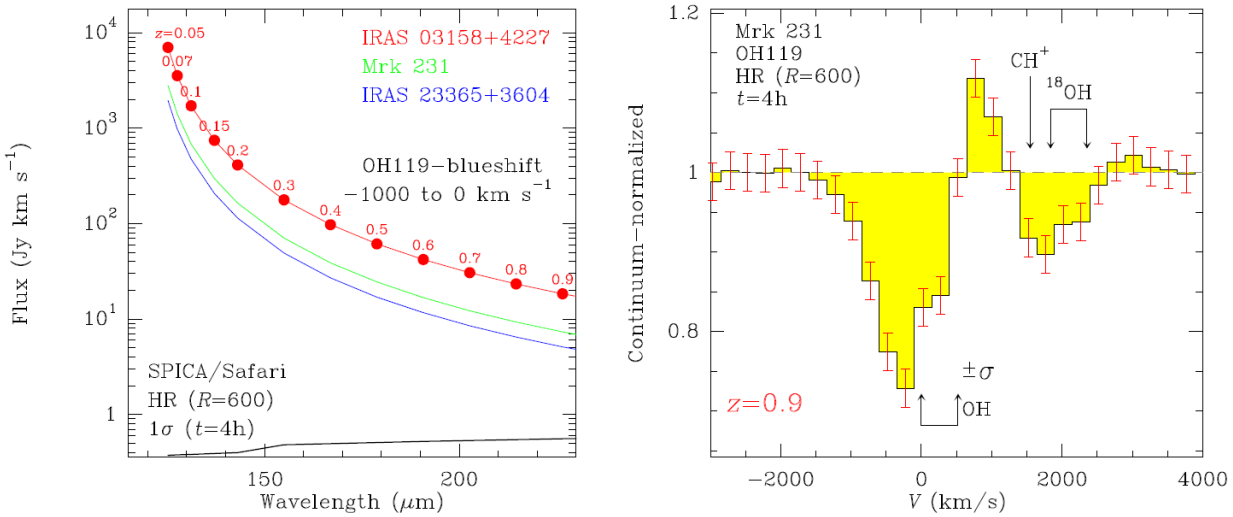

Figure 5.18: Left: Predicted integrated absorbing flux of the OH119µm doublet in three local ULIRGs (IRAS 03158+4227, Mrk 231, and IRAS 23365+3604) as a function of redshift (red numbers) and observed wavelength (x-axis). The black curve shows the sensitivity (1σ) expected for SPICA/SAFARI HR (R = 600) with 4 hours of observing time, indicating that molecular outflows would be easily detected in ULIRGs up to z=1.3-1.9. **Right:** The continuum-normalized OH119 spectrum of Mrk 231 as observed with Herschel/PACS smoothed to the resolution of SPICA/SAFARI HR, with 2 spectral points per resolution element. The error bars in each spectral channel indicate the uncertainty for SAFARI with 4 hours of observing time at redshifts z ≈ 0.94. Contribution to the absorption by ^{18}OH would also be detectable, constraining the metallicity of the sources (Figure from González-Alfonso et al. 2017b)

Chapter 6

Application to other facilities/Future work

6.1 Introduction

The lines and features presented in this work can be observed in galaxies by present and future IR/(sub)-mm facilities. At the present time, the Stratospheric Observatory for Infrared Astronomy (SOFIA, Gehrz et al. 2009), observing from the high atmosphere, can observe the mid- to far-IR emission for the brightest galaxies in the local Universe, although with limitations from residual atmospheric absorption and emission. The ALMA and Very Large Telescope (VLT, Enard 1991), covering the 0.3-3.6 mm and 0.3-20μm range respectively, allow to observe from the near-UV to the millimeter range, although with large gaps in the mid- to far-IR, due to atmospheric absorption, in both local and high-redshift galaxies, thus probing the different aspects of the baryon cycle at various points in cosmic time. *JWST* will be the next NASA observatory to explore the Universe in the near- and mid-IR spectral range. In particular, the *JWST* Mid-InfraRed Instrument (MIRI, Rieke et al. 2015; Wright et al. 2015) will be able to obtain imaging and spectra with unprecedented sensitivity in the 4.9–$28.9\,\mu\mathrm{m}$ range. The Near InfraRed Spectrograph (NIRSpec, Posselt et al. 2004) will instead be able to perform spectroscopic mapping in the 0.6-5μm interval, thus allowing to cover the optical-UV emission of high redshift sources. In a near future the extremely large ground-based telescopes under construction, with dedicated instruments for *N*-band spectroscopy will be able to obtain observations of the mid-IR spectral range 8–13 $\mu\mathrm{m}$ and thus will be able to measure the SFR through the $[\mathrm{SIV}]_{10.5\mu\mathrm{m}}$ + $[\mathrm{NeII}]_{12.8\mu\mathrm{m}}$ relation, for local star forming galaxies, and the PAH at $11.25\,\mu\mathrm{m}$ for AGN. The ESO Extremely Large telescope (E-ELT; Gilmozzi & Spyromilio 2007) is expected to obtain first light at the end of 2025, with the Mid-infrared ELT Imager and Spectrograph (METIS, Brandl et al. 2021) instrument covering the N band with imaging and low resolution spectroscopy; the Thirty Meter Telescope (TMT; Schöck et al. 2009) will have completed first light and will be ready for science at the end of 2027, and the Giant Magellan Telescope (GMT; Johns et al. 2012) will be operational in 2029.

In this chapter, I analyze the possibility of detecting star formation and BHA tracers using the MIRI-JWST instrument and the ALMA telescope, respectively in Sections 6.3.1 and 6.3.2, comparing the predicted flux of key lines as a function of redshift and sensitivity of the two instruments. For MIRI-JWST, the tracers analyzed in Chapter 3 Section 3.4 and 3.5 can be used only up to redshift z∼1 due to the redshift displacement that shifts these tracers out of the spectral range covered by MIRI. It is however possible to use different lines, at shorter wavelength, to trace both processes up to redshift z∼3. For ALMA, instead, the [CII]158 $\mu\mathrm{m}$ line is confirmed as one of the best SFR tracer, which can be observed up to redshift z∼9, even though it is not possible to probe lines at redshifts lower than $z \simeq 3$, thus missing the Cosmic Noon. It is important to

Table 6.1: Fine-structure lines in the mid-IR range. The columns correspond to the central wavelength, frequency, ionisation potential, excitation temperature, critical density from: Satyapal et al. (2021)

Line	λ (μm)	ν (GHz)	**I.P.** (eV)	**E** (K)	n_{cr} (cm^{-3})
[MgIV]	4.49	66811.78	80	–	1.258×10^{7}
[ArVI]	4.53	66208.58	75	–	7.621×10^{5}
[ArII]	6.98	42929.48	16	–	4.192×10^{5}
[NeVI]	7.65	39188.56	126.21	1888	2.5×10^{5}
[ArIII]	8.99	33351.11	28	–	3.491×10^{5}

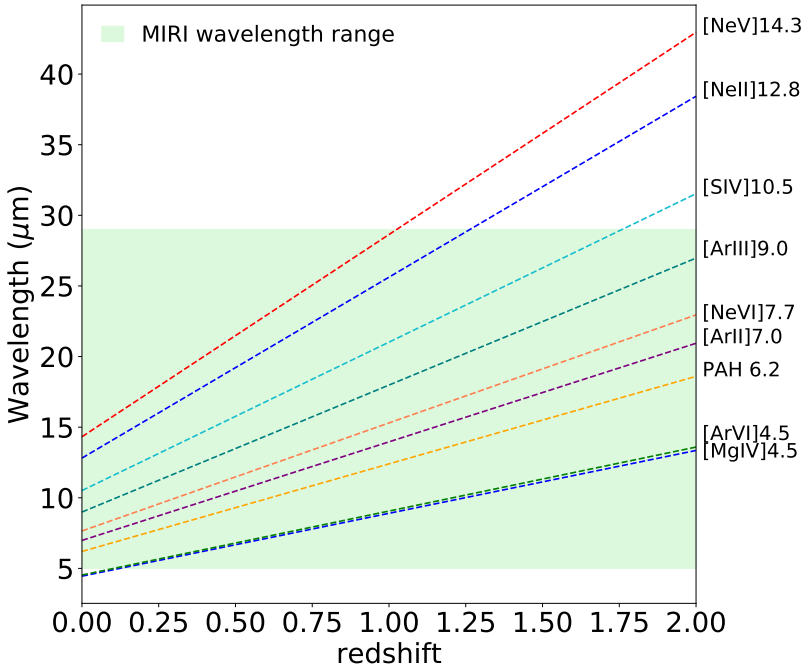

Figure 6.1: Observability of key mid-IR (dashed lines) lines compared to the *JWST*-MIRI instrument (shaded area) in the 0-1.6 redshift interval.

note, however, that both instruments are not efficient in performing wide-field blind surveys, except for those with a limited area (few $arcsec^2$) and thus require to observe targets already discovered by other facilities, e.g. single dish large sub-mm telescopes (e.g. SPT or LMT). Although pointed observations with JWST can probe the BHAR (using weak lines in the mid-IR) and SFR (mostly through PAHs) in galaxies at the Cosmic Noon, and the ALMA telescope can probe galaxies beyond redshift z∼3, a comprehensive study of galaxy evolution can only be achieved with a SPICA-like mission, capable of performing spectroscopic surveys in the mid- to far-IR range of large cosmological volumes.

6.1.1 The Cosmic Noon as seen by JWST in the mid-IR

The JWST-MIRI instrument can perform spectroscopic imaging observations in the 4.9–28.9 μm range through integral field units. Fig. 6.1 shows the instrument spectral range and the maximum redshift at which key lines and features in the mid-IR range can be observed. The JWST-MIRI cut-off wavelength of ∼29μm significantly limits the possibility of probing accretion phenomena through the brightest lines,

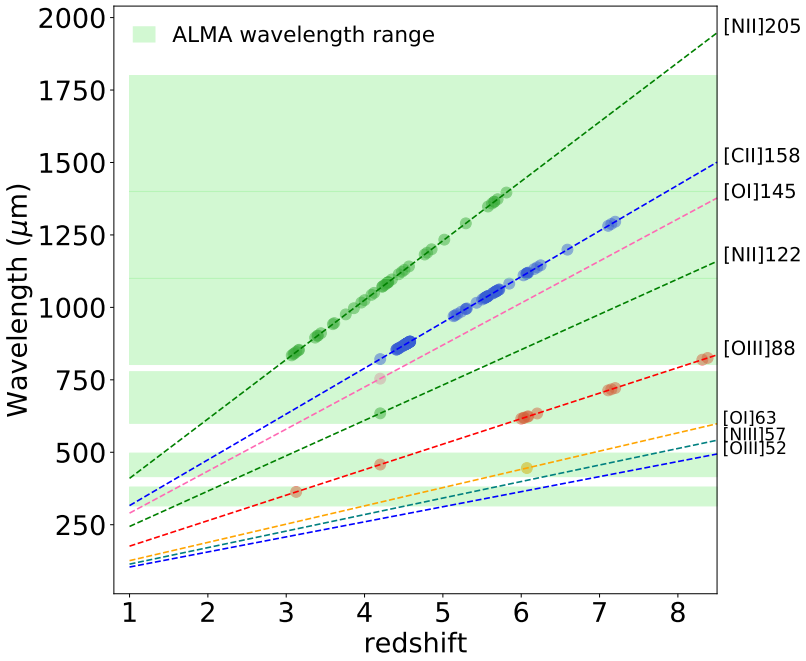

Figure 6.2: Observability of key far-IR (dashed lines) lines compared to the ALMA bands (shaded area) in the 1-8 redshift interval. Dots represent current detection for each line.

unobservable beyond redshift z>1, missing about half of the accretion history. The best spectroscopic tracers to measure the BHAR in the mid-IR, i.e. [NeV]14.3μm and [OIV]25.9μm, cannot be observed beyond the local Universe, $z \gtrsim 0.9$ in the best case (see, e.g. Meléndez et al. 2008; Sturm et al. 2002; Tommasin et al. 2010, 2008). The [NeV]24.3 μm and [OIV]25.9 μm lines are not shown in this figure due to the limited range available: the former line can be observed up to redshift z≃0.15, and the latter line can be observed up to redshift z≃0.1. The [NeV]14.3 μm line can be observed by JWST-MIRI up to redshift z≃1.

Alternative tracers for BHAR that could be used with the JWST-MIRI to probe the accretion processes beyond redshift z∼1 have been proposed by Satyapal et al. (2021): these authors analyze the possibility of detecting Compton-thick AGNs using an integrated modeling approach in which both the line and emergent continuum are predicted from gas exposed to the ionizing radiation from a young starburst or an AGN, focusing specifically on the spectral diagnostics available through the instruments MIRI and NIRSpec (Near Infrared Spectrograph; Bagnasco et al. 2007; Birkmann et al. 2016). In particular, they provide predictions of the detectability of key diagnostic lines such as [MgIV]4.49 μm, [ArVI]4.53μm and [NeVI]7.65μm, which appear to be ideal tracers of heavily obscured AGN and can potentially be detected in AGN with moderate activity up to redshift z∼3. These lines, however, have not been extensively observed so far, and their behaviour is mainly derived from photo-ionization models.

At the same time, star forming galaxies up to redshift z∼2 could be traced only by the PAH features, which behaviour at high redshifts is not yet well understood. These features could in fact be destroyed by a strong radiation field, or be less efficiently formed due to low metallicity, (e.g. Cormier et al. 2015; Engelbracht et al. 2008; Galliano et al. 2021). On the other hand, while alternative SFR tracers can be found in optical lines (e.g. Álvarez-Márquez et al. 2019) or photometric bands (e.g. Senarath et al. 2018), mid-IR spectroscopic tracers have not yet been analyzed.

Table 6.2: Line ratios derived from CLOUDY simulations by Fernández-Ontiveros et al. (2016) for AGN, SFG and LMG: log(U) indicates the logarithm of the ionization parameter, while $\log(n_H)$ indicates the logarithm of the hydrogen density.

AGN	log U	-1.5	-1.5	-2.5	-2.5
	$\log(n_H/cm^{-3})$	2	4	2	4
	[MgIV]4.49/[NeV]14.3	0.09	0.11	0.72	1.00
	[ArVI]4.53/[NeV]14.3	0.10	0.14	0.03	0.04
	[NeVI]7.68/[NeV]14.3	0.58	0.78	0.04	0.06
SFG	log U	-2.5	-2.5	-3.5	-3.5
	$\log(n_H/cm^{-3})$	1	3	1	3
	[ArII]6.98/[NeII]12.8	0.05	0.06	0.12	0.12
	[ArIII]8.99/[NeII]12.8	0.66	0.68	0.32	0.32
	$\frac{[ArII]6.98+[ArIII]8.99}{[NeII]12.8+[NeIII]15.6}$	0.30	0.30	0.38	0.38
LMG	log U	-2	-2	-3	-3
	$\log(n_H/cm^{-3})$	1	3	1	3
	[ArII]6.98/[NeII]12.8	0.12	0.12	0.12	0.11
	[ArIII]8.99/[NeII]12.8	8.31	8.29	1.41	1.40
	$\frac{[ArII]6.98+[ArIII]8.99}{[NeII]12.8+[NeIII]15.6}$	0.19	0.18	0.27	0.27

6.1.2 Galaxy evolution with ALMA beyond the Cosmic Noon

While JWST will allow us to probe galaxies at redshift below $z \lesssim 3$ using mid-IR lines, the ALMA telescope will allow us to probe galaxies at redshifts $z \gtrsim 3$. In particular, the SFR could be traced using far-IR lines, like the [OIII]88μm and the [CII]158μm lines up to redshift $z \simeq 8$, as shown in the Fig. 6.2, providing important information on the evolution of galaxies with cosmic time. An analogous figure can be found in Carilli & Walter (2013, see their fig. 1), where the CO transitions and other key tracers of the ISM are shown as a function of redshift versus frequency in terms of the observability by ALMA and JVLA (Karl J. Jansky Very Large Array, Perley et al. 2011). As can be seen in the figure, the [OIII]88μm, [CII]158μm and [NII]205μm lines have been detected over an extended redshift interval, from z~3-4 to z~6-8, while the shorter wavelength lines, such as [OI]63μm, present very few results. No detections have been reported so far for the [OIII]52μm and [NIII]57μm lines. This is due to the difficulty of observing in the bands at higher frequency, for which the atmospheric absorption allows good visibility only for ~10% of the total observational time. While ALMA cannot detect these far-IR fine-structure lines in galaxies at the peak of their activity ($1 \lesssim z \lesssim 3$), it allows us to probe galaxies at earlier epochs, thus shedding light on what processes led to the Cosmic Noon. The observations available in the rest-frame far-IR continuum, due to thermal emission, suggest that, even before the Cosmic Noon, dust was already present in galaxies active regions (e.g. Laporte et al. 2017), and IR tracers are needed in order to probe these obscured regions and understand the physical processes taking place.

6.2 Methods

I assess how the JWST-MIRI and ALMA instruments can measure the star formation rate (SFR) and the black hole accretion rate (BHAR) covering, respectively, the $z \lesssim 3$ and $z \gtrsim 3$ redshift intervals. The predictions for

JWST-MIRI have been derived using the CLOUDY (Ferland et al. 2017) photo-ionization models computed by Fernández-Ontiveros et al. (2016), using the BPASS v2.2 stellar population synthetic library (Stanway & Eldridge 2018) for the case of the star forming models. I consider, in particular, three classes of objects, as presented in Chapter 3: AGN, SFG, and LMG covering the ∼7≤12 + log (O/H)≤8.5 metallicity range (Cormier et al. 2015; Madden et al. 2013). This is motivated by the detection of massive galaxies (∼10^{10} $M_{\odot}$) in optical surveys with sub-solar metallicities during the Cosmic Noon, which may experience a fast chemical evolution above z∼2 (Maiolino et al. 2008; Mannucci et al. 2009; Onodera et al. 2016; Troncoso et al. 2014). These changes are expected to have an impact on the ISM structure of high-z galaxies, favouring stronger radiation fields (e.g. Kashino et al. 2019; Sanders et al. 2020; Steidel et al. 2016) and a more porous ISM similar to that observed in dwarf galaxies (Cormier et al. 2019).

To measure the BHAR, I consider the [MgIV] 4.49μm, [ArVI] 4.53μm (see, e.g., Satyapal et al. 2021) and the [NeVI] 7.65μm line. The properties of these lines are summarized in Table 6.1. I then use the template of an AGN of total IR luminosity of $L_{IR}=10^{12}L_{\odot}$, to represent the bulk of the population at redshift z∼2. I use four different photo-ionization models to derive the line intensities, with two values of the ionization parameter: log U=-1.5 and log U=-2.5, and two values of the hydrogen density: $\log(n_H/cm^{-3})=2$ and $\log(n_H/cm^{-3})=4$. The calibration of the line luminosities, against the total IR luminosities, has been derived using the ratios of the high-excitation magnesium, argon and neon lines relative to the [NeV]14.3μm line in the photo-ionization models, and the calibration of the [NeV]14.3μm presented in Chapter 3.

As SFR tracers, I take into account the [ArII]6.98μm and [ArIII]8.99μm lines, and consider both SFG and LMG, deriving, in both cases, the line intensities dependent on the calibration of the [NeII]12.8μm line. For the SFG, I consider photo-ionization models with an ionization parameter of log U=-2.5 and log U=-3.5, and a hydrogen density of $\log(n_H/cm^{-3})=1$ and $\log(n_H/cm^{-3})=3$, for a total of four different cases. For the LMG, instead, I consider a ionization parameter of log U=-2 and log U=-3, and hydrogen densities of $\log(n_H/cm^{-3})=1$ and $\log(n_H/cm^{-3})=3$. In both cases, the total IR luminosity of the galaxy was fixed at $L_{IR}=10^{12}L_{\odot}$.

While the spectral range covered by ALMA has no unambiguous high ionization line that can be used to trace the BHAR, I explore what lines, or combination of them, can be used to trace the SFR. I consider the [CII]158μm line and the sum of two oxygen lines, either the [OI]63μm and [OIII]88μm, or the [OI]145μm and [OIII]88μm.

Table 6.1 gives the key properties of the lines used in this Chapter and not previously reported. Table 6.2 reports the line ratios used to derive the line intensities for the [MgIV]4.49μm, [ArVI]4.53μm, [ArII]6.98μm, [NeVI]7.65μm and [ArIII]8.99μm lines, given the different combinations of ionization parameter and hydrogen densities. Table 6.3 reports the calibrations computed from the photo-ionization models scaled to the [NeII]12.8 μm and [NeV]14.3μm lines (see Section 6.3.1).

6.3 Results

6.3.1 Predictions for JWST

In this section, I predict the intensities of the mid-IR lines and features in the 5-9μm range, as derived from CLOUDY models, and compare them with the JWST-MIRI sensitivity, to verify if these lines, used as tracers for SFR and BHAR, can be observed in objects at redshifts z>1. Table 6.3 reports the derived correlations of the lines used in this Chapter for the most common values of ionization potential (log U) and gas density [$\log(n_H/cm^{-3})$] for each type of object. For the AGN lines, I use the calibration of the

Table 6.3: Calibrations of the fine-structure line luminosities against the total IR luminosities ($\log L_{Line} = a \log L_{IR} + b$), derived from the line ratios reported in Table 6.2. For the AGN lines, the $\log U = -2.5$ $\log(n_H/cm^{-3}) = 2$ values were used, $\log U = -3.5$ $\log(n_H/cm^{-3}) = 3$ for the SFG and $\log U = -2$ $\log(n_H/cm^{-3}) = 1$ for LMG.

Line	AGN		SFG		LMG	
	a	*b*	*a*	*b*	*a*	*b*
[MgIV]4.49	1.32	-5.15	–	–	–	–
[ArVI]4.53	1.32	-6.53	–	–	–	–
[NeVI]7.65	1.32	-6.41	–	–	–	–
[ArII]6.98	–	–	1.04	-4.4	1.37	-5.28
[ArIII]8.99	–	–	1.04	-3.97	1.37	-3.44

[NeV]14.3μm line, while for SFG and LMG I use the [NeII]12.8μm line. Since these correlations are derived from CLOUDY simulations, I do not report the error on the coefficients. Fig. 6.3 shows the sensitivity of JWST-MIRI, highlighting the wavelengths at which the various fine-structure lines and PAH spectral features can be observed in a galaxy at redshift z=1. In the $\sim 5 - 16$μm rest-frame interval, the MIRI sensitivity is below $\sim 2\times10^{-20}$W m^{-2} for a 1hr, 5σ observation, while in the $\sim 16 - 29$μm rest-frame wavelength interval, instead, the sensitivity is increasingly worse, going from $\sim 6\times10^{-20}$W m^{-2} at ∼16μm, to $\sim 10^{-18}$W m^{-2} at ∼29μm. This makes observing the [SIV]10.5μm, [NeII]12.8μm and [NeV]14.3μm lines a challenging task, and rises the need to find and analyze new possible tracers.

In the 5-16μm interval range, possible tracers for AGN activity are given by the [MgIV]4.49μm, [ArVI]4.53μm and [NeVI]7.65μm lines, while the [ArII]6.98μm and the [ArIII] 8.99μm lines can be used as tracers for star formation activity, together with the PAH feature at 6.2μm. Given their relatively short wavelength, these lines can be exploited by JWST to probe the highly obscured galaxies at the Cosmic Noon ($1 \lesssim z \lesssim 3$). While lines in the mid- to far-IR range do not typically suffer from absorption, the [MgIV] and [ArVI] lines, at wavelength $\lambda \sim 4.5$, can be partially affected. In particular, an optical extinction of $A_V \sim 10$ would absorb about $\sim 30\%$ of the radiation at 4.5μm, following the extinction curve of Cardelli et al. (1989). This value increases to $\sim 80\%$ for an extinction of $A_V \sim 50$.

Fig. 6.4 shows the predicted fluxes, as a function of redshift, compared to the MIRI sensitivity for the [NeV]14.3μm (panel a), [ArVI]4.53μm (panel b), [MgIV]4.49μm (panel c) and [NeVI]7.65μm (panel d) lines, for an AGN with a total IR luminosity of $L_{IR}=10^{12}L_{\odot}$. This luminosity was chosen because it better represents the population at the knee of the luminosity function for galaxies at redshift $z \lesssim 3$. For comparison, this figure and the following ones include also the sensitivity of SPICA SMI. Considering an integration time of 1 hr. and a signal to noise ratio of SNR=5, MIRI will be able to detect the [NeV] line up to redshift z∼0.8. The [ArVI] line can be observed up to redshift z∼1.8 for objects with an ionization parameter of logU=-1.5, almost independently of the gas density, while objects with lower ionization can be observed up to redshift z∼1. The [MgIV] line, instead, can be observed up to redshift z∼1.8 for objects with an ionization parameter of logU=-1.5, independently of the gas density. A ionization parameter of logU=-2.5 expands the observational limit to z∼2.8. The [NeVI]7.65μm line can be observed up to redshift z∼1.2 for objects with an ionization parameter of logU=-2.5, independently of gas density. However, for a higher ionization parameter of logU=-1.5 and a gas density of $\log(n_H/cm^{-3})$=2 this line can be detected up to redshift z∼1.5, and up to redshift z∼1.6 if the gas density is $\log(n_H/cm^{-3})$=4.

Satyapal et al. (2021), performing similar simulations, assume different physical parameters. In particular,

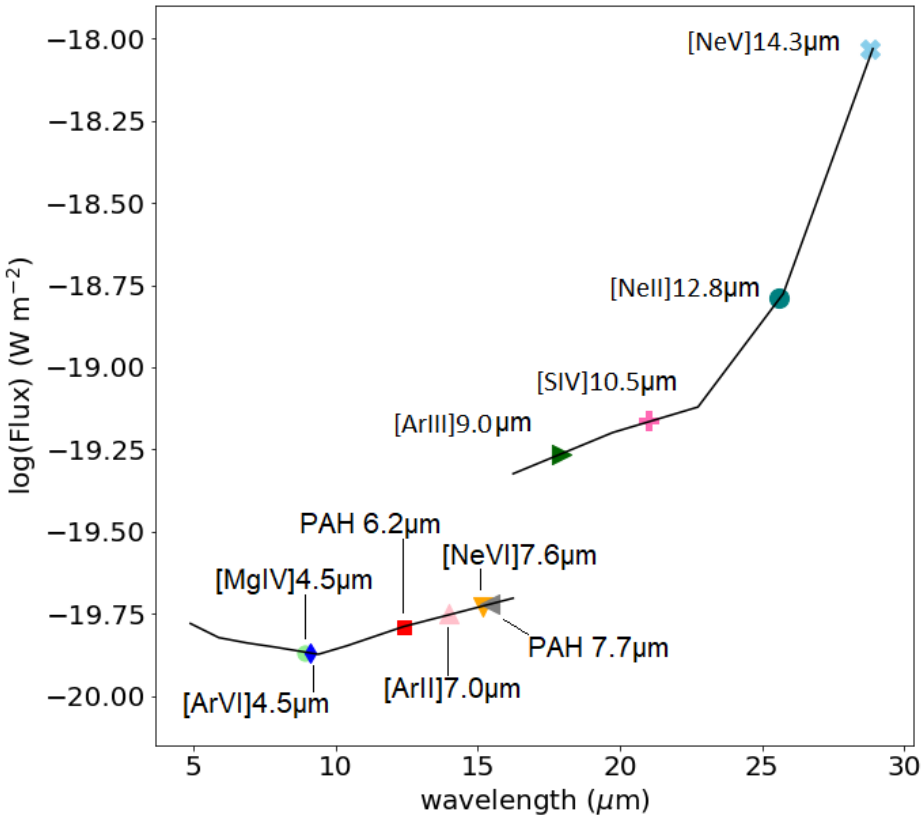

Figure 6.3: Sensitivity of the JWST-MIRI instrument at different wavelengths, for a 1 hr., 5σ observation. The symbols show the position, in the MIRI wavelength range, at which the different lines are observed in a galaxy at redshift z = 1. From left to right, the considered lines and feature, at their rest frame wavelength, are: [MgIV]4.49μm, [ArVI]4.53μm, PAH feature at 6.2μm, [ArII]6.98μm, [NeVI]7.65μm, PAH feature at 7.7μm, [ArIII]8.99μm, [SIV]10.5μm, [NeII]12.8μm and [NeV]14.3μm.

the authors fix the $\log(n_H/cm^{-3})$ parameter to 2.5, and assume a $\log U$ parameter either equal to -1 or -3. I obtain, however, similar result, with the [MgIV] line emerging as the strongest tracer in low ionization objects, and the [NeVI] line dominating instead at higher ionization.

Fig. 6.5 and 6.6 show the predicted fluxes, as a function of redshift, compared to the MIRI sensitivity, of the [NeII]12.8μm (panel a), [ArII]6.98μm (panel b) and [ArIII]8.99μm (panel c) lines for a SFG and a LMG of total IR luminosity of $L_{IR}=10^{12}L_{\odot}$. For the SFG, the [NeII] line can be detected up to redshift z∼1 with a 1 hr. observation, while the [ArII] line can be observed up to redshift z∼1.5 for models with an ionization parameter of logU=-2.5, while for logU=-3.5 the limiting redshift is increased to z∼2.2. For the [ArIII] line, the limiting redshift is of z∼1.2 independently of the adopted model.

For the LMG, the simulation yields similar results. Considering a source of total IR luminosity of $L_{IR}=10^{12}L_{\odot}$, the [NeII] line can be detected up to z∼1.25; the [ArII] line can be detected up to z∼1.5 independently of the adopted model. For the [ArIII] line the maximum redshift is reached for an ionization parameter of $\log U$=-2, and is equal to z∼2, while for an ionization parameter of $\log U$=-3 the maximum redshift is of z∼1.7, independent of gas density.

Fig.6.7 shows the predicted fluxes, as a function of redshift, compared to the MIRI sensitivity for the PAH features at 6.2 and 7.7μm (panel a and b respectively), and for the [SIV]10.5μm line considering both the SFG and LMG (panel c) calibrations for a source with total IR luminosity $L_{IR}=10^{12}L_{\odot}$. Given the high intensity of the PAH features, these can be easily detected by MIRI up to redshift z∼3.6 for the 6.2μm feature,

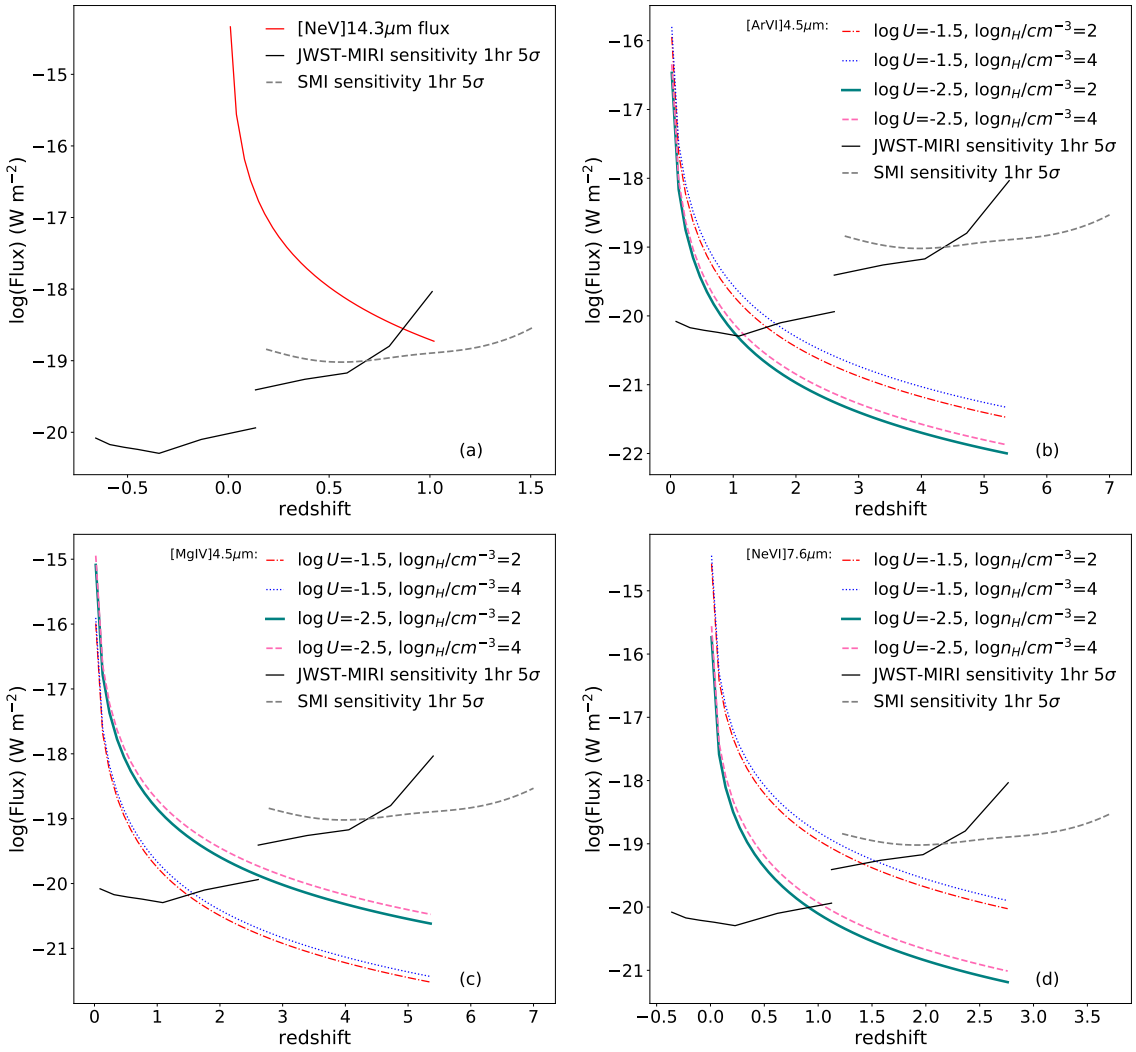

Figure 6.4: Predicted fluxes, as a function of redshift, for an AGN with a total IR luminosity of L_{IR}=$10^{12}L_{\odot}$ for the [NeV]14.3μm (a:top left, red solid line); the [ArVI]4.5μm line (b:top right); the [MgIV]4.49μm line **(c:bottom left)** and for the [NeVI]7.65μm line (d: bottom right). In all figures, the black solid line shows the 1 hr., 5 σ sensitivity of JWST-MIRI, while the grey dashed line shows the 1 hr., 5 σ sensitivity of the SPICA SMI-LR instrument (Kaneda et al. 2017). In panels b, c and d, the red dash-dotted line shows the predicted flux for a galaxy with an ionization parameter of log U=-1.5 and a hydrogen density of log(n_H/cm^{-3})=2, the blue dotted line indicates log U=-1.5 and log(n_H/cm^{-3})=4, the green solid line shows log U=-2.5 and log(n_H/cm^{-3})=2, and the pink dashed line shows log U=-2.5 and log(n_H/cm^{-3})=4.

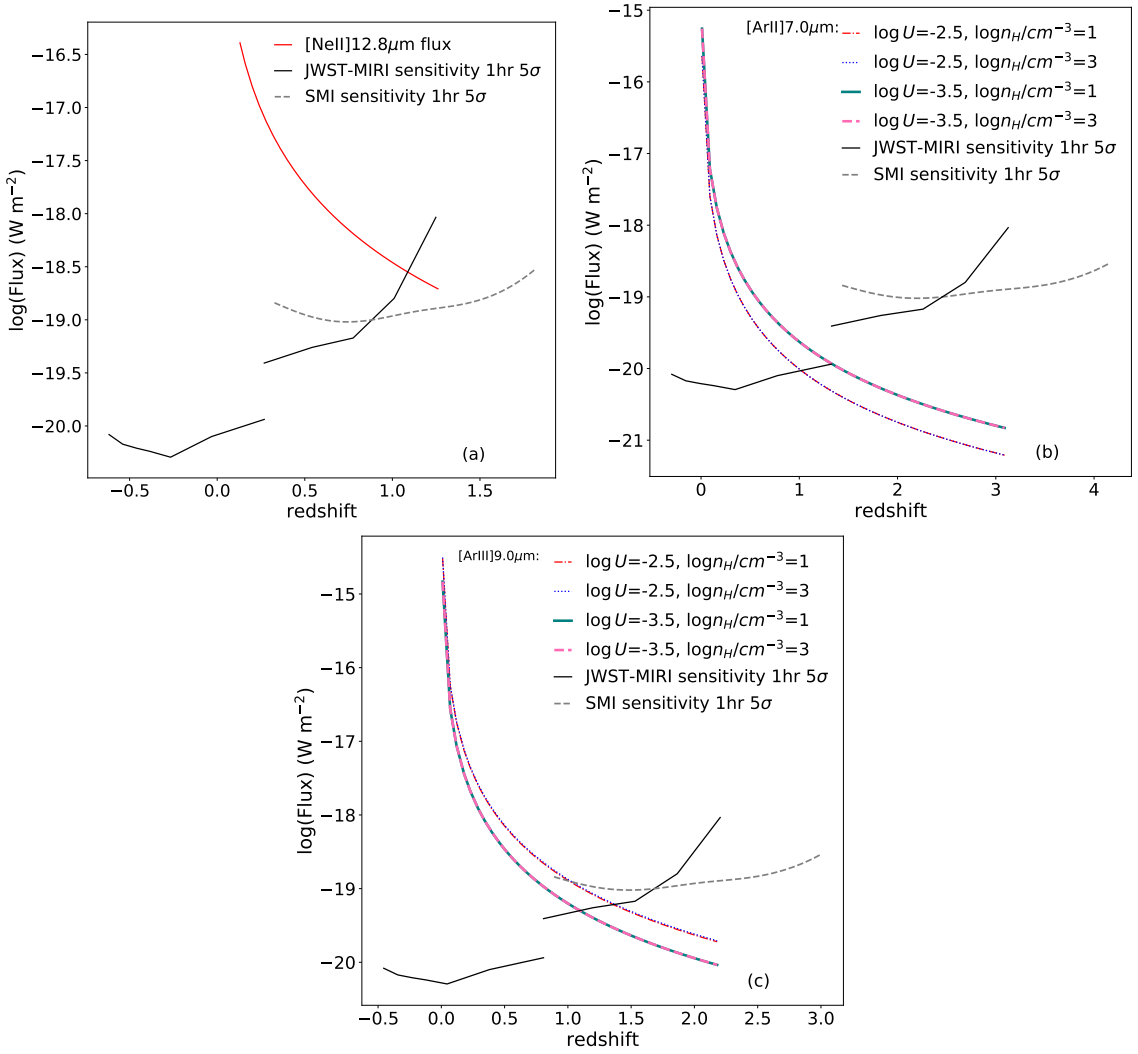

Figure 6.5: Predicted fluxes, as a function of redshift, of a SFG with a total IR luminosity of L_{IR}=$10^{12}L_{\odot}$ for the [NeII]12.8μm (a:top left, red solid line); [ArII]6.98μm line (b:top right) and for the [ArIII]8.99μm line (c: bottom). In all figures, the black solid line shows the 1 hr., 5 σ sensitivity of JWST-MIRI, while the grey dashed line shows the 1 hr., 5 σ sensitivity of the SPICA SMI-LR instrument (Kaneda et al. 2017). In panels b and c, the red dash-dotted line shows a galaxy with an ionization parameter of log U=-2.5 and a hydrogen density of log(n_H/cm^{-3})=1, the blue dotted line indicates log U=-2.5 and log(n_H/cm^{-3})=3, the green solid line shows log U=-3.5 and log(n_H/cm^{-3})=1, and the pink dashed line shows log U=-3.5 and log(n_H/cm^{-3})=3.

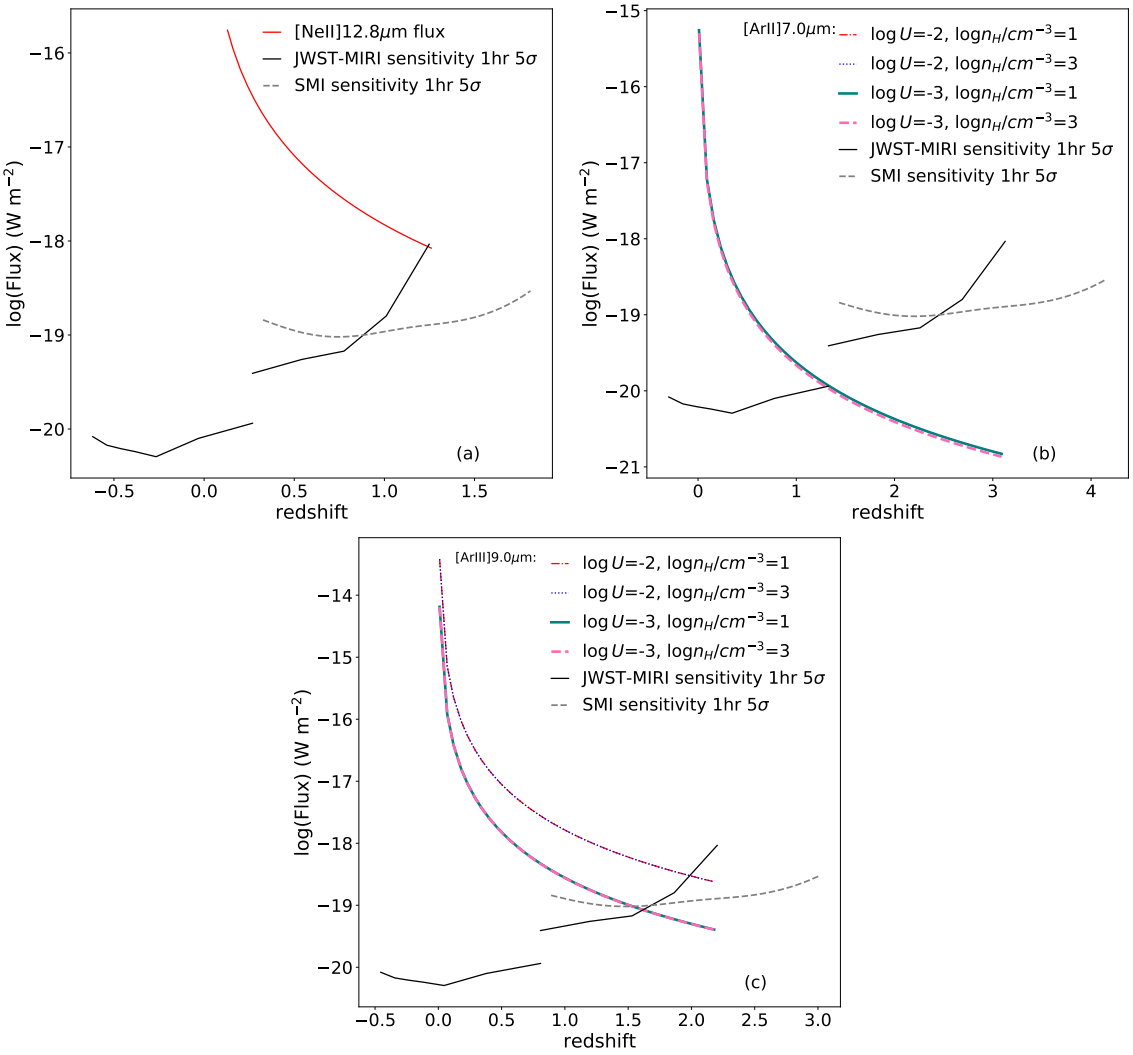

Figure 6.6: Predicted fluxes, as a function of redshift, of a LMG with a total IR luminosity of L_{IR}=$10^{12}L_{\odot}$ for the [NeII]12.8μm (a:top left, red solid line); the [ArII]6.98μm line (b:top right) and the [ArIII]8.99μm line (c: bottom). In all figures, the black solid line shows the 1 hr., 5 σ sensitivity of JWST-MIRI, while the grey dashed line shows the 1 hr., 5 σ sensitivity of the SPICA SMI-LR instrument (Kaneda et al. 2017). In panels b and c, the red dash-dotted line shows a galaxy with an ionization parameter of log U=-2 and a hydrogen density of log(n_H/cm^{-3})=1, the blue dotted line indicate log U=-2 and log(n_H/cm^{-3})=3, the green solid line shows log U=-3 and log(n_H/cm^{-3})=1, and the pink dashed line shows log U=-3 and log(n_H/cm^{-3})=3.

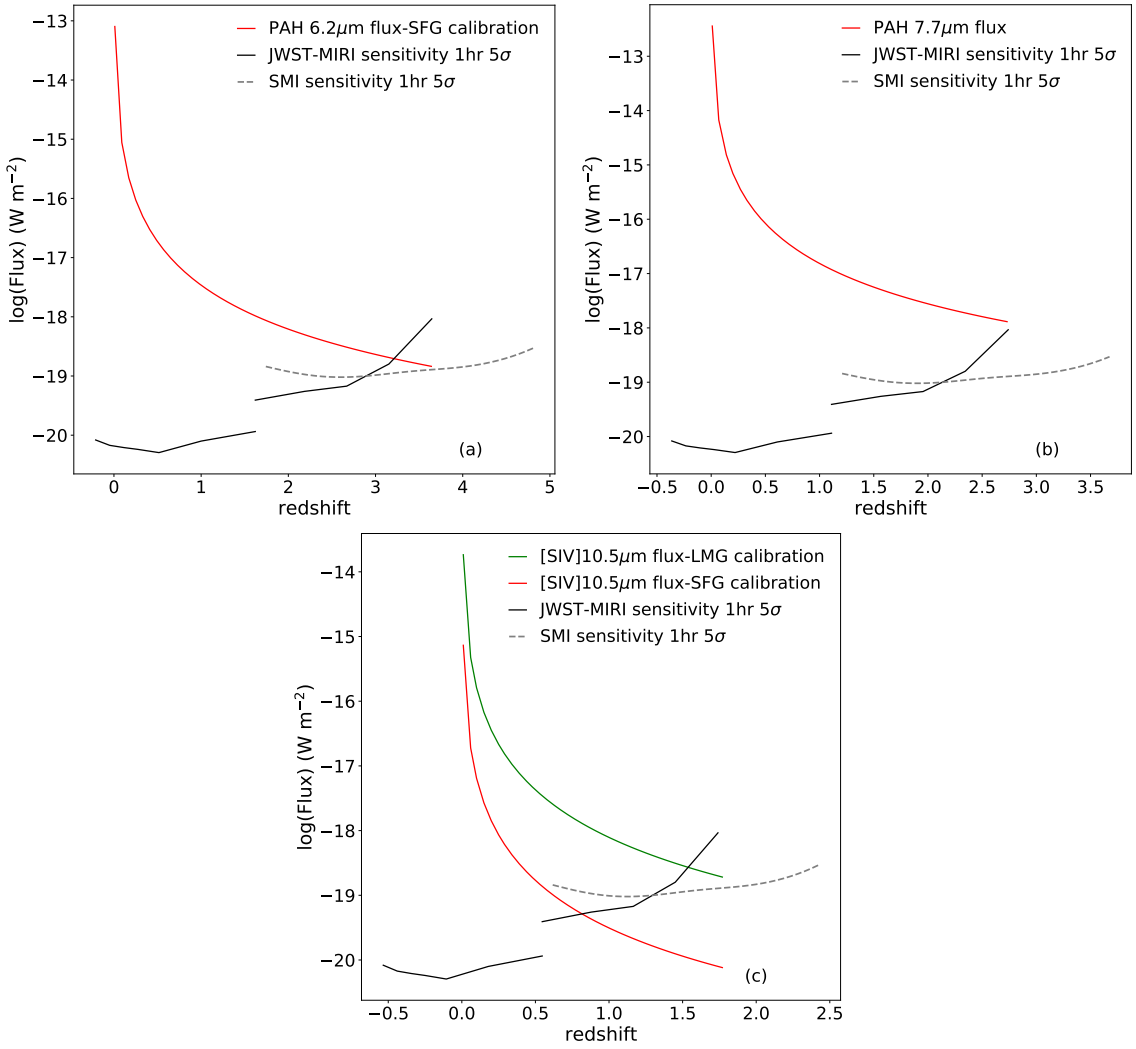

Figure 6.7: Predicted fluxes, as a function of redshift, of a source with a total IR luminosity of $L_{IR}=10^{12}L_{\odot}$ for the 6.2μm PAH feature (a:top left); the 7.7μm PAH feature (b:top right) and for the [SIV]10.5μm line considering the SFG calibration (red solid line) and the LMG calibration (green solid line) (c:bottom). In all figures, the black solid line shows the 1 hr., 5 σ sensitivity of JWST-MIRI, while the grey dashed line shows the 1 hr., 5 σ sensitivity of the SPICA SMI-LR instrument (Kaneda et al. 2017).

and up to redshift z∼2.7 for the 7.7μm feature. The [SIV] line can instead be observed up to redshift z∼1.7, but would require longer integration times to be detected in SFG above redshift z∼0.8.

In all simulations, the decrease in sensitivity of MIRI in the 16-29μm interval raises the required exposure times to values much longer than 1 hr., in order to detect sources at higher redshift and thus probe the highly obscured galaxies at the Cosmic noon.

6.3.2 Predictions for ALMA

In this section I compare the predicted flux of the [OI]63 and 145μm, [OIII]88μm, [NII]122 and 205μm and [CII]158μm lines as a function of redshift to the sensitivity that the ALMA telescope can achieve in 1 hr. and 5 hr. observations, in order to determine the limits of the instrument in studying galaxy evolution through cosmic time.

Fig. 6.8 shows the atmospheric transmission at the ALMA site on Llano de Chajnantor. The transmission curve is obtained from the atmospheric radiative transfer model for ALMA by Pardo (2019), and covers the 35 to 950 GHz frequency interval, equivalent to the 300μm to 3.6mm wavelength range. The figure shows the zenith atmospheric transmission for a precipitable water vapour (PWV) of 2.0mm, 1.0mm and 0.5mm. The PWV indicates the depth of water in the atmospheric column, if all the water in that column were measured as rainfall in mm. The PWV at the ALMA site is typically below 2.0mm for 65% of the year, below 1.0mm for 50% of the time and goes below 0.5mm for 25% of the time. Bands at higher frequencies (Band 9 and 10) are more affected by atmospheric transmission: considering a PWV of 1.0mm, the atmospheric transmission is ∼30% at 850 GHz (Band 10). Going toward shorter frequencies, the transmission goes up to ∼50% at 550GHz (Band 8), and ∼90% below 300GHz (Band 3-6).

When determining the integration time using the ALMA sensitivity calculator[1], the PWV is automatically selected by the on-line tool to the most representative value for each band of observation.

As can be seen from Fig. 6.9-6.11 it has to be noticed that the ALMA sensitivity as a function of redshift is not a simple monotonic function, but contains discontinuities due to atmospheric absorption at particular frequencies. These figures show the fluxes predicted for various lines as a function of redshift for a source of total IR luminosity of $L_{IR}=10^{12.5}L_{\odot}$, compared to the ALMA sensitivity in 1 hr. and 5 hrs. reaching a signal-to-noise σ=5, assuming the line calibrations for SFG, LMG and AGN presented in Chapter 3. Where available, I have also included in the figures the detections so far reported in high redshift galaxies (indicated as yellow stars: ⋆). For predicting the fluxes at each redshift, I have chosen the luminosity of $L_{IR}=10^{12.5}L_{\odot}$ because it corresponds to the luminosity of a MS galaxy of mass of $M_{\star}=10^{10.7}$ $M_{\odot}$ at a redshift z=4 (Scoville et al. 2017). This permits to predict the observability of galaxies at the knee of the luminosity and mass function at redshift $z\gtrsim3$.

Fig. 6.9 shows the fluxes predicted for the [OI]63μm (top) and [OIII]88μm (bottom) lines as a function of redshift. The [OI]63μm line could in principle be observed by ALMA starting from the redshift of z∼4 and up to a redshift of z∼8. However, the line is observable only using ALMA bands 9 and 10, making it rather difficult to detect, due to the low atmospheric transmission. Considering the LMG calibration, the line would require an integration time of ∼5 hrs. to be detected, while for the SFG and AGN calibrations the observational time would be between 10 and 20 hrs. This value is unrealistic for a ground-based telescope, such as ALMA, and in principle could be achieved only by summing up the results of various observing runs of few hours each. As a matter of fact, the only detection of the [OI]63μm line available so far for a

[1] https://almascience.eso.org/proposing/sensitivity-calculator

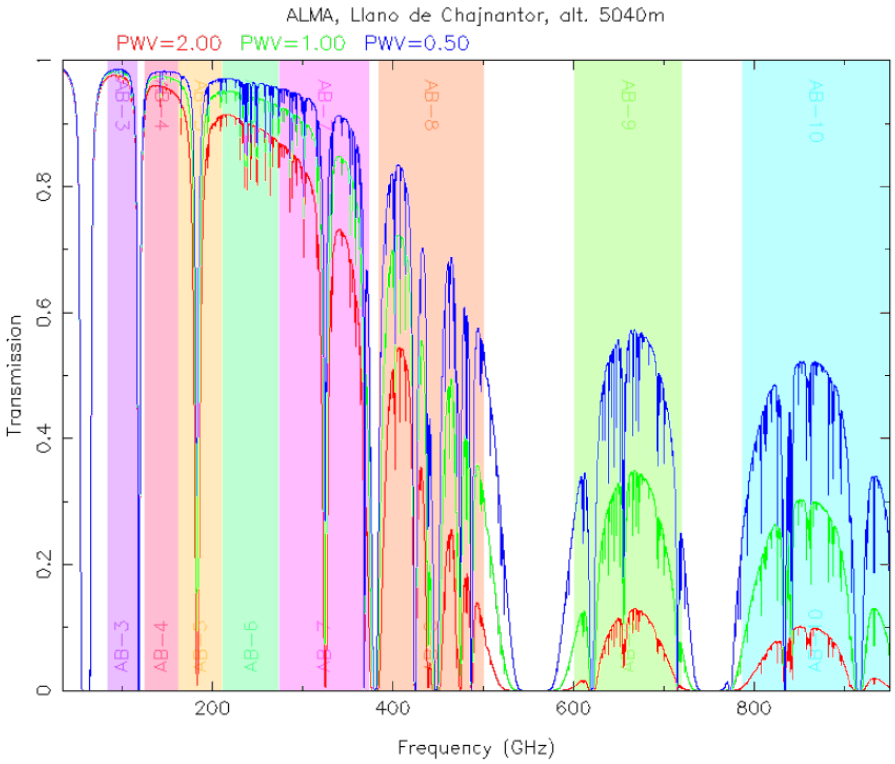

Figure 6.8: Atmospheric transmission at the ALMA site on Llano de Chajnantor, at different frequencies, for three values of precipitable water vapour (PWV): 2.0mm (red), 1.0mm (green) and 0.5mm (blue). The vertical shaded areas show the frequency coverage of the different ALMA Bands, from AB-3 to AB-10. Figure elaborated via the on-line calculator at `https://almascience.nrao.edu/about-alma/atmosphere-model`.

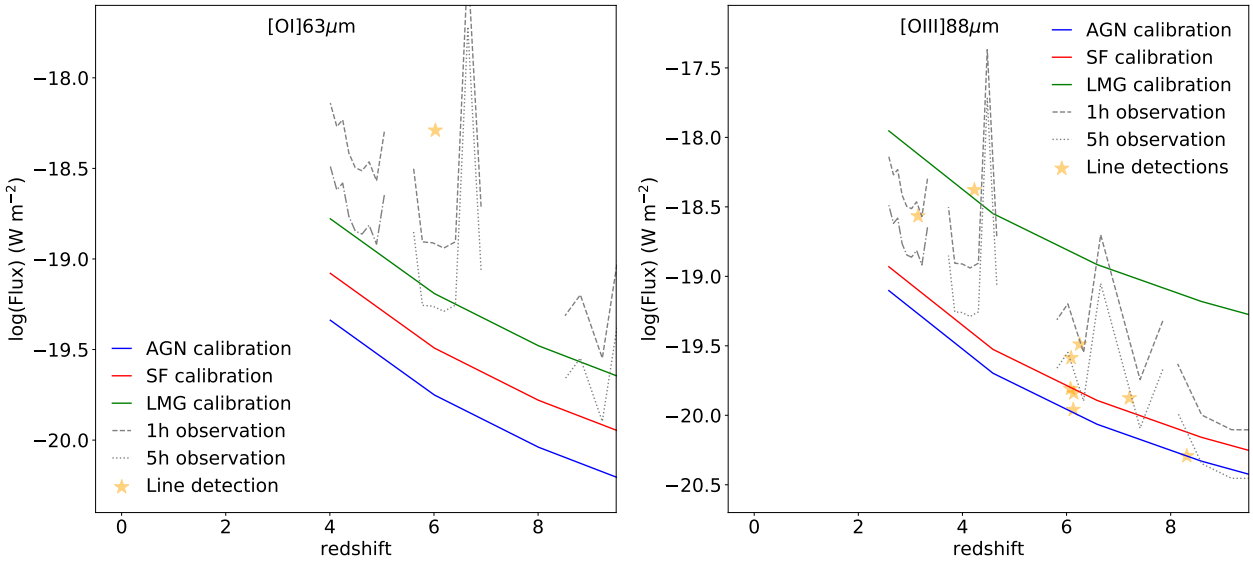

Figure 6.9: Predicted fluxes as a function of redshift for the [OI]63μm line (**left**) and the [OIII]88μm line (**right**), compared to the ALMA sensitivity for a 1 hr. (grey dashed line) and for a 5 hrs. observation (grey dotted line) up to redshift z~9. The blue solid line shows the predicted flux using the calibration for local AGN, the red line with the calibration for local SFG, and the green solid line with the one for local LMG. The various atmospheric absorption peaks show redshift intervals that cannot be observed. The orange stars show detections for each line.

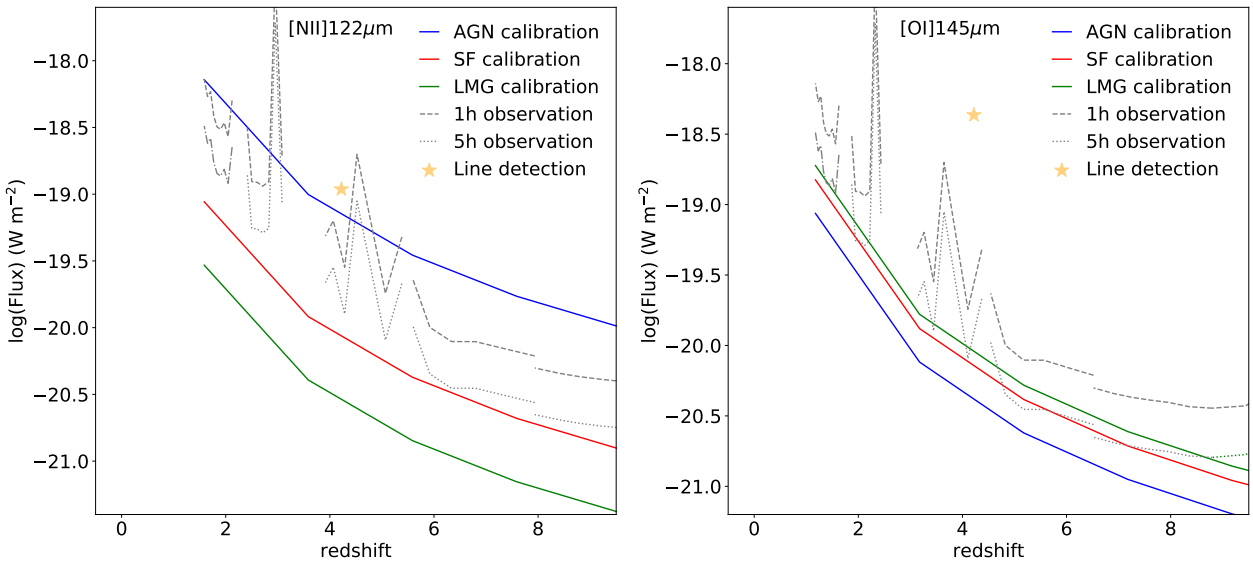

Figure 6.10: Predicted fluxes as a function of redshift for the [NII]122µm line (**left**) and the [OI]145µm line (**right**), compared to the ALMA sensitivity for a 1 hr. (grey dashed line) and for a 5 hrs. observation (grey dotted line) up to redshift z∼9. The blue solid line shows the predicted flux considering the calibration for local AGN, the red line shows the calibration for local SFG, and the green solid line shows the calibration for local LMG. The orange stars show detections for each line.

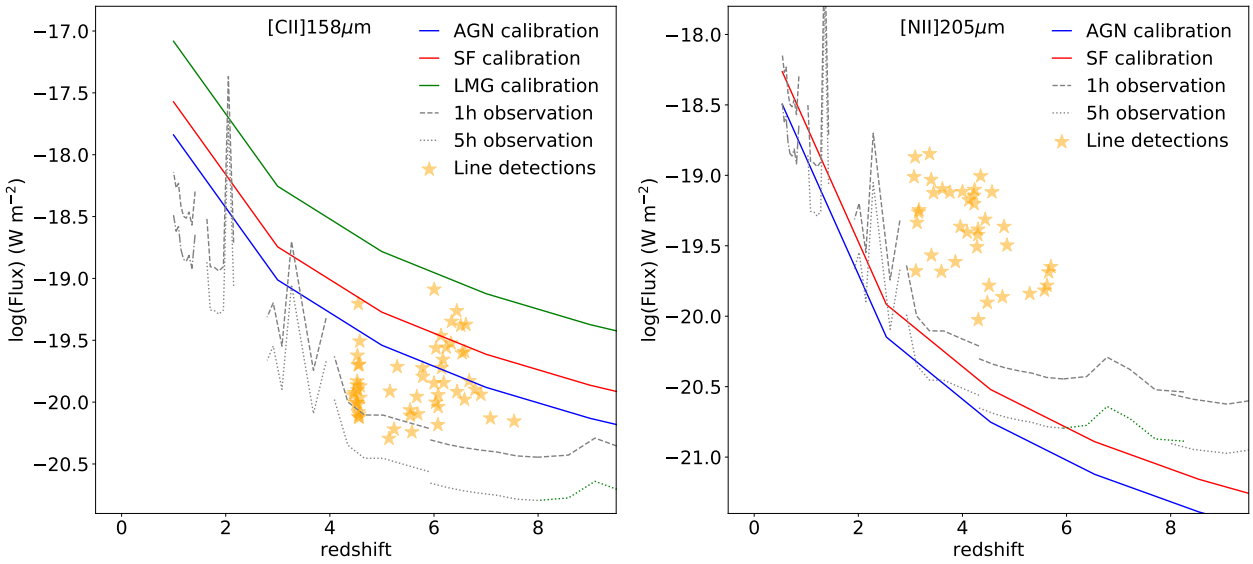

Figure 6.11: Predicted fluxes as a function of redshift for the [CII]158µm line (**left**) and the [NII]205µm line (**right**), compared to the ALMA sensitivity for a 1 hr. observation (grey dashed line) and for a 5 hrs. observation (grey dotted line) up to redshift z∼9. The blue solid line shows the predicted flux considering the calibration for local AGN, the red line shows the calibration for local LMG. The orange stars show detections for each line.

high-redshift galaxy is the one reported by Rybak et al. (2020) for a strongly gravitationally lensed galaxy (magnification $\mu_{\rm FIR} \simeq 9$) obtained with the APEX 12m telescope (Güsten et al. 2006), and the Swedish ESO PI (SEPIA) Band 9 receiver (Belitsky et al. 2018), shown in the figure. The [OIII]88μm line, on the other hand, can be observed from redshift z∼3. For this line, galaxies that present physical characteristics similar to local LMG can be easily detected with observations shorter than 1 hr., while for SFG and AGN, observational times longer than 5 hrs. are required up to redshift z∼8. The figure aslo shows the [OIII]88μm detections by De Breuck et al. (2019); Harikane et al. (2020); Tamura et al. (2019); Vishwas et al. (2018); Walter et al. (2018). While all reported detections have σ=5 or higher, the integration times can reach values of the order of 7.5 hrs. Moreover, I do not correct the line luminosities for the magnification effect, when present.

Fig. 6.10 shows the fluxes predicted for the [NII]122μm (top) and [OI]145μm (bottom) lines as a function of redshift. In AGN, the [NII] line can be detected with an integration time of less than 1 hr., from a redshift of z∼1.8. For SFG, the line can be detected with observations of the order of 5 hrs. only for redshifts above z∼6, while at lower redshifts, or for LMG, the observational times needed to detect this line are larger than 5 hrs. The [OI]145μm line can be observed with integration times of the order of 5hr. above redshift z∼4 in SFG and LMG, while in AGN or for lower redshifts, longer integration times are needed. The figure also reports a detection for [NII]122μm and [OI]145μm (De Breuck et al. 2019). It is important to note, when considering nitrogen and oxygen lines, that the proposed predictions are derived from local galaxies, where the nitrogen to oxygen ratio show typically values of about $\log(\mathrm{N/O}) \sim -0.6$ (Pilyugin et al. 2014). When considering high redshift objects, however, this ratio may vary (e.g. Amorín et al. 2010), since it depends, among other parameters, on the IMF, the star formation efficiency, and the star formation history due to the secondary origin of nitrogen in the CNO cycle in intermediate-mass stars. For this reason, while the detections for high redshift objects are in agreement with our calibration (see Chapter 4), different N/O ratios from the solar value $\log(\mathrm{N/O}) \sim -0.6$ would introduce an additional scatter in the calibration of the nitrogen lines for galaxies at high redshift.

Finally, Fig. 6.11 shows the predicted fluxes for the [CII]158 μm (top) and the [NII]205μm (bottom) lines. The [CII] line is by far the brightest far-IR fine-structure line in galaxies and given its longer wavelength it can be detected in the redshift ranges of $0.9 \lesssim z \lesssim 2$ and $3 \lesssim z \lesssim 9$, requiring integration times shorter than 1 hr. independently of the galaxy type. The [NII]205μm line can be detected from redshift z∼0.5, however it requires at least 1 hr. of observation up to z∼3, and a longer integration at higher redshifts for SFG. For AGN the line appears weaker, and requires integration times longer than 5 hrs. to be detected. The figure includes the detections for the [CII]158μm line reported by Faisst et al. (2020); Venemans et al. (2020) and for the [NII]205μm line by Cunningham et al. (2020), considering only objects with σ=5 or higher.

While these predictions consider a source with a total IR luminosity of $\mathrm{L_{IR}}=10^{12.5}\mathrm{L_{\odot}}$, brighter galaxies, or sources whose apparent flux is enhanced by gravitational lensing, can be detected in shorter integration times.

6.4 Measuring the star formation rate and the black hole accretion rate

I derive here the prescriptions to measure the SFR and the BHAR with the JWST-MIRI spectrometer at the Cosmic Noon ($1 \lesssim z \lesssim 3$), and the SFR with ALMA at higher redshift ($z \gtrsim 3$).

For the JWST predictions, I follow the same method presented in Chapter 5 for the SPICA mission (Roelfsema et al. 2018). Fig.6.12(a) shows the SFR of a galaxy in the Main Sequence (MS; Elbaz et al.

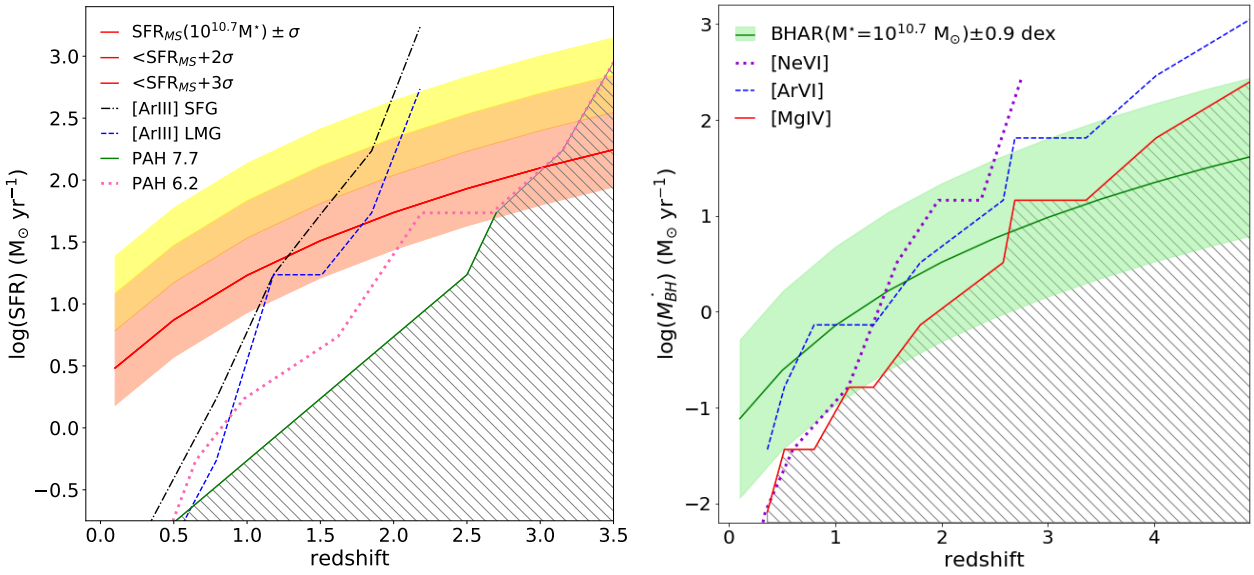

Figure 6.12: (**left:**) Star formation rate (SFR, in $M_{\odot}$ yr^{-1}) as a function of redshift for a $10^{10.7}$ $M_{\odot}$ galaxy in the Main Sequence (MS, Scoville et al. 2017) as a red solid line. The red-shaded area shows the $\sigma = 0.35$ dex intrinsic scatter around the MS (Schreiber et al. 2015), while the dark- and light-orange shaded areas indicate the +2σ and +3σ lines above the MS, respectively. The observability limits for the lines are shown as: black dash-dotted line: [ArIII]8.99μm for a SFG with t_{INT} =1hr; blue dashed line: same line for a LMG (in both cases the highest line ratio present in Table 6.2 was adopted); pink dotted line: the PAH feature at 6.2μm; green solid line: the PAH feature at 7.7μm. (**right:**) the green solid line indicates the instantaneous BH accretion rate (BHAR, in $M_{\odot}$ yr^{-1}) as a function of redshift expected for a MS galaxy with a mass of $10^{10.7}$ $M_{\odot}$ during its active BH accretion phase at each epoch, using the SFR-BHAR relation of Diamond-Stanic & Rieke (2012). The green shaded area shows the associated dispersion. The observability limits for the lines are shown as: purple dotted line: the [NeVI]7.65μm line; blue dashed line: the [ArVI]4.53μm; red solid line: the [MgIV]4.49μm line. For all three lines, I considered a 1hr. pointed observation, and the highest line ratio as reported in Table 6.2. In both panels, the grey hatched areas indicate the parameter space that requires observations longer than 1hr.

2011; Rodighiero et al. 2010), with values of luminosities as a function of redshift taken from Scoville et al. (2007), assuming a galaxy with a stellar mass of $M_{\star}$=$10^{10.7}$ $M_{\odot}$ (Adams et al. 2021; Muzzin et al. 2013) and an associated dispersion around the MS of 0.35 dex (red shaded area; Schreiber et al. 2015). The relation between luminosity and SFR has been taken from Kennicutt & Evans (2012). The various colored lines indicate the JWST-MIRI sensitivity limit for a 1 hr. pointed observation, considering the PAH features at 6.2 and 7.7μm for SFG and the [ArIII]8.99μm line for both SFG and LMG, as discussed in Section 6.3.1. For the [ArIII] line calibration I adopted the higher line ratio to the [NeII] line reported in Table 6.2, and thus the physical conditions yielding the brightest lines. The PAH features at 6.2μm and 7.7μm are the best tracers for the SFR, covering the population below the MS up to redshift z~3, with a minimum luminosity of $L_{IR} \sim 10^{9.5}\,L_{\odot}$ at z~1 and $L_{IR} \sim 10^{12.5}\,L_{\odot}$ at z~3. The [ArIII]8.99μm line, on the other hand, can be detected in MS galaxies up to redshift z~1.8 (limiting luminosities between $L_{IR} \sim 10^{11}\,L_{\odot}$ at z~1 and $L_{IR} \sim 10^{13}\,L_{\odot}$ at z~2.2). This poses a limit to the study of LMG at higher redshifts, since the reduced formation efficiency and the increased stellar radiation hardness reduces the strength of the PAH features in these objects, which are only detected at metallicities above 1/8-1/10 $Z_{\odot}$ (Cormier et al. 2015; Engelbracht et al. 2008; Galliano et al. 2021).

In analogy with the [NeII]12.8μm plus [NeIII]15.6μm SFR tracer (see Ch.3 Sec. 3.4.3), I derive the correlation between the SFR and the sum of the [ArII]6.98μm and [ArIII]8.99μm lines, considering the ([ArII]+[ArIII])/([NeII]+[NeIII]) ratio (reported in Table 6.2), as computed from the photoionization

models. This leads to a SFR to ([ArII]+[ArIII]) lines luminosity correlation for SFG and LMG reported in equation 6.1 and 6.2, respectively:

$$\log\left(\frac{\mathrm{SFR}}{\mathrm{M_\odot\,yr^{-1}}}\right) = 1.2 + 0.96\log\left(\frac{\mathrm{L_{[ArII]+[ArIII]}}}{10^{41}\,\mathrm{erg\,s^{-1}}}\right) \tag{6.1}$$

$$\log\left(\frac{\mathrm{SFR}}{\mathrm{M_\odot\,yr^{-1}}}\right) = 1.57 + 0.96\log\left(\frac{\mathrm{L_{[ArII]+[ArIII]}}}{10^{41}\,\mathrm{erg\,s^{-1}}}\right) \tag{6.2}$$

While the predictions of line ratios for the single [ArII] and [ArIII] lines are strongly model dependent, with significant variations depending on metallicity and gas density, considering the sum of the two lines gives a more stable line ratio. This allows to derive a SFR tracer independent of metallicity, thus broadening its use. Moreover, in objects that present both an AGN and a star forming component, the ratio of the [ArVI]4.5μm to the [ArII] or [ArIII] lines can help measure the fraction of the two components, ad was presented in Chapter 3 Sec. 3.6.1 for the [NeV] to [NeIII] lines ratio.

In a similar way, while the single PAH feature can give adequately trace SFR, a combination of two o more feature can better keep into account the different conditions of the ISM surrounding star forming regions. The combination of the 6.2+7.7μm PAH features to measure the SFR, proposed in Chapter 3 Sec.3.4.4, can be used by JWST up to redshift z∼2.7.

The results presented for the ALMA telescope suggest that the [CII]158μm line, a proxy for measuring the SFR, can be easily observed in objects at redshift z≳3, thus allowing to trace the evolution of SFR throughout cosmic time. At the present time, this line has been observed by ALMA in the z∼4-7 redshift interval (see e.g. Faisst et al. 2020; Hashimoto 2019). An alternative can be offered by the sum of the [OIII]88μm and [OI]145μm lines, proposed in Chapter 3 Sec.3.4.2: the [OI]145μm can be detected with ALMA above redshift z∼1.5 with observations of ∼5 hr for SFG and LMG-like sources, and, unlike the [OI]63μm line, is not affected by self-absorption (see, e.g., Liseau et al. 2006).

Fig.6.12(b) shows the instantaneous BHAR, that can be measured by JWST-MIRI, as a function of redshift for an AGN in a MS star-forming galaxy with $M^*=10^{10.7}$ $M_\odot$, using the SFR-BHAR calibration derived by Diamond-Stanic & Rieke (2012) for a sample of nearby Seyfert galaxies. The green shaded area corresponds to the dispersion of the SFR-BHAR relation, i.e. ∼ 0.9 dex. This estimate, however, considers only the portion of galaxies in the MS undergoing a BH accreting phase at each epoch, with the instantaneous BHAR that has not been averaged over the duty cycle of the active nucleus. The dashed lines represent the three proposed tracers for BHAR in Section 6.3.1, considering a 1 hr. pointed observation: the [MgIV]4.49μm line appears to be the best tracer for BHAR, reaching galaxies below the main sequence up to redshift z∼2.5 (observable luminosities between $L_{IR} \sim 10^{10.5}\,L_\odot$ at z∼1 and $L_{IR} \sim 10^{12.5}\,L_\odot$ at z∼4). The possibility of detecting the [ArVI] and [NeVI] lines only in bright galaxies is due to the higher ionization potential needed to excite these lines (respectively of 80 eV and 126 eV, see Table 6.1). The line ratios derived from the [NeVI] and [MgIV] detections reported in Sturm et al. (2002) are all consistent with AGN characterized by a ionization parameter of log U=-1.5 and hydrogen density of $\log(n_H/cm^{-3})$=4 , or higher, with a line ratio of the order of [NeVI]/[NeV]∼0.67-1.4 and [MgIV]/[NeV]∼0.06. The low number of detections (8 for the [NeVI] line and 3 for the [MgIV] line) suggest that while the [NeVI] line is more easily observable in AGNs whose ISM is characterized by a high ionization potential, the average AGN is relatively weaker. For this reason, while the [MgIV] line can give an accurate measure of the BHAR in average AGNs, a comprehensive measure of AGN activity can be achieved using a combination of [MgIV] and [ArVI] or [NeVI] lines, in order to include also powerful AGNs.

It is important to consider that the lines analyzed in this work have not been extensively observed yet, and these predictions are based on CLOUDY photo-ionization models. Considering the line ratios reported in Table 6.2 and the BHAR-[NeV]14.3μm correlation derived in Ch.3 Sec. 1.2.2, I obtain a correlation between the BHAR and the [MgIV]4.49μm line (reported in equation 6.3), and between the BHAR and the [ArVI]4.53μm line (reported in equation 6.4).

$$\log\left(\frac{\dot{\mathrm{M}}_{\mathrm{BH}}}{\mathrm{M}_{\odot}\,\mathrm{yr}^{-1}}\right) = -0.85 + 1.04\log\left(\frac{\mathrm{L}_{[\mathrm{MgIV}]4.49}}{10^{41}\,\mathrm{erg\,s}^{-1}}\right) \tag{6.3}$$

$$\log\left(\frac{\dot{\mathrm{M}}_{\mathrm{BH}}}{\mathrm{M}_{\odot}\,\mathrm{yr}^{-1}}\right) = 0.58 + 1.04\log\left(\frac{\mathrm{L}_{[\mathrm{ArVI}]4.53}}{10^{41}\,\mathrm{erg\,s}^{-1}}\right) \tag{6.4}$$

The hatched areas in both panels of Fig.6.12 indicate the region where observations longer than 1 hr are required. A longer exposure time can significantly improve these limits, allowing the JWST-MIRI spectrometer to study both SFR and BHAR in MS galaxies up to redshift z∼3.

Among the far-IR lines covered by the ALMA telescope at redshifts higher than z∼3, the only available tracers for BH activity are represented by the [OIII]52 and 88μm lines. Their ionization potential (∼35 eV, see Table 6.1) is sufficiently high to be excited by AGN. However, these lines are also associated to stellar and HII regions excitation, thus limiting their potential as BHA tracer. A set of observed far-IR lines or the specific photo-ionization models that could simulate the two emission components (see, e.g. Spinoglio et al. 1995) are needed to disentangle the stellar emission from the total observed emission of these lines.

6.5 Discussion

The inability of performing wide area surveys (of the order of square degrees) with either of the two facilities, JWST and ALMA, however, imposes a significant limit to the possibility of characterizing galaxy evolution: while the tracers proposed in this work can be used to trace both star formation and BHA at the Cosmic Noon, a complete study of galaxy evolution also requires to account for the environment within which galaxies evolve, thus incorporating the large scale structure of the Universe, by mapping large cosmological volumes. Moreover, even using both facilities together, it is not possible to perform an accurate analysis of galaxy evolution covering both the Cosmic Noon and the higher redshifts. On the one hand, in fact, while the PAH features can be detected with JWST up to redshift z∼2.5 in MS galaxies, and at higher redshifts the ALMA telescope can trace star formation activity with the [CII]158μm line, there is the problem of tracing SF in low metallicity environments, where the PAH features are weak or absent, or in high luminosity galaxies, where the [CII] deficit can lead to lower determinations of the SFR (see e.g. Ferrara et al. 2019). On the other hand, ALMA lacks an unambiguous tracer for BHA activity, and the proposed tracers for JWST only reach redshift z∼3 for MS galaxies.

Chapter 7

Summary

In the current picture of galaxy evolution studies, the internal cycling of matter within galaxies, the so-called baryon cycle, acts as the formal driver of their evolution. The baryon cycle comprehends several processes in which the different galaxy components exchange matter and energy with the ISM and the external medium surrounding them. As a matter of fact, galaxy evolution studies are in the agenda of all the top astronomical facilities currently in operation (e.g. ALMA) and of those planned for the next decade (e.g. JWST, ELTs).

This thesis work aims to derive a method to analyze the main divers of galaxy evolution through cosmic time, focusing in particular on star formation and BHA. Lines and features in the mid- to far-IR spectral range offer a unique instrument to probe the dust obscured regions where the bulk of star formation and BHA take place, both in local galaxies and at high redshift. It thus emerges the need to derive reliable tracers for SFR and BHAR, in order to study how the two phenomena evolve with time. In particular, it emerges the need to physically characterize galaxy activity at the so-called 'cosmic noon' in the z∼1-3 redshift interval, where the bulk of both star formation and BHA takes place.

A comprehensive study on the evolution of SFR and BHAR needs to also take into account the environment in which star formation and BHA take place, and to characterize the host galaxies in terms of stellar mass, metallicity of the ISM, and in general to gather a complete picture of the different physical processes that influence the evolution of galaxies. This would allow to better constrain the different parameters that influence the numerical simulations on galaxy evolution.

The first step in this analysis was to systematically revise the calibration of lines and features in the 6-205μm spectral range, deriving new line-to-L_{IR} calibrations for three different galaxy types, namely AGN, SFG and LMG, starting from a statistically significant sample of objects with available IR spectroscopy data obtained mainly from *Herschel* and *Spitzer*. Starting from these calibrations, I then derived spectroscopic tracers for SFR and BHAR. While for BHA processes the best tracers can be found in high ionization lines mainly or exclusively produced by accretion processes, for the SFR I analyzed different lines and features, thus considering the different components of the ISM surrounding star forming regions. When possible, the analyzed tracers were also compared to high redshift detections by the ALMA telescope, in order to evaluate whether the different tracers can be used only for local galaxies or can be applied also to high redshift objects.

To gain a better understanding of how star formation and BHA co-evolve with cosmic time it is however necessary to study the physical processes taking place inside galaxies at different redshifts, and in different environments. This would allow for a more comprehensive view of the phenomena concurring to the baryon cycle throughout cosmic time. For this reason, I propose a survey strategy with the aim of quantify how many observations are needed in order to constrain the effects of star formation and BHA, and their evolution

with redshift. The study is based on spectro-photometric surveys carried out with the SPICA telescope, one of the three candidates for the M5 'Cosmic Vision' ESA call. While the SPICA mission was cancelled before the completion of this work, the various scientific and technological studies carried out using a SPICA like mission model can still be used as a reference for future work in the field. In this work , the first step was to study three different blind surveys, covering different sky areas (15, 1, and 0.033 deg^2) at different depth, in order to gain information both on the large scale structure of the Universe and on the extremely bright or dim objects in the local and distant Universe. These blind surveys would allow to derive a 3D view of the Universe up to redshift z~4, gaining spectro-photometric information on an unprecedented number of objects, including redshift, SFR, or classification.

Starting from the results of the simulated blind surveys, I also determine the number of objects, for luminosity and redshift interval, for which pointed spectroscopic observations are needed in order to derive a complete census of the star formation and BHA processes, how they evolve with cosmic time and their dependence on other parameters such as stellar mass, galaxy environment or ISM metallicity.

Even though the SPICA mission was specifically design to study galaxy evolution, in its different denominations, up to the cosmic noon, other present and future instruments can be used to partially carry out the study. The JWST and ALMA telescopes, in particular, can be used to analyze both star formation and BHA processes at various redshifts, the first reaching sources up to redshift z~3, and the second for sources beyond the cosmic noon. The limited spectral range of JWST-MIRI with respect to the proposed SPICA-SAFARI instrument implies that the lines proposed as SFR and BHAR tracers in this work, excluding the PAH features, can only be observed up to redshift z~1.5, and usually only up to z~1. For this reason, I analyze the possibility of detecting lines at shorter wavelengths.

The main results in this work are:

- I derived a statistically robust calibration for the main lines an features in the mid- and far-IR range in respect to the total IR luminosity, including calibrations for the 6.2μm, 7.7μm, 11.3μm and 17μm PAH features, the H_2 pure rotational lines at 9.7μm, 12.3μm, 17.0μm and 28.2μm, and the main fine-structure lines in the 10-35μm range and the 57-205μm range. Where possible, I considered local AGN, LMG and SFG for each line and feature. For lines in the 57-205μm range I tested the calibrations against high-redshift galaxies detected with the ALMA telescope, finding good agreement between the calibrations obtained for local galaxies and the high-redshift data.

- Starting from the lines and features calibrations, I also derived calibrations for the SFR and BHAR. In particular, besides the [CII]158μm line of the PAH features as SFR tracers or the [NeV]14.3,24.3μm and [OIV]25.9μm lines as BHAR tracers, I also calibrated as SFR tracers the sum of the [OI]63μm and [OIII]88μm, the H_2 molecular lines at 9.7, 12.3, and 17.0μm, the sum of [SIV]10.5μm and [SIII]18.7μm lines. A combination of low- and intermediate-ionisation lines from neon and/or sulfur is also a robust proxy for the SFR, independent of the metallicity. In particular, the [SIV]$10.5\,\mu m$+[NeII]$12.8\,\mu m$ tracer will be accessible to ELT facilities in the near future for galaxies in the local Universe. I also tested the [CII]158μm line as SFR tracer with data from high redshift galaxies, finding good agreement.

- Among the different SFR tracers analyzed, for galaxies dominated by SF processes the best tracers are the [CII]158μm line or the combination of the [OI] and [OIII] lines for high-redshift galaxies observed from the ground with sub-millimetre telescopes. For galaxies observed from space or airborne facilities (but also from the new generation of the very large optical ground-based telescopes in the 8-13μm atmospheric window, for local galaxies), the best SFR tracers are the combination of the [NeII] and

[NeIII] lines or the combination of the other mid-IR fine-structure lines. For galaxies containing an AGN, the PAH features can reliably be used, and the PAH 11.3μm feature is probably the best SFR tracer. When measuring the BHAR, the [NeV] lines at 14.3 and 24.3μm are exclusive probes of AGN activity, because their emission is a direct signature of the hard ionising spectrum due to the accretion process. However, these lines are fainter than the [OIV]25.9μm line, which can be detected more easily in faint objects. When using the [OIV] line as a BHAR tracer, it is important to take account of the possible contamination due to SF processes, because its emission can also be attributed, to some extent, to starburst activity.

- Using the proposed M5 mission SPICA as a template for a cryogenically cooled IR space telescope, I simulated spectro-photometric blind surveys with the goal of detecting galaxies at the knee of the luminosity function at the cosmic noon (z∼1-3). Of the proposed surveys, the deepest survey of 120 arcmin^2(denominated hyper-deep survey), would be able to detect star-forming galaxies about two orders of magnitude below the knee of the luminosity function at various cosmic times up to redshift z∼4. It would also detect either LMG and AGN about one order of magnitude below the knee of the LF up to redshift z∼2 for LMG and up to z∼3 for AGN. The second deepest surveys of 1 deg^2 (denominated ultra-deep survey) would be able to detect spectroscopically through PAH features all star-forming galaxies detected photometrically in the deepest Herschel cosmological fields, down to one dex below the knee of their luminosity functions up to redshift z∼3.5, and would also detect AGN, through high-ionisation fine-structure lines, at the knee of the luminosity functions at each redshift up to redshift z∼3. The shallow survey (denominated deep survey) would instead cover 15 deg^2 and be able to reach the knee of the luminosity function up to redshift z∼3.5, but also study the large scale structure of the Universe detecting galaxies in different environments an at different redshifts. Together, the blind surveys would help build a 3D view of the Universe, determining redshift and class of tens of thousands of galaxies.

- A consistent spectroscopic characterization of the evolution of galaxies through cosmic time needs to analyze a suitable sample of galaxies selected with the intent of covering the main physical parameters like luminosity, SFR, BHAR and galaxy stellar mass and will need to select galaxies in both over-dense and sub-dense regions. Numerically, it will have to include about ∼1000 galaxies. Mid- to far-IR spectroscopic observations of this sample of galaxies will trace galaxy evolution all the way down to ∼0.5 dex below the knee of the luminosity functions of star forming galaxies and AGN by measuring the SFR, the BHAR, and the metallicity as a function of cosmic time. Follow-up observations will also be used to characterise the physical properties of the ISM in low metallicity environments, both in star-forming galaxies and AGN at high redshift.

- Even though the SPICA telescope was developed with the specific intent of studying the peak of galaxy activity at the cosmic noon performing both wide blind surveys and follow up pointed observations, the galaxy evolution program proposed for SPICA can be partially carried out by present and future facilities. JWST, in particular, can trace both SFR and BHAR up to redshift z∼1 using the same tracers proposed for the SPICA mission. In order to reach higher redshifts it is however necessary to use lines at lower wavelength, that have not been observed by previous facilities. In particular, for the SFR, besides the PAH features at 6.2μm and 7.7μm, that can be detected up to redshift z∼2.5-3, the SFR could be traced by low ionization lines like [ArII] at 7.0μm, detectable up to z∼3, and [ArIII] at 9.0μm, detectable up to redshift z∼2. For the BHAR, instead, I have tested the observational limits

of high ionization lines like [ArVI]4.5µm, detectable up to redshift z∼2.5, [MgIV]4.5µm, observable up to redshift z∼2.5-3.5, and [NeVI]7.6µm, observable up to redshift z∼2. The ALMA telescope, on the other hand, can cover the higher end of galaxy evolution, tracing the SFR in galaxies at redshifts above z∼3 with the [CII]158µm line or the combination of the [OI]145µm and [OIII]88µm lines.

In conclusion, while both JWST and the ALMA telescope can significantly contribute to the study of galaxy evolution throughout cosmic time, the impossibility of performing wide-field blind surveys or to probe the far-IR regime in the local universe significantly limit their capabilities. The latest decadal survey, Pathways to Discovery in Astronomy and Astrophysics for the 2020s (National Academies of Sciences, Engineering, and Medicine 2021), highlights the need for a new far-IR imaging or spectroscopy mission, in order to address key aspects in galaxy evolution, such as measuring the formation and buildup of galaxies, heavy elements, and interstellar dust throughout cosmic time, and probing the co-evolution of galaxies and their supermassive black holes. While the SPICA observatory would have been an ideal tool to advance in these fields, a new far-IR mission could address these topics in the future and fully exploit the main scientific results presented in this Thesis.

Bibliography

Adams, N. J., Bowler, R. A. A., Jarvis, M. J., Häußler, B., & Lagos, C. D. P. 2021, MNRAS, 506, 4933

Aird, J., Nandra, K., Laird, E. S., et al. 2010, MNRAS, 401, 2531

Akylas, A., Georgakakis, A., Georgantopoulos, I., Brightman, M., & Nandra, K. 2012, A&A, 546, A98

Akylas, A. & Georgantopoulos, I. 2009, A&A, 500, 999

Alavi, A., Siana, B., Richard, J., et al. 2014, ApJ, 780, 143

Allen, S. W., Schmidt, R. W., Ebeling, H., Fabian, A. C., & van Speybroeck, L. 2004, MNRAS, 353, 457

Álvarez-Márquez, J., Colina, L., Marques-Chaves, R., et al. 2019, A&A, 629, A9

Amorín, R. O., Pérez-Montero, E., & Vílchez, J. M. 2010, ApJ, 715, L128

André, P., Hughes, A., Guillet, V., et al. 2019, PASA, 36, e029

Antonucci, R. 1993, ARA&A, 31, 473

Armus, L., Mazzarella, J. M., Evans, A. S., et al. 2009, PASP, 121, 559

Bagnasco, G., Kolm, M., Ferruit, P., et al. 2007, in Society of Photo-Optical Instrumentation Engineers (SPIE) Conference Series, Vol. 6692, Cryogenic Optical Systems and Instruments XII, ed. J. B. Heaney & L. G. Burriesci, 66920M

Baldry, I. K., Balogh, M. L., Bower, R., Glazebrook, K., & Nichol, R. C. 2004, in American Institute of Physics Conference Series, Vol. 743, The New Cosmology: Conference on Strings and Cosmology, ed. R. E. Allen, D. V. Nanopoulos, & C. N. Pope, 106–119

Baldwin, J. A. 1977, ApJ, 214, 679

Baldwin, J. A., Phillips, M. M., & Terlevich, R. 1981, PASP, 93, 5

Beckmann, V. & Shrader, C. R. 2012, Active Galactic Nuclei (Wiley-VCH)

Beckmann, V., Soldi, S., Ricci, C., et al. 2009, A&A, 505, 417

Beckwith, S. V. W., Stiavelli, M., Koekemoer, A. M., et al. 2006, AJ, 132, 1729

Behroozi, P. S., Conroy, C., & Wechsler, R. H. 2010, ApJ, 717, 379

Belitsky, V., Lapkin, I., Fredrixon, M., et al. 2018, A&A, 612, A23

Bennett, C. L., Hill, R. S., Hinshaw, G., et al. 2011, ApJS, 192, 17

Bernard Salas, J., Pottasch, S. R., Beintema, D. A., & Wesselius, P. R. 2001, A&A, 367, 949

Bernard-Salas, J., Spoon, H. W. W., Charmandaris, V., et al. 2009, ApJS, 184, 230

Bernardi, M., Meert, A., Sheth, R. K., et al. 2013, MNRAS, 436, 697

Birkmann, S. M., Ferruit, P., Rawle, T., et al. 2016, in Society of Photo-Optical Instrumentation Engineers (SPIE) Conference Series, Vol. 9904, Space Telescopes and Instrumentation 2016: Optical, Infrared, and Millimeter Wave, ed. H. A. MacEwen, G. G. Fazio, M. Lystrup, N. Batalha, N. Siegler, & E. C. Tong, 99040B

Black, J. H. & van Dishoeck, E. F. 1987, ApJ, 322, 412

Boggs, P. T. & Rogers, J. E. 1990, Contemporary Mathematics, Vol. 112, Orthogonal Distance Regression (American Mathematical Society), 186
Bolatto, A. D., Jackson, J. M., & Ingalls, J. G. 1999, ApJ, 513, 275
Bonato, M., De Zotti, G., Leisawitz, D., et al. 2019, PASA, 36, e017
Bouwens, R. J., Illingworth, G. D., Oesch, P. A., et al. 2012, ApJ, 754, 83
Brandl, B., Bettonvil, F., van Boekel, R., et al. 2021, The Messenger, 182, 22
Brandl, B. R., Bernard-Salas, J., Spoon, H. W. W., et al. 2006, ApJ, 653, 1129
Brandt, W. N. & Hasinger, G. 2005, ARA&A, 43, 827
Brightman, M. & Nandra, K. 2011, MNRAS, 413, 1206
Buchanan, C. L., Gallimore, J. F., O'Dea, C. P., et al. 2006, AJ, 132, 401
Bullock, J. S. & Boylan-Kolchin, M. 2017, ARA&A, 55, 343
Bundy, K., Bershady, M. A., Law, D. R., et al. 2015, ApJ, 798, 7
Calzetti, D., Kennicutt, R. C., Engelbracht, C. W., et al. 2007, ApJ, 666, 870
Cardelli, J. A., Clayton, G. C., & Mathis, J. S. 1989, ApJ, 345, 245
Carilli, C. L. & Walter, F. 2013, ARA&A, 51, 105
Chary, R. & Elbaz, D. 2001, ApJ, 556, 562
Ciesla, L., Charmandaris, V., Georgakakis, A., et al. 2015, A&A, 576, A10
Clegg, P. E., Ade, P. A. R., Armand, C., et al. 1996, A&A, 315, L38
Clements, D. L., Serjeant, S., & Jin, S. 2020, Nature, 587, 548
Coc, A., Vangioni-Flam, E., Descouvemont, P., Adahchour, A., & Angulo, C. 2004, ApJ, 600, 544
Coppin, K. E. K., Danielson, A. L. R., Geach, J. E., et al. 2012, MNRAS, 427, 520
Cormier, D., Abel, N. P., Hony, S., et al. 2019, A&A, 626, A23
Cormier, D., Lebouteiller, V., Madden, S. C., et al. 2012, A&A, 548, A20
Cormier, D., Madden, S. C., Lebouteiller, V., et al. 2015, A&A, 578, A53
Cortese, L., Boissier, S., Boselli, A., et al. 2012, A&A, 544, A101
Crampton, D. 1993, JRASC, 87, 182
Croxall, K. V., Smith, J. D., Pellegrini, E., et al. 2017, ApJ, 845, 96
Cucciati, O., De Lucia, G., Zucca, E., et al. 2012, A&A, 548, A108
Cunningham, D. J. M., Chapman, S. C., Aravena, M., et al. 2020, MNRAS, 494, 4090
Daddi, E., Dickinson, M., Morrison, G., et al. 2007, ApJ, 670, 156
Das, S., Sherwin, B. D., Aguirre, P., et al. 2011, Phys. Rev. Lett., 107, 021301
Davé, R., Finlator, K., & Oppenheimer, B. D. 2012, MNRAS, 421, 98
de Bernardis, P., Ade, P. A. R., Bock, J. J., et al. 2000, Nature, 404, 955
De Breuck, C., Weiss, A., Bethermin, M., et al. 2019, arXiv e-prints, arXiv:1909.12554
de Graauw, T., Haser, L. N., Beintema, D. A., et al. 1996, A&A, 315, L49
De Looze, I., Cormier, D., Lebouteiller, V., et al. 2014, A&A, 568, A62
Delvecchio, I., Gruppioni, C., Pozzi, F., et al. 2014, MNRAS, 439, 2736
Deo, R. P., Richards, G. T., Crenshaw, D. M., & Kraemer, S. B. 2009, ApJ, 705, 14
Di Matteo, T., Springel, V., & Hernquist, L. 2005, Nature, 433, 604
Diamond-Stanic, A. M. & Rieke, G. H. 2012, ApJ, 746, 168
Díaz-Santos, T., Armus, L., Charmandaris, V., et al. 2017, ApJ, 846, 32

Dole, H., Lagache, G., Puget, J. L., et al. 2006, A&A, 451, 417
Dors, O. L., Pérez-Montero, E., Hägele, G. F., Cardaci, M. V., & Krabbe, A. C. 2016, MNRAS, 456, 4407
Draine, B. T. & Li, A. 2007, ApJ, 657, 810
Elbaz, D., Dickinson, M., Hwang, H. S., et al. 2011, A&A, 533, A119
Enard, D. 1991, Journal of Optics, 22, 33
Engelbracht, C. W., Gordon, K. D., Rieke, G. H., et al. 2005, ApJ, 628, L29
Engelbracht, C. W., Rieke, G. H., Gordon, K. D., et al. 2008, ApJ, 678, 804
Fabian, A. C. 2006, in ESA Special Publication, Vol. 604, The X-ray Universe 2005, ed. A. Wilson, 463
Fabian, A. C., Iwasawa, K., Reynolds, C. S., & Young, A. J. 2000, PASP, 112, 1145
Fabian, A. C., Rees, M. J., Stella, L., & White, N. E. 1989, MNRAS, 238, 729
Faisst, A. L., Schaerer, D., Lemaux, B. C., et al. 2020, ApJS, 247, 61
Farrah, D., Lebouteiller, V., Spoon, H. W. W., et al. 2013, ApJ, 776, 38
Fazio, G. G., Hora, J. L., Allen, L. E., et al. 2004, ApJS, 154, 10
Ferguson, H. C. 1995, Space Telesc. Sci. Inst, 12, 5
Ferland, G. J., Chatzikos, M., Guzmán, F., et al. 2017, Rev. Mexicana Astron. Astrofis., 53, 385
Fernández-Ontiveros, J. A., Armus, L., Baes, M., et al. 2017, PASA, 34, e053
Fernández-Ontiveros, J. A., Pérez-Montero, E., Vílchez, J. M., Amorín, R., & Spinoglio, L. 2021, A&A, 652, A23
Fernández-Ontiveros, J. A., Spinoglio, L., Pereira-Santaella, M., et al. 2016, ApJS, 226, 19
Ferrara, A., Vallini, L., Pallottini, A., et al. 2019, MNRAS, 489, 1
Ferrarese, L. 2002, ApJ, 578, 90
Ferrarese, L. & Merritt, D. 2000, ApJ, 539, L9
Fiore, F., Brusa, M., Cocchia, F., et al. 2003, A&A, 409, 79
Fischer, J., Sturm, E., González-Alfonso, E., et al. 2010, A&A, 518, L41
Franceschini, A., Aussel, H., Cesarsky, C. J., Elbaz, D., & Fadda, D. 2001, A&A, 378, 1
Fukugita, M. & Peebles, P. J. E. 2004, ApJ, 616, 643
Galliano, F., Nersesian, A., Bianchi, S., et al. 2021, arXiv e-prints, arXiv:2101.00456
Gardner, J. P., Mather, J. C., Clampin, M., et al. 2006, Space Sci. Rev., 123, 485
Gebhardt, K., Bender, R., Bower, G., et al. 2000, ApJ, 539, L13
Gehrz, R. D., Becklin, E. E., de Pater, I., et al. 2009, Advances in Space Research, 44, 413
Giavalisco, M., Lee, K. S., Ferguson, H. C., et al. 2004, in American Astronomical Society Meeting Abstracts, Vol. 205, 94.12
Gilmozzi, R. & Spyromilio, J. 2007, The Messenger, 127, 11
Goldsmith, P. F., Langer, W. D., Pineda, J. L., & Velusamy, T. 2012, ApJS, 203, 13
González-Alfonso, E., Armus, L., Carrera, F. J., et al. 2017a, PASA, 34, e054
González-Alfonso, E., Armus, L., Carrera, F. J., et al. 2017b, PASA, 34, e054
González-Alfonso, E., Fischer, J., Graciá-Carpio, J., et al. 2014, A&A, 561, A27
González-Alfonso, E., Fischer, J., Spoon, H. W. W., et al. 2017c, ApJ, 836, 11
Goulding, A. D. & Alexander, D. M. 2009, MNRAS, 398, 1165
Goulding, A. D., Alexander, D. M., Bauer, F. E., et al. 2012, ApJ, 755, 5
Green, J., Schechter, P., Baltay, C., et al. 2012, arXiv e-prints, arXiv:1208.4012

Greenhouse, M. A., Feldman, U., Smith, H. A., et al. 1993, ApJS, 88, 23

Griffin, M. J., Abergel, A., Abreu, A., et al. 2010, A&A, 518, L3

Grogin, N. A., Kocevski, D. D., Faber, S. M., et al. 2011, ApJS, 197, 35

Gruppioni, C., Berta, S., Spinoglio, L., et al. 2016, MNRAS, 458, 4297

Gruppioni, C., Pozzi, F., Rodighiero, G., et al. 2013, MNRAS, 432, 23

Güsten, R., Nyman, L. Å., Schilke, P., et al. 2006, A&A, 454, L13

Hanson, D., Hoover, S., Crites, A., et al. 2013, Phys. Rev. Lett., 111, 141301

Harikane, Y., Ouchi, M., Inoue, A. K., et al. 2019, arXiv e-prints, arXiv:1910.10927

Harikane, Y., Ouchi, M., Inoue, A. K., et al. 2020, ApJ, 896, 93

Harrison, C. M., Alexander, D. M., Mullaney, J. R., & Swinbank, A. M. 2014, MNRAS, 441, 3306

Hashimoto, T. 2019, in American Astronomical Society Meeting Abstracts, Vol. 233, American Astronomical Society Meeting Abstracts #233, 106.05

Hashimoto, T., Inoue, A. K., Tamura, Y., et al. 2018, arXiv e-prints, arXiv:1811.00030

Heckman, T. M. & Best, P. N. 2014, ARA&A, 52, 589

Herrera-Camus, R., Bolatto, A. D., Wolfire, M. G., et al. 2015, ApJ, 800, 1

Ho, L. C. & Keto, E. 2007, ApJ, 658, 314

Hollenbach, D. & McKee, C. F. 1989, ApJ, 342, 306

Hönig, S. F., Smette, A., Beckert, T., et al. 2008, A&A, 485, L21

Hopkins, P. F., Hernquist, L., Cox, T. J., Robertson, B., & Springel, V. 2006, ApJS, 163, 50

Hopkins, P. F., Richards, G. T., & Hernquist, L. 2007, ApJ, 654, 731

Houck, J. R., Roellig, T. L., van Cleve, J., et al. 2004, ApJS, 154, 18

Hubble, E. P. 1936, Realm of the Nebulae (Yale University Press)

Hunter, D. A., Kaufman, M., Hollenbach, D. J., et al. 2001, ApJ, 553, 121

Inami, H., Armus, L., Charmandaris, V., et al. 2013, ApJ, 777, 156

Inoue, A. K., Tamura, Y., Matsuo, H., et al. 2016, Science, 352, 1559

Ivezić, Ž., Kahn, S. M., Tyson, J. A., et al. 2019, ApJ, 873, 111

Johns, M., McCarthy, P., Raybould, K., et al. 2012, in Society of Photo-Optical Instrumentation Engineers (SPIE) Conference Series, Vol. 8444, Ground-based and Airborne Telescopes IV, ed. L. M. Stepp, R. Gilmozzi, & H. J. Hall, 84441H

Juarez, Y., Maiolino, R., Mujica, R., et al. 2009, A&A, 494, L25

Kaneda, H., Ishihara, D., Oyabu, S., et al. 2017, PASA, 34, e059

Kashino, D., Silverman, J. D., Sanders, D., et al. 2019, ApJS, 241, 10

Kennicutt, Robert C., J. 1998, ARA&A, 36, 189

Kennicutt, R. C. & Evans, N. J. 2012, ARA&A, 50, 531

Kessler, M. F., Steinz, J. A., Anderegg, M. E., et al. 1996, A&A, 500, 493

Keto, E. 2002, ApJ, 580, 980

Keto, E. 2007, ApJ, 666, 976

Kewley, L. J., Groves, B., Kauffmann, G., & Heckman, T. 2006, MNRAS, 372, 961

Kormendy, J. & Bender, R. 2011, Nature, 469, 377

Kormendy, J., Bender, R., & Cornell, M. E. 2011, Nature, 469, 374

Kormendy, J. & Gebhardt, K. 2001, in American Institute of Physics Conference Series, Vol. 586, 20th

Texas Symposium on relativistic astrophysics, ed. J. C. Wheeler & H. Martel, 363–381
Kormendy, J. & Ho, L. C. 2013, ARA&A, 51, 511
LaMassa, S. M., Heckman, T. M., & Ptak, A. 2012, ApJ, 758, 82
Laporte, N., Ellis, R. S., Boone, F., et al. 2017, ApJ, 837, L21
Launay, J. M. & Roueff, E. 1977, A&A, 56, 289
Laureijs, R., Amiaux, J., Arduini, S., et al. 2011, arXiv e-prints, arXiv:1110.3193
Le Floc'h, E., Papovich, C., Dole, H., et al. 2005, ApJ, 632, 169
Lebouteiller, V., Barry, D. J., Goes, C., et al. 2015, ApJS, 218, 21
Lee, J. C., Hwang, H. S., & Ko, J. 2013, ApJ, 774, 62
Lehmann, I., Hasinger, G., Schmidt, M., et al. 2001, in X-ray Astronomy: Stellar Endpoints, AGN, and the Diffuse X-ray Background, ed. N. E. White, G. Malaguti, & G. G. C. Palumbo, Vol. 599, 189–198
Lequeux, J., Peimbert, M., Rayo, J. F., Serrano, A., & Torres-Peimbert, S. 1979, A&A, 500, 145
Leung, T. K. D., Olsen, K. P., Somerville, R. S., et al. 2020, ApJ, 905, 102
Lilly, S. J., Le Fevre, O., Hammer, F., & Crampton, D. 1996, ApJ, 460, L1
Lilly, S. J., Peng, Y., Carollo, M., & Renzini, A. 2013, in IAU Symposium, Vol. 295, The Intriguing Life of Massive Galaxies, ed. D. Thomas, A. Pasquali, & I. Ferreras, 141–150
Lilly, S. J., Tresse, L., Hammer, F., Crampton, D., & Le Fevre, O. 1995, ApJ, 455, 108
Liseau, R., Justtanont, K., & Tielens, A. G. G. M. 2006, A&A, 446, 561
Lorenzoni, S., Bunker, A. J., Wilkins, S. M., et al. 2013, MNRAS, 429, 150
Luridiana, V., Morisset, C., & Shaw, R. A. 2015, A&A, 573, A42
Lusso, E., Comastri, A., Simmons, B. D., et al. 2012, MNRAS, 425, 623
Lutz, D., Kunze, D., Spoon, H. W. W., & Thornley, M. D. 1998, A&A, 333, L75
Lutz, D., Sturm, E., Genzel, R., et al. 2000, ApJ, 536, 697
Lutz, D., Sturm, E., Tacconi, L. J., et al. 2008, ApJ, 684, 853
Macaulay, E., Wehus, I. K., & Eriksen, H. K. 2013, Phys. Rev. Lett., 111, 161301
Madau, P. & Dickinson, M. 2014, ARA&A, 52, 415
Madau, P., Ferguson, H. C., Dickinson, M. E., et al. 1996, MNRAS, 283, 1388
Madden, S. C. 2000, New A Rev., 44, 249
Madden, S. C., Poglitsch, A., Geis, N., Stacey, G. J., & Townes, C. H. 1997, ApJ, 483, 200
Madden, S. C., Rémy-Ruyer, A., Galametz, M., et al. 2013, PASP, 125, 600
Magnelli, B., Popesso, P., Berta, S., et al. 2013, A&A, 553, A132
Magorrian, J., Tremaine, S., Richstone, D., et al. 1998, AJ, 115, 2285
Maiolino, R., Nagao, T., Grazian, A., et al. 2008, A&A, 488, 463
Maloney, P. R. 1997, Ap&SS, 248, 105
Mannucci, F., Cresci, G., Maiolino, R., et al. 2009, MNRAS, 398, 1915
Marconi, A., Risaliti, G., Gilli, R., et al. 2004, MNRAS, 351, 169
Martin, D. H. & Puplett, E. 1970, Infrared Physics, 10, 105
Meléndez, M., Kraemer, S. B., Armentrout, B. K., et al. 2008, ApJ, 682, 94
Merloni, A. & Heinz, S. 2008, MNRAS, 388, 1011
Miyaji, T., Hasinger, G., & Schmidt, M. 2000, Advances in Space Research, 25, 827
Moster, B. P., Somerville, R. S., Maulbetsch, C., et al. 2010, ApJ, 710, 903

Moustakas, J., Kennicutt, Robert C., J., Tremonti, C. A., et al. 2010, ApJS, 190, 233

Muzzin, A., Marchesini, D., Stefanon, M., et al. 2013, ApJ, 777, 18

Nagao, T., Maiolino, R., & Marconi, A. 2006, A&A, 447, 863

Nagao, T., Maiolino, R., Marconi, A., & Matsuhara, H. 2011, A&A, 526, A149

Nakagawa, T., Shibai, H., Onaka, T., et al. 2014, in Society of Photo-Optical Instrumentation Engineers (SPIE) Conference Series, Vol. 9143, Space Telescopes and Instrumentation 2014: Optical, Infrared, and Millimeter Wave, 91431I

Nakagawa, T. & Spica Working Group. 2002, Advances in Space Research, 30, 2129

Nakagawa, T. & Spica Working Group. 2004, Advances in Space Research, 34, 645

Nandra, K., Barret, D., Barcons, X., et al. 2013, arXiv e-prints, arXiv:1306.2307

National Academies of Sciences, Engineering, and Medicine. 2021, Pathways to Discovery in Astronomy and Astrophysics for the 2020s (Washington, DC: The National Academies Press)

Negishi, T., Onaka, T., Chan, K. W., & Roellig, T. L. 2001, A&A, 375, 566

Negrello, M., Gonzalez-Nuevo, J., De Zotti, G., et al. 2017, MNRAS, 470, 2253

Nesvadba, N., Kneissl, R., Cañameras, R., et al. 2016, A&A, 593, L2

Netzer, H. 2013, The Physics and Evolution of Active Galactic Nuclei (Cambridge University Press)

Oliva, E., Marconi, A., & Moorwood, A. F. M. 1999, A&A, 342, 87

Onaka, T. & Nakagawa, T. 2005, Advances in Space Research, 36, 1123

Onodera, M., Carollo, C. M., Lilly, S., et al. 2016, ApJ, 822, 42

Onoue, M., Bañados, E., Mazzucchelli, C., et al. 2020, ApJ, 898, 105

Papovich, C., Rudnick, G., Le Floc'h, E., et al. 2007, ApJ, 668, 45

Pardo, J. R. 2019, in ALMA Development Workshop, 36

Penzias, A. A. & Wilson, R. W. 1965, ApJ, 142, 419

Pereira-Santaella, M., Diamond-Stanic, A. M., Alonso-Herrero, A., & Rieke, G. H. 2010, ApJ, 725, 2270

Pereira-Santaella, M., Rigopoulou, D., Farrah, D., Lebouteiller, V., & Li, J. 2017, MNRAS, 470, 1218

Pérez-Montero, E. & Contini, T. 2009, MNRAS, 398, 949

Pérez-Torres, M., Mattila, S., Alonso-Herrero, A., Aalto, S., & Efstathiou, A. 2021, A&A Rev., 29, 2

Perley, R. A., Chandler, C. J., Butler, B. J., & Wrobel, J. M. 2011, ApJ, 739, L1

Pilbratt, G. L., Riedinger, J. R., Passvogel, T., et al. 2010, A&A, 518, L1

Pilyugin, L. S., Grebel, E. K., & Kniazev, A. Y. 2014, AJ, 147, 131

Planck Collaboration, Ade, P. A. R., Aghanim, N., et al. 2014, A&A, 571, A16

Poglitsch, A., Waelkens, C., Geis, N., et al. 2010, A&A, 518, L2

Polletta, M. d. C., Wilkes, B. J., Siana, B., et al. 2006, ApJ, 642, 673

Pope, A., Wagg, J., Frayer, D., et al. 2013, ApJ, 772, 92

Posselt, W., Holota, W., Kulinyak, E., et al. 2004, in Society of Photo-Optical Instrumentation Engineers (SPIE) Conference Series, Vol. 5487, Optical, Infrared, and Millimeter Space Telescopes, ed. J. C. Mather, 688–697

Puget, J. L. & Leger, A. 1989, ARA&A, 27, 161

Raveri, M. 2016, Phys. Rev. D, 93, 043522

Reddy, N. A., Pettini, M., Steidel, C. C., et al. 2012, ApJ, 754, 25

Rémy-Ruyer, A., Madden, S. C., Galliano, F., et al. 2015, A&A, 582, A121

Rieke, G. H., Wright, G. S., Böker, T., et al. 2015, PASP, 127, 584
Rieke, G. H., Young, E. T., Engelbracht, C. W., et al. 2004, ApJS, 154, 25
Rigopoulou, D., Kunze, D., Lutz, D., Genzel, R., & Moorwood, A. F. M. 2002, A&A, 389, 374
Rodighiero, G., Daddi, E., Baronchelli, I., et al. 2011, ApJ, 739, L40
Rodighiero, G., Vaccari, M., Franceschini, A., et al. 2010, A&A, 515, A8
Roelfsema, P. R., Shibai, H., Armus, L., et al. 2018, PASA, 35, e030
Röllig, M., Ossenkopf, V., Jeyakumar, S., Stutzki, J., & Sternberg, A. 2006, A&A, 451, 917
Rush, B., Malkan, M. A., & Spinoglio, L. 1993a, ApJS, 89, 1
Rush, B., Malkan, M. A., & Spinoglio, L. 1993b, ApJS, 89, 1
Rybak, M., Calistro Rivera, G., Hodge, J. A., et al. 2019, ApJ, 876, 112
Rybak, M., Zavala, J. A., Hodge, J. A., Casey, C. M., & Werf, P. v. d. 2020, ApJ, 889, L11
Salama, F. 2008, in Organic Matter in Space, ed. S. Kwok & S. Sanford, Vol. 251, 357–366
Sanders, D. B. & Mirabel, I. F. 1996, ARA&A, 34, 749
Sanders, R. L., Shapley, A. E., Jones, T., et al. 2020, arXiv e-prints, arXiv:2009.07292
Sargsyan, L., Lebouteiller, V., Weedman, D., et al. 2012, ApJ, 755, 171
Satyapal, S., Kamal, L., Cann, J. M., Secrest, N. J., & Abel, N. P. 2021, ApJ, 906, 35
Schaerer, D., Ginolfi, M., Béthermin, M., et al. 2020, A&A, 643, A3
Schaller, M., Dalla Vecchia, C., Schaye, J., et al. 2015, MNRAS, 454, 2277
Schechter, P. 1976, ApJ, 203, 297
Schenker, M. A., Robertson, B. E., Ellis, R. S., et al. 2013, ApJ, 768, 196
Schöck, M., Els, S., Riddle, R., et al. 2009, PASP, 121, 384
Schreiber, C., Pannella, M., Elbaz, D., et al. 2015, A&A, 575, A74
Scoville, N., Abraham, R. G., Aussel, H., et al. 2007, ApJS, 172, 38
Scoville, N., Lee, N., Vanden Bout, P., et al. 2017, ApJ, 837, 150
Senarath, M. R., Brown, M. J. I., Cluver, M. E., et al. 2018, ApJ, 869, L26
Shankar, F., Weinberg, D. H., & Miralda-Escudé, J. 2009, ApJ, 690, 20
Shipley, H. V., Papovich, C., Rieke, G. H., Brown, M. J. I., & Moustakas, J. 2016, ApJ, 818, 60
Shirley, R.; Roehlly, Y. e. a. 2020, HELP main catalogue, VO resource provided by The Virtual Observatory at susseX (VOX)
Sibthorpe, B., Helmich, F., Roelfsema, P., Kaneda, H., & Shibai, H. 2015, in EAS Publications Series, Vol. 75-76, 411–417
Silk, J. & Mamon, G. A. 2012, Research in Astronomy and Astrophysics, 12, 917
Smith, J. D. T., Draine, B. T., Dale, D. A., et al. 2007a, ApJ, 656, 770
Smith, K. M., Zahn, O., & Doré, O. 2007b, Phys. Rev. D, 76, 043510
Sodroski, T. J., Odegard, N., Arendt, R. G., et al. 1997, ApJ, 480, 173
Soifer, B. T. & Neugebauer, G. 1991, AJ, 101, 354
Somerville, R. S. & Davé, R. 2015, ARA&A, 53, 51
Spergel, D. N., Verde, L., Peiris, H. V., et al. 2003, ApJS, 148, 175
Spinoglio, L., Alonso-Herrero, A., Armus, L., et al. 2017, PASA, 34, e057
Spinoglio, L., Dasyra, K. M., Franceschini, A., et al. 2012, ApJ, 745, 171
Spinoglio, L., Dasyra, K. M., Franceschini, A., et al. 2014, ApJ, 791, 138

Spinoglio, L. & Malkan, M. A. 1989, ApJ, 342, 83
Spinoglio, L. & Malkan, M. A. 1992, ApJ, 399, 504
Spinoglio, L., Malkan, M. A., Rush, B., Carrasco, L., & Recillas-Cruz, E. 1995, ApJ, 453, 616
Spinoglio, L., Malkan, M. A., Smith, H. A., González-Alfonso, E., & Fischer, J. 2005, ApJ, 623, 123
Spoon, H. W. W., Farrah, D., Lebouteiller, V., et al. 2013, ApJ, 775, 127
Spoon, H. W. W. & Holt, J. 2009, ApJ, 702, L42
Stanway, E. R. & Eldridge, J. J. 2018, MNRAS, 479, 75
Steffen, A. T., Barger, A. J., Cowie, L. L., Mushotzky, R. F., & Yang, Y. 2003, ApJ, 596, L23
Steidel, C. C., Adelberger, K. L., Shapley, A. E., et al. 2003, ApJ, 592, 728
Steidel, C. C., Shapley, A. E., Pettini, M., et al. 2004, ApJ, 604, 534
Steidel, C. C., Strom, A. L., Pettini, M., et al. 2016, ApJ, 826, 159
Stern, J. & Laor, A. 2012, MNRAS, 426, 2703
Stierwalt, S., Armus, L., Charmandaris, V., et al. 2014, ApJ, 790, 124
Stone, M., Veilleux, S., Meléndez, M., et al. 2016, ApJ, 826, 111
Sturm, E., González-Alfonso, E., Veilleux, S., et al. 2011, ApJ, 733, L16
Sturm, E., Lutz, D., Verma, A., et al. 2002, A&A, 393, 821
Sutter, J., Dale, D. A., Croxall, K. V., et al. 2019, ApJ, 886, 60
Sutter, J., Dale, D. A., Sandstrom, K., et al. 2021, arXiv e-prints, arXiv:2102.08865
Swinyard, B., Nakagawa, T., Merken, P., et al. 2009, Experimental Astronomy, 23, 193
Tacchella, S., Dekel, A., Carollo, C. M., et al. 2016, MNRAS, 457, 2790
Tamura, Y., Mawatari, K., Hashimoto, T., et al. 2019, ApJ, 874, 27
Tielens, A. G. G. M. & Hollenbach, D. 1985, ApJ, 291, 722
Tinsley, B. M. 1977, ApJ, 211, 621
Togi, A. & Smith, J. D. T. 2016, ApJ, 830, 18
Tombesi, F., Meléndez, M., Veilleux, S., et al. 2015, Nature, 519, 436
Tommasin, S., Spinoglio, L., Malkan, M. A., & Fazio, G. 2010, ApJ, 709, 1257
Tommasin, S., Spinoglio, L., Malkan, M. A., et al. 2008, ApJ, 676, 836
Tremonti, C. A., Heckman, T. M., Kauffmann, G., et al. 2004, ApJ, 613, 898
Troncoso, P., Maiolino, R., Sommariva, V., et al. 2014, A&A, 563, A58
Tueller, J. 2011, in American Astronomical Society Meeting Abstracts, Vol. 218, American Astronomical Society Meeting Abstracts #218, 115.02
Vaccari, M. 2016, in The Universe of Digital Sky Surveys, ed. N. R. Napolitano, G. Longo, M. Marconi, M. Paolillo, & E. Iodice, Vol. 42, 71
Veilleux, S., Cecil, G., & Bland-Hawthorn, J. 2005, ARA&A, 43, 769
Veilleux, S., Meléndez, M., Sturm, E., et al. 2013, ApJ, 776, 27
Venemans, B. P., Walter, F., Neeleman, M., et al. 2020, ApJ, 904, 130
Véron-Cetty, M. P. & Véron, P. 2010, A&A, 518, A10
Vidal, T. H. G., Loison, J.-C., Jaziri, A. Y., et al. 2017, MNRAS, 469, 435
Vincenzo, F., Belfiore, F., Maiolino, R., Matteucci, F., & Ventura, P. 2016, MNRAS, 458, 3466
Vishwas, A., Ferkinhoff, C., Nikola, T., et al. 2018, ApJ, 856, 174
Wagg, J., Aravena, M., Brisbin, D., et al. 2020, MNRAS, 499, 1788

Walter, F., Riechers, D., Novak, M., et al. 2018, ApJ, 869, L22
Wang, L., Pearson, W. J., Cowley, W., et al. 2019, A&A, 624, A98
Wechsler, R. H. & Tinker, J. L. 2018, ARA&A, 56, 435
Werner, M. W., Roellig, T. L., Low, F. J., et al. 2004, ApJS, 154, 1
Wootten, A. & Thompson, A. R. 2009, IEEE Proceedings, 97, 1463
Wright, A. H., Robotham, A. S. G., Driver, S. P., et al. 2017, MNRAS, 470, 283
Wright, G. S., Wright, D., Goodson, G. B., et al. 2015, PASP, 127, 595
Wu, H., Cao, C., Hao, C.-N., et al. 2005, ApJ, 632, L79
Wu, Y., Charmandaris, V., Hao, L., et al. 2006, ApJ, 639, 157
Wu, Y., Charmandaris, V., Huang, J., Spinoglio, L., & Tommasin, S. 2009, ApJ, 701, 658
Xie, Y. & Ho, L. C. 2019, ApJ, 884, 136
Xie, Y., Li, A., & Hao, L. 2017, ApJS, 228, 6
Young, E. T., Becklin, E. E., Marcum, P. M., et al. 2012, ApJ, 749, L17
Yun, M. S., Reddy, N. A., & Condon, J. J. 2001, ApJ, 554, 803
Zahid, H. J., Dima, G. I., Kudritzki, R.-P., et al. 2014, ApJ, 791, 130
Zhang, K., Wang, T.-G., Gaskell, C. M., & Dong, X.-B. 2013, ApJ, 762, 51
Zhuang, M.-Y., Ho, L. C., & Shangguan, J. 2019, ApJ, 873, 103

Appendix A: Line correlations

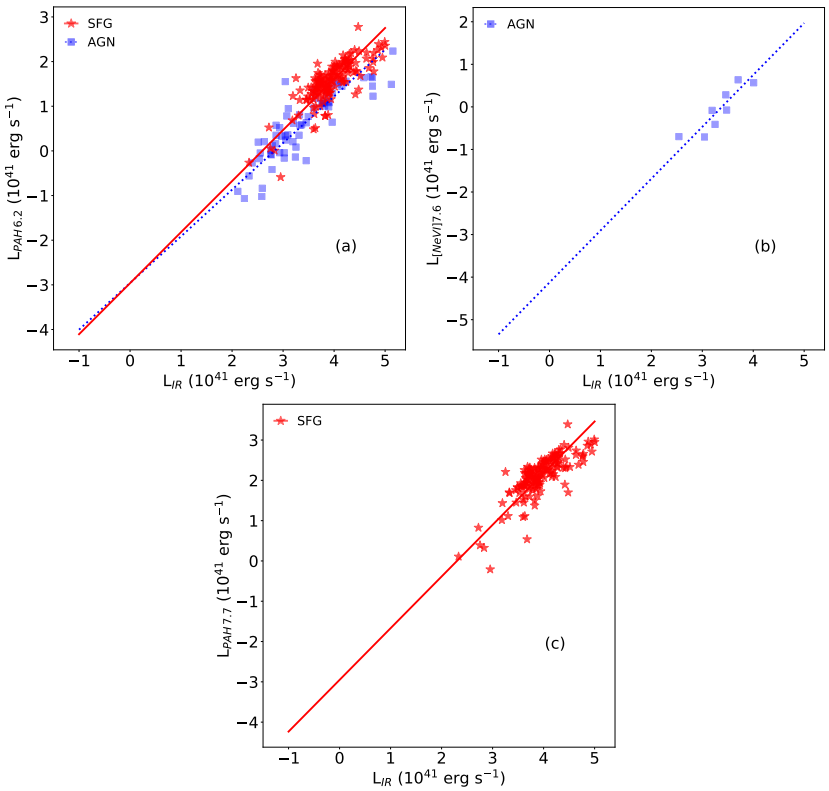

Figure 1: (a: left) Luminosity of the PAH feature at 6.2 µm as a function of the total IR luminosity. **(b: centre)** [NeVI]7.65 µm line luminosity as a function of the total IR luminosity. **(c: right)** Luminosity of the PAH feature at 7.7 µm as a function of the total IR luminosity. The same legend as in Fig. 3.5 was used.

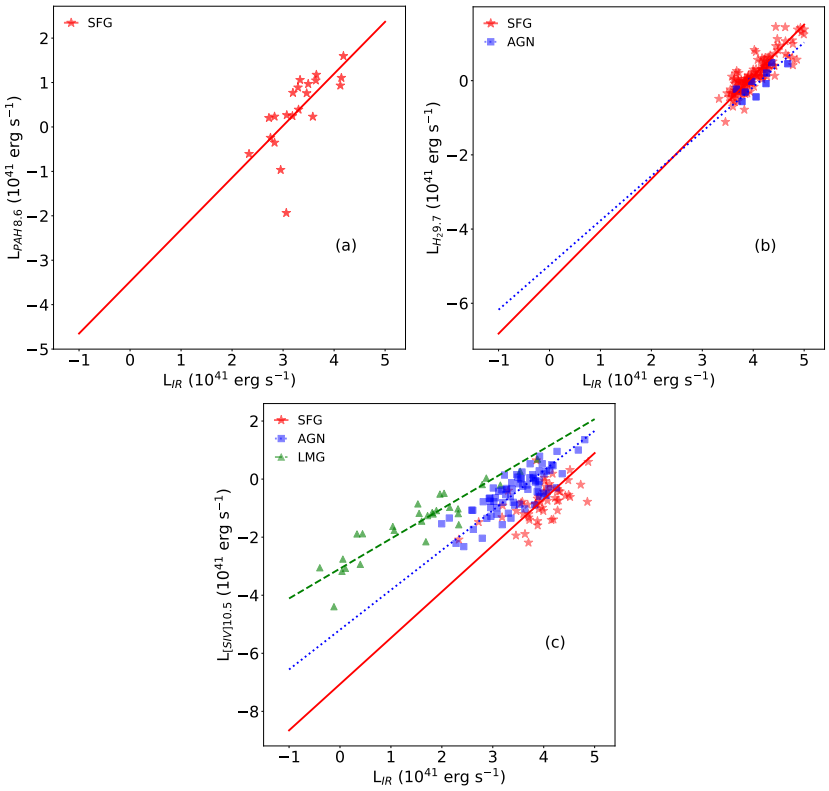

Figure 2: (a: left) Luminosity of the PAH feature at 8.6 µm as a function of the total IR luminosity. **(b: centre)** Luminosity of the H_2 molecular line at 9.7 µm as a function of the total IR luminosity. **(c: right)** [SIV]10.5 µm line luminosity as a function of the total IR luminosity. The same legend as in Fig. 3.5 was used.

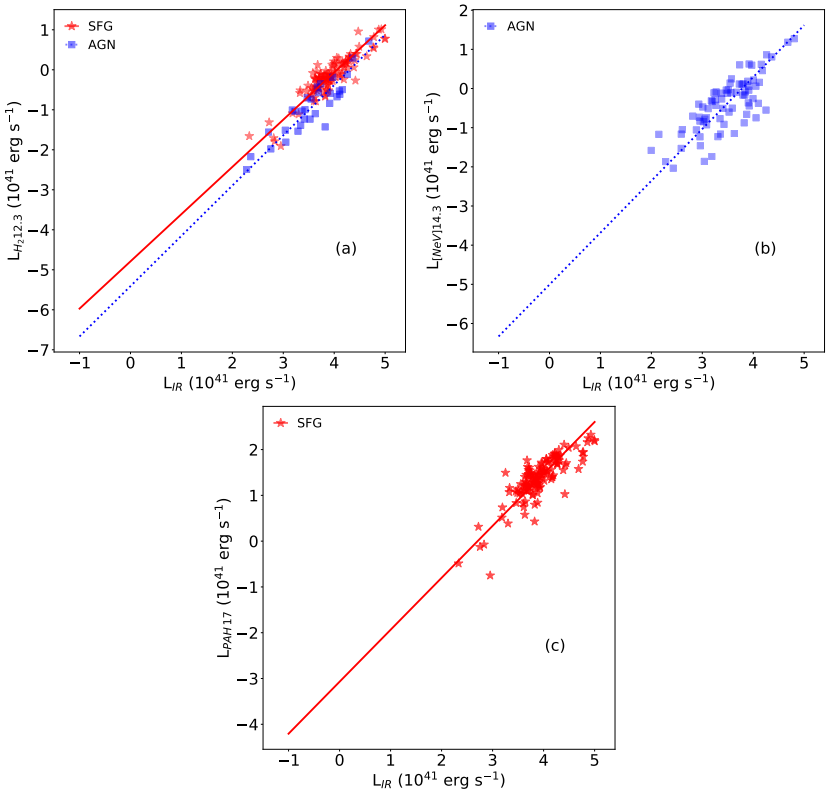

Figure 3: (a: left) Luminosity of the H_2 molecular line at 12.28 µm as a function of the total IR luminosity. **(b: centre)** [NeV]14.3 µm line luminosity as a function of the total IR luminosity. **(c: right)** Luminosity of the PAH feature at 17 µm as a function of the total IR luminosity. The same legend as in Fig. 3.5 was used.

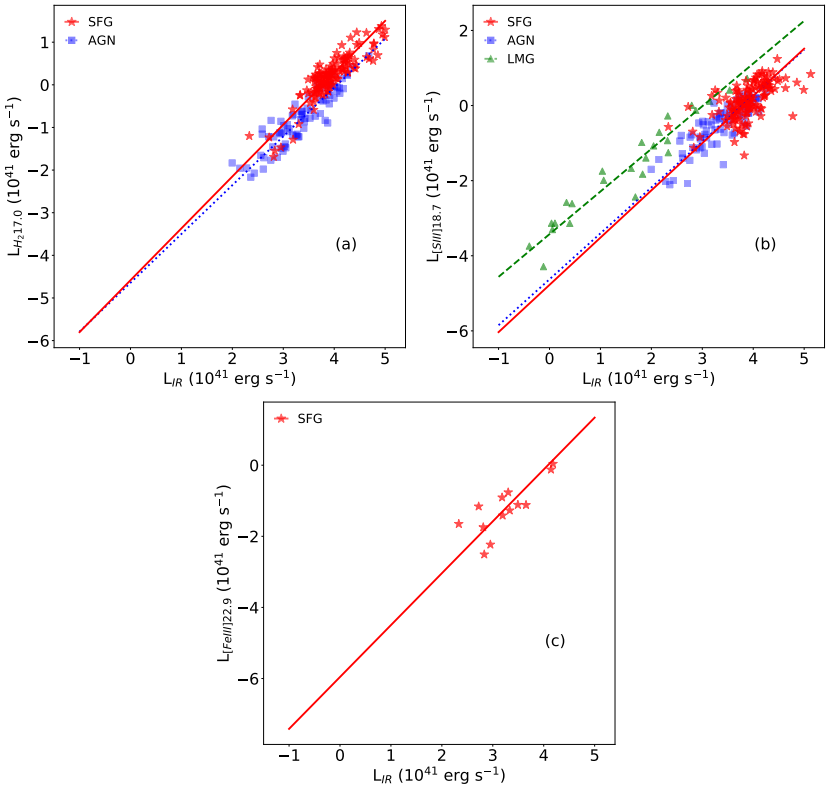

Figure 4: (a: left) Luminosity of the H_2 molecular line at 17.03 µm as a function of the total IR luminosity. **(b: centre)** [SIII]18.7 µm line luminosity as a function of the total IR luminosity. **(c: right)** [FeIII]22.93 µm line luminosity as a function of the total IR luminosity. The same legend as in Fig. 3.5 was used.

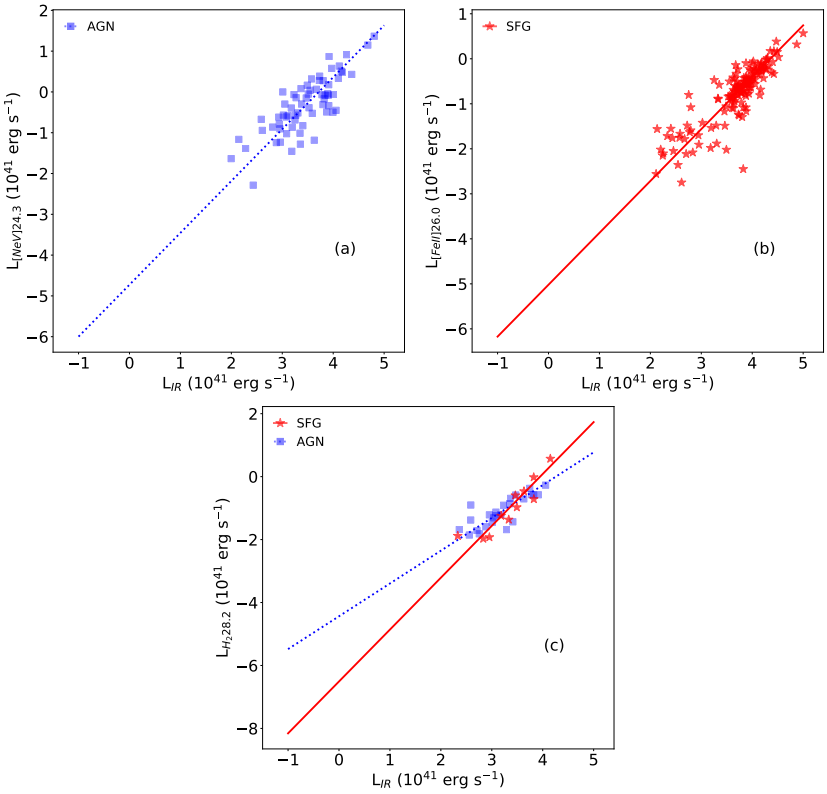

Figure 5: (a: left) [NeV]24.3 µm line luminosity as a function of the total IR luminosity. **(b: centre)** [FeII]25.99 µm line luminosity as a function of the total IR luminosity. **(c: right)** Luminosity of the H_2 molecular line at 28.22 µm as a function of the total IR luminosity. The same legend as in Fig. 3.5 was used.

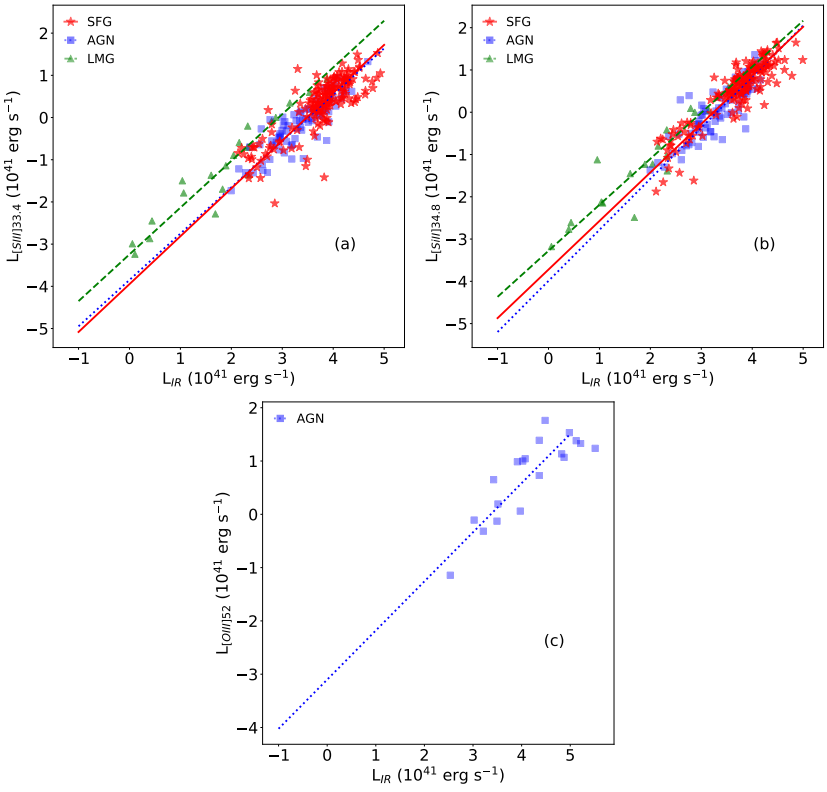

Figure 6: (a: left) [SIII]33.4 µm line luminosity as a function of the total IR luminosity. **(b: centre)** [SiII]34.8 µm line luminosity as a function of the total IR luminosity. **(c: right)** [OIII]52 µm line luminosity as a function of the total IR luminosity. The same legend as in Fig. 3.5 was used.

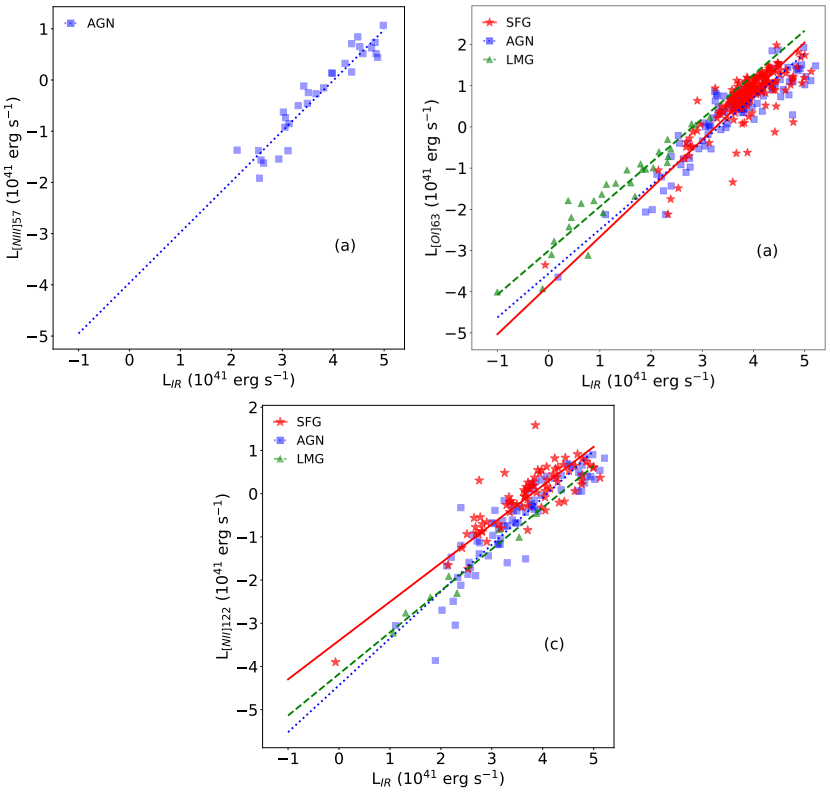

Figure 7: (a: left) [NIII]57 µm line luminosity as a function of the total IR luminosity. **(b: centre)** [OI]63.18 µm line luminosity as a function of the total IR luminosity. **(c: right)** [NII]122 µm line luminosity as a function of the total IR luminosity. The same legend as in Fig. 3.5 was used.

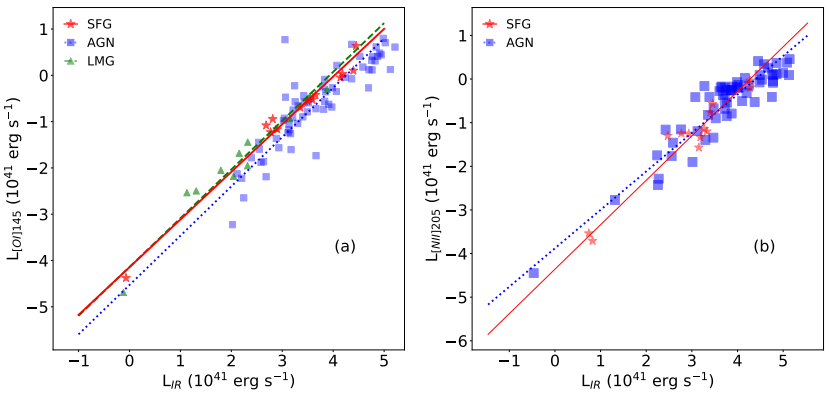

Figure 8: (a: left) [OI]145 µm line luminosity as a function of the total IR luminosity. **(b: right)** [NII]205 µm line luminosity as a function of the total IR luminosity. The same legend as in Fig. 3.5 was used.

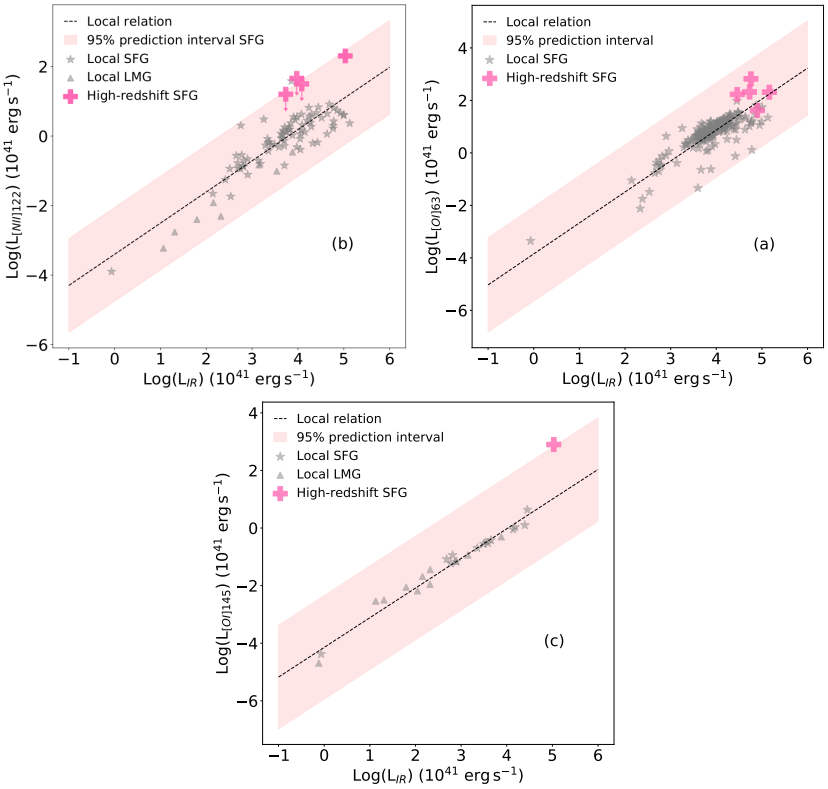

Figure 9: (a: left) Comparison between the local L_{IR}-$L_{[NII]122}$ relation for local SFGs (black dashed line) and high-redshift detections of [NII]122 µm line. The shaded area shows the 95% prediction interval for the local relation. The pink + sign indicates a detection for the [NII]122 µm line (De Breuck et al. 2019), while symbols with arrows indicate upper limits for high-redshift sources (Harikane et al. 2019). **(b: centre)** Comparison between the local L_{IR}-$L_{[OI]63}$ relation for local SFGs (black dashed line) and high-redshift detections of the [OI]63 µm line (pink symbol Rybak et al. 2019). **(c: right)** Comparison between the local L_{IR}-$L_{[OI]145}$ relation for local SFGs (black dashed line) and high-redshift detections of [OI]145 µm line (pink symbol De Breuck et al. 2019). The shaded area shows the 95% prediction interval for the local relation. Grey stars show local SFGs, while grey triangles show local LMGs.